

Inaugural dissertation
for
obtaining the doctoral degree
of the
Combined Faculty of Mathematics, Engineering and Natural Sciences
of the
Ruprecht - Karls – University
Heidelberg

Presented by
M.Sc. Lars Hellweg
born in: Ibbenbüren, Germany
Oral examination: 21.06.2024

Development of Chemogenetic Biosensors with Large Dynamic Ranges and Spectral Flexibility

Referees: Prof. Dr. Michael Brunner
Prof. Dr. Kai Johnsson

Abstract

Understanding cellular processes at the molecular level is fundamental for gaining insights into biological mechanisms and their implications in health and disease. Fluorescent biosensors have emerged as powerful tools in this regard, as they enable real-time monitoring of these processes with high spatiotemporal resolution using live-cell imaging. Despite significant progress in the development of biosensors, limitations still exist. While intensimetric biosensors often exhibit large dynamic ranges, they are susceptible to changes in sensor concentration and photobleaching, potentially resulting in skewed experimental results. In contrast, ratiometric FRET-based biosensors offer a more robust quantification, but often suffer from a low dynamic range and occupy a substantial part of the spectral space, hindering their multiplexing capability with other fluorescent tools.

To address these limitations, I developed a chemogenetic FRET system called ChemoX, based on a fluorescent protein FRET donor and rhodamine-based FRET acceptor, which is conjugated to the self-labeling protein HaloTag7. Engineering of a specific interface between the fluorescent protein and HaloTag7, enabled the generation of high efficiency FRET pairs. The spectral properties of ChemoX can be modified by either replacing the FRET donor with a fluorescent protein of different color, or by labeling HaloTag7 with spectrally distinct fluorophores, all while ensuring that a high FRET efficiency is maintained. The utilization of FRET pairs with large spectral separation combined with the ability to fine-tune their FRET efficiency, allowed for the generation of ChemoX biosensors with different colors and large dynamic ranges. I demonstrated the generalizability of this approach by developing biosensors for Ca^{2+} , ATP and NAD^+ with improved dynamic ranges compared to established FRET-based biosensors. Furthermore, the increased multiplexing capacity of ChemoX sensors enabled real-time monitoring of free NAD^+ at different subcellular localizations within the same cell, representing a valuable addition to existing tools for the investigation of compartmentalized NAD^+ dynamics.

Moreover, I leveraged the ChemoX interface to modulate the fluorescence intensity of bright rhodamine-based fluorophores and develop single-channel fluorescence lifetime-based ChemoX

sensors with far-red emission wavelengths. The spectral properties of these sensors hold promise for their use in *in vivo* applications. Finally, I generated bioluminescent ChemoX biosensors through simple fusion of the luciferase NanoLuc to the N-terminus of fluorescent ChemoX biosensors and demonstrated their compatibility for high-throughput screenings using microplate reader systems.

In summary, I developed a versatile chemogenetic system that allows for the development of biosensors with large dynamic ranges and spectral flexibility, providing the scientific community with a complemented toolbox for the investigation of important cell metabolites.

Zusammenfassung

Das Verständnis zellulärer Prozesse auf molekularer Ebene ist von grundlegender Bedeutung, um Einblicke in biologische Mechanismen und deren Auswirkungen auf Gesundheit und Krankheit zu gewinnen. Fluoreszierende Biosensoren haben sich in dieser Hinsicht als leistungsfähige Werkzeuge erwiesen, da sie die Echtzeitüberwachung dieser Prozesse mit hoher räumlicher und zeitlicher Auflösung ermöglichen. Trotz erfolgreicher Fortschritte bei der Biosensorik gibt es immer noch Einschränkungen. Während intensimetrische Biosensoren oft einen großen dynamischen Bereich aufweisen, sind sie anfällig für Veränderungen der Sensorkonzentration und Photobleichen, was zu verzerrten experimentellen Ergebnissen führen kann. Im Gegensatz dazu bieten ratiometrische FRET-basierte Biosensoren eine robustere Quantifizierung, leiden aber oft unter geringen dynamischen Bereichen und hohem spektralem Bedarf, was ihre Multiplexfähigkeit mit anderen fluoreszenten Werkzeugen einschränkt.

Um diese Einschränkungen zu überwinden, habe ich ein chemogenetisches FRET-System namens ChemoX entwickelt, das auf einem fluoreszenten Protein FRET-Donor und einem Rhodamin-basierten FRET-Akzeptor beruht, der mit dem selbstmarkierenden Protein HaloTag7 konjugiert ist. Durch die Entwicklung einer spezifischen Interaktionsoberfläche zwischen dem fluoreszenten Protein und HaloTag7 konnte ich hocheffiziente FRET-Paare erzeugen. Die spektralen Eigenschaften des chemogenetischen FRET-Paares können durch genetische Substitution mit andersfarbigen fluoreszenten Proteinen und durch Markierung von HaloTag7 mit verschiedenen Fluorophoren angepasst werden, wobei die hohe FRET-Effizienz erhalten bleibt. Die Verwendung von FRET-Paaren mit großem spektralem Abstand in Verbindung mit der Möglichkeit, ihre FRET-Effizienz fein abzustimmen, ermöglichte die Herstellung einer Farbpalette von ChemoX-Biosensoren mit großen dynamischen Bereichen. Ich habe gezeigt, dass dieser Ansatz verallgemeinert werden kann, indem ich Biosensoren für Ca^{2+} , ATP und NAD^+ entwickelt habe, die im Vergleich zu etablierten FRET-basierten Biosensoren verbesserte dynamische Bereiche aufweisen. Darüber hinaus ermöglichte die erhöhte Multiplexing-Kapazität der ChemoX-Sensoren die Echtzeit-Überwachung von freiem NAD^+ an verschiedenen subzellulären Lokalisationen innerhalb

derselben Zelle, was eine wertvolle Ergänzung zu den bestehenden Werkzeugen für die Untersuchung der Kompartimentierung von NAD^+ Konzentrationen darstellt.

Des Weiteren habe ich die Interaktionen in ChemoX genutzt, um die Fluoreszenzintensität von hellen Rhodamin-basierten Fluorophoren zu modulieren. Dies erlaubte die Entwicklung von Sensoren mit langen Emissionswellenlängen, dessen Fluoreszenzlebenszeit genutzt werden konnte um biologische Prozesse zu überwachen. Die spektralen Eigenschaften dieser Sensoren sind vielversprechend für den Einsatz in *in vivo*-Anwendungen. Abschliessend habe ich biolumineszente Biosensoren durch eine Fusion der Luciferase NanoLuc mit dem N-Terminus von ChemoX-Biosensoren hergestellt und ihre Kompatibilität für Hochdurchsatz-Screenings mit Mikroplatten-Lesesystemen nachgewiesen.

Zusammenfassend lässt sich sagen, dass ich ein vielseitiges chemogenetisches System entwickelt habe, das die Entwicklung von Biosensoren mit einem großen dynamischen Bereich und einer großen spektralen Flexibilität ermöglicht und der wissenschaftlichen Gemeinschaft einen vielseitigen Werkzeugkasten für die Untersuchung wichtiger Zellmetaboliten an die Hand gibt.

Acknowledgements

First and foremost, I would like to thank my supervisor Prof. Dr. Kai Johnsson for giving me the opportunity to work on this project. I highly appreciate your open-minded attitude and that you gave me the freedom to explore different projects. You helped me to grow as a scientist, to embrace my creativity and to adapt to changing circumstances. I could not have asked for a better supervisor during my time here in the lab.

Another big thank you goes to Dr. Julien Hiblot. I am very grateful for all your help and advices during my time as your master student as well as during my time as a PhD student. I learnt a lot from you and would not want to have missed the chance to work together with you. Especially, our work on the ChemoX project was an amazing time; I enjoyed our scientific discussions a lot.

I also want to thank Prof. Dr. Michael Brunner, Prof. Dr. Tobias Dick and PD Dr. Richard Wombacher for agreeing to be part of my thesis advisory and defense committee, and providing valuable input during our annual meetings.

A big thank you to Dr. Birgit Koch, Jana Kress and Paula Breuer for the generation of stable cell lines; Bettina Réssy and Dominik Schmidt for the synthesis of fluorophore substrates; Carmen Grosskurth for the supply with buffers and reagents; Dr. Sebastian Fabritz, Tatjana Rudi and Juliana Kling for mass spectrometry measurements; and Miroslaw Tarnawski for the crystallization, acquisition and structural refinement of proteins. Special thanks go to Andrea Bergner; not only did you support me wherever and whenever possible, but working next to you at the bench was always a special and happy moment for me.

I also want to thank Gwenaëlle Matthies, Ioannis Karagiannis, Mario Walter and Stephanie Mandras. Your help with administrative and logistical issues made my daily work incredibly easy.

Furthermore, I want to thank my two outstanding students Lucas Barck and Anna Edenhofer. I am genuinely grateful to have had the opportunity to supervise you and work with you on the ChemoX project. Your contributions were invaluable for the progress of the project. I am certain that both of you will have a bright future ahead of you.

Next, I want to thank the entire lab for making every day in the lab a good one on a scientific but also personal level. I would like to highlight my former and current office mates Dr. Fabio Raith, Dr. Konstantin Hinnah and Dr. Guy Mann. Our daily chats always cheer me up and get me into a good mood. I always like to think back about our start as 146strassenbande; the chemistry between us was simply incomparable. I also want to mention Dr. Stefanie Kühn, Yin-Hsi Lin, Dr. Magnus Huppertz and Dr. Jonas Wilhelm for our numerous coffee breaks, and post-work beer and dinner sessions. These joyful moments definitely made the time in the lab special.

I want to thank Dr. Konstantin Hinnah for proof-reading my thesis and providing valuable feedback during my time here; I learnt a lot from you.

I also want to express my deepest gratitude for my family and friends, in particular my parents Ingrid and Michael Hellweg, as well as my brothers Lukas and Jan Hellweg, who were always supportive of my decisions. I could always rely on you; without you I would not have achieved any of this.

Last but not least, I want to thank my partner-in-crime, Esther Rodríguez Correa. You were always there for me, supported me throughout this exciting journey and never let me down. I am incredibly grateful for having you by my side and I am very much looking forward to our future endeavors.

Table of Contents

Abstract.....	v
Zusammenfassung	vii
Acknowledgements.....	ix
Table of Contents.....	xi
List of Figures.....	xv
List of Tables	xvii
Chapter 1 – Introduction.....	1
1.1. Cellular processes.....	1
1.1.1. Compartmentalization of cellular processes.....	1
1.1.2. Methods for the detection of cellular processes.....	2
1.2. Fluorescence.....	3
1.2.1. Principles of fluorescence and FRET	3
1.2.2. Fluorescent proteins	6
1.2.3. Synthetic fluorophores	9
1.2.4. Self-labeling proteins	11
1.3. Fluorescent biosensors	14
1.3.1. Design and development.....	14
1.3.2. Classes of biosensors	17
1.3.2.1. Intensiometric biosensors.....	17
1.3.2.2. Ratiometric biosensors	19
1.3.2.3. Limitations of FRET biosensors	20
1.4. Previous work.....	22
1.5. Aims and Scope of the thesis.....	23
Chapter 2 – Results.....	25

Table of Contents

2.1.	Structural characterization of ChemoG1.....	25
2.2.	Development of an optimized chemogenetic FRET pair.....	26
2.3.	Expanding the spectral properties of ChemoG5.....	31
2.4.	Development of chemogenetic calcium sensors.....	39
2.5.	Development of chemogenetic ATP biosensors with superior performance	47
2.6.	Development of chemogenetic NAD ⁺ biosensors for multiplexing purposes.....	54
2.7.	Converting ChemoG-NAD into a red-shifted single-channel fluorescence lifetime sensor.....	68
2.8.	Converting fluorescence-based ChemoG biosensors into bioluminescence-based ChemoL biosensors.....	75
2.9.	Development of a fluorescent biosensor for NMN	81
Chapter 3 – Discussion.....		91
3.1.	Design of FRET pairs with high FRET efficiencies.....	91
3.2.	Improving the dynamic range of FRET-based biosensors	93
3.3.	Multiplexing capacity of current ChemoX biosensors.....	95
3.4.	Specificity and selectivity of current ChemoX biosensors	98
3.5.	Future <i>in vivo</i> applications of ChemoX biosensors	103
Chapter 4 – Conclusion and Outlook		105
Materials and Methods.....		107
Reagents, chemicals and fluorophores.....		107
Plasmids and cloning		110
Protein production.....		112
Protein crystallization		113
X-ray diffraction data collection and structure determination.....		114
Fluorescence spectroscopy measurements.....		116
Luminescence spectroscopy measurements		118
Analysis of biosensor response to varying concentrations of analytes.....		118

Calcium titrations	118
pH sensitivity assay	119
Determination of the FRET efficiency	119
Determination of the spectral overlap.....	119
Determination of the FRET ratio and FRET ratio changes	120
Determination of fluorescence intensity changes	120
Data processing and fitting.....	120
Cell culture.....	121
Generation of stable cell lines	121
Transfection and labeling of HeLa Kyoto and U-2 OS Flp-In T-REx cells.....	122
Co-localization staining with Hoechst and MitoTracker	122
Preparation of neuron cultures.....	122
Production of recombinant AAVs.....	123
AAV transduction and labeling of rat hippocampal neurons	124
Confocal microscopy.....	124
Widefield microscopy	125
Fluorescence lifetime imaging microscopy	125
Live cell experiments with ChemoG-CaM in HeLa Kyoto cells.....	127
Live cell experiments with ChemoG-CaM in rat hippocampal neurons.....	127
Live cell experiments with ATP biosensors in HeLa Kyoto cells	127
Live cell experiments with NAD ⁺ biosensors in U-2 OS cells	128
Image analysis	128
siRNA Knockdown experiments	129
Flow cytometry analysis	130
Quantitative PCR analysis.....	130

Table of Contents

Quantification of intracellular NMN and NAD ⁺ levels via mass spectrometry	132
Statistics and reproducibility.....	134
Graphical design	134
Bibliography.....	135
Appendix.....	147
Protein sequences.....	147
List of peer-reviewed publications.....	157

List of Figures

Figure 1 Compartmentalization of biological processes across scales.	1
Figure 2 Principles of fluorescence and FRET.	4
Figure 3 Criteria for FRET.	6
Figure 4 Overview of fluorescent proteins.	8
Figure 5 Overview of rhodamine fluorophores.	10
Figure 6 Overview of self-labeling proteins.	13
Figure 7 General design of fluorescent biosensors.	15
Figure 8 Overview of intensimetric biosensors.	18
Figure 9 Overview of ratiometric biosensors.	20
Figure 10 Design of the chemogenetic FRET pair ChemoG1.	22
Figure 11 Structural characterization of the chemogenetic FRET pair ChemoG1 _{TMR}	25
Figure 12 Engineering of an optimized chemogenetic FRET pair.	26
Figure 13 Structural analysis of ChemoG5 _{TMR}	28
Figure 14 Sensitivity of ChemoG FRET pairs to environmental changes.	29
Figure 15 Performance of ChemoG FRET pairs at different subcellular localizations.	30
Figure 16 Expanding the spectral properties of the ChemoG5 FRET acceptor.	32
Figure 17 Evaluation of cyanine fluorophores as ChemoG FRET acceptors.	34
Figure 18 Expanding the spectral properties of the ChemoG FRET donor.	37
Figure 19 Incorporation of red fluorescent proteins into the ChemoX design.	38
Figure 20 Development of the chemogenetic calcium sensor ChemoG-CaM.	40
Figure 21 Color palette of chemogenetic calcium biosensors.	43
Figure 22 Characterization of ChemoG-CaM in HeLa Kyoto cells and rat hippocampal neurons.	45
Figure 23 Development of the chemogenetic ATP biosensor ChemoG-ATP.	48
Figure 24 Characterization of ChemoG-ATP.	50
Figure 25 ChemoX-ATP sensors based on different fluorescent proteins.	50
Figure 26 Characterization of ChemoX-ATP sensors in HeLa Kyoto cells.	52
Figure 27 Development of the chemogenetic NAD ⁺ biosensor ChemoG-NAD.	56
Figure 28 Characterization of ChemoG-NAD.	58
Figure 29 Color palette of chemogenetic NAD ⁺ biosensors.	59
Figure 30 Characterization of ChemoG-NAD in U-2 OS cells.	61
Figure 31 Performance of ChemoG-NAD at different subcellular localizations.	64
Figure 32 Characterization of ChemoX-NAD sensors in U-2 OS cells.	65
Figure 33 Multiplexing of subcellular NAD ⁺ pools during acute genotoxic stress.	66

List of Figures

Figure 34 Multiplexing of subcellular NAD ⁺ pools in the nucleus and mitochondria.....	67
Figure 35 Fluorescence intensity of SiR is modulated in the ChemoG sensor context.	69
Figure 36 Development of single-channel NAD ⁺ biosensors with far-red emission wavelengths.....	70
Figure 37 ChemoD-NAD as fluorescence lifetime sensor for NAD ⁺	72
Figure 38 Characterization of ChemoD-NAD in U-2 OS cells.	74
Figure 39 Converting ChemoG-NAD into the bioluminescent sensor ChemoL-NAD.....	76
Figure 40 Characterization of ChemoL-NAD in U-2 OS cells.....	77
Figure 41 Bioluminescent calcium sensor ChemoL-CaM.	79
Figure 42 Bioluminescent ATP sensor ChemoL-ATP.....	80
Figure 43 Conformational changes of the bacterial DNA ligase A.	82
Figure 44 Development of the chemogenetic NMN biosensor ChemoG-NMN.	83
Figure 45 ChemoG-NMN is sensitive to changes in NAD ⁺ concentrations.	85
Figure 46 Structural analysis of eLigA(V69R-Y227R).	86
Figure 47 Assessing intracellular NMN and NAD ⁺ levels upon perturbation of the salvage pathway.	88
Figure 48 Possible strategies to develop selective sensing units for biosensors.	101

List of Tables

Table 1 Overview of different ChemoG variants.....	27
Table 2 ChemoG5 FRET pairs with different FRET acceptors.....	33
Table 3 Photophysical properties of fluorophores used as ChemoG5 FRET acceptors.....	33
Table 4 ChemoX FRET pairs.	39
Table 5 ChemoX calcium biosensors.	42
Table 6 ChemoG-CaM biosensors based on different FRET acceptors.....	43
Table 7 Overview of chemogenetic ATP biosensors.	51
Table 8 Overview of chemogenetic NAD ⁺ biosensors.	60
Table 9 Overview of ChemoD-NAD biosensors.	71
Table 10 Overview of ChemoD-NAD sensors based on fluorescence lifetime.....	73
Table 11 Overview of the bioluminescent ChemoL sensors.....	80
Table M1 Reagents and chemicals used for all experiments.....	107
Table M2 Chloroalkane fluorophore substrates used in all experiments.	109
Table M3 Buffers used for protein purification.	113
Table M4 Data collection and refinement statistics	115
Table M5 Tecan settings used for fluorescence-based measurements.	117
Table M6 Spectral settings for fluorescence microscopy.	126
Table M7 siRNA properties.	130
Table M8 qPCR primers.	132
Table M9 MRM method information for the LC-MS/MS analysis of NMN and NAD ⁺	133

List of Abbreviations

2DG	2-deoxy-D-glucose
2DG6P	2-deoxy-D-glucose-6-phosphate
A280	absorbance at 280 nm
AAV	adeno-associated virus
ADP	adenosine diphosphate
AMP	adenosine monophosphate
AP	action potential
APAT	average photon arrival time
APV	DL-2-amino-5-phosphonovaleric acid
ATP	adenosine triphosphate
BFP	blue fluorescent protein
BG	benzylguanine
BODIPY	boron dipyrromethene
BP	bandpass
BRET	bioluminescence resonance energy transfer
C ₅₀	concentration at half-maximal response
CA	chloroalkane
Ca ²⁺	calcium
CaM	calmodulin
CD38	cluster of differentiation 38
CFP	cyan fluorescent protein
CHR	chromophore
cp	circularly permuted
CPY	carborhodamine
C _t	threshold cycle
Ctrl	control
Cyto	cytosol
DIV	days <i>in vitro</i>
DMEM	Dulbeccos modified Eagle medium

DMSO	dimethyl sulfoxide
DNA	deoxyribonucleic acid
E	FRET efficiency
<i>E. coli</i>	<i>Escherichia coli</i>
<i>e.g.</i>	<i>exempli gratia</i>
efLigA	<i>Enterococcus faecalis</i> bacterial DNA ligase A
EGTA	ethylene glycol-bis(β -aminoethyl ether)-N,N,N',N'-tetraacetic acid
Em	emission
Ex	excitation
FACS	fluorescence-activated cell sorting
FBS	fetal bovine serum
FI	fluorescence intensity
FK866	(<i>E</i>)- <i>N</i> -[4-(1-benzoylpiperidin-4-yl)butyl]-3-(pyridin-3-yl)acrylamide
FLIM	fluorescence lifetime imaging microscopy
FLuc	firefly luciferase
FP	fluorescent protein
FRET	Förster resonance energy transfer
FSC	forward scatter
GFP	green fluorescent protein
Glc	glucose
GLUT	glucose transporter
Gly	glycine
GTP	guanosine triphosphate
HBSS	Hanks balanced salt solution
HEPES	4-(2-hydroxyethyl)-1-piperazineethanesulfonic acid
hiLigA	<i>Haemophilus influenzae</i> bacterial DNA ligase A
His	histidine
HT7	HaloTag7
<i>i.e.</i>	<i>id est</i>
IPTG	isopropyl- β -D-thiogalactopyranoside
IS	ion spray
J	spectral overlap

JF	Janelia Fluorophore
K_D	dissociation constant
$K_{D, app}$	apparent dissociation constant
LB	lysogeny broth
LC-MS/MS	liquid chromatography-mass spectrometry
LED	light-emitting diode
LI	luminescence intensity
LigA	bacterial DNA ligase A
$^{Max}\Delta FI/FI_0$	maximal fluorescence intensity change
$^{Max}\Delta R/R_0$	maximal FRET ratio change
$^{Max}\Delta\tau$	maximal fluorescence lifetime change
MEM	modified Eagle medium
Mito	mitochondria
MNNG	<i>N</i> -methyl- <i>N'</i> -nitro- <i>N</i> -nitrosoguanidine
MRM	multiple reaction monitoring
MS	mass spectrometry
N.D.	not determined
NAAD ⁺	nicotinic acid adenine dinucleotide
NaCl	sodium chloride
NAD ⁺	nicotinamide adenine dinucleotide
NADH	reduced nicotinamide adenine dinucleotide
NADP ⁺	nicotinamide adenine dinucleotide phosphate
NAM	nicotinamide
NAMPT	nicotinamide phosphoribosyltransferase
NB	neurobasal medium
NBQX	2,3-dioxo-6-nitro-7-sulfamoyl-benzo[f]quinoxaline
NIR	near-infrared
NLS	nuclear localization sequence
NMN	nicotinamide mononucleotide
NMNAT	nicotinamide mononucleotide adenylyltransferase
NR	nicotinamide riboside
NRK	nicotinamide riboside kinase

Nuc. env.	nuclear envelope
o.n.	over night
OD ₆₀₀	optical density at 600 nm
OPSL	optically-pumped semiconductor laser
PARP	poly-ADP-ribose polymerase
PARylation	poly-ADP-ribosylation
PBS	phosphate-buffered saline
PCR	polymerase chain reaction
PDB	Protein Data Bank
PEG	polyethylene glycol
Pen/Strep	penicillin/streptomycin
pH	potential hydrogen
PM	plasma membrane
PMSF	phenylmethylsulfonyl fluoride
POI	protein of interest
QY	quantum yield
R	distance
R ₀	Förster radius
rAAV	recombinant adeno-associated virus
RFP	red fluorescent protein
ROI	region of interest
RT	room temperature
RT-PCR	real-time polymerase chain reaction
S ₀	singlet ground state
S ₁	singlet excited state
SARM1	sterile alpha and TIR motif-containing 1
sdAb	single domain antibody
Ser	serine
SiR	silicon rhodamine
siRNA	short interfering ribonucleic acid
SLP	self-labeling protein
SMD	single molecule detection

Snifit	SNAP-tag-based indicators with a Fluorescent Intramolecular Tether
SSC	side scatter
STED	stimulated emission depletion
TCS	true confocal scanner
TEV	tobacco etch virus
TMR	tetramethylrhodamine
ttLigA	<i>Thermus thermophilus</i> bacterial DNA ligase A
Tyr	tyrosine
UV	ultraviolet
v/v	volume per volume
xHTL	exchangeable HaloTag ligand
YC 3.6	yellow cameleon 3.6
YFP	yellow fluorescent protein
ΔC_t	difference of threshold cycles
$\Delta FI/FI_0$	fluorescence intensity change
$\Delta R/R_0$	FRET ratio change
$\Delta \tau$	fluorescence lifetime change
ϵ	extinction coefficient
κ	orientation factor
λ	wavelength
τ	average fluorescence lifetime

Chapter 1 – Introduction

1.1. Cellular processes

1.1.1. Compartmentalization of cellular processes

Life relies on an intricate network of biomolecules including lipids, proteins and nucleic acids, which establish and orchestrate distinct physiological functions. To ensure correct functioning of this network, biological systems require a high degree of organization. Compartmentalization emerged as a key concept in achieving this through spatial sequestration of enzymes, metabolites and other biomolecules. Compartmentalization exists at different scales, ranging from the macroscopic level of organs and tissues that are specialized for certain tasks such as metabolism, cognition, or immune response, down to cellular organelles or even membrane-less condensates that act as chemical reactors¹ (**Figure 1**).

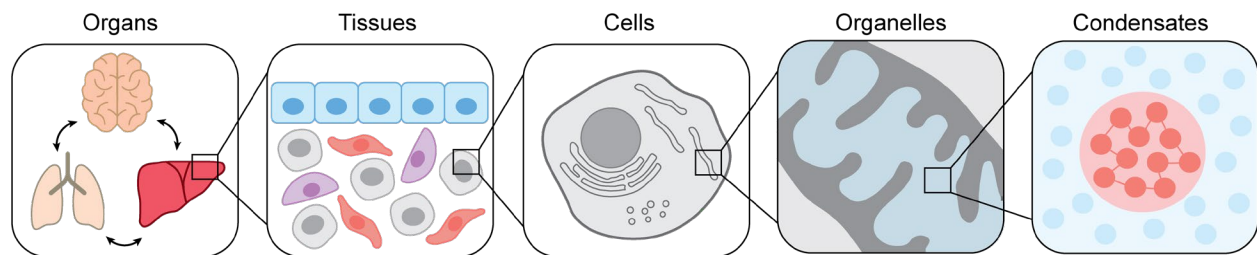


Figure 1| Compartmentalization of biological processes across scales.

Organs are in charge for distinct physiological functions such as cognition, respiration or metabolism. An organ is composed of multiple cell types, that are organized in highly specific patterns. The overall composition, architecture and interactions between the cells shape the function of an organ. Cells contain subcellular organelles, such as mitochondria and the nucleus, that execute distinct biochemical reactions maintaining cellular functions. Within subcellular compartments, membraneless local condensates can be formed through multivalent molecular assembly of biomolecules. Such ‘nano-compartmentalization’ can serve different functions including the acceleration of biochemical reactions. Adapted from Liron Bar-Peled and Nora Kory¹.

This spatial separation enables execution of incompatible biochemical reactions, such as those requiring a specific pH or redox status², and prevents undesirable crosstalk between pathways. It also shields the cell from potentially harmful or toxic intermediates generated during metabolic processes³. Moreover, it facilitates the regulation of signaling pathways⁴, epigenetic modifications⁵ or

metabolism⁶ by controlling the effective concentration of signaling molecules, metabolites and effectors. Dysregulation of compartmentalization is implicated in various diseases, including cancer, metabolic disorders, and neurodegenerative diseases^{7,8}. Thus, understanding how biomolecules are organized and regulated in such compartments at the molecular level provides insights into the underlying mechanisms of pathological disorders, which can help for the identification of potential targets for therapeutic interventions in health and disease.

1.1.2. Methods for the detection of cellular processes

To gain a comprehensive understanding of cellular behavior, including interactions, temporal dynamics, spatial organization and crosstalk between different pathways, one would ideally monitor all the different processes in the same cell simultaneously, and in real-time. Hence, researchers depend on experimental tools capable of dynamic, quantitative, and spatiotemporal measurements of these events. Various methods have been developed for this purpose, each with its own set of advantages and disadvantages. Omics technologies like metabolomics, proteomics, and transcriptomics offer valuable insights into the molecular composition, interactions, and dynamics of biological systems, detecting hundreds of molecules with high sensitivity and specificity. Furthermore, the combination of omics approaches with imaging or immunoprecipitation techniques enabled the detection of biomolecules in single cells or even organelles⁹⁻¹¹. However, the spatiotemporal resolution of these measurements is not sufficient for monitoring dynamic subcellular processes in real-time. Moreover, they require time-consuming sample preparation and cell lysis. Such samples thus might not represent the native state of the cell. Enzymatic assays represent an alternative approach that allows the detection of metabolites or enzymatic activity through the production of light or a change in color¹². These assays are fast, simple and cost-efficient, making them well-suited for high-throughput screenings. However, they typically involve lysis of entire cell populations resulting in loss of spatial information across cells and subcellular compartments. Additionally, they provide often only indirect measurements based on enzymatic conversion of the target molecule.

In contrast, imaging techniques such as fluorescence or electron microscopy provide high spatial resolution and allow direct visualization of cellular dynamics. Fluorescent readouts, in particular, are highly advantageous for monitoring cellular processes due to their high sensitivity and compatibility with live-cell imaging. Multiple fluorescent probes can be specifically targeted to subcellular localizations, allowing for precise localization and multiplexed quantification within cellular compartments. Moreover, fluorescence imaging offers the ability to monitor dynamic changes in real-time, providing valuable insights into the spatiotemporal regulation of cellular functions.

1.2. Fluorescence

1.2.1. Principles of fluorescence and FRET

Fluorescence describes the capacity of a substance to absorb a photon or electromagnetic radiation, and rapidly emit the absorbed energy in form of light. First described by the Spanish physician Nicolas Monardes in 1565¹³, this phenomenon was later coined by the physicist George G. Stokes, who characterized the fluorescence of uranium glass under ultraviolet (UV) light¹⁴. He described the conversion of light from shorter to longer wavelengths, which is commonly referred to as Stoke's shift. Fluorescent molecules, or fluorophores, typically consist of conjugated double bonds that allow excitation of electrons by photons (**Figure 2a**). Upon irradiation with light of appropriate energy, *i.e.*, wavelength, electrons are excited from the singlet ground state (S_0) to a higher-energy singlet state (S_1). From there, the electron transitions to the lowest vibrational level of the excited S_1 state through radiation-less loss of energy (*i.e.*, heat), before returning to its singlet ground state by emission of a photon (fluorescence). As a result of vibrational relaxation, the emitted photon exhibits lower energy, *i.e.*, a longer wavelength, compared to the absorbed photon (**Figure 2b-c**). The time it takes for a fluorophore to return to its ground state after excitation determines its fluorescence lifetime, which typically falls within the order of nanoseconds.

The energy of the excited electron can be also transferred from the excited fluorophore (donor) to a secondary fluorophore (acceptor) in a non-radiative manner (**Figure 2d**), *i.e.*, without the emission of a photon. This results in the excitation of the acceptor fluorophore, which can in turn emit a photon *via* fluorescence. Theodor Förster described this phenomenon first in 1948¹⁵, which gave

rise to its name Förster resonance energy transfer, or short FRET. Since FRET represents an alternative route for the excited donor fluorophore to relax back to its ground state, the number of emitted donor photons decreases. This results in a reduced average fluorescence lifetime and fluorescence intensity of the donor, whereas the fluorescence intensity of the acceptor increases (**Figure 2e-f**).

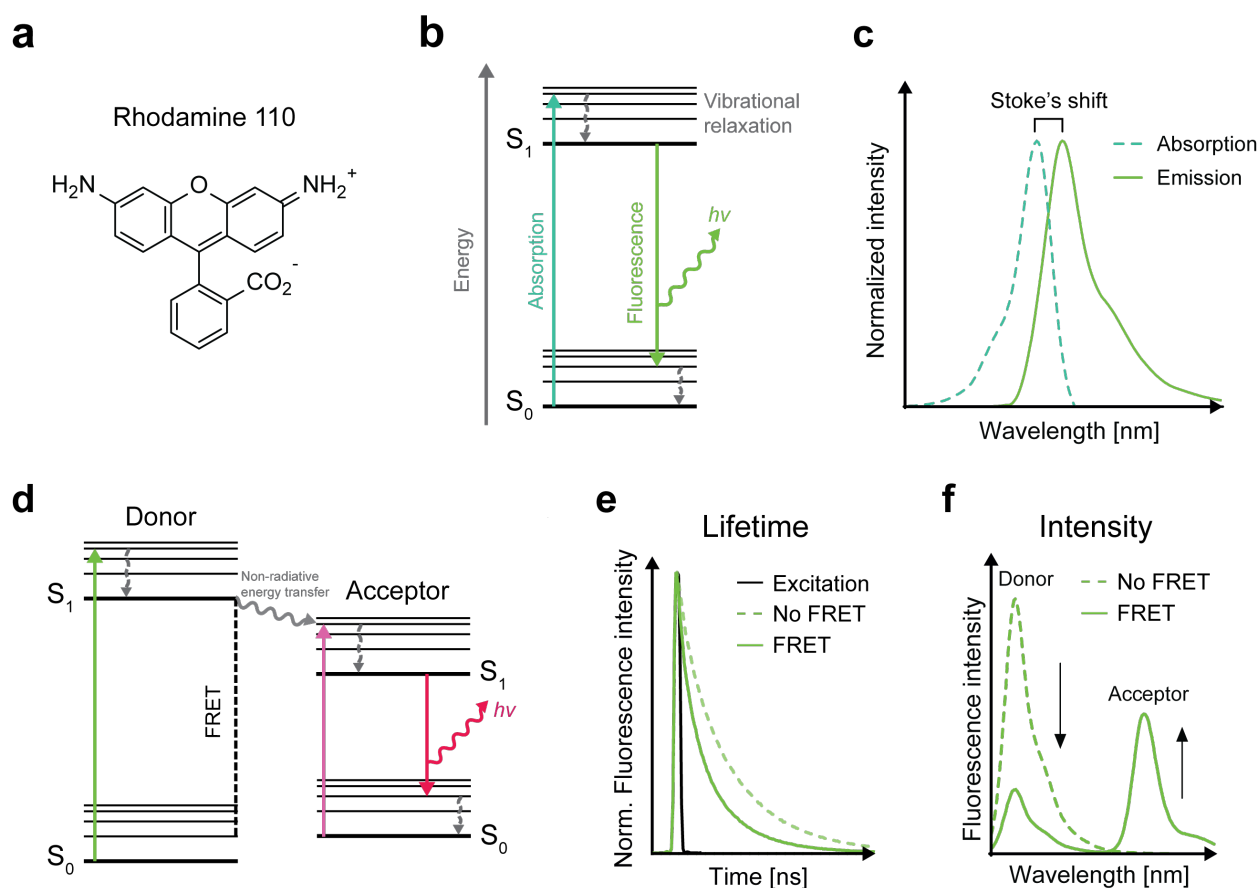


Figure 2| Principles of fluorescence and FRET.

a. Chemical structure of the fluorophore rhodamine 110, containing conjugated double bonds that can be excited by the absorption of a photon. **b.** Simplified Jablonski diagram depicting the principles of fluorescence. Absorption of a photon leads to the excitation of an electron from the singlet ground state (S_0) to a higher-energy excited singlet state (S_1). Within this state, the electron relaxes towards the lowest vibrational level (vibrational relaxation) before returning to the ground singlet state through emission of a photon (fluorescence). The energy lost during the vibrational relaxation results in a decreased energy, *i.e.*, longer wavelength, of the emitted compared to the absorbed photon. **c.** Exemplary spectra of the absorption (dashed line) and emission of a fluorophore. The shift in the wavelength between maximal absorption and emission is known as Stoke's shift. **d.** Simplified Jablonski diagram depicting the principles of FRET. The energy of an excited electron of one fluorophore (donor) can be transferred in a non-radiative manner (*i.e.*, without the emission of a photon) to an electron of a secondary fluorophore (acceptor), which leads to excitation of the

acceptor fluorophore. After vibrational relaxation, the excited acceptor electron loses its energy by emission of a photon returning to the ground singlet state. **e.** Exemplary fluorescence decay curves of a FRET donor in absence (No FRET) or presence of a FRET acceptor (FRET). The short excitation pulse is depicted in black. **f.** Exemplary fluorescence emission spectra of a FRET donor in absence (No FRET) or presence of a FRET acceptor (FRET). The fluorescence lifetime (**e**) and fluorescence intensity (**f**) of the FRET donor decreases in presence of the FRET acceptor due to a decreased number of emitted donor photons. Instead, the fluorescence intensity of the excited FRET acceptor emerges (**f**).

Several factors determine the occurrence of FRET: the energy transferred by the excited donor fluorophore must align with the energy needed to excite the acceptor fluorophore, which generally occurs if the fluorescence emission spectrum of the donor overlaps with the excitation spectrum of the acceptor (spectral overlap); the fluorophores need to be in close proximity (typically 1-10 nm); and the dipoles of the fluorophores need to be properly aligned (relative orientation), *i.e.*, high FRET when parallel *versus* low FRET when perpendicular (**Figure 3**). Together, these factors determine the FRET efficiency (E), which is particularly sensitive to changes in the distance of the FRET pair. This is summarized by the Förster equation:

$$E = \frac{R_0^6}{R^6 + R_0^6}$$

where R represents the given distance between the donor and acceptor fluorophore, and R_0 the distance at which E is half-maximal. R_0 is influenced by various factors, including the spectral overlap and relative orientation of the FRET pair:

$$R_0 = 0.211 \sqrt[6]{\kappa^2 \times n^{-4} \times QY_D \times J(\lambda)}$$

where κ stands for the orientation factor, n for the refractive index of the ambient medium, QY_D for the quantum yield of the donor (*i.e.*, fraction of emitted over absorbed photons), and $J(\lambda)$ for the spectral overlap. The spectral overlap can be determined based on the following equation:

$$J(\lambda) = \frac{\int_0^\infty FI_D(\lambda) \times \epsilon_A(\lambda) \times \lambda^4 d\lambda}{\int_0^\infty F_D(\lambda) d\lambda}$$

where FI_D represents the normalized donor fluorescence intensity, ϵ_A the extinction coefficient of the acceptor (*i.e.*, maximum absorption of light at a given wavelength), and λ the wavelength.

Thus, FRET pairs with long wavelengths, a high quantum yield and extinction coefficient of the donor and acceptor, respectively, favor efficient FRET in addition to the aforementioned criteria. Ultimately, all of these factors should be considered when selecting effective FRET pairs.

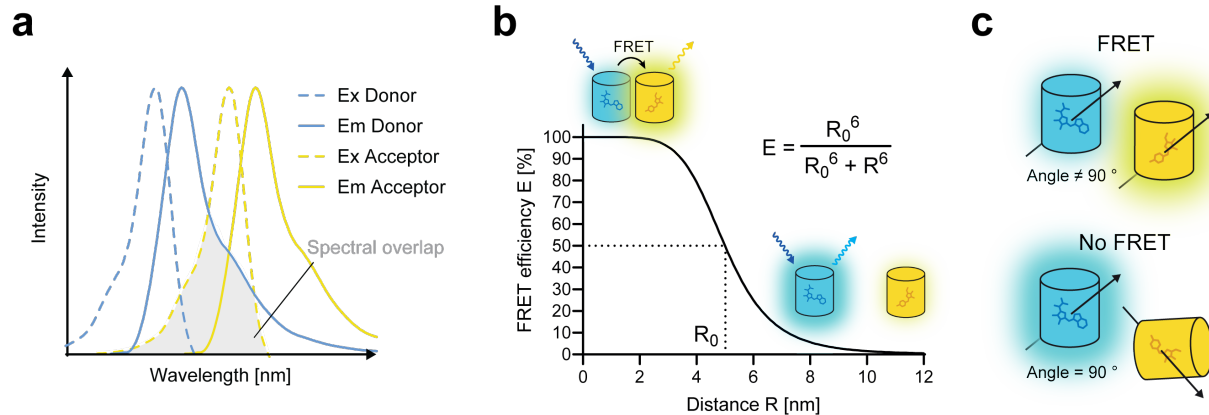


Figure 3| Criteria for FRET.

a. Spectral overlap (grey area) between the FRET donor emission (Em) spectrum (blue, solid line) and the FRET acceptor excitation (Ex) spectrum (yellow, dashed line). **b.** Distance dependency of the FRET efficiency (E) according to the Förster equation (depicted in the upper right corner). An exemplary example is shown for a Förster radius (R_0) set to 5 nm. The FRET efficiency is plotted against the distance (R) between the FRET donor and acceptor. A short distance promotes efficient FRET. **c.** The relative orientation between the dipoles (black arrows) of FRET donor and acceptor affects the FRET efficiency. Parallel orientation favors efficient FRET, opposed to a perpendicular orientation.

1.2.2. Fluorescent proteins

In 1961, Osamu Shimomura noticed a green protein that co-purified during the isolation of the photo-protein Aequorin from the jellyfish *Aequorea victoria*¹⁶. This green by-product turned out to be a fluorescent protein (FP), an unexpected finding that would revolutionize biological research. Only decades later, the three-dimensional structure of this green fluorescent protein (GFP) was solved through X-ray crystallography^{17, 18} revealing a barrel-like structure made of 11 anti-parallel β -sheets (**Figure 4a**), which is sealed at both ends through an α -helix that runs through its center. The chromophore is formed by a tripeptide within the α -helix (Ser65-Tyr66-Gly67)^{19, 20}, which undergoes a series of autocatalytic reactions including cyclization and oxidation, facilitated by the protective environment of the β -barrel (**Figure 4b**). The matured chromophore exists in an

equilibrium between a neutral protonated and an anionic deprotonated state, that affects the absorption and fluorescence intensity of GFP, rendering it sensitive to changes in pH (**Figure 4c**)²¹.

Pioneered by Roger Y. Tsien, the spectral properties of GFP were diversified through substitution of Tyr66 with other aromatic amino acids and the mutation of amino acids in close proximity to the chromophore. This yielded spectrally distinct FPs ranging from blue to yellow (BFP and YFP, respectively)^{22, 23}. The color palette of FPs was further expanded with red FPs (RFPs) derived from Anthozoa species²⁴, and so-called near-infrared (NIR) FPs based on bacterial phytochrome receptors²⁵ (**Figure 4d**). However, the latter ones depend on the binding of a biliverdin chromophore, rendering their use in cellular systems less straightforward compared to auto-fluorescent GFP-like FPs. In addition to expanding the spectral properties of FPs, efforts were made to improve their photo- and biophysical properties, which yielded monomeric FPs like the recently developed mStayGold2 or mScarlet3 with unprecedented brightness and photostability²⁶⁻³². These optimizations have broadened the applicability of FPs as fluorescent markers, reporters of gene expression and reporter units for biosensors. Despite the impactful contribution of FPs in biological research and the continuous progress in developing brighter and more robust FPs, they still entail certain limitations. Notably, FPs are relatively large (*e.g.*, GFP: 27 kDa), which can influence the stability, folding or function of a protein to which they are genetically fused. Furthermore, they exhibit significant heterogeneity in their brightness, photostability, pH sensitivity and maturation time, potentially resulting in artifacts during fluorescence-based measurements.

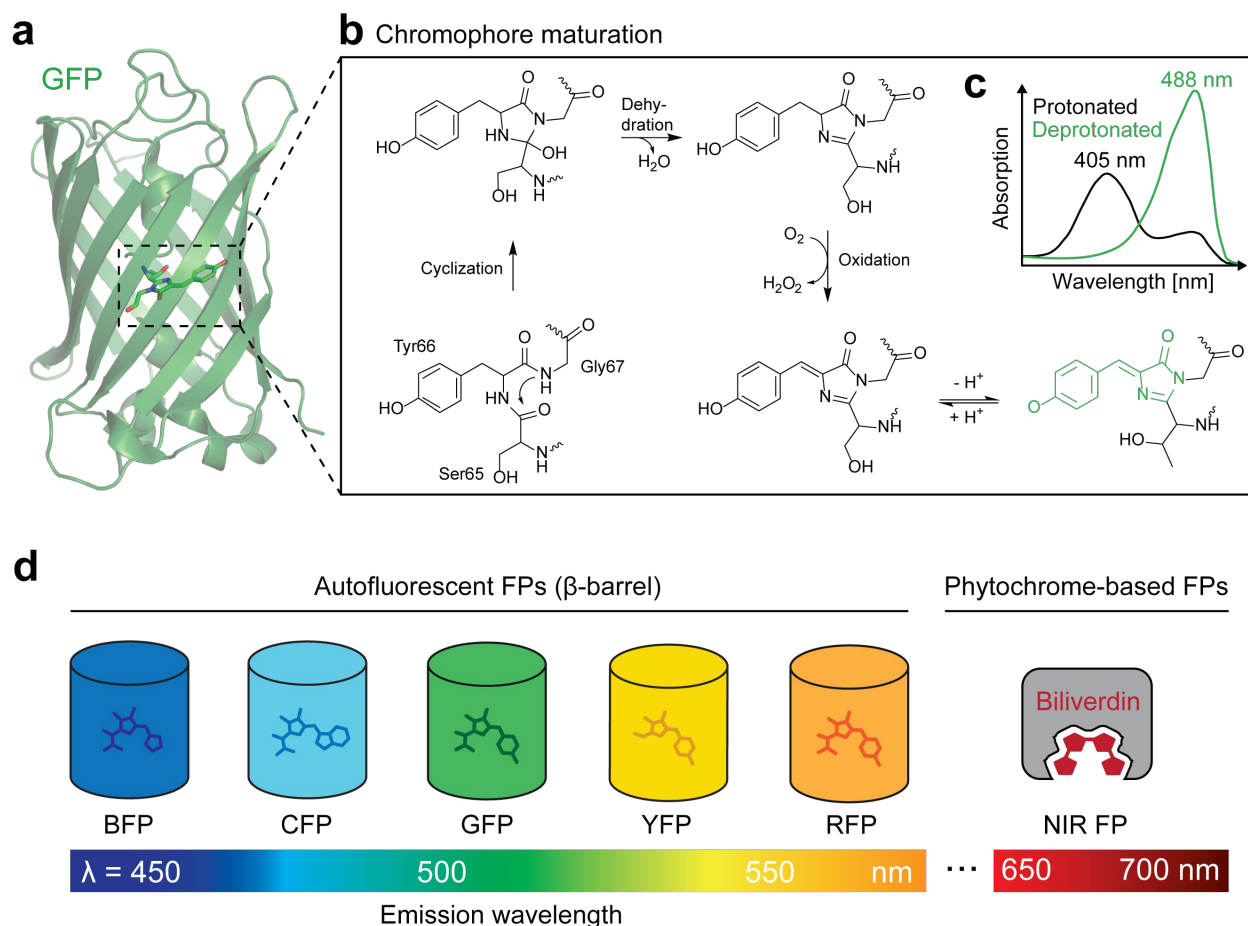


Figure 4 | Overview of fluorescent proteins.

a. X-ray crystal structure of the green fluorescent protein (GFP, PDB ID: 2Y0G), depicted as semi-transparent cartoon. 11 anti-parallel β -strands form a barrel-like structure that is sealed on both ends through a central α -helix. Within the barrel, the GFP chromophore is formed through autocatalytic reaction of a tripeptide within the α -helix. The chromophore is depicted as sticks. **b.** GFP chromophore maturation. After torsional rearrangements, the backbone nitrogen of Gly67 makes a nucleophilic attack onto the carbonyl group of Ser65 resulting in cyclization of the backbones. The imidazolin-5-one intermediate is formed through dehydration, before oxidation (in presence of molecular oxygen) of the C α -C β bond of Tyr66, resulting in an extended conjugated electron system. The matured chromophore exists in an equilibrium between a neutral protonated and anionic deprotonated state. **c.** In the protonated state, the chromophore exhibits a maximum absorption wavelength around 405 nm, which shifts towards 488 nm in the deprotonated state. The maximum emission wavelength is not affected by the protonation state. **d.** Schematic representation of different fluorescent proteins (FPs), based on a β -barrel-like structure or on a bacterial phytochrome that binds biliverdin acting as fluorophore. NIR = near-infra-red. Depicted below is a pseudo-colored representation of the emission wavelengths of the different FPs.

1.2.3. Synthetic fluorophores

Synthetic fluorophores have a long history dating back to 1856, when William H. Perkin coincidentally produced a fluorescent molecule, mauvine, during his attempts to synthesize the anti-malaria drug quinine³³. Over the years, significant advances have been made in the design and synthesis of fluorescent molecules, giving rise to different fluorophore classes such as fluoresceins, rhodamines, cyanines or boron-dipyrromethenes (BODIPYs)³⁴.

Today, rhodamines represent one of the most commonly used class of fluorophores owing to their enhanced brightness, spectral versatility and high cell permeability. They are based on a xanthene core linked to an isobenzofuran. A unique feature of rhodamines is their ability to transition between an ‘open’ zwitterionic form and a ‘closed’ spirolactone form (**Figure 5a**). In the open state, they are charged and fluorescent, while in the closed state, they are non-fluorescent, but more cell-permeable. This open-closed equilibrium is affected by several factors, including changes in the local environment and the presence of electron-withdrawing groups in the chemical structure^{35, 36}. Substitution of the oxygen of the xanthene core with dimethylated carbon or silicon gave rise to so-called carbo- and siliconrhodamines, respectively (**Figure 5b**)^{37, 38}. These rhodamine derivatives exhibit red-shifted excitation and emission wavelengths, and an open-closed equilibrium that is shifted towards the closed cell-permeable form, making them particularly useful for live-cell imaging purposes. Additionally, chemical modification of rhodamine-based fluorophores with azetidines, fluorine or sulfonamides enabled fine-tuning of the open-closed equilibrium, which further improved their applicability for fluorescence microscopy^{35, 36}.

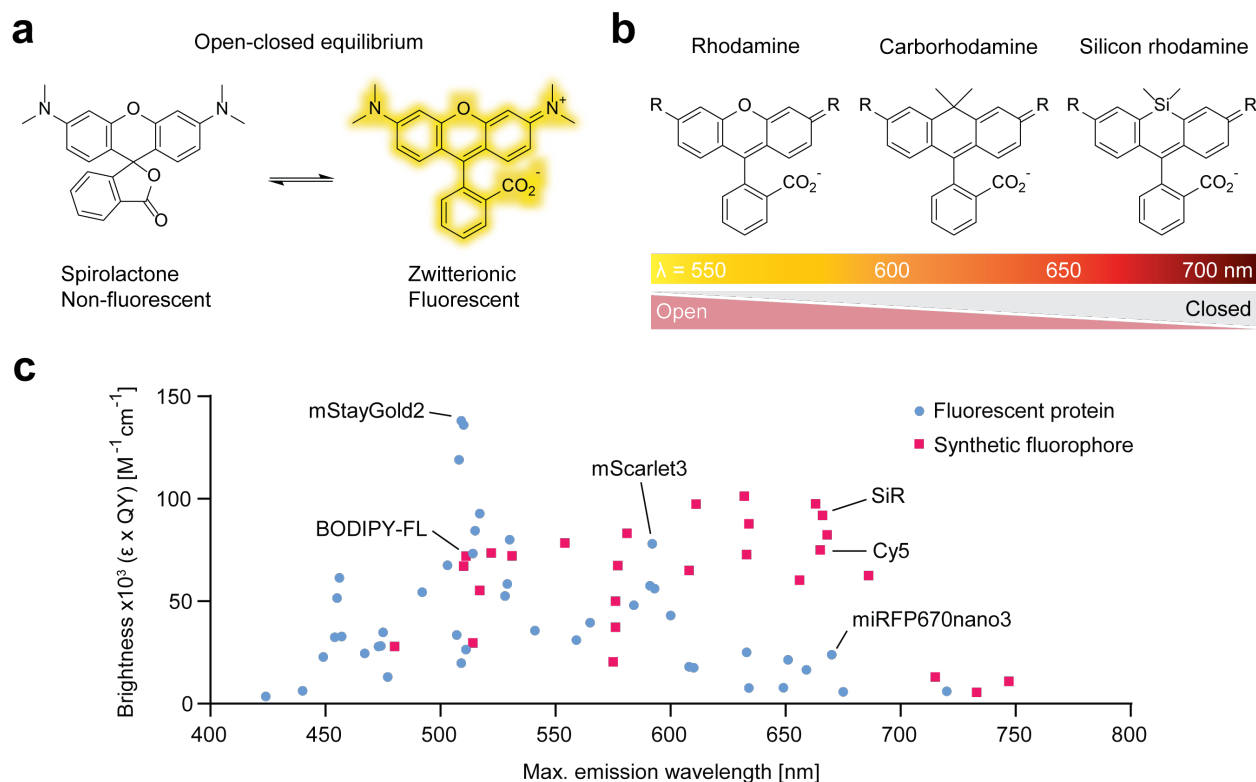


Figure 5 | Overview of rhodamine fluorophores.

a. Open-closed equilibrium of rhodamine fluorophores, exemplified with tetramethylrhodamine. In the closed spirolactone state, the fluorophore is non-fluorescent, but cell-permeable. In the open zwitterionic form, it is fluorescent, but less cell-permeable. **b.** Chemical structures of different rhodamine derivatives. Substitution of the oxygen in the xanthen core of rhodamines with dimethylated carbon or silicon leads to red-shifted excitation and emission wavelengths and shifts the open-closed equilibrium towards a more closed state. **c.** Comparison of fluorescent proteins and synthetic fluorophores according to brightness. Plotted is the brightness (extinction coefficient (ϵ) \times quantum yield (QY)) against the maximum emission wavelength. Selected fluorophores are indicated.

Compared to FPs, synthetic fluorophores are significantly smaller (~ 1 kDa *versus* ~ 30 kDa), and generally exhibit superior brightness and photostability. This becomes particularly evident when comparing their brightness at emission wavelengths above 600 nm (**Figure 5c**). Furthermore, chemical modifications allow for precise control over their spectral, photo- and biophysical properties, tailoring them for specific experimental requirements. While some rhodamine fluorophores tend to accumulate inside mitochondria of living cells³⁹, most synthetic fluorophores alone cannot be localized to specific subcellular localizations. In contrast, FPs can be genetically encoded, which allows straightforward targeting to subcellular compartments or fusion to a protein of interest

(POI). To overcome this caveat, researchers have devised different ways to specifically localize synthetic fluorophores. This includes conjugation to a small molecule that binds to a biomolecule of interest with high affinity (*e.g.*, jasplakinolide for binding to actin⁴⁰), or the incorporation of unnatural amino acids into a POI allowing covalent attachment of a fluorophore *via* bioorthogonal chemistry (*e.g.*, click-chemistry⁴¹). While these strategies have been successfully used for site-specific labeling, they are limited by the availability of high affinity ligands for a target biomolecule, or the low incorporation efficiency of unnatural amino acids.

1.2.4. Self-labeling proteins

An alternative approach for site-specific labeling of a synthetic fluorophore is the use of so-called self-labeling proteins (SLPs). They can be genetically encoded and can label themselves covalently with synthetic fluorophores through enzymatic reaction with a specific substrate conjugated to the fluorophore. This enables researchers to harness the advantages of genetic encodability and the superior photophysical properties of synthetic fluorophores. Because SLPs combine genetically encoded proteinaceous parts with synthetic substrates based on organic chemistry, they are often referred to as ‘chemogenetic’.

Originally developed in 2003 by Keppler *et al.*⁴², the first designed SLP, SNAP-tag, was based on the human DNA repair protein *O*-alkylguanine-DNA alkyltransferase, which reacts irreversibly with its substrate *O*-benzylguanine (BG). The cell-permeable BG substrate can be chemically modified with different functional groups, including fluorophores, and thereby enables specific labeling of the SNAP-tag in cells (**Figure 6a**). In the following years, additional SLPs such as CLIP-tag⁴³ and HaloTag7⁴⁴ have been developed, which react with substrates orthogonal to SNAP-tag and thereby enable multicolor imaging (**Figure 6b**). Among these SLPs, HaloTag7 exhibits superior properties for labeling with rhodamine-functionalized substrates, such as rapid labeling kinetics, high cell-permeability of the substrate and enhanced brightness of labeled fluorophores⁴⁵.

HaloTag7 is based on a bacterial dehalogenase (DhaA) from *Rhodococcus rhodochrous*, which covalently reacts with halogenated alkanes *via* its catalytic aspartate (Asp106) buried in the center of the protein (**Figure 6c**). In its natural form, the dehalogenase releases the alkane as an alcohol

regenerating itself for the next reaction. For the development of HaloTag7, this reversible reaction was rendered irreversible through mutation of histidine 272, which is crucial for the base-catalyzed release of the alkane, into an asparagine (**Figure 6d**). Hence, upon reaction with a chloroalkane functionalized with a fluorophore, HaloTag7 can be irreversibly labeled with synthetic fluorophores, or other functional groups (**Figure 6e**).

An additional feature of HaloTag7 and other SLPs is their ability to increase the fluorescence intensity of rhodamine-based fluorophores upon binding, a phenomenon referred to as fluorogenicity (**Figure 6f**)⁴⁶. This ‘turn-on’ effect is based on a change in the open-closed equilibrium of rhodamine fluorophores, shifting it towards the open fluorescent form. Consequently, the fluorogenic response is particularly pronounced for rhodamines that, before binding to the SLP, exist predominantly in the closed non-fluorescent form. Due to the low fluorescence signal of unreacted highly fluorogenic rhodamines, it is possible to perform ‘no-wash’ live cell imaging with high signal-to-background ratios, *i.e.*, high fluorescence signal of the labeled target over low fluorescence signal of unreacted fluorophore substrate. In recent years, the surface of HaloTag7 has been engineered to change the local environment of the labeled fluorophore. This yielded variants with altered fluorescence intensities and fluorescence lifetimes of the labeled fluorophores compared to the original HaloTag7⁴⁷. By exploiting the distinct fluorescence lifetimes, it was possible to image up to three subcellular structures using the same fluorophore labeled to different HaloTag7 variants.

These features have made SLPs invaluable tools for fluorescence microscopy and enabled researchers to exploit the superior photophysical properties of synthetic fluorophores for numerous applications, including super-resolution microscopy, single-particle tracking and biosensors^{48, 49}. Nevertheless, the adoption of self-labeling proteins in fluorescence microscopy requires consideration of certain limitations. Similar to FPs, the fusion of SLPs to POIs may potentially alter protein structure or function, necessitating careful validation of biological activity and localization. Furthermore, fluorescent labeling requires external administration of a fluorophore substrate. While the substrates of commonly used SLPs like HaloTag7 exhibit good cell permeability, which

enables straightforward use in cell cultures or acute tissue slices, their *in vivo* pharmacokinetics are still suboptimal for use in complex organisms.

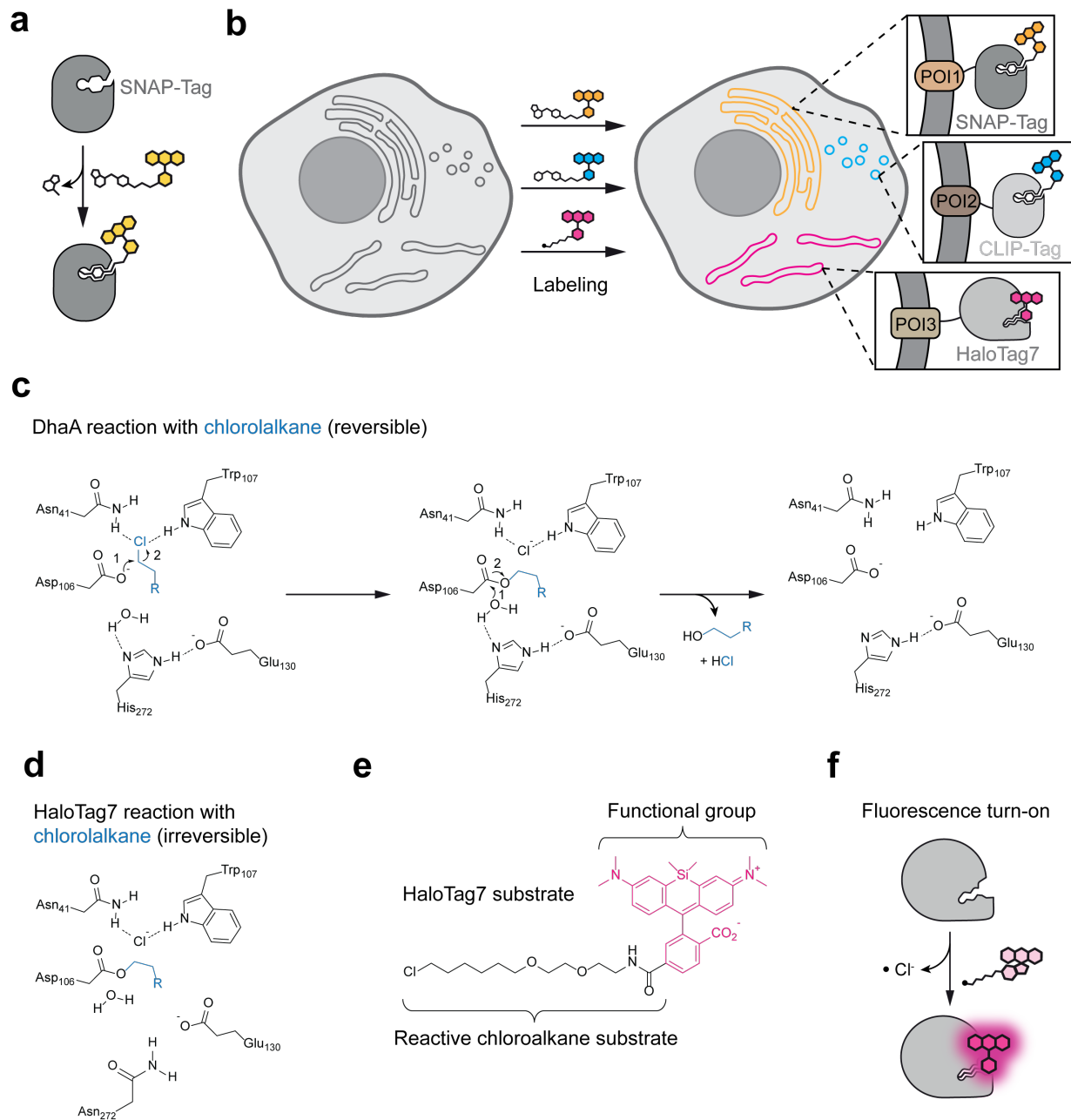


Figure 6| Overview of self-labeling proteins.

a. Schematic representation of SNAP-tag labeling with its substrate benzylguanine functionalized with a fluorophore (yellow). **b.** Schematic representation of multicolor labeling using multiple self-labeling proteins (SLPs). Upon incubation of cells with cognate SLP substrates functionalized with different fluorophores, it is possible to label multiple SLPs fused to different proteins of interest (POI) at distinct subcellular localizations simultaneously. **c.** Reaction mechanism of the dehalogenase DhaA from *Rhodococcus rhodochrous*. Nucleophilic attack of Asp106 on the terminal chlorine of the chlorolalkane (blue) forms a covalent alkyl intermediate.

Base-catalyzed hydrolysis of this intermediate, mediated by His272, releases the alkane as alcohol regenerating the dehalogenase for the next round. **d.** Mutation of His272 into Asn272, traps the alkyl-enzyme intermediate enabling irreversible conjugation of the DhaA mutant (*i.e.*, HaloTag7) with the chloroalkane. **e.** Chemical structure of a HaloTag7 chloroalkane substrate functionalized with silicon rhodamine (pink). **f.** Schematic representation of fluorogenicity. Labeling of a rhodamine fluorophore that predominantly exists in the closed non-fluorescent state (light pink) to HaloTag7 shifts the equilibrium of the fluorophore towards the open fluorescent state.

1.3. Fluorescent biosensors

Fluorescent biosensors represent a class of molecular tools designed to detect and quantify specific biological molecules or processes within living systems using fluorescence-based readouts. They have proven invaluable for studying dynamic processes such as protein-protein interactions, enzyme activity, intracellular signaling pathways, or ion and metabolite concentration dynamics in live cells and multicellular organisms⁵⁰.

1.3.1. Design and development

Fluorescent biosensors typically consist of a sensing unit that selectively interacts with the target molecule or process of interest, coupled with a fluorescent reporter unit that produces a quantifiable signal in response to the binding event or biological activity (**Figure 7**). The recognition unit can vary depending on the target molecule or process being detected. It may include antibodies, enzymes, receptors, small protein domains, aptamers or synthetic molecules engineered to specifically recognize the target analyte or undergo physical changes upon a biological activity of interest. The fluorescent reporter element typically consists of one or multiple fluorophores that emit light in response to excitation by an external light source. Upon binding to the target molecule or occurrence of the specific biological activity, the sensing unit undergoes a conformational change that is translated into the fluorescent reporter unit. The fluorescent reporter unit produces a measurable signal (*e.g.*, change in fluorescence intensity, wavelength, or FRET efficiency) that can be detected using optical readouts like fluorescence microscopy or spectroscopy. The amplitude of the output signal can be correlated with the concentration or activity of the target molecule or process, respectively.

Fluorescence microscopy represents a particularly powerful method in this regard, as it allows for real-time monitoring of dynamic cellular processes using fluorescent biosensors⁵¹. Furthermore, the combination of fluorescent biosensors with high- or super-resolution techniques, such as confocal or stimulated emission depletion (STED) microscopy, provides spatial information with high local precision⁵². Moreover, the use of spectrally distinguishable fluorophores, allows the detection of multiple biological processes simultaneously, *i.e.*, multiplexing.

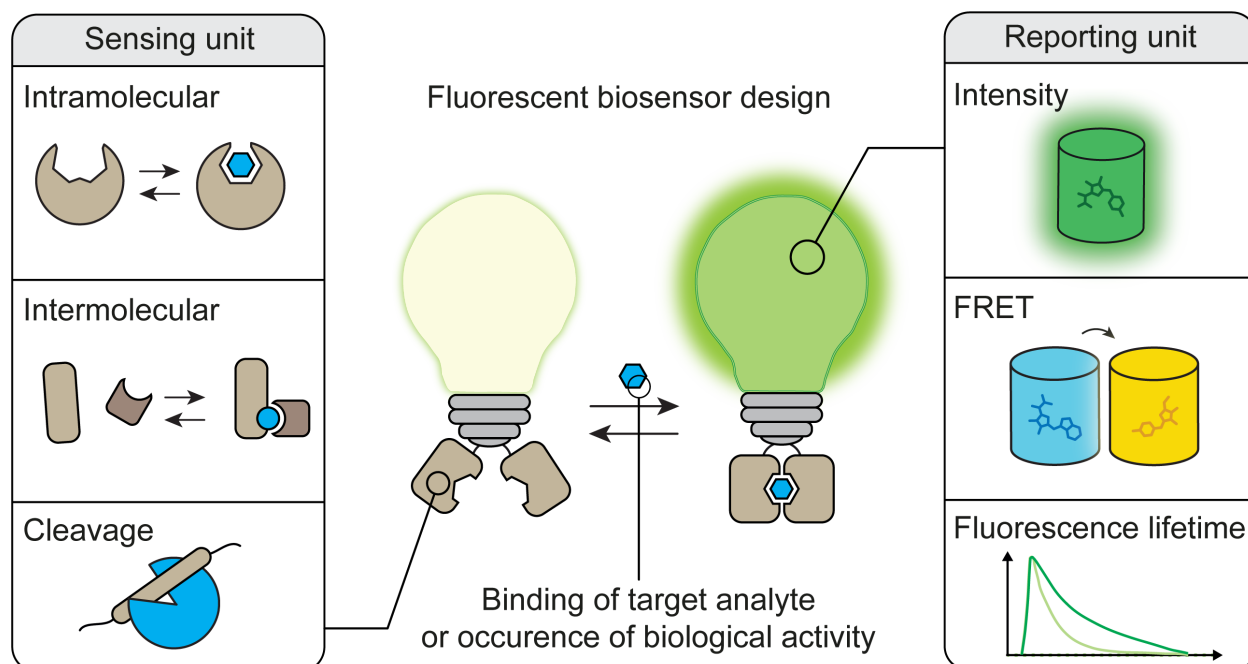


Figure 7 | General design of fluorescent biosensors.

Schematic representation of fluorescent biosensors based on a sensing and fluorescent reporting unit. The presence of a target analyte or occurrence of a biological activity of interest can be sensed through different types of mechanisms such as intra- and intermolecular binding events, or cleavage of a specific motif (sensing unit). The sensing unit is coupled to a fluorescent readout such as intensity, FRET or fluorescence lifetime (reporting unit), which can be correlated to changes in the biological activity or concentration of the analyte of interest.

Ideally, a fluorescent biosensor should exhibit the following properties to ensure robust and reliable measurements:

- High sensitivity, *i.e.*, being able to detect even subtle changes of the biological activity of interest.

The sensitivity of a biosensor is determined by the relative change in the fluorescent output signal upon sensing of the analyte or biological activity of interest. For example, the fold-increase in fluorescence intensity upon binding of the target analyte to the sensing unit. The maximal change in presence of the analyte compared to its absence determines the dynamic range of a biosensor, and is often used as a measure for its sensitivity.

- High specificity and selectivity, *i.e.*, responding only to the target or biological activity of interest.

Specificity and selectivity ensure accurate detection by minimizing interference from non-target molecules or activities.

- Relevant response range.

The response range, or the range over which the biosensor produces a measurable signal, should be well-matched to the biological context to ensure detection of relevant changes.

- Robustness.

The biosensor should not be susceptible to environmental changes such as pH, temperature or ionic strength.

- High brightness and photostability.

A bright and photostable fluorescent signal increases the signal-to-background ratio, enables measurements over longer periods of time, and increases the compatibility with super-resolution microscopy techniques.

- Ease of use.

Lastly, the biosensor should be easily implementable into the experimental design. Data acquisition and subsequent analysis should be readily accessible and simple to facilitate their use by a broad community. Together, these criteria guide the development and evaluation of fluorescent biosensors.

The development of biosensors starts with the construction of prototypical variants by combining different sensing and reporter units. The variants are produced and evaluated for their performance based on the aforementioned criteria. Depending on the outcome of the initial prototypes, a more

detailed optimization process is carried out for the most promising candidates. In the case of protein-based biosensors, this typically involves the generation of a mutant library. The position and type of mutation can be either rationalized, for example with the help of structural information on the components of the biosensor, or introduced randomly *via* error-prone PCR or site-saturated mutagenesis⁵³. The DNA of the mutant library is then introduced into a host system of choice (*e.g.*, bacteria, yeast or mammalian cells) for monoclonal expression of the mutants. Different readout modalities can be used to evaluate the performance of the sensor mutants, including analysis from (purified) bacterial lysates, fluorescence-activated cell sorting (FACS), or fluorescence microscopy. While the use of bacterial lysates is practically convenient and easily accessible, fluorescent biosensors are often intended to be used for applications in mammalian systems. This poses the risk that improved performances observed in a bacterial system might not translate into equivalent performances in other systems. Alternatively, the mutant library can be expressed and analyzed directly in the target system, for example a mammalian cell line, which allows the use of high-throughput methods like FACS. To extract spatiotemporal information on the performance of the mutants, it is also possible to employ imaging-based techniques that provide a functional readout in real-time⁵⁴. However, these techniques require advanced experimental setups.

1.3.2. Classes of biosensors

Based on the type of readout, fluorescent biosensors can be grouped into two different main classes, namely intensimetric and ratiometric.

1.3.2.1. Intensimetric biosensors

Intensimetric biosensors typically rely on changes in the fluorescence intensity of a single fluorophore, which can occur through various mechanisms, including changes in the local environment of the fluorophore affecting its photophysical properties. In the case of FP-based intensimeters, this is often due to changes in the protonation state of the chromophore⁵⁵. One of the most widely used examples is the calcium indicator GCaMP, which utilizes GFP as reporter unit and the calcium-dependent dimerization of calmodulin (CaM) with its cognate binding peptide M13 as sensing unit. To render the fluorescence intensity of GFP dependent on calcium, researchers have generated circularly permuted versions of GFP (cpGFP), and fused CaM and M13 to the new N-

and C-termini, which are in close proximity to the chromophore (**Figure 8a**)⁵⁶. Binding of calcium to CaM and subsequent dimerization of CaM and M13 induces conformational changes near the chromophore. This alters its protonation state due to changes in electrostatic potential, which ultimately causes an increase in fluorescence intensity⁵⁷. Inspired by this design, a chemogenetic strategy has been adopted to develop intensimetric biosensors based on HaloTag7^{58, 59}. HaloTag7 was circularly permuted and connected to CaM and M13, which change the local environment of the fluorophore labeled to HaloTag7 in a calcium-dependent manner (**Figure 8b-c**). In the case of fluorogenic rhodamine-based fluorophores, such as JF₆₃₅, this is due to a shift in the open-closed equilibrium. SLP-based sensors offer a high degree of spectral flexibility since they can be labeled on demand with bright fluorophores of different colors.

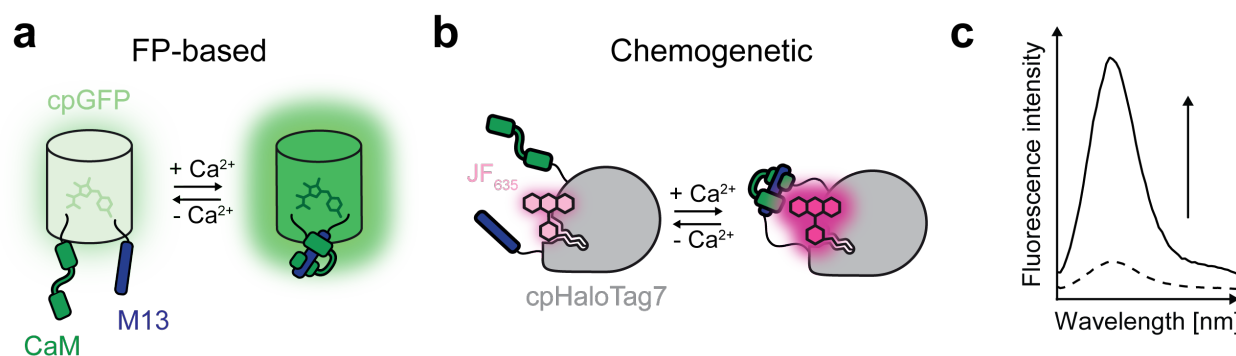


Figure 8 | Overview of intensimetric biosensors.

a. Schematic representation of a FP-based intensimeter for calcium (Ca^{2+}). Circular permutation of GFP (cpGFP, reporting unit) creates new N- and C-termini, which can be fused to calmodulin (CaM) and its cognate binding peptide M13 (sensing unit). Upon binding of Ca^{2+} , CaM and M13 dimerize undergoing a large conformational change, which alter the photophysical properties of the cpGFP chromophore and thereby lead to an increase in fluorescence intensity. **b.** Analogous to the FP-based Ca^{2+} sensor, HaloTag7 can be circularly permuted, fused with CaM and M13, and labeled with a fluorogenic rhodamine fluorophore (*e.g.*, JF₆₃₅). The large conformational change of CaM and M13 upon binding to Ca^{2+} alters the open-closed equilibrium of the fluorophore, shifting it towards the open fluorescent state. **c.** Binding of the target analyte results in an increased fluorescence intensity, shown with an exemplary fluorescence emission spectrum in absence (dashed line) and presence of Ca^{2+} (solid line).

While intensimetric biosensors often exhibit very large dynamic ranges (*e.g.*, 422.2 ± 15.3 -fold change in fluorescence intensity of the calcium sensor NEMOc⁶⁰) and provide a simple readout

(single excitation and emission wavelength), they are susceptible to fluctuations in sensor concentration and photobleaching, potentially resulting in skewed experimental results. Additionally, sensors based on the protonation state of the chromophore are sensitive to changes in local pH. Moreover, the change in the chromophore's local environment is often very subtle and mechanistically complex to decipher, necessitating time-consuming screening of numerous variants when implementing new sensing and reporting units.

1.3.2.2. Ratiometric biosensors

Ratiometric biosensors rely on the ratio of two fluorescent signals, which enable normalization and calibration of the fluorescent readout, rendering ratiometric biosensors independent of overall fluorescence intensity or changes in sensor concentration. While some of these sensors are based on a fluorescence ratio of fluorophores with distinct excitation wavelengths, the most commonly used design involves two fluorophores acting as FRET pair. One of the first FRET-based sensors was the calcium sensor 'cameleon', developed by Atsushi Miyawaki and Roger Y. Tsien in 1997. They utilized the calcium-dependent conformational change of CaM and M13 as reporting unit coupled to a CFP-YFP FRET pair serving as reporter unit (**Figure 9a**)⁶¹. Upon binding of calcium, CaM and M13 undergo a large conformational change, which brings the FRET pair in close proximity and thereby increases their FRET efficiency. This results in a decrease of the FRET donor fluorescence intensity and a concomitant increase in the FRET acceptor fluorescence intensity (**Figure 9b**). The $\text{FRET}_{\text{acceptor}}/\text{donor}$ fluorescence intensity ratio then serves as readout for changes in the concentration of calcium (**Figure 9d**).

FRET-based biosensors typically involve the use of recognition units with large conformational changes leveraging the strong distance dependency of FRET. This architecture makes FRET sensors highly modular and allows for the straightforward substitution of the recognition or reporting unit with alternative components. This enabled the development of a plethora of FRET biosensors for numerous target molecules and biological activities⁵⁰. For example, by exchanging the FPs of established FRET biosensors with the SLPs SNAP-tag and HaloTag7 that are labeled with rhodamine-based fluorophores, Vecchia and colleagues recently developed chemogenetic FRET biosensors, which could be multiplexed with other fluorescent biosensors (**Figure 9c**)⁶².

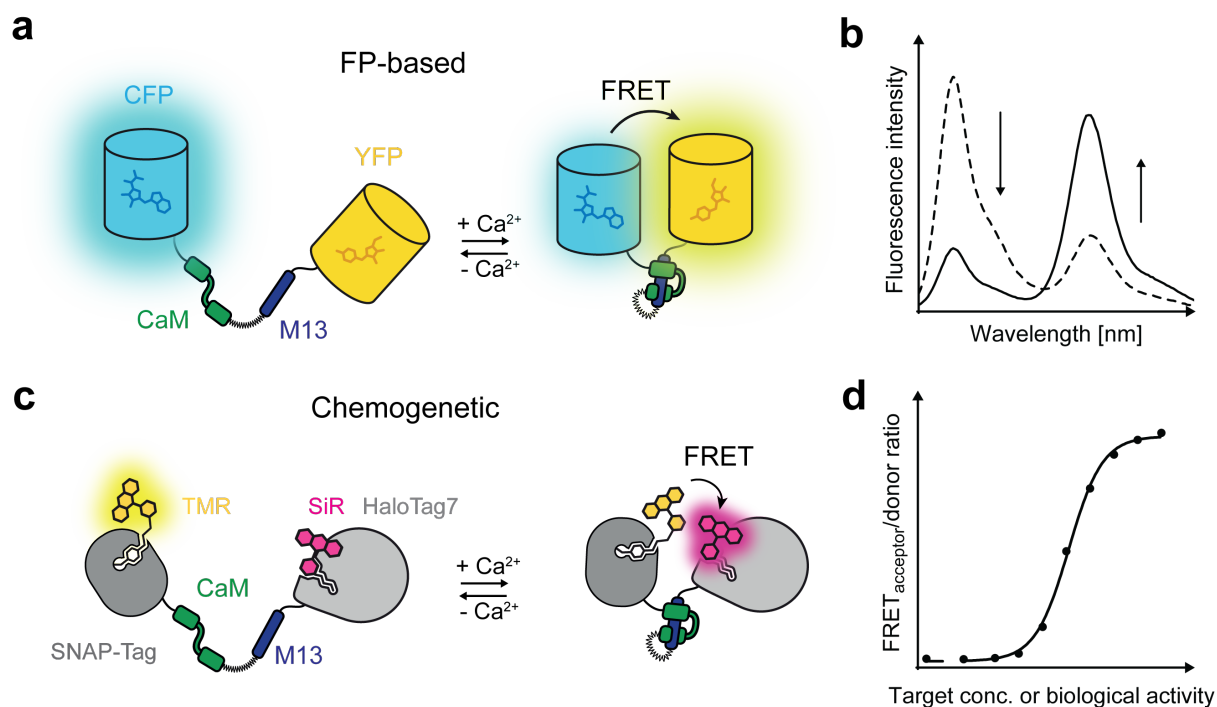


Figure 9 | Overview of ratiometric biosensors.

a. Schematic representation of a ratiometric sensor for Ca^{2+} . CaM and M13 are connected *via* a protein linker and flanked either with two fluorescent proteins (**a**), or two SLPs labeled with synthetic fluorophores (**c**) acting as FRET pair. Upon binding of Ca^{2+} , CaM and M13 dimerize undergoing a large conformational change, which brings the FRET pair in close proximity resulting in enhanced FRET. **b.** Binding of the target analyte results in a decreased FRET donor fluorescence intensity (arrow down) and a concomitant increase in FRET acceptor fluorescence intensity (arrow up), shown with an exemplary fluorescence emission spectrum in absence (dashed line) and presence of Ca^{2+} (solid line). **d.** The ratio derived from the fluorescence intensity of the FRET acceptor and donor ($\text{FRET}_{\text{acceptor/donor}}$) can be plotted against the concentration of the target analyte or biological activity of interest and used for quantification.

1.3.2.3. Limitations of FRET biosensors

While ratiometric biosensors provide more robust quantification compared to intensimetric biosensors, their dynamic ranges are often inferior. The dynamic range of FRET biosensors is defined by the maximal change in FRET efficiency comparing the open *versus* closed state of the sensor. Consequently, the dynamic range can be improved by increasing the FRET efficiency in the closed state of the sensor, and/or by decreasing the FRET efficiency in the open state of the sensor (or *vice versa*, depending on the design of the sensor). Common strategies to improve the FRET

efficiency are based on shortening the distance between the FRET pair or optimizing their relative orientation. For this purpose, the termini of FPs were truncated⁶³, different orientations of FRET pairs were tested by changing the order between the FRET pair and the sensing unit or using circular permutations⁶⁴⁻⁶⁶, or different linkers or linker lengths were implemented^{67,68}. On the other hand, strategies to decrease the FRET efficiency are predominantly based on increasing the distance between the FRET pair by incorporating extended and/or rigid linkers⁶⁷. However, lack of structural information on the sensor architecture often limits rational optimization of relative orientation or distance requiring time-consuming screening of numerous variants⁶⁴.

Alternative strategies aimed at enhancing the FRET efficiency by promoting dimerization of the FRET pair. Such approaches involved mutations on the surface of the FRET pair⁶⁹⁻⁷² or the incorporation of weak dimerization domains⁷³. While these adaptations, in some cases, yielded improved dynamic ranges of biosensors, most of them were based on CFP-YFP FRET pairs whose large spectral overlap causes increased spectral crosstalk, *i.e.*, cross excitation of FRET donor and acceptor, and emission bleed-through from donor to acceptor. Excessive spectral crosstalk poses challenges during imaging and limits the dynamic range of FRET-based biosensors. To address this issue, efforts were made to implement FRET pairs with increased spectral separation, such as GFP and RFP⁷⁴, or green and red rhodamine-based fluorophores labeled to SLPs⁶². However, the dynamic ranges of these sensors were relatively low as well ($\sim 0.6 - 1.0$ -fold change in the $\text{FRET}_{\text{acceptor}}/\text{donor}$ ratio).

Besides low dynamic ranges, FRET biosensors often require a large spectral space due to the use of two fluorophores, which limits their capacity to be multiplexed with other fluorescent tools. Moreover, CFP and YFP represent one of the most commonly used FRET pair to this day, despite being spectrally incompatible with widely used GFP-based intensimetric sensors. As mentioned before, attempts to develop red-shifted FRET biosensors did improve the multiplexing capacity, however, at the cost of poor dynamic ranges. While other strategies, like the chemogenetic Snifit sensors⁷⁵, enabled the development of red-shifted FRET biosensors with large dynamic ranges (*e.g.*, ~ 8 -fold increase in the $\text{FRET}_{\text{acceptor}}/\text{donor}$ ratio of the NAD-Snifit⁷⁶), they require labeling with complex molecules, which can exhibit limited cell-permeability.

1.4. Previous work

During my master's thesis in the Johnson lab, I assessed the potential of combining a fluorescent protein (FP) with a rhodamine-based fluorophore conjugated to a self-labeling protein (SLP) as efficient FRET pair⁷⁷. I evaluated the performance of different designs and found that C-terminal fusion of HaloTag7 (hereafter referred to as HT7) to EGFP (*i.e.*, EGFP-HT7) upon labeling with the far-red fluorophore silicon rhodamine (SiR; *i.e.*, EGFP-HT7_{SiR}) resulted in very high FRET. This observation was surprising considering the minor spectral overlap between EGFP and SiR. Furthermore, the FRET was substantially higher compared to N-terminal fusion of HT7 (*i.e.*, HT7-EGFP, **Figure 10a-b**), indicating a short distance and/or favorable relative orientation between EGFP and SiR for the C-terminal fusion construct. Given its chemogenetic nature and the incorporation of EGFP, the C-terminal fusion construct was named ChemoG1.

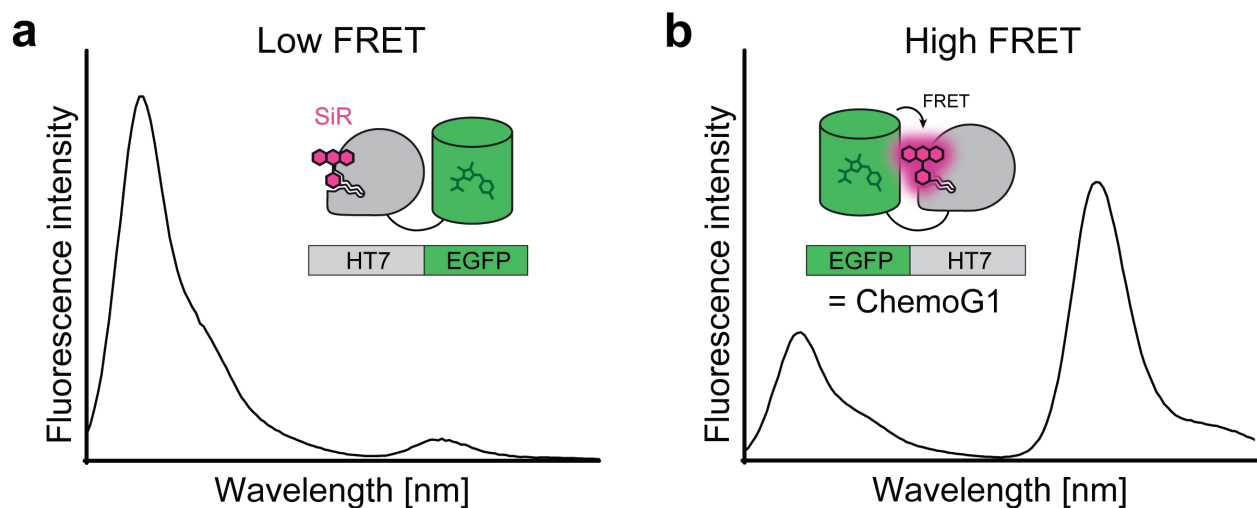


Figure 10| Design of the chemogenetic FRET pair ChemoG1.

Design of chemogenetic FRET pairs based on N- (a) or C-terminal (b) fusion of HT7 to enhanced GFP (EGFP). Shown are exemplary fluorescence emission spectra of the chemogenetic fusion constructs labeled with silicon rhodamine (SiR). The C-terminal fusion exhibited high FRET and was named ChemoG1.

1.5. Aims and Scope of the thesis

Current strategies aiming to develop improved FRET biosensors primarily focus on the optimization of either their dynamic range, or their spectral properties. However, combining both a large dynamic range and an increased multiplexing capacity remains challenging for this class of biosensors. To address this technological gap, I aimed to develop a system that enables straightforward creation of FRET-based biosensors with large dynamic ranges and high spectral flexibility. I envisioned that the combination of FRET pairs with large spectral separation would minimize spectral crosstalk and reduce basal FRET efficiency in the open state of FRET biosensors. On the other hand, by establishing a stable interface between the FRET pair, it would be possible to enhance the FRET efficiency in the closed state of the sensor. Combining both approaches would result in increased dynamic ranges.

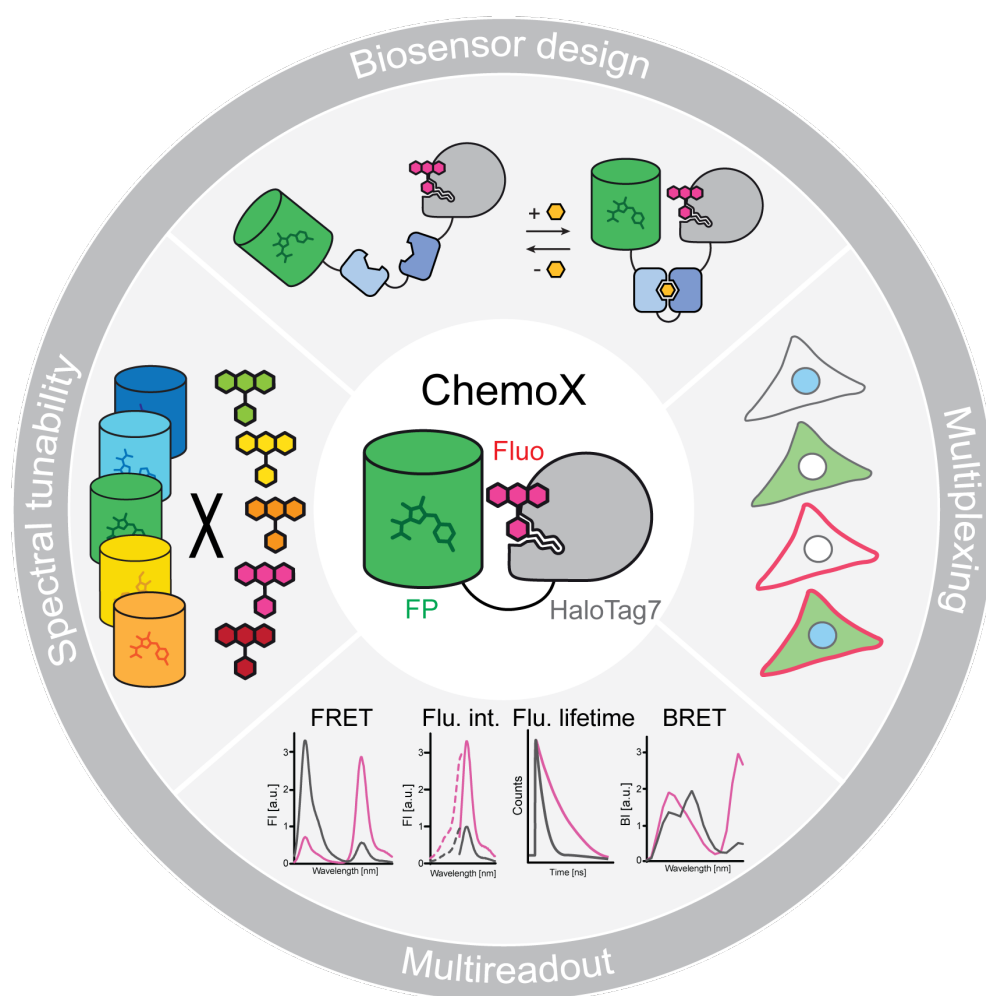
Given the promising preliminary results of the chemogenetic FRET pair ChemoG1_{SIR} (*i.e.*, high FRET between fluorophores with large spectral separation), I aimed to base this system on the ChemoG1 design. Additionally, the implementation of HT7 in this design would allow flexible incorporation of bright fluorophores with different colors, increasing the spectral flexibility of FRET biosensors that are based on this system.

In a first step, I established an interface between EGFP and HT7 labeled to a fluorophore that is spectrally well-separated from EGFP. I evaluated the spectral versatility of the optimized design by exchanging EGFP with different FPs, and different fluorophores labeled to HT7. After thorough characterization of the optimized FRET pairs, I tested their potential for the development of multicolor FRET biosensors based on the common sensor architecture of calcium biosensors. The performance of the biosensors was evaluated through a side-by-side comparison with an established calcium sensor, and their capacity to detect intracellular calcium waves was tested in different cell types.

Secondly, to probe the generalizability of my approach, I aimed to expand this design for the development of biosensors for important metabolites, such as adenosine triphosphate (ATP), nicotinamide adenine dinucleotide (NAD⁺) and nicotinamide mononucleotide (NMN). Furthermore,

I aimed to evaluate the robustness of the chemogenetic biosensors in regards to specificity and sensitivity to environmental changes by performing thorough characterizations with biochemical assays and cell experiments.

Finally, I aimed to diversify the readout modalities of this chemogenetic system to render the biosensors adaptable for specific experimental requirements. To this end, I planned on leveraging the fluorogenicity of rhodamine fluorophores for the development of biosensors based on changes in their fluorescence lifetime. Furthermore, I envisioned to create bioluminescent versions of the biosensors through implementation of a luciferase into the sensor design.



Graphical abstract.

Chapter 2 – Results

2.1. Structural characterization of ChemoG1

Since EGFP and SiR exhibit only a minor spectral overlap, I hypothesized that the C-terminal fusion of HT7 in ChemoG1 might bring SiR in close proximity to the EGFP chromophore, thereby promoting efficient FRET. To gain structural insights into the mechanism behind the enhanced FRET, I pursued crystallization trials for ChemoG1_{SiR} in collaboration with Dr. Mirosław Tarnawski (Max-Planck-Institute for Medical Research, Heidelberg). Unfortunately, no crystals could be obtained. However, labeling ChemoG1 with the structurally-related fluorophore tetramethylrhodamine (TMR; *i.e.*, ChemoG1_{TMR}) yielded crystals suitable for structural characterization. The X-ray crystal structure of ChemoG1_{TMR} confirmed a short distance (15.2 Å) between the EGFP chromophore and TMR (**Figure 11a**). Furthermore, the crystal structure revealed a close interface between EGFP and HT7_{TMR}, predominantly formed by the EGFP surface residues Y39, K41 and F223, and TMR (**Figure 11b**). K41 participates in electrostatic interactions with the benzyl-carboxylate of TMR, while Y39 and F223 engage in π -stacking interactions with the benzyl and xanthene core of TMR, respectively. Mutation of either of these three residues resulted in substantially decreased FRET (**Figure 11c**), underscoring their crucial role in stabilizing the observed interface.

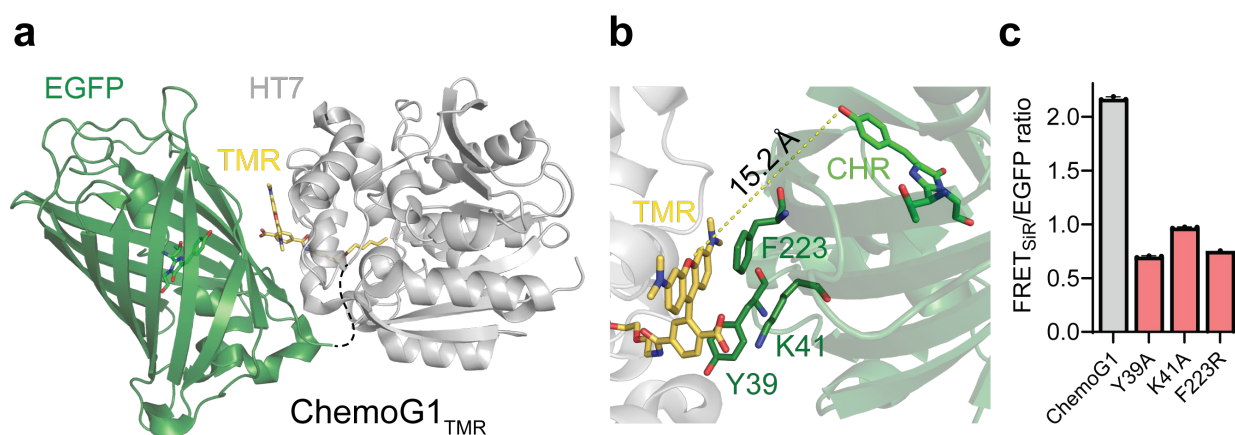


Figure 11| Structural characterization of the chemogenetic FRET pair ChemoG1_{TMR}.

a. X-ray crystal structure of ChemoG1 labeled with tetramethylrhodamine (TMR, PDB: 8B6S). EGFP (dark green) and HT7 (grey) are shown as cartoon, the EGFP chromophore (green) and the labeled fluorophore substrate (yellow) are shown as sticks.

The unresolved C-terminal region of EGFP (TLGMDELY) is annotated as dashed line. **b.** Zoom-in of the ChemoG1 interface between EGFP (dark green) and TMR (yellow). The surface residues of EGFP (dark green) interacting with TMR, the EGFP chromophore (CHR, green) and TMR (yellow) are shown as sticks. The distance between the oxygen of the TMR xantheno core and the oxygen of the phenolate of the EGFP chromophore is indicated as dotted line (15.2 Å). **c.** FRET_{SiR}/EGFP ratios of ChemoG1 and three variants with mutations involved in the ChemoG1 interface. Dr. Mirosław Tarnawski acquired the X-ray crystal structures. Adapted from Hellweg *et al.*⁷⁸

2.2. Development of an optimized chemogenetic FRET pair

Building upon the structural characterization of ChemoG1_{TMR}, I hypothesized that reinforcing interactions between EGFP and HT7 within the ChemoG interface could enhance the FRET efficiency between EGFP and SiR. To this end, I introduced a series of mutations on the surface of EGFP and HT7, guided by the structural information previously obtained for ChemoG1 (**Figure 12a**).

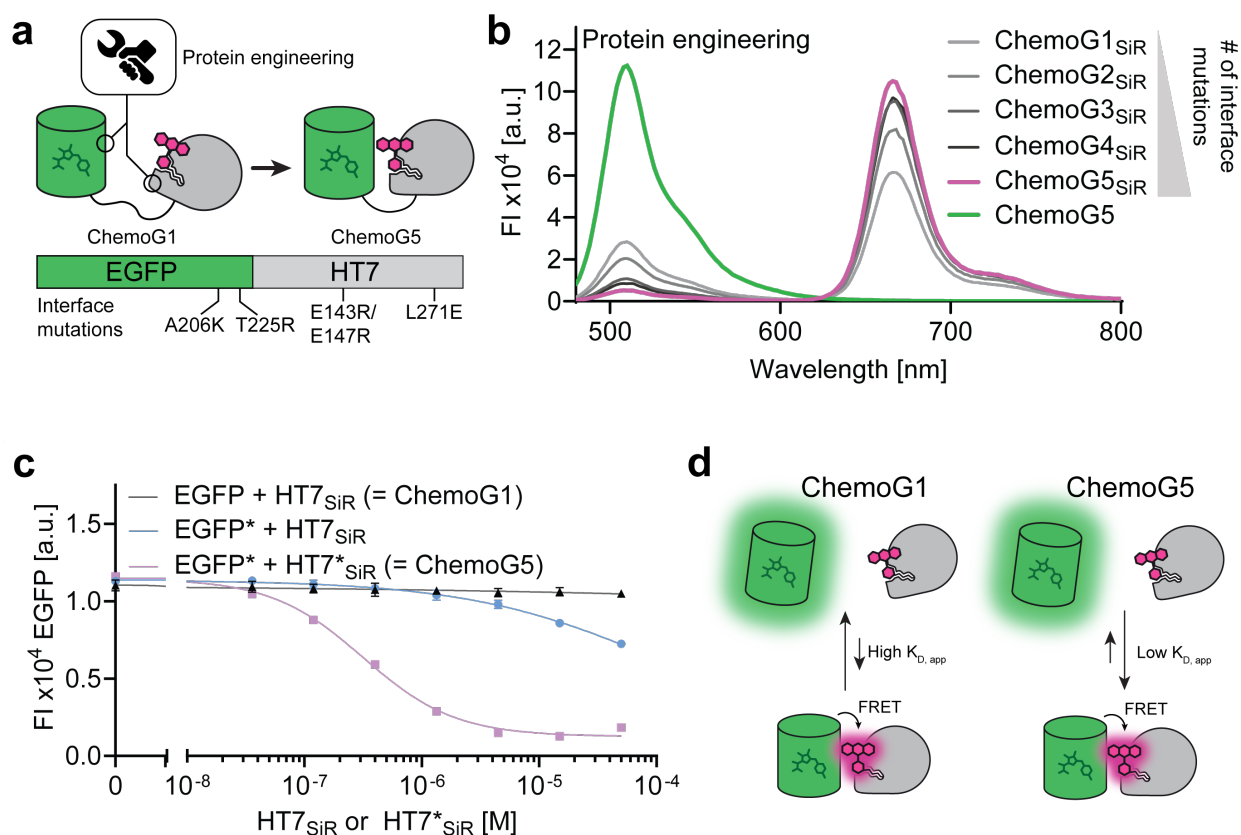


Figure 12 | Engineering of an optimized chemogenetic FRET pair.

a. Schematic representation of the optimization process from ChemoG1 to ChemoG5 by mutation of certain surface residues on EGFP and HT7. **b.** Fluorescence intensity (FI) emission spectra of ChemoG1-5 labeled with SiR and unlabeled ChemoG5. **c.** Titration of SiR-labeled HT7 or optimized HT7 (HT7*) against EGFP or optimized EGFP (EGFP*). EGFP fluorescence is

plotted against the concentration of SiR-labeled HT7/HT7*. **d.** Schematic representation of the equilibrium dissociation of EGFP and SiR-labeled HT7 with (right) or without (left) ChemoG5 mutations. Introduction of ChemoG5 mutations increased the affinity of EGFP and SiR-labeled HT7. Adapted from Hellweg *et al.*⁷⁸

The different variants were labeled with SiR and assessed for improved FRET, yielding a set of two EGFP mutations (A206K and T225R) and three HT7 mutations (E143R, E147R and L271E [HT7 numbering]). Sequential integration of all five mutations led to a gradual increase in FRET, culminating in the optimized variant ChemoG5 (**Figure 12b**). The FRET efficiency of ChemoG1_{SiR} increased from 74.8 ± 0.4 % (mean \pm standard deviation [s.d.]) to 95.8 ± 0.1 % for ChemoG5_{SiR} (**Table 1**), remarkable considering the minor spectral overlap between EGFP and SiR. Importantly, the overall fluorescence intensity of EGFP was not affected by ChemoG5 mutations (data not shown).

Table 1 | Overview of different ChemoG variants.

Adapted from Hellweg *et al.*⁷⁸

Construct	Interface mutations		FRET _{SiR} /EGFP	FRET efficiency [%]
	EGFP	HT7		
ChemoG1	-	-	2.2 ± 0.1	74.8 ± 0.4
ChemoG2	A206K	-	4.0 ± 0.1	84.1 ± 0.6
ChemoG3	A206K	L271E	8.9 ± 0.1	90.9 ± 0.1
ChemoG4	A206K	L271E-E143R-E147R	11.6 ± 0.3	93.2 ± 0.1
ChemoG5	A206K-T225R	L271E-E143R-E147R	20.3 ± 0.8	95.8 ± 0.1

I titrated SiR-labeled HT7 containing all three ChemoG5 mutations (HT7*_{SiR}) against EGFP containing both ChemoG5 mutations (EGFP*), and determined an apparent equilibrium dissociation constant ($K_{D, app}$) of 315 nM based on the quenching of EGFP fluorescence (**Figure 12c-d**). In contrast, I did not observe any apparent interaction between the original EGFP and HT7_{SiR} at concentrations as high as 50 μ M, supporting the hypothesis that stabilization of the ChemoG interface resulted in enhanced FRET efficiency. To get further insights into the structural

mechanism, I prepared ChemoG5 labeled with TMR for crystallization trials, in collaboration with Dr. Mirosław Tarnawski (Max-Planck-Institute for Medical Research, Heidelberg). The X-ray crystal structure of ChemoG5_{TMR} revealed a virtually identical alignment with ChemoG1_{TMR} (Figure 13a).

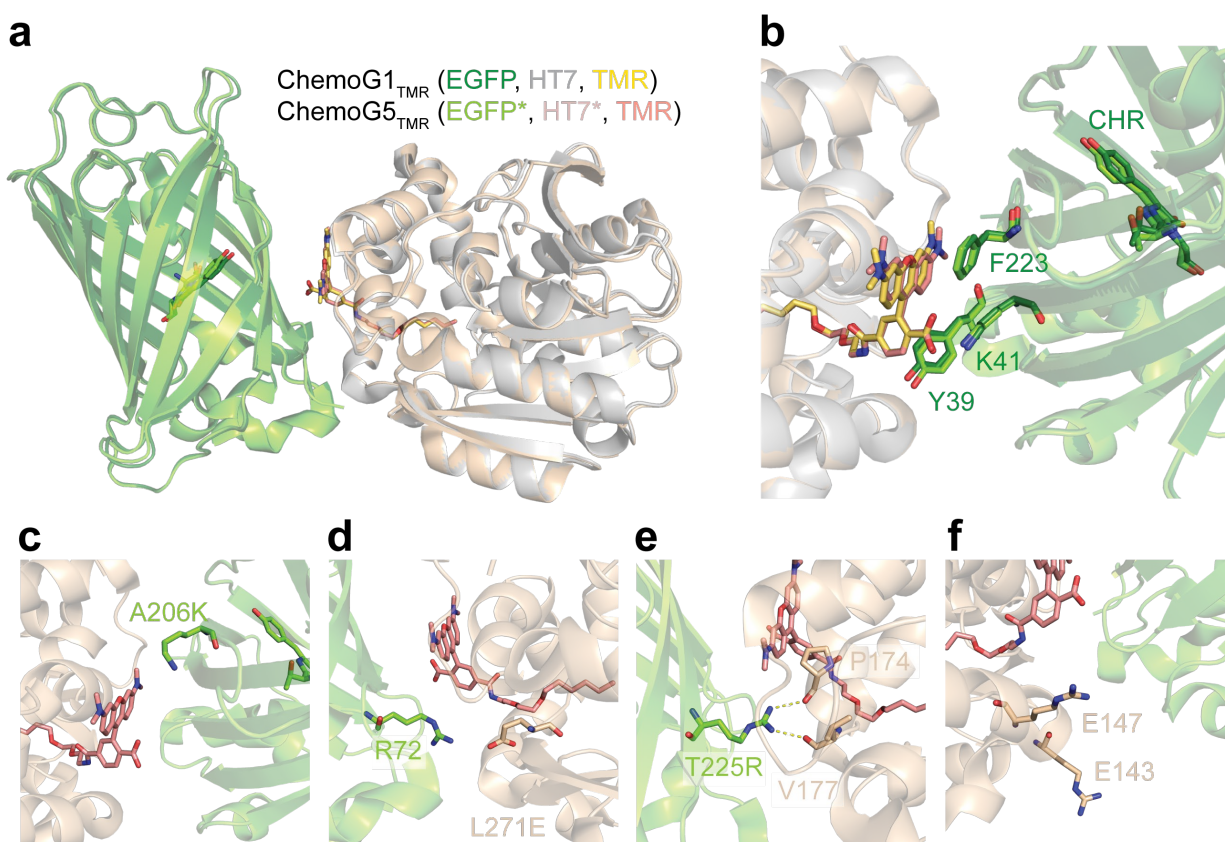


Figure 13 | Structural analysis of ChemoG5_{TMR}.

a-b. X-ray crystal structure of ChemoG5_{TMR} (PDB: 8B6S) aligned with the X-ray crystal structure of ChemoG1_{TMR} (PDB: 8B6T). EGFP/EGFP* and HT7/HT7* are shown as cartoons, EGFP/EGFP* chromophore (CHR), TMR and protein surface residues are shown as sticks. **b.** Zoom-in of the ChemoG interface. The EGFP/EGFP* surface residues interacting with TMR are indicated. **c-f.** Zoom-in of ChemoG5 surface mutations. A206K (**c**) and E143R-E147R (**f**) showed no direct interactions with HT7 or TMR. L271E (**d**) and T225R (**e**) showed direct interactions with R72 (EGFP*) and P174/V177 (HT7*), respectively. Dr. Mirosław Tarnawski acquired the X-ray crystal structures. Adapted from Hellweg *et al.*⁷⁸

Notably, the EGFP chromophores, the labeled TMR, as well as the EGFP residues that directly interact with TMR, aligned closely between the two structures (Figure 13b). This suggested that

stabilization of the ChemoG interface, rather than changes in the relative orientation or distance between the EGFP chromophore and TMR contributed to the enhanced FRET efficiency. In addition to the interactions observed in both crystal structures, two of the five ChemoG5 mutations engage in direct interactions within the ChemoG interface: L271E (HT7) and T225R (EGFP) form hydrogen bonds with R72 (EGFP) and P174/V177 (HT7), respectively (**Figure 13d-e**). A206K (EGFP) and E143R-E147R (HT7), on the other hand, show no direct interactions with adjacent surface residues (**Figure 13c, f**). Nevertheless, the positive charges introduced at these positions might contribute to overall electrostatic attraction or reduce electrostatic repulsion between EGFP and HT7, similar to observations made in a previous study⁷³. Despite the introduction of charged surface residues and apparent electrostatic interactions, the FRET_{SiR/EGFP} ratio of ChemoG5_{SiR} and other ChemoG variants was hardly affected by changes in pH (5.5 – 8.0) or ionic strength (NaCl = 0 – 500 mM, **Figure 14**).

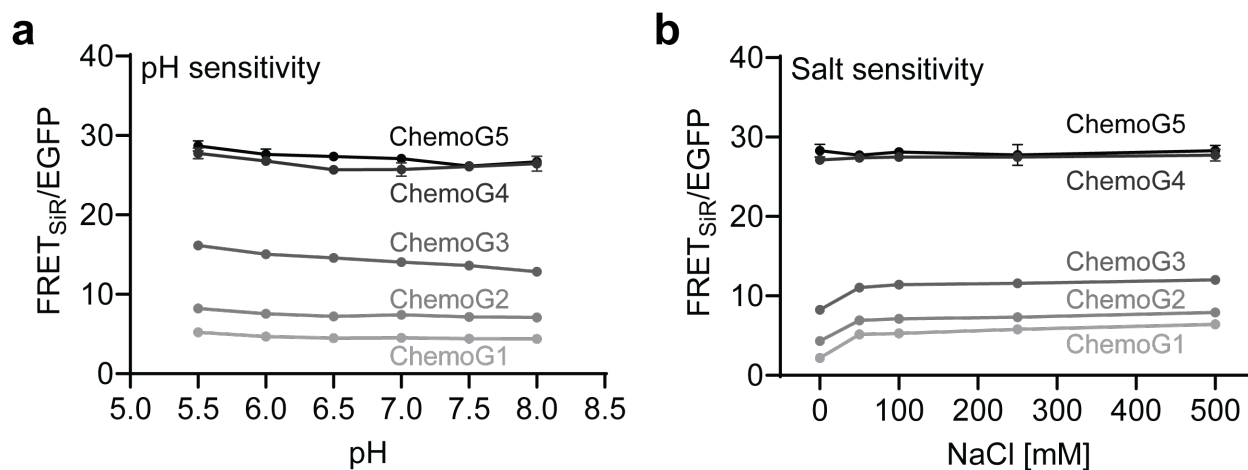


Figure 14 | Sensitivity of ChemoG FRET pairs to environmental changes.

FRET_{SiR/EGFP} ratios of ChemoG1-5 constructs labeled with SiR at different pH (**a**) or different concentrations of NaCl (**b**). Adapted from Hellweg *et al.*⁷⁸

To assess whether the improved FRET efficiency of ChemoG5 would also translate to a cellular context, I expressed ChemoG5 targeted to different subcellular localizations, including the cytosol, nucleus, plasma membrane, mitochondria and nuclear envelope. Upon labeling with SiR, I observed a very pronounced fluorescence signal in the FRET emission channel for all localizations,

whereas the EGFP fluorescence signal was hardly detectable (**Figure 15**), indicative for a high FRET efficiency. Moreover, the $\text{FRET}_{\text{SiR}}/\text{EGFP}$ ratio increased gradually from ChemoG1 to ChemoG5, in line with the results I obtained *in vitro* using purified recombinant proteins. Noteworthy, the $\text{FRET}_{\text{SiR}}/\text{EGFP}$ ratio increased by approximately 166-fold comparing ChemoG5_{SiR} (16.4 ± 2.7) and HT7_{SiR}-EGFP (0.1 ± 0.05), confirming the substantial improvement in FRET efficiency of the chemogenetic FRET pair through structure-guided protein engineering.

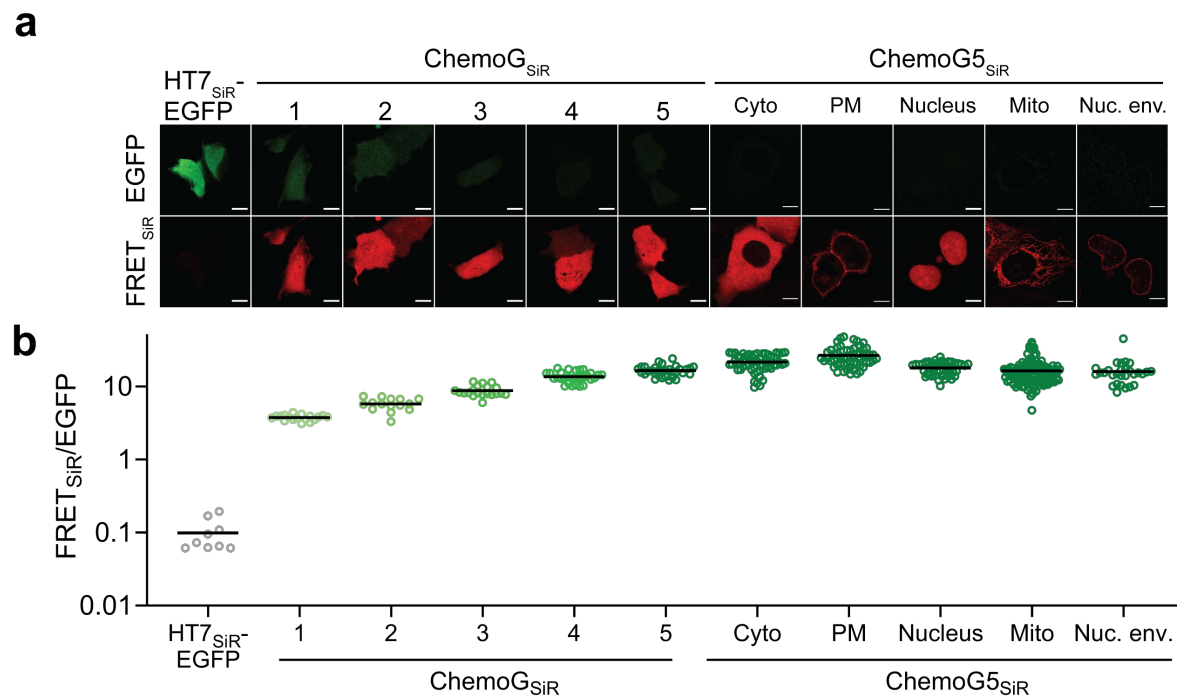


Figure 15 | Performance of ChemoG FRET pairs at different subcellular localizations.

a. Fluorescence images of U-2 OS cells expressing different chemogenetic FRET pairs labeled with SiR. Shown are the EGFP and FRET_{SiR} emission channels. Images were acquired with a confocal microscope. Localization of ChemoG5 at different subcellular localizations is indicated accordingly (Cyto = cytosol, PM = plasma membrane, Mito = mitochondria, Nuc. env. = nuclear envelope). **b.** $\text{FRET}_{\text{SiR}}/\text{EGFP}$ ratios of chemogenetic FRET pairs expressed in U-2 OS cells. The different constructs correspond to the images in **a**. Shown are the mean values of individual cells (hollow spheres) and the mean of all cells per condition (black bar). Scale bars = 10 μm . Anna Edenhofer helped with the analysis of the ChemoG constructs in cells. Adapted from Hellweg *et al.*⁷⁸

2.3. Expanding the spectral properties of ChemoG5

Since HT7 can be readily labeled with a diverse set of fluorophore substrates⁴⁵, I sought to leverage this feature to systematically tailor the spectral properties of the FRET acceptor (**Figure 16a**). I labeled ChemoG5 with different rhodamine-based fluorophores that possess maximum emission wavelengths ranging from 556 nm (JF₅₂₅) up to 686 nm (JF₆₆₉). I determined FRET efficiencies of $\geq 94.7\%$ for each FRET pair, regardless of the maximum emission wavelength of the labeled fluorophore (**Figure 16b**, **Table 2**). This observation suggested that the distance and relative orientation between EGFP and the fluorophore labeled to HT7 are highly optimized in the ChemoG context, resulting in efficient FRET even between FRET donors and acceptors with negligible spectral overlap (*e.g.*, EGFP and JF₆₆₉, **Table 3**). The ChemoG design therefore offers the added advantage of using FRET pairs with reduced spectral crosstalk (*i.e.*, cross-excitation and emission bleed-through between FRET donor and acceptor), while maintaining very high FRET efficiency.

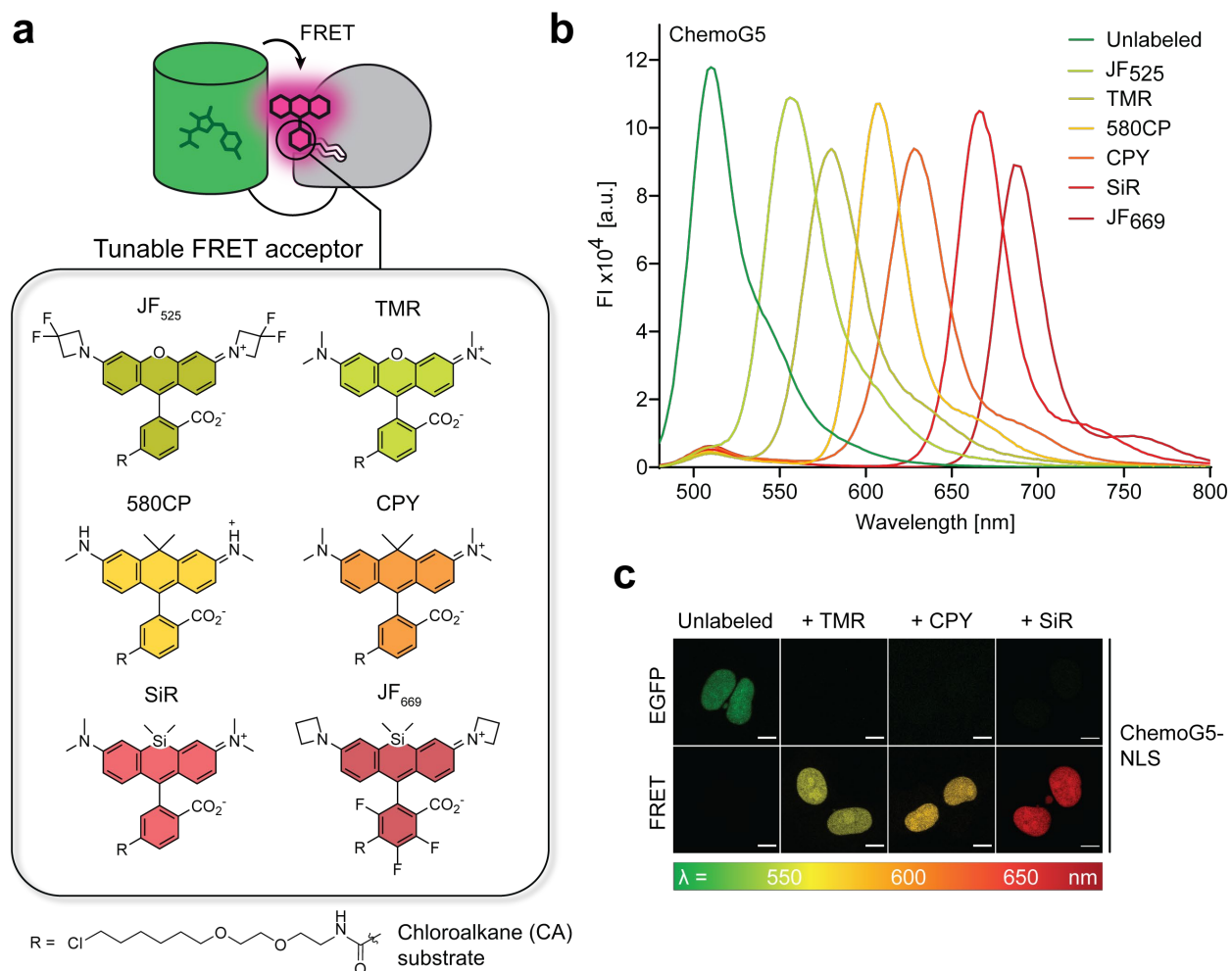


Figure 16| Expanding the spectral properties of the ChemoG5 FRET acceptor.

a. Schematic representation of ChemoG. The ChemoG FRET acceptor can be adjusted by labeling HT7 with different fluorophores. Examples of rhodamine-based fluorophores and their chemical structures are shown in the box below. **b.** Fluorescence intensity (FI) emission spectra of ChemoG5 unlabeled or labeled with different rhodamine-based fluorophores. **c.** Fluorescence images of U-2 OS cells expressing ChemoG5 in the nucleus (ChemoG5-NLS). Cells were labeled with TMR, CPY or SiR. Unlabeled cells served as control. Shown are the EGFP and FRET emission channels. Images were acquired with a confocal microscope. Scale bars = 10 μ m. Adapted from Hellweg *et al.*⁷⁸

I validated these findings by expressing ChemoG5 in the nucleus of U-2 OS cells and labeling it with different fluorophores (**Figure 16c**). I determined high FRET/EGFP ratios for all FRET pairs, *i.e.*, strong fluorescent signals in the FRET channel and highly diminished fluorescence in the EGFP channel, demonstrating the practicality of utilizing HT7 in a chemogenetic design to tune the spectral properties of the FRET acceptor on demand.

Table 2| ChemoG5 FRET pairs with different FRET acceptors.Max λ_{Em} = maximum emission wavelength of the FRET acceptor. Adapted from Hellweg *et al.*⁷⁸

Construct	FRET acceptor	Max λ_{Em}	FRET/EGFP	FRET efficiency [%]
ChemoG5	JF ₅₂₅	556 nm	18.0 ± 1.4	94.9 ± 0.3
ChemoG5	TMR	580 nm	23.6 ± 2.7	96.6 ± 0.3
ChemoG5	580CP	606 nm	23.8 ± 2.6	96.1 ± 0.5
ChemoG5	CPY	628 nm	15.8 ± 1.3	94.9 ± 0.4
ChemoG5	SiR	668 nm	20.2 ± 0.8	95.6 ± 0.1
ChemoG5	JF ₆₆₉	686 nm	14.2 ± 0.1	94.7 ± 0.4

Table 3| Photophysical properties of fluorophores used as ChemoG5 FRET acceptors. $\lambda_{Ex}/\lambda_{Em}$ = maximum excitation/emission wavelength, ϵ = extinction coefficient, Φ = quantum yield, $J(\lambda)$ = spectral overlap between EGFP and the different fluorophores, R_0 = Foerster radius. Adapted from Hellweg *et al.*⁷⁸

Fluorophore	$\lambda_{Ex}/\lambda_{Em}$ [nm]	ϵ [$M^{-1}cm^{-1}$]	Φ	$J(\lambda) \times 10^{15}$ [$M^{-1}cm^{-1}nm^4$]	R_0 [\AA]
EGFP	488/510	55,900 ^a	0.6 ^a	-	-
JF ₅₂₅	533/556	95,000 ^a	0.83 ^a	3.46	58.2
TMR	554/578	82,000 ^b	0.61 ^b	3.07	57.1
580CP	588/608	100,000 ^c	0.65 ^c	1.66	51.5
CPY	615/634	122,000 ^b	0.72 ^b	1.01	47.4
SiR	650/666	167,000 ^b	0.55 ^b	0.38	40.3
JF ₆₆₉	673/686	139,000 ^a	0.45 ^a	0.29	38.5
Cy3	548/566	136,000 ^a	0.15 ^a	4.78	61.4
Cy5	648/668	250,000 ^a	0.30 ^a	1.32	49.6
mCerulean3; Venus	433/475; 517/530	40,000; 92,200 ^a	0.87; 0.57 ^a	2.11	57.0

^a <https://www.fpbases.org/fret/>^b Reference⁷⁹^c Reference⁸⁰

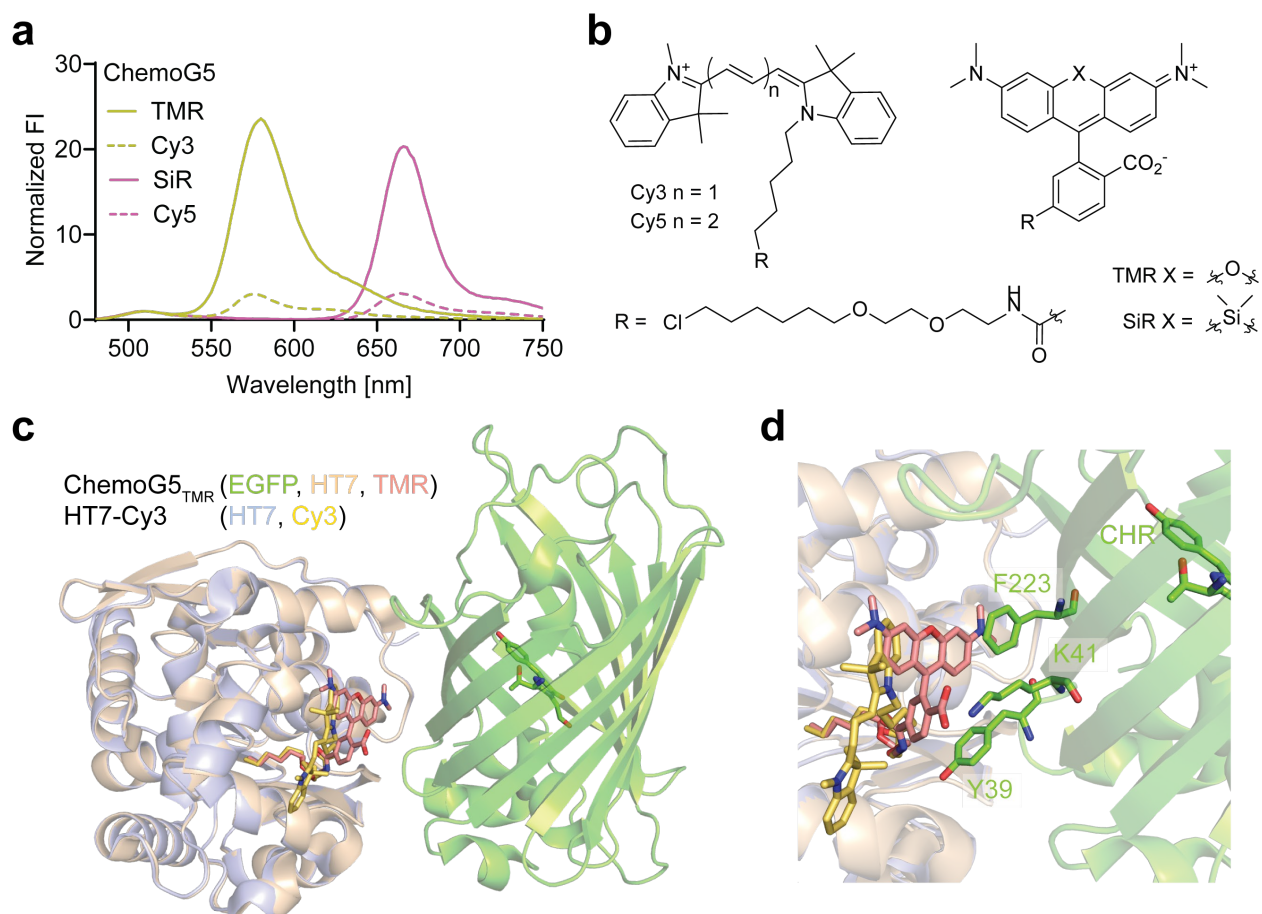


Figure 17| Evaluation of cyanine fluorophores as ChemoG FRET acceptors.

a. Fluorescence intensity (FI) emission spectra of ChemoG5 labeled to the cyanine fluorophores Cy3 or Cy5, or the rhodamine-based fluorophores TMR and SiR. Emission spectra were normalized to the maximal EGFP signal. **b.** Chemical structures of the chloroalkane (CA) fluorophore substrates used in **a.** R = chloroalkane. **c, d.** X-ray crystal structure of ChemoG5_{TMR} (PDB: 8B6T) aligned with HT7_{Cy3} (PDB: 8B6R). Protein structures are shown as cartoon. TMR, Cy3 and the EGFP chromophore are shown as sticks. **d.** Zoom-in of the ChemoG5 interface. The EGFP surface residues Y39, K41 and F223 involved in the interface are shown as sticks. Dr. Miroslaw Tarnawski acquired the X-ray crystal structures. Adapted from Hellweg *et al.*⁷⁸

When I labeled ChemoG5 with the cyanine fluorophores Cy3 and Cy5, which are structurally different from rhodamine-based fluorophores, I observed substantially lower FRET compared to TMR and SiR, which possess comparable spectral properties, respectively (**Figure 17a-b**). This preference for rhodamine-based fluorophores could be explained by the interactions observed in the crystal structure of ChemoG5_{TMR}; more specifically, the EGFP surface residues Y39, K41 and F223, which directly interact with the rhodamine TMR on the HT7 surface. Aligning the crystal structure of Cy3-labeled HT7 (PDB: 8B6R) with ChemoG5_{TMR} (PDB: 8B6T) suggested that

cyanine fluorophores adopt a conformation on HT7 that is hardly compatible with the ChemoG interface (**Figure 17c-d**). This observation supported the hypothesis that a stable interface between the FRET pair is crucial for efficient FRET. Although certain fluorophores may not align well with this chemogenetic design, the abundance of rhodamine-based fluorophores, renowned for their enhanced brightness, robust photostability, and high cell permeability^{35,38,81}, offers a plethora of options spanning a wide range of colors.

Having successfully demonstrated the capacity to fine-tune the spectral properties of the FRET acceptor by labeling HT7 with different fluorophores, my next aim was to further expand the spectral versatility of the ChemoG design by substitution of the FRET donor. Since many fluorescent proteins share a common β -barrel structure, I hypothesized that EGFP could be replaced with other fluorescent proteins establishing the same type of interface observed for ChemoG. Initially, I selected EBFP2⁸² (maximum excitation wavelength (λ_{Ex}) = 383 nm, maximum emission wavelength (λ_{Em}) = 448 nm), mCerulean3⁸³ (λ_{Ex} = 433 nm, λ_{Em} = 475 nm) and Venus⁸⁴ (λ_{Ex} = 515 nm, λ_{Em} = 528 nm) based on their brightness and to cover a wide range of emission wavelengths. Furthermore, these FPs originate from the same ancestor as EGFP (*i.e.*, avGFP⁸⁵) and share a high sequence homology, in particular with respect to surface residues that are essential for stabilization the ChemoG interface (**Figure 18a-b**).

Upon labeling of the FP-HT7 constructs with SiR, I observed a moderate FRET signal for all tested constructs (**Figure 18c-h**). The FRET signal was the strongest for mCerulean3-HT7_{SiR}, which could be attributed to ChemoG5 mutation A206K already being present in mCerulean3. EBFP2-HT7_{SiR} exhibited the weakest FRET, likely due to the absence of Y39 on EBFP2 (here N39), which is critical for the ChemoG interface. To enhance the FRET efficiency, I incorporated all ChemoG5 mutations into each of the constructs accordingly, including N39Y for EBFP2. This resulted in a substantial increase in FRET across all constructs, reaching FRET efficiencies $\geq 94.6\%$ (**Figure 18i-k, Table 4**), even for EBFP2 and SiR. This is particularly striking considering that their maximum emission wavelengths are separated by 218 nm (λ_{Em} EBFP2 = 448 nm and λ_{Em} SiR = 666 nm) and that their spectral overlap is 42-fold smaller compared to the commonly used FRET pair mCerulean3-Venus (0.05×10^{15} versus $2.11 \times 10^{15} \text{ M}^{-1} \text{ cm}^{-1} \text{ nm}^4$). The overall

design was named ChemoX, with 'X' referring to the color of the corresponding fluorescent protein (*e.g.*, EBFP2 = Blue = ChemoB).

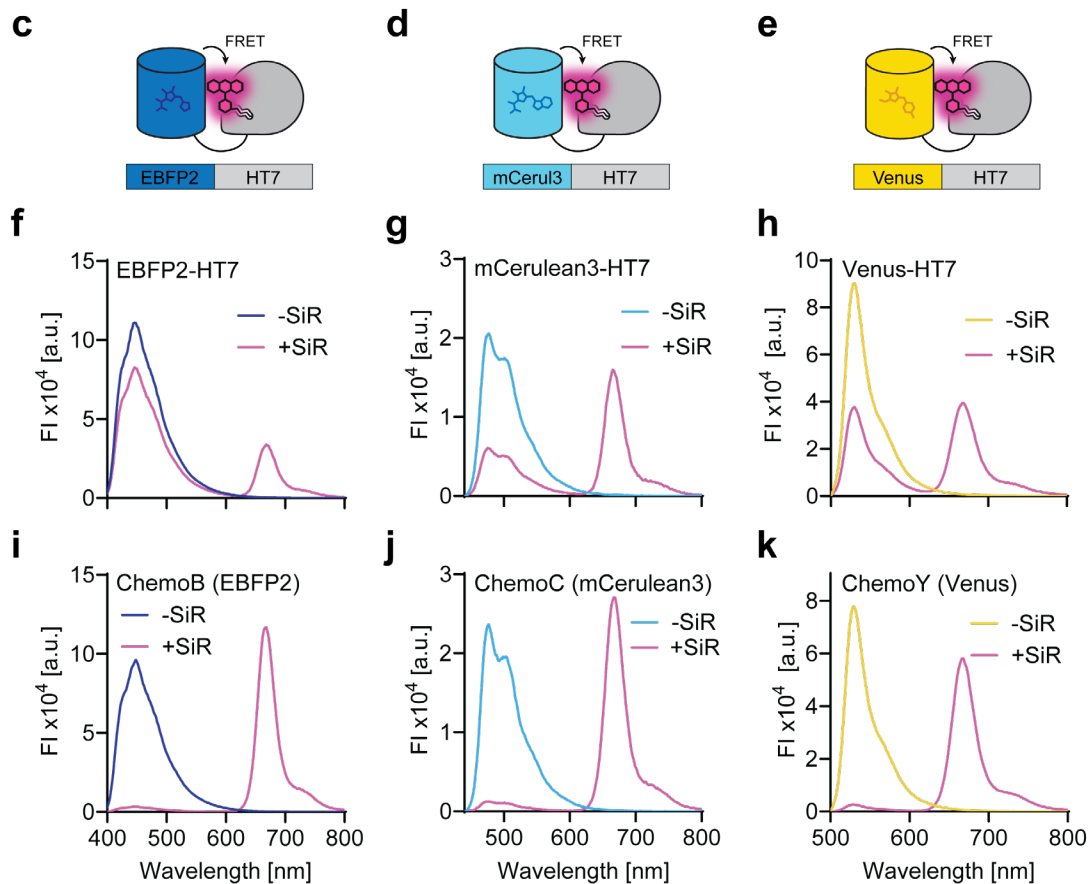
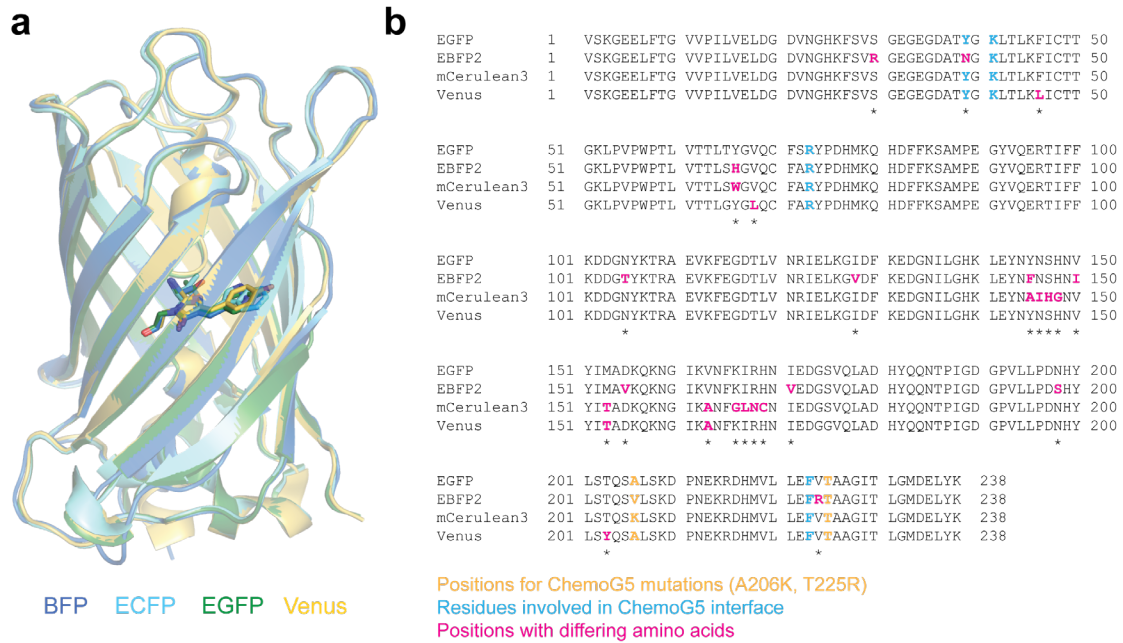


Figure 18| Expanding the spectral properties of the ChemoG FRET donor.

a. X-ray crystal structure of EGFP (PDB: 2Y0G) aligned with the crystal structures of BFP, ECFP and Venus (PDB: 1BFP, 2WSN and 1MYW, respectively). Proteins are shown as cartoon. FP chromophores are shown as sticks. **b.** Protein sequence alignment of EGFP, EBFP2, mCerulean3 and Venus. Asterisks indicate positions with different side chain residues. **c-e.** Schematic representations of chemogenetic FRET pairs based on different FP FRET donors. **f-k.** Fluorescence intensity (FI) emission spectra of chemogenetic FRET pairs unlabeled (-SiR) or labeled with SiR (+SiR). **f-h.** Initial chemogenetic FRET pairs. **i-k.** Optimized chemogenetic FRET pairs (= ChemoX) after incorporation of ChemoG5 interface mutations. Lucas Barck helped with the characterization of the different FRET pairs. Adapted from Hellweg *et al.*⁷⁸

Many fluorescent tools are based on green or yellow FPs⁵⁰ and thereby limited in their capacity for multiplexing with the current ChemoX design. Therefore, I aimed to incorporate FPs with longer emission wavelengths. To this end, EGFP in ChemoG5 was substituted with the red FP mScarlet⁸⁶ ($\lambda_{\text{Ex}} = 569 \text{ nm}$, $\lambda_{\text{Em}} = 594 \text{ nm}$), based on its superior brightness. mScarlet shares the common β -barrel structure with EGFP (**Figure 19a-b**), but sequence alignment revealed an overall low sequence homology (**Figure 19c**). Encouraged by the successful improvement in FRET for previous ChemoX constructs, I introduced single point mutations on the surface of mScarlet and HT7 that correspond to the ChemoG5 mutations. However, most of the mutations did not improve or even diminished the FRET_{SiR/mScarlet} ratio (**Figure 19d**). The mutation E39Y led to a drastic decrease in overall brightness of mScarlet and was therefore excluded from the analysis (data not shown). D200K on mScarlet, the equivalent mutation to A206K on EGFP, was the only surface mutation that enhanced the FRET efficiency and was therefore incorporated in the final variant, termed ChemoR. Despite the poor outcome of the surface engineering for ChemoR, the large spectral overlap between mScarlet and SiR inherently favors efficient FRET, yielding a FRET efficiency of $91.3 \pm 0.3 \%$ for ChemoR_{SiR}, which is comparable to other ChemoX FRET pairs (**Table 4**). Based on the low sequence homology between EGFP and mScarlet, it is possible that other surface residues of mScarlet, which do not correspond to the ChemoG interface, might hinder the formation of a stable interface with HT7 and the labeled fluorophore; for example, due to electrostatic repulsion or steric compatibility. A more comprehensive mutagenesis screen on the surface of mScarlet and HT7 might yield more success in finding compatible mutations that enhance the FRET efficiency.

Overall, I established a toolbox of chemogenetic FRET pairs with customizable spectral properties while maintaining very high FRET efficiencies.

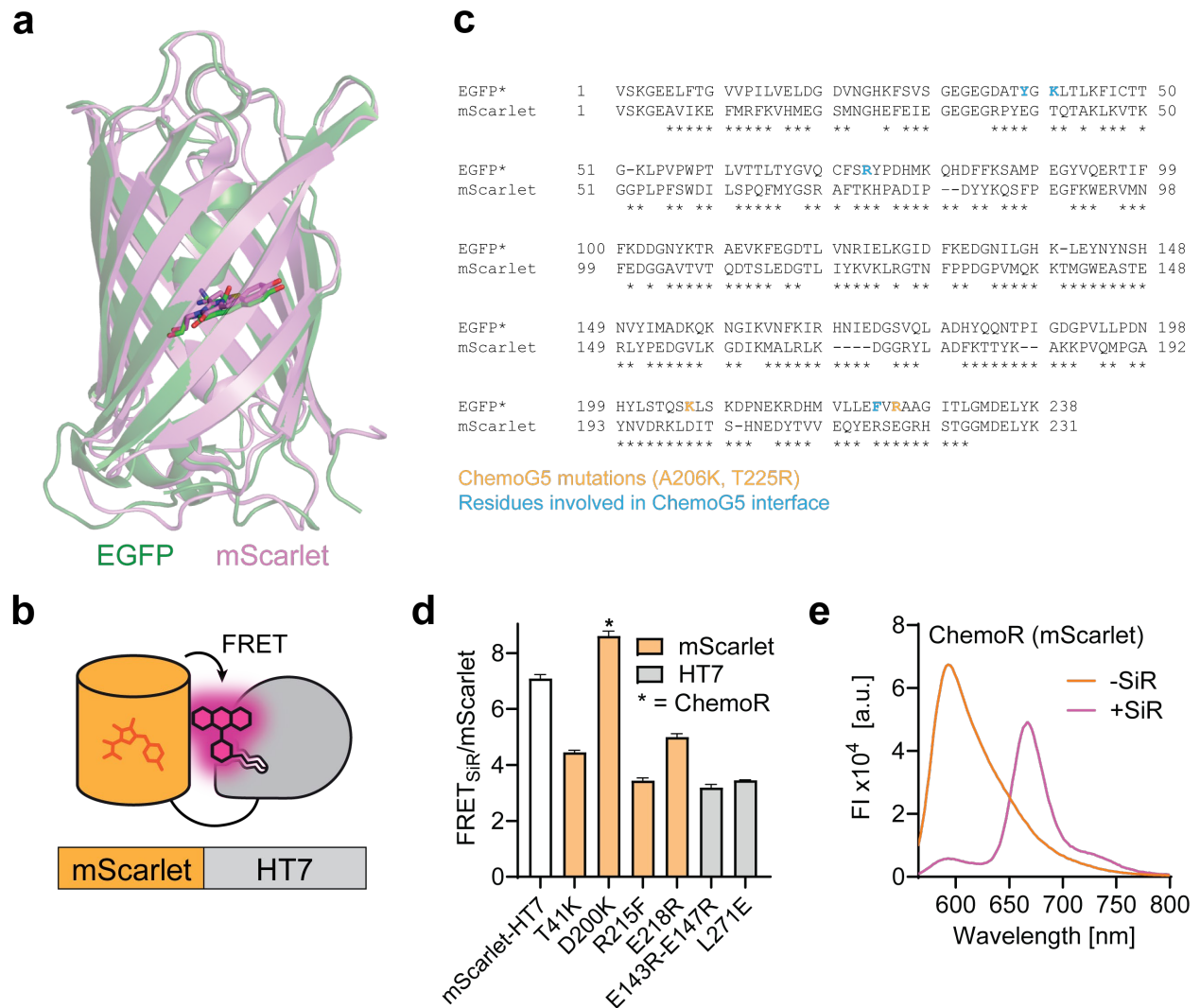


Figure 19 | Incorporation of red fluorescent proteins into the ChemoX design.

a. X-ray crystal structure of EGFP (PDB: 2Y0G) aligned with the crystal structure of mScarlet (PDB: 5LK4). Proteins are shown as cartoon. FP chromophores are shown as sticks. **b.** Schematic representation of chemogenetic FRET pair based on mScarlet. **c.** Protein sequence alignment of EGFP and mScarlet. Asterisks indicate positions with different side chain residues. **d.** FRET_{SiR}/mScarlet ratios of mScarlet-HT7 and different surface mutants labeled with SiR. The nomenclature of the mutations corresponds to the mScarlet numbering (orange) or HT7 numbering (grey). Asterisk indicates optimized construct, named ChemoR. **e.** Fluorescence intensity (FI) emission spectra of ChemoR unlabeled (-SiR) or labeled with SiR (+SiR). Lucas Barck helped with the characterization of the different variants. Adapted from Hellweg *et al.*⁷⁸

Table 4| ChemoX FRET pairs.Constructs were labeled with SiR. Adapted from Hellweg *et al.*⁷⁸

Construct	FP	Interface mutations		FRET _{SiR} /FP	FRET efficiency [%]
		FP	HT7		
EBFP2-HT7	EBFP2	-	-	0.4 ± 0.01	25.9 ± 1.2
ChemoB	EBFP2	N39Y-V206K-T225R	L271E-E143R-E147R	36.2 ± 0.3	96.6 ± 0.1
mCerulean3-HT7*	mCerulean3	K206	-	2.6 ± 0.03	70.2 ± 0.4
ChemoC	mCerulean3	K206-T225R	L271E-E143R-E147R	22.3 ± 0.7	94.6 ± 0.3
Venus-HT7	Venus	-	-	1.0 ± 0.01	58.3 ± 0.2
ChemoY	Venus	A206K-T225R	L271E-E143R-E147R	22.4 ± 1.9	96.6 ± 0.1
mScarlet-HT7	mScarlet	-	-	6.9 ± 0.1	86.1 ± 0.4
ChemoR	mScarlet	D200K	-	8.4 ± 0.2	91.3 ± 0.3

* mCerulean3 contains interface mutation K206 already

2.4. Development of chemogenetic calcium sensors

With the optimized ChemoX design in hand, I aimed to utilize this system for the development of FRET-based biosensors with superior performance and spectral flexibility. Given the large variety of calcium (Ca^{2+}) biosensors and their extensive characterization, developing a Ca^{2+} biosensor represented a promising starting point to probe the strengths and weaknesses of the system. Inspired by the cameleon design⁶¹, I positioned EGFP and HT7 around the Ca^{2+} sensing unit calmodulin (CaM) and its cognate binding peptide myosin light chain kinase (M13, **Figure 20a**). CaM and M13 were connected *via* a rigid poly-proline linker, whereas EGFP and HT7 were fused to CaM and M13 *via* a flexible glycine-glycine-serine (GGS) linker, respectively. Analogous to the cameleon design, binding of Ca^{2+} to CaM induces a large conformational change, which increases the FRET efficiency by altering the distance, relative orientation and intramolecular concentration of the chemogenetic FRET pair. This change in FRET efficiency can then serve as a measure to quantify relative concentrations of Ca^{2+} .

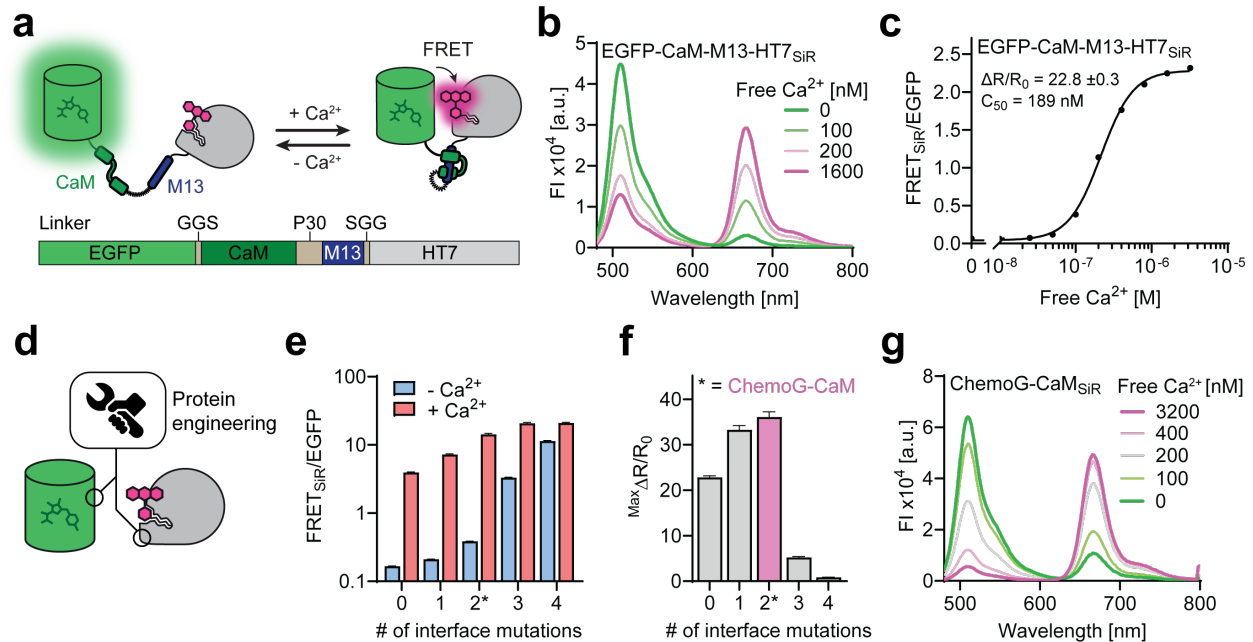


Figure 20 | Development of the chemogenetic calcium sensor ChemoG-CaM.

a. Schematic representation of the chemogenetic calcium sensor design. CaM = calmodulin, M13 = myosin light chain kinase peptide, P30 = poly-proline linker, GGS = glycine-glycine-serine linker. **b, g.** Fluorescence intensity (FI) emission spectra of initial chemogenetic calcium sensor (**b**) and optimized ChemoG-CaM sensor (**g**) labeled with SiR. **c.** Dose-response curve of initial chemogenetic calcium sensor. $\Delta R/R_0$ = maximal FRET_{SiR}/EGFP ratio change. C_{50} = free calcium concentration at half-maximal response. **d.** Schematic representation of interface engineering of chemogenetic FRET pair to increase FRET efficiency and optimize dynamic range. **e.** FRET_{SiR}/EGFP ratios of chemogenetic calcium sensor containing different number (#) of ChemoG interface mutations. Ratios were determined in absence (-Ca²⁺) or presence of calcium (+Ca²⁺). **f.** Dynamic range ($^{Max} \Delta R/R_0$) of chemogenetic calcium sensors. Asterisk indicates optimized sensor variant, named ChemoG-CaM. Adapted from Hellweg *et al.*⁷⁸

Upon titration of the initial construct EGFP-CaM-M13-HT7_{SiR} with Ca²⁺, I observed a substantial change in the fluorescence emission spectrum, transitioning from low FRET efficiency at low Ca²⁺ concentrations to high FRET efficiency at high Ca²⁺ concentrations (**Figure 20b**). By plotting the FRET_{SiR}/EGFP ratio against the free Ca²⁺ concentration, I determined a C_{50} (concentration at which the response of the sensor is half-maximal) of around 189 nM, which is in line with values reported for other Ca²⁺ biosensors based on CaM and M13⁶⁵ (**Figure 20c**). Furthermore, the sensor demonstrated a remarkable dynamic range ($^{Max} \Delta R/R_0 = 22.8 \pm 0.3$, see *Determination of the FRET ratio and FRET ratio changes* for calculation), exceeding that of other FRET-based Ca²⁺ biosensors^{65, 87}. In contrast to cameleon biosensors, which are based on a CFP-YFP FRET pair, the ChemoG design allows for a large spectral separation of the FRET pair, reducing FRET

in the open state of the sensor (low Ca^{2+}). Formation of the ChemoG interface in the closed state of the sensor (high Ca^{2+}), on the other hand, enabled efficient FRET, resulting in a large dynamic range.

Building on these results, I aimed to further optimize the dynamic range of the chemogenetic sensor. Upon re-examination of the emission spectra, it became apparent that the FRET efficiency in the closed state of the sensor could be further improved. Therefore, I introduced ChemoG5 interface mutations in a step-wise manner and evaluated the dynamic range of the corresponding variants (**Figure 20d**). As expected, the more interface mutations were introduced, the higher the FRET efficiency was in both the open and closed state of the sensor. With the incorporation of one and two interface mutations, the relative increase in FRET efficiency was greater in the closed than in the open state of the sensor (**Figure 20e**), resulting in an improved dynamic range (**Figure 20f**). However, this trend reversed after the addition of three or more interface mutations, which is plausible considering that the FRET efficiency in the closed state would reach its maximum eventually, while in the open state, the FRET efficiency would continue to increase due to reinforced interactions within the ChemoG interface. Thus, it is important to find the right balance between stabilizing the ChemoG interface in the closed state, but not to artificially force the sensor to close in absence of Ca^{2+} due to the introduced interactions. In the end, the variant containing two interface mutations (*i.e.*, A206K [EGFP] and L271E [HT7]) exhibited the greatest dynamic range ($^{\text{Max}}\Delta R/R_0 = 36.1 \pm 1.0$) and maintained a C_{50} comparable to that of the initial construct (179 nM, **Table 5, Figure 20g**). This optimized Ca^{2+} biosensor was named ChemoG-CaM.

Table 5 | ChemoX calcium biosensors.

C_{50} = calcium concentration at half-maximal response, Max R/R_0 = maximal change of FRET/FP ratio in absence and presence of calcium. Adapted from Hellweg *et al.*⁷⁸

Construct	FRET pair	Interface mutations			C_{50}	Max $\Delta R/R_0$	Hill slope
		# of mut.	FP	HT7			
1	EGFP/SiR	0	-	-	189 nM	22.8 \pm 0.3	2.2
2	EGFP/SiR	1	A206K	-	203 nM	33.3 \pm 0.8	1.8
3 (ChemoG-CaM)	EGFP/SiR	2	A206K	L271E	179 nM	36.1 \pm 1.0	2.2
4	EGFP/SiR	3	A206K	L271E-E143R-E147R	121 nM	5.2 \pm 0.2	1.5
5	EGFP/SiR	4	A206K-T225R	L271E-E143R-E147R	207 nM	0.8 \pm 0.1	1.1
ChemoB-CaM	EBFP2/SiR	2	N39Y-V206K	-	206 nM	12.7 \pm 0.2	1.8
ChemoC-CaM	mCerulean3/SiR	1	A206K	-	158 nM	2.3 \pm 0.1	3.2
ChemoY-CaM	Venus/SiR	1	A206K	-	226 nM	21.7 \pm 0.6	2.0
ChemoR-CaM0.1	mScarlet/SiR	1	-	-	n.d.	2.6 \pm 0.1	n.d.
ChemoR-CaM	mRuby2/SiR	0	-	-	202 nM	3.4 \pm 0.1	2.7
ChemoR-CaM0.2	mRuby3/SiR	0	-	-	n.d.	2.5 \pm 0.1	n.d.
ChemoR-CaM0.3	mCherry/SiR	0	-	-	n.d.	2.1 \pm 0.1	n.d.
ChemoR-CaM0.4	mKO2/SiR	0	-	-	n.d.	1.9 \pm 0.1	n.d.
ChemoR-CaM0.5	TagRFP/SiR	0	-	-	n.d.	2.0 \pm 0.1	n.d.
YC 3.6	ECFP/Venus	-	-	-	243 nM	5.7 \pm 0.1	1.6

By labeling the sensor with different rhodamine-based fluorophores, I could customize the spectral properties of the FRET acceptor (**Figure 21a-c, Table 6**). The dynamic range was greatest in combination with SiR and smallest with TMR. Similar to CFP-YFP FRET sensors, the large spectral overlap between EGFP and TMR resulted in high FRET in the open state of the sensor and resulted in spectral cross-talk, consequently reducing the dynamic range.

In addition, I exchanged EGFP with other fluorescent proteins and optimized the number of interface mutations as described for ChemoG-CaM, ultimately yielding a palette of ChemoX-CaM biosensors with various colors (**Figure 21d-f**).

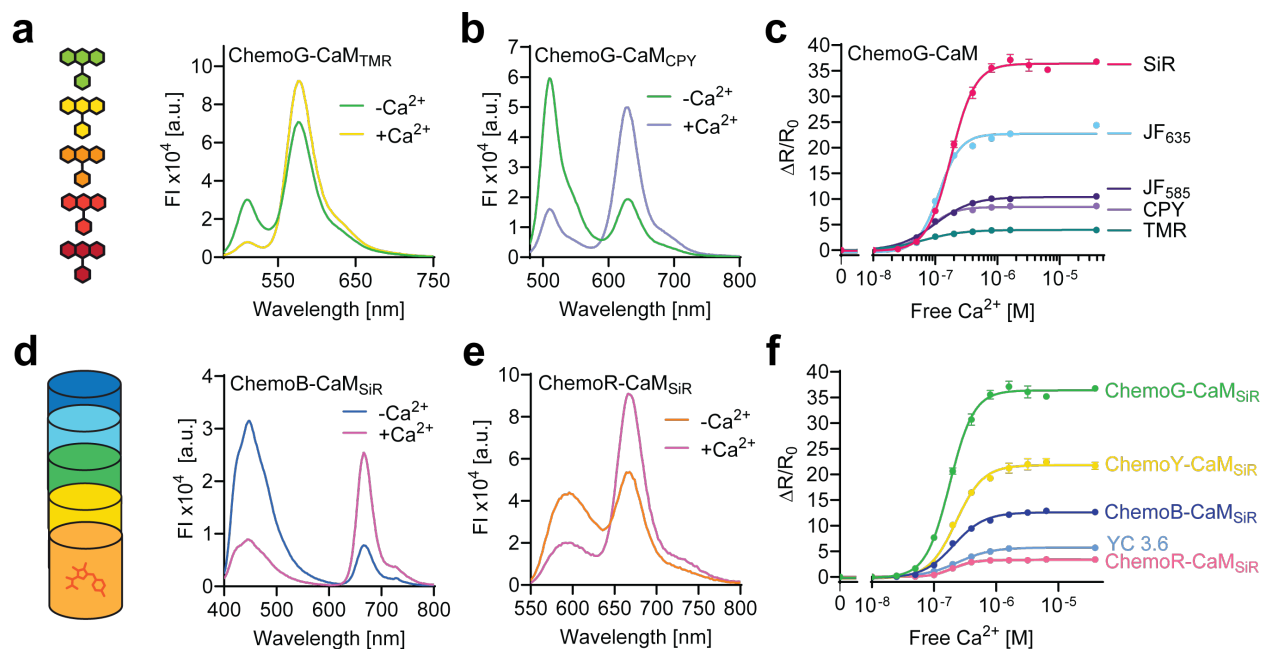


Figure 21 | Color palette of chemogenetic calcium biosensors.

a, b, d, e. Fluorescence intensity (FI) emission spectra of ChemoG-CaM labeled with different FRET acceptors (**a, b**) or ChemoX-CaM_{SiR} sensors based on different fluorescent protein FRET donors (**d, e**). **c, f.** Dose-response curves of ChemoG-CaM labeled with different FRET acceptors (**c**) or ChemoX-CaM_{SiR} sensors compared to the CFP-YFP FRET calcium sensor yellowameleon 3.6 (YC 3.6, **f**). Plotted are the FRET/FP ratio changes ($\Delta R/R_0$). Lucas Barck helped with the characterization of the ChemoX-CaM sensors. Adapted from Hellweg *et al.*⁷⁸

Table 6 | ChemoG-CaM biosensors based on different FRET acceptors.

C_{50} = calcium concentration at half-maximal response, $\text{Max } \Delta R/R_0$ = maximal change of FRET/EGFP ratio in absence and presence of calcium. Adapted from Hellweg *et al.*⁷⁸

Construct	FRET acceptor	Max emission acceptor	C_{50}	Max $\Delta R/R_0$	Hill slope
ChemoG-CaM	TMR	580 nm	66 nM	3.9 ± 0.1	1.4
ChemoG-CaM	JF ₅₈₅	610 nm	100 nM	10.5 ± 0.4	1.5
ChemoG-CaM	CPY	628 nm	76 nM	$8.6.0 \pm 0.1$	2.2
ChemoG-CaM	JF ₆₃₅	656 nm	114 nM	24.4 ± 0.3	2.5
ChemoG-CaM	SiR	668 nm	179 nM	36.8 ± 0.2	2.2

The dynamic range of an initial sensor construct based on mScarlet was very low ($\text{Max } \Delta R/R_0 = 2.6 \pm 0.1$). Consequently, I explored alternative red FPs, leading to an improved sensor based on mRuby2 ($\text{Max } \Delta R/R_0 = 3.4 \pm 0.1$, **Table 5**), which was called ChemoR-CaM. In

comparison to ChemoR-CaM, ChemoX sensors based on EGFP, Venus and EBFP2 exhibited a substantially larger dynamic range, presumably because of the larger spectral separation of the FRET pairs (= low FRET in open state of the sensor) and the increased capacity to tune the ChemoX interface (= high FRET in closed state of the sensor). In a benchmark comparison, all ChemoX sensors outperformed the CFP-YFP-based Ca²⁺ sensor yellow cameleon 3.6 (YC 3.6), with the exception of ChemoR-CaM (**Figure 21f, Table 5**), demonstrating the potential of the chemogenetic design in developing biosensors with large dynamic ranges and spectral flexibility. Notably, the dynamic range of ChemoG-CaM_{SiR} was 6.3-fold higher than that of YC 3.6 ($^{\text{Max}}\Delta R/R_0 = 5.7 \pm 0.1$).

To test whether the large dynamic ranges of the ChemoX biosensors would translate into high sensitivity in detecting changes of free Ca²⁺ inside cells, I expressed ChemoG-CaM in the cytosol of HeLa Kyoto cells and labeled the sensor with SiR. The sensor exhibited very low FRET at resting conditions ($\text{FRET}_{\text{SiR/EGFP}} = 0.14 \pm 0.02$, **Figure 22a**), indicating that the free Ca²⁺ concentration in the cytosol of HeLa Kyoto cells falls within the low nanomolar range, being in line with values reported in the literature⁸⁸. Upon addition of 10 μM histamine, which is known to induce a transient rise in intracellular Ca²⁺ in HeLa cells⁸⁹, the $\text{FRET}_{\text{SiR/EGFP}}$ ratio increased rapidly up to 2.43 ± 0.62 with a maximal ratio change of $^{\text{Max}}\Delta R/R_0 = 15.1 \pm 3.9$. Subsequently, this increase subsided, returning close to baseline levels within 5 minutes following histamine stimulation (**Figure 22a-b**), demonstrating the reversibility of the chemogenetic biosensors.

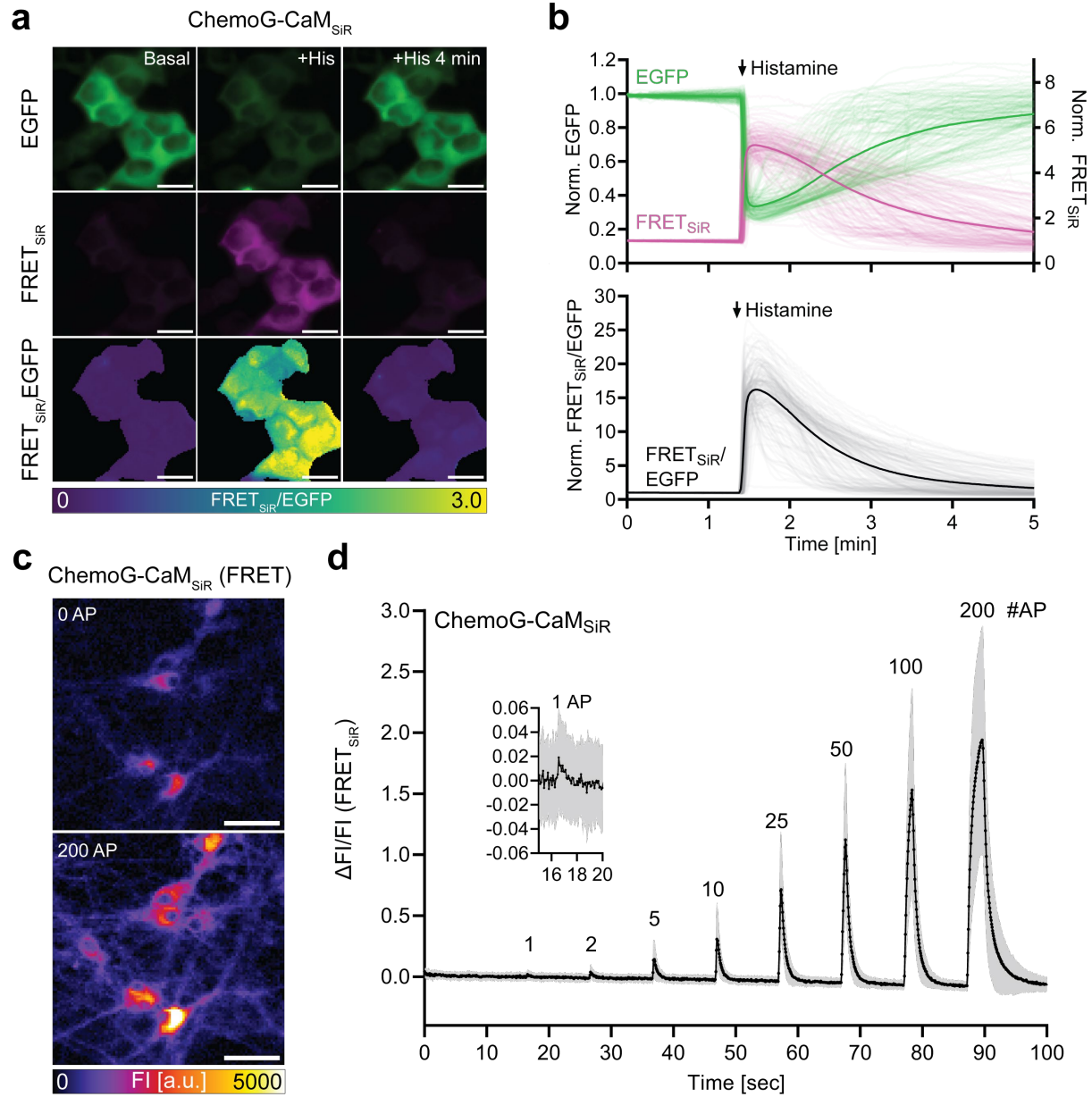


Figure 22 | Characterization of ChemoG-CaM in HeLa Kyoto cells and rat hippocampal neurons.

a. Fluorescent images of HeLa Kyoto cells expressing ChemoG-CaM in the cytosol labeled with SiR. Images were acquired with a widefield microscope. Shown are the EGFP and FRET_{SiR} emission channels, and the ratiometric projection of the FRET_{SiR} and EGFP emission channels at baseline conditions (basal), right after the addition of 10 μ M histamine (+His) and 4 min post-histamine addition (+His 4 min). Scale bars = 25 μ m. **b.** Plotted are the mean (thick line) and individual traces (thin lines) of EGFP and FRET_{SiR} fluorescence signals (top graph), and the corresponding FRET_{SiR}/EGFP ratio (bottom graph) of HeLa Kyoto cells expressing ChemoG-CaM_{SiR} in the cytosol. Cells were treated as described in **a**. Addition of histamine is indicated with an arrow. EGFP, FRET_{SiR} and FRET_{SiR}/EGFP ratios were normalized to $t = 0$ min. **c.** Fluorescent images of rat hippocampal neurons expressing ChemoG-CaM in the cytosol labeled with SiR. Images were acquired with a widefield microscope. Shown is the FRET_{SiR} emission channel at baseline conditions (0 action potentials, AP) and after electric field stimulation (200 AP). Scale bars = 50 μ m. FI = fluorescence intensity. **d.** Plotted is the FRET_{SiR} FI change over baseline (Δ FI/FI₀) of rat hippocampal neurons

expressing ChemoG-CaM_{SiR} in the cytosol. Shown are the mean (thick line) and individual traces (thin lines) of neurons. Different numbers (#) of APs were evoked by electric field stimulation, as indicated. FRET_{SiR} fluorescence was normalized to $t = 0$ min. Inlet shows $\Delta FI/FI_0$ during stimulation with 1 AP. Anna Edenhofer helped with the time course experiments in HeLa Kyoto cells. Adapted from Hellweg *et al.*⁷⁸

Since short-lived spikes of intracellular Ca^{2+} are known to play an important role in neuronal functions including synaptic signaling and memory formation⁹⁰, I also assessed the performance of ChemoG-CaM in detecting action potentials (APs) triggered by electric field stimulation. For this purpose, I expressed ChemoG-CaM in isolated rat hippocampal neurons and labeled the sensor with SiR. To account for the brief duration of Ca^{2+} transients during an action potential, I recorded the fluorescence intensity (FI) exclusively of the FRET_{SiR} emission channel, optimizing the acquisition time to 81 ms per frame. The FI rapidly increased upon electric field stimulation and the amplitude of the FI increase correlated with the number of evoked APs, reaching a maximum FI change ($^{Max}\Delta FI/FI_0$) of 206 ± 90 % for 200 APs (**Figure 22c-d**). Furthermore, the sensor was sensitive enough to detect a single AP. Compared to intensimetric Ca^{2+} biosensors commonly used to record Ca^{2+} transients in neurons, such as the recently developed jGCaMP8 series⁹¹, ChemoG-CaM_{SiR} showed a significantly smaller FI change in response to a single AP (~ 2 % *versus* ~ 100 %). Nevertheless, the maximum response of ChemoG-CaM_{SiR} is comparable to the recently developed HaloCaMP series, which is also based on the FI change of a rhodamine-based fluorophore labeled to HT7⁵⁹. Based on these results, I could confirm the strong performance of ChemoG-CaM observed *in vitro* also in a cellular and physiologically relevant context.

2.5. Development of chemogenetic ATP biosensors with superior performance

After demonstrating the potential of the ChemoX design for the development of high-performance FRET-based biosensors, I focused on leveraging its benefits to address limitations of existing biosensors for other crucial analytes. To this end, I chose adenosine triphosphate (ATP) as an analyte of interest based on its pivotal role as a universal energy currency for cellular functions, and as a signaling molecule within purinergic signaling pathways⁹². To better understand how ATP is regulated within cells, a number of fluorescent biosensors have been developed that enabled researchers to monitor ATP levels with high spatiotemporal precision and in real-time⁹³. Despite the recent progress in the development of ATP biosensors, most of them suffer from poor dynamic ranges and/or are limited in their capacity to be multiplexed with other fluorescent tools since they are based on cyan, green or yellow FPs^{74, 94-96}. To bridge this technological gap, I aimed to utilize the ChemoX design for the development of ATP biosensors with larger dynamic ranges and greater compatibility for multiplexing purposes.

Similar to the approach taken for the development of ChemoG-CaM, I exchanged the CFP-YFP FRET pair of the established ATP biosensor ATeam 1.03⁹⁴ with EGFP^{A206K} and HT7 positioned around the ϵ subunit from a bacterial F₀-F₁ ATP synthase (*Bacillus subtilis*). This subunit serves as sensing unit of the designated ATP biosensor, exploiting its large conformational change upon binding to ATP (**Figure 23a**).

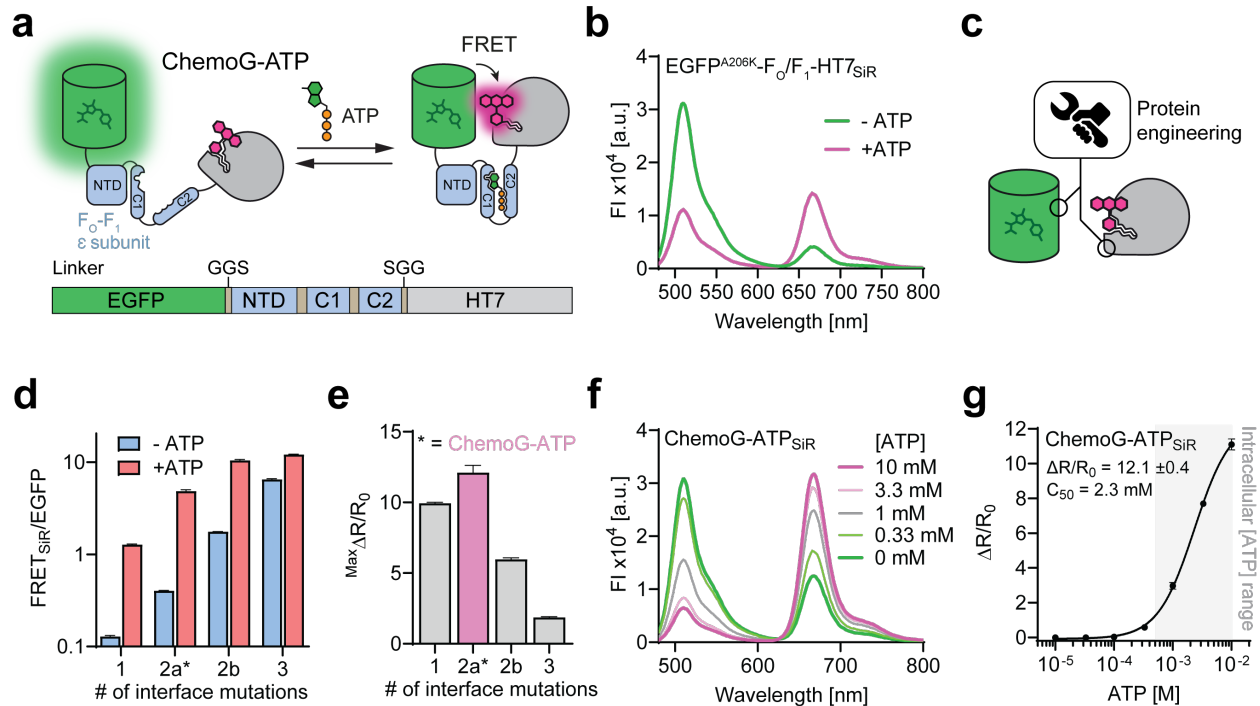


Figure 23 | Development of the chemogenetic ATP biosensor ChemoG-ATP.

a. Schematic representation of the chemogenetic ATP sensor design. F_0 - F_1 ϵ subunit = epsilon subunit of the F_0 - F_1 ATP-synthase from *Bacillus subtilis*. GGS = glycine-glycine-serine linker. **b, f.** Fluorescence intensity (FI) emission spectra of initial chemogenetic ATP sensor (**b**) and optimized ChemoG-ATP sensor (**f**) labeled with SiR. **c.** Schematic representation of interface engineering of chemogenetic FRET pair to increase FRET efficiency and optimize dynamic range. **d.** $FRET_{SiR}/EGFP$ ratios of chemogenetic ATP sensors containing different number (#) of ChemoG interface mutations (**Table 7**). Ratios were determined in absence (-ATP) or presence (+ATP) of ATP. **e.** Dynamic range ($Max \Delta R/R_0$) of chemogenetic ATP sensors. Asterisk indicates optimized sensor variant, named ChemoG-ATP. **g.** Dose-response curve of ChemoG-ATP labeled with SiR. Plotted are the FRET/FP ratio changes ($\Delta R/R_0$). Intracellular ATP concentration range is highlighted with a grey box. Adapted from Hellweg *et al.*⁷⁸

I labeled the initial sensor construct $EGFP^{A206K}$ - F_0 - F_1 -HT7 with SiR, and evaluated its response towards ATP. The sensor exhibited a very low $FRET_{SiR}/EGFP$ ratio in absence of ATP (0.13 ± 0.01), which increased substantially in presence of 10 mM ATP (1.28 ± 0.02), resulting in a dynamic range of 9.94 ± 0.15 (**Figure 23b**). Similar to the observations that I made for the initial ChemoG calcium sensor, the $FRET_{SiR}/EGFP$ ratio was relatively weak in the closed state of the sensor (+ATP). Therefore, I introduced additional ChemoG interface mutations to improve the dynamic range (**Figure 23c**). As expected, the overall $FRET_{SiR}/EGFP$ ratio increased upon introduction of additional interface mutations with a trend comparable to the optimization of ChemoG-CaM (**Figure 20e**). Notably, the addition of a second interface mutation resulted in

different outcomes depending on the specific mutation introduced. Incorporation of L271E on HT7 increased the FRET_{SiR/EGFP} in the closed state of the sensor (+ ATP) to a greater extent than in the open state of the sensor (- ATP), resulting in an improved dynamic range (**Figure 23d-e**). Incorporation of T225R on EGFP, on the other hand, led to an overall stronger increase of the FRET_{SiR/EGFP} ratio in both states of the sensor compared to L271E. However, the increase was particularly strong in the open state, reducing the dynamic range. This finding suggested that certain interface mutations have a more pronounced impact on stabilizing the ChemoG interface than others. Thus, by selecting specific interface mutations, it is possible to further fine-tune the FRET efficiency of the sensor and, consequently, its dynamic range.

The optimized variant containing the two interface mutations A206K (EGFP) and L271E (HT7), was chosen as the final sensor design and named ChemoG-ATP. When labeled with SiR, ChemoG-ATP exhibited a large change in the emission spectrum upon titration with ATP in a dose-dependent manner (**Figure 23f-g**), yielding a dynamic range of $f^{\text{Max}}\Delta R/R_0 = 11.1 \pm 0.3$ and a C_{50} of 2.3 mM, which is in the range of intracellular ATP concentrations ($\sim 2 - 8 \text{ mM}^{97}$). Titration with different nucleotides revealed that the sensor is highly specific for ATP and showed no response for AMP or ADP (**Figure 24a**). GTP led to a minor decrease in the FRET_{SiR/EGFP} ratio at millimolar concentrations, which is negligible considering physiological intracellular GTP concentrations ($468 \pm 224 \mu\text{M}^{98}$). However, the sensor is sensitive towards changes of pH and temperature (**Figure 24b-c**). Comparing these results with reported data on the template biosensor ATeam 1.03 and other biosensors utilizing the same sensing unit^{74, 94, 95}, it is likely that the observed sensitivities are due to the sensing unit rather than the ChemoG FRET pair. This is further supported by the data on ChemoG1-5_{SiR} at different pH (**Figure 14a**), which showed no obvious impact of pH on the FRET_{SiR/EGFP} ratio. Nevertheless, it is important to consider these sensitivities when using the sensor in cell experiments where changes in intracellular pH or fluctuations in the ambient temperature might cause changes in the FRET ratio unrelated to changes in the ATP concentration.

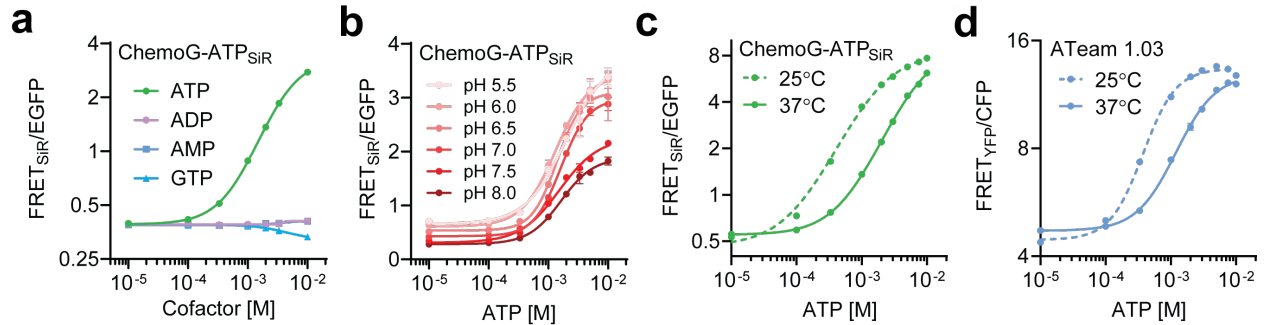


Figure 24 | Characterization of ChemoG-ATP.

a-d. Shown are the FRET/FP ratios of ChemoG-ATP_{SiR} (**a-c**) and ATeam 1.03 (**d**) upon titration with ATP and other nucleotides (**a**), titration of ATP at different pH (**b**), titration of ATP at different temperatures (**c**), and titration of ATeam 1.03 at different temperatures (**d**). Adapted from Hellweg *et al.*⁷⁸

To expand the spectral properties of ChemoG-ATP, I substituted EGFP with EBFP2 and mRuby2, and introduced interface mutations on EBFP2 equivalent to those incorporated in ChemoG-ATP (*i.e.*, N39Y-V206K [both EBFP2] and L271E [HT7], **Figure 25a-b**). All ChemoX-ATP sensors maintained a C_{50} between 2.3 – 3.2 mM (**Table 7, Figure 25c**). ChemoB-ATP_{SiR} ($^{Max}\Delta R/R_0 = 5.0 \pm 0.1$) and ChemoG-ATP_{SiR} ($^{Max}\Delta R/R_0 = 11.1 \pm 0.3$) outperformed the FRET sensor ATeam 1.03 ($^{Max}\Delta R/R_0 = 1.4 \pm 0.1$), whereas ChemoR-ATP_{SiR} showed an inferior dynamic range ($^{Max}\Delta R/R_0 = 0.8 \pm 0.1$). This trend is in line with the benchmark comparison of the ChemoX-CaM sensors, corroborating the limited capacity to optimize the dynamic range of ChemoR FRET sensors.

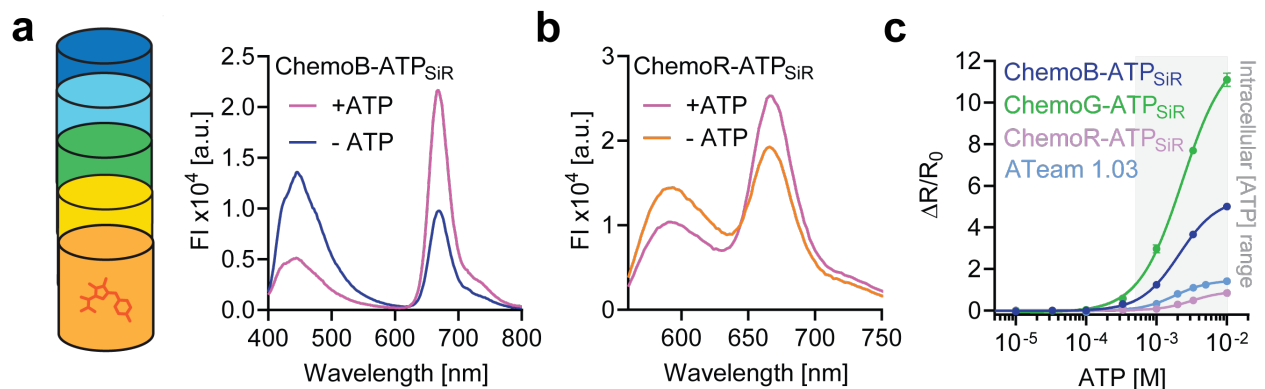


Figure 25 | ChemoX-ATP sensors based on different fluorescent proteins.

a-b. Fluorescence intensity (FI) emission spectra of ChemoB-ATP (**a**) and ChemoR-ATP (**b**) in absence (-ATP) or presence of 10 mM ATP (+ATP). Sensors were labeled with SiR. **c.** Dose-response curves of ChemoX-ATP sensors labeled with SiR and ATeam 1.03. Plotted are the FRET/FP ratio changes ($\Delta R/R_0$). Intracellular ATP concentration range is highlighted with a grey box. Adapted from Hellweg *et al.*⁷⁸

Table 7 | Overview of chemogenetic ATP biosensors.

C_{50} = ATP concentration at half-maximal response, Max $\Delta R/R_0$ = maximal change of FRET/FP ratio in absence and presence of ATP. N.D. = not determined. Adapted from Hellweg *et al.*⁷⁸

Construct	FRET pair	Interface mutations		C_{50}	Max $\Delta R/R_0$	Hill slope
		FP	HT7			
1	EGFP/SiR	A206K	-	N.D.	9.9 ± 0.1	N.D
2a (ChemoG-ATP)	EGFP/SiR	A206K	L271E	2.3 mM	11.1 ± 0.3	1.4
2b	EGFP/SiR	A206K-T225R	-	N.D.	6.0 ± 0.1	N.D
3	EGFP/SiR	A206K-T225R	L271E	N.D.	1.9 ± 0.0	N.D
ChemoB-ATP	EBFP2/SiR	N39Y-V206K	L271E	2.8 mM	5.0 ± 0.1	1.6
ChemoR-ATP	mRuby2/SiR	-	-	3.2 mM	0.8 ± 0.1	2.0
ATeam 1.03	mseCFP/cpVenus	-	-	1.8 mM	1.4 ± 0.1	1.8

Next, I characterized the performance of the ChemoX-ATP biosensors in HeLa Kyoto cells. To perturb intracellular levels of ATP, I used 2-deoxy-D-glucose (2DG), which is taken up by cells *via* glucose transporters (GLUTs). After conversion into 2-deoxy-D-glucose-6-phosphate (2DG6P), it blocks glycolysis through inhibition of hexokinase II and glucose-6-phosphate isomerase, ultimately resulting in decreased production of ATP^{99, 100} (**Figure 26a**). I expressed ChemoG-ATP in the cytosol of HeLa Kyoto cells and labeled the sensor with SiR. Upon addition of 2DG to the cells, the FRET_{SiR}/EGFP ratio decreased instantaneously from 1.17 ± 0.37 down to 0.40 ± 0.06 as a result of the reduced ATP production (**Figure 26b-c**). Subsequent addition of excess D-glucose partially recovered the basal ATP levels, as indicated by the increase in FRET_{SiR}/EGFP to 0.63 ± 0.13 .

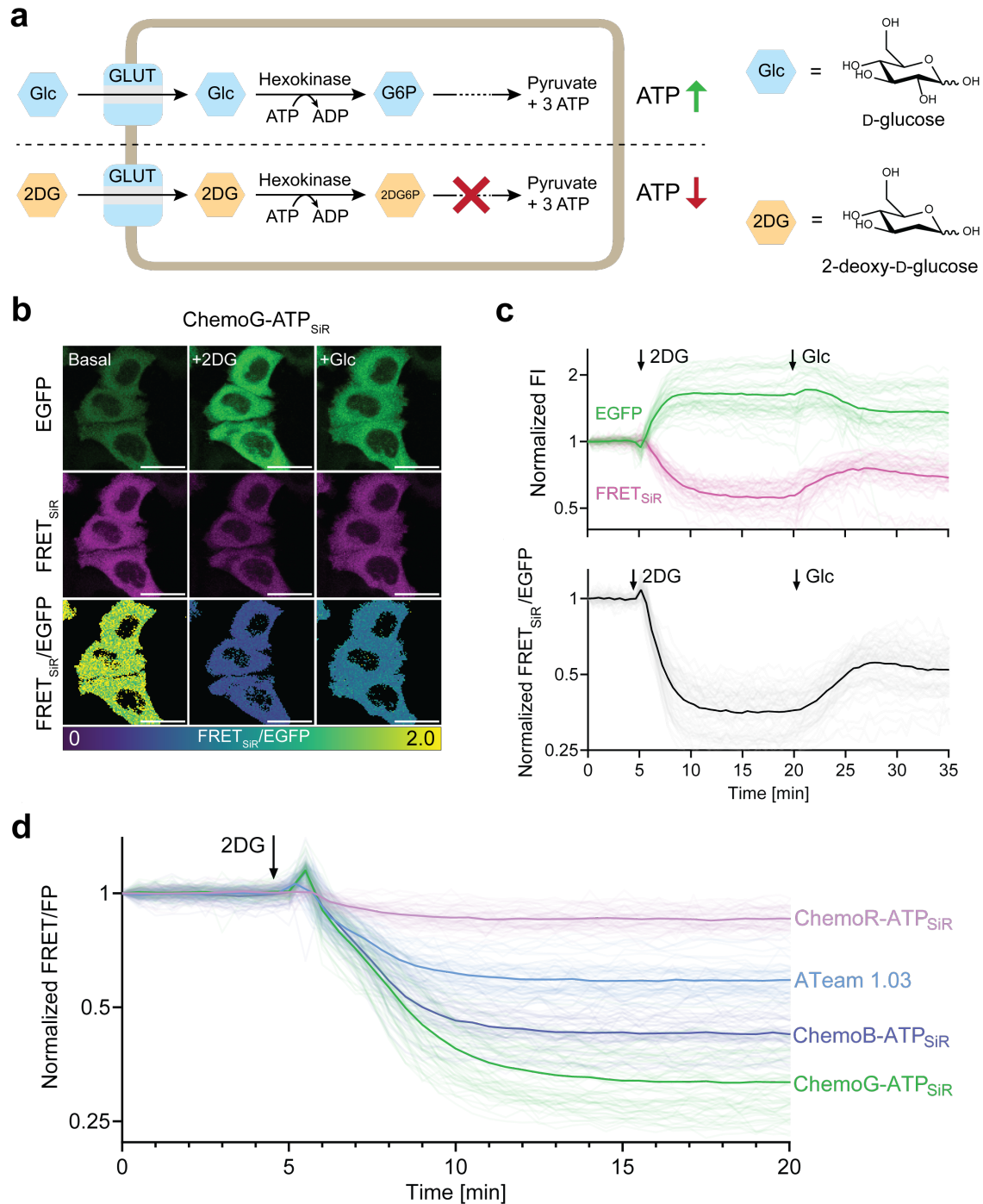


Figure 26 | Characterization of ChemoX-ATP sensors in HeLa Kyoto cells.

a. Cartoon depicting the inhibitory effect of 2-deoxy-D-glucose (2DG) on intracellular glycolysis. D-glucose (Glc) and 2DG are taken up by cells *via* glucose transporters (GLUT) and are subsequently metabolized by hexokinase II. The phosphorylated product Glc-6-phosphate (G6P) is further metabolized to yield pyruvate and ATP (glycolysis), while 2DG-6-phosphate (2DG6P) cannot be used for glycolysis, reducing the production of ATP. **b.** Fluorescent images of HeLa Kyoto cells expressing ChemoG-ATP in the cytosol labeled with SiR. Images were acquired with a confocal microscope. Shown are the EGFP and FRET_{SiR} emission channels, and the ratiometric projection of the FRET_{SiR} and EGFP emission channels at baseline conditions (basal), right after the

addition of 10 mM 2DG (+2DG) and subsequent addition of Glc (+Glc). Scale bars = 25 μm . **c.** Plotted are the mean (thick line) and individual traces (thin lines) of EGFP and FRET_{SIR} fluorescence signals (top graph), and the corresponding FRET_{SIR}/EGFP ratio (bottom graph) of HeLa Kyoto cells expressing ChemoG-ATP_{SIR} in the cytosol. Cells were treated as described in **b.** Addition of 2DG and Glc are indicated with an arrow. EGFP, FRET_{SIR} and FRET_{SIR}/EGFP ratios were normalized to $t = 0$ min. **d.** Plotted are the mean (thick line) and individual traces (thin lines) of FRET/FP ratios of HeLa Kyoto cells expressing ATP biosensors in the cytosol. Cells were treated as described in **b.** Addition of 2DG and Glc are indicated with an arrow. FRET/FP ratios were normalized to $t = 0$ min. Adapted from Hellweg *et al.*⁷⁸

In order to compare the performance of the ChemoX-ATP biosensors with ATeam 1.03, I conducted a side-by-side comparison in cells. Consistent with the dynamic ranges obtained from the *in vitro* titrations, ChemoG-ATP_{SIR} ($\Delta R/R_0 = -67.9 \pm 6.3 \%$) and ChemoB-ATP_{SIR} ($\Delta R/R_0 = -57.5 \pm 4.7 \%$) showed a larger response compared to ATeam 1.03 ($\Delta R/R_0 = -41.1 \pm 5.1 \%$), whereas ChemoR-ATP_{SIR} exhibited a substantially smaller change ($\Delta R/R_0 = -14.5 \pm 4.9 \%$, **Figure 26d**). The FRET/FP ratio for ChemoB-ATP_{SIR}, ChemoG-ATP_{SIR} and ATeam 1.03 briefly increased right after the addition of 2DG. Despite temperature-equilibration of reagents and the imaging plate, this short rise in the FRET ratio was likely caused by small temperature fluctuations upon opening of the microscope chamber to add 2DG. In summary, I was able to apply the ChemoX design to build a set of ATP biosensors with superior dynamic ranges and tunable emission wavelengths that are suitable for the detection of changes in intracellular ATP.

2.6. Development of chemogenetic NAD⁺ biosensors for multiplexing purposes

Nicotinamide adenine dinucleotide (NAD⁺) represents another essential metabolite, which is commonly known for its function as redox cofactor¹⁰¹. It also serves as a direct substrate for a variety of enzymes including poly-ADP-ribose polymerases (PARPs), sirtuins and NAD⁺ hydrolases¹⁰¹. Since the activity of these enzymes is intricately tied to the availability of free NAD⁺, alterations in its concentration have a direct impact on diverse biological functions, linking cell metabolism with cellular processes such as signaling¹⁰², or transcriptional and epigenetic regulation¹⁰³. Through the development and application of fluorescent NAD⁺ biosensors^{76, 104}, it was discovered that regulation of free NAD⁺ at the subcellular level plays an important role during cell differentiation¹⁰⁵, protein homeostasis¹⁰⁶ or DNA repair¹⁰⁷. However, spectral incompatibility of current NAD⁺ sensors limits their capability to monitor subcellular NAD⁺ pools at multiple sites simultaneously and thus poses a challenge to expand our understanding on the roles of compartmentalized NAD⁺. By developing ChemoX biosensors for NAD⁺, I aimed to complement the existing toolbox of NAD⁺ biosensors and increase the multiplexing capacity for subcellular NAD⁺.

The bacterial DNA Ligase (LigA) represented a promising candidate as the sensing unit of a FRET-based NAD⁺ biosensor, given its large conformational change of the two subdomains 1a and 1b upon binding of NAD⁺¹⁰⁸. Furthermore, the LigA from *Enterococcus faecalis* has been successfully used as sensing unit for the development of an intensimetric NAD⁺ biosensor¹⁰⁴. Since proteins derived from thermophilic organisms often possess increased thermostability, I chose to work with the LigA from the extreme thermophile *Thermus thermophilus* (ttLigA). I flanked EGFP^{A206K} and HT7 around a mutant ttLigA containing 2 point mutations (K116L and D288N) that are known to render LigAs enzymatically inactive¹⁰⁴ (ttLigAⁱ, **Figure 27a**). This prevents the self-adenylation of the LigA using NAD⁺. The initial construct EGFP^{A206K}-ttLigAⁱ-HT7_{TMR} showed a large change in the emission spectrum upon addition of 1 mM NAD⁺ (**Figure 27b**) with a dynamic range of $^{Max}\Delta R/R_0 = 10.1 \pm 0.1$ and a C₅₀ of approximately 38 μ M (**Figure 27c**). To optimize the response range of the sensor for intracellular NAD⁺ concentrations (50-400 μ M^{76, 104}), I mutated either of two ttLigAⁱ residues involved in the binding of the adenosine part

of NAD⁺ (*i.e.*, Y225W and V291A, **Figure 27d**). Both mutations shifted the C₅₀ towards higher NAD⁺ concentrations (Y225W = 129 μM, V291A = 75 μM), but also lowered the FRET in the closed state of the sensor reducing its dynamic range (^{Max}ΔR/R₀ Y225W = 6.3 ± 0.1, ^{Max}ΔR/R₀ V291A = 6.2 ± 0.1, **Figure 27e**). The decreased FRET is potentially a consequence of changes in the conformation of the ttLigAⁱ in the NAD⁺-bound state that alter the relative orientation or distance of the FRET pair. The combination of both mutations yielded a C₅₀ of approximately 205 μM, suitable for the detection of intracellular NAD⁺ (**Figure 27e**). However, the dynamic range of the double mutant was further decreased (^{Max}ΔR/R₀ = 3.6 ± 0.1). To compensate for the loss in dynamic range, I introduced between two to four ChemoG5 interface mutations and labeled the sensor with SiR, which increased the overall FRET_{SiR}/EGFP ratio and allowed me to identify variants with improved performance (**Figure 27f-h**).

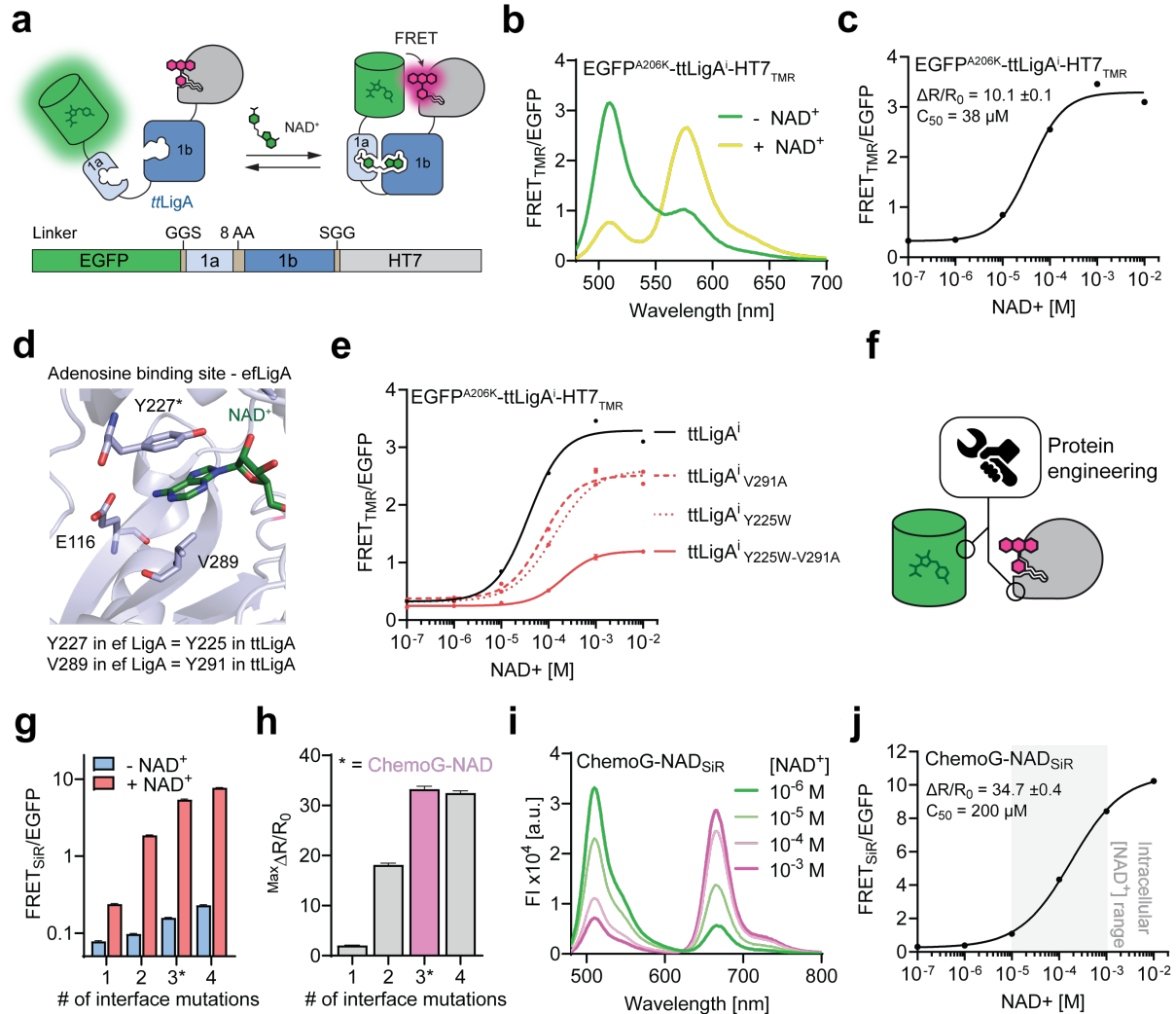


Figure 27 | Development of the chemogenetic NAD^+ biosensor ChemoG-NAD.

a. Schematic representation of the chemogenetic NAD^+ sensor design. ttLigA = bacterial DNA ligase A from *Thermus thermophilus* consisting of two domains, 1a and 1b. GGS = glycine-glycine-serine linker. ttLigA was rendered catalytically inactive (ttLigA^i) by introducing the mutations K116L and D288N. **b, i.** Fluorescence intensity (FI) emission spectra of initial chemogenetic NAD^+ sensor labeled with TMR (**b**) and optimized ChemoG-NAD sensor labeled with SiR (**i**). **c, e, j.** Dose-response curves of initial chemogenetic NAD^+ sensor labeled with TMR (**c**), intermediate affinity mutants labeled with TMR (**e**) or the optimized ChemoG-NAD sensor labeled with SiR (**j**). $\Delta R/R_0$ = maximal $\text{FRET}_{\text{SiR}}/\text{EGFP}$ ratio change. C_{50} = NAD^+ concentration at half-maximal response. Intracellular NAD^+ concentration range is highlighted with a grey box. **d.** X-ray crystal structure of LigA from *Enterococcus faecalis* (efLigA) in complex with NAD^+ (PDB: 1TAE), zoomed in on the adenosine binding site (1b domain). Protein is shown as cartoon. NAD^+ and side chain residues involved in the binding of NAD^+ are shown as sticks. The residues in ttLigA corresponding to the residues shown in the efLigA crystal structure, are depicted below. **f.** Schematic representation of interface engineering of chemogenetic FRET pair to increase FRET efficiency and optimize dynamic range. **g.** $\text{FRET}_{\text{SiR}}/\text{EGFP}$ ratios of chemogenetic NAD^+ sensors containing different number (#) of ChemoG interface mutations (**Table 8**). Ratios were determined in absence (- NAD^+) or presence of 10 mM NAD^+ (+ NAD^+). **h.** Dynamic range ($^{\text{Max}}\Delta R/R_0$) of chemogenetic NAD^+ sensors. Asterisk indicates optimized sensor variant, named ChemoG-NAD. Adapted from Hellweg *et al.*⁷⁸

Incorporation of three interface mutations (A206K and T225R [both EGFP], L271E [HT7]) yielded the final sensor variant with a dynamic range of $^{\text{Max}}\Delta R/R_0 = 34.7 \pm 0.4$ and a C_{50} of approximately 200 μM , termed ChemoG-NAD (**Figure 27i-j**). ChemoG-NAD is highly specific for NAD^+ and showed no response for other metabolites structurally related to NAD^+ (**Figure 28a**), with the exception of NADP^+ and NADH . However, millimolar concentrations of NADP^+ and NADH are needed to evoke a change in the $\text{FRET}_{\text{SiR}}/\text{EGFP}$ ratio, which is negligible considering that their intracellular concentrations are estimated to lie in the low micromolar range^{109, 110}. The $\text{FRET}_{\text{SiR}}/\text{EGFP}$ ratio upon titration with NAD^+ was affected by presence of 100 μM nicotinamide riboside (NR), nicotinamide mononucleotide (NMN) or the nicotinic acid form of NAD^+ (NAAD^+ , **Figure 28b**). However, intracellular concentrations of these metabolites are estimated to be $\leq 1 \mu\text{M}$ ¹¹⁰ and should therefore not affect the response of the sensor in cell experiments. Furthermore, millimolar concentrations of ATP, ADP and AMP each affected the $\text{FRET}_{\text{SiR}}/\text{EGFP}$ ratio to the same extent (**Figure 28c**). These concentrations are physiologically relevant; however, as long as the total concentration of free ATP, ADP and AMP combined is unchanged, the impact on the $\text{FRET}_{\text{SiR}}/\text{EGFP}$ ratio should remain constant and not affect the response of the sensor in cell experiments. The sensor response was insensitive to changes in temperature between 25 °C and 37 °C (**Figure 28d**), but a decrease in pH shifted the C_{50} of the sensor towards lower NAD^+ concentrations (**Figure 28e**). This sensitivity should be considered in cell experiments, for example, by monitoring the pH with a spectrally compatible pH sensor.

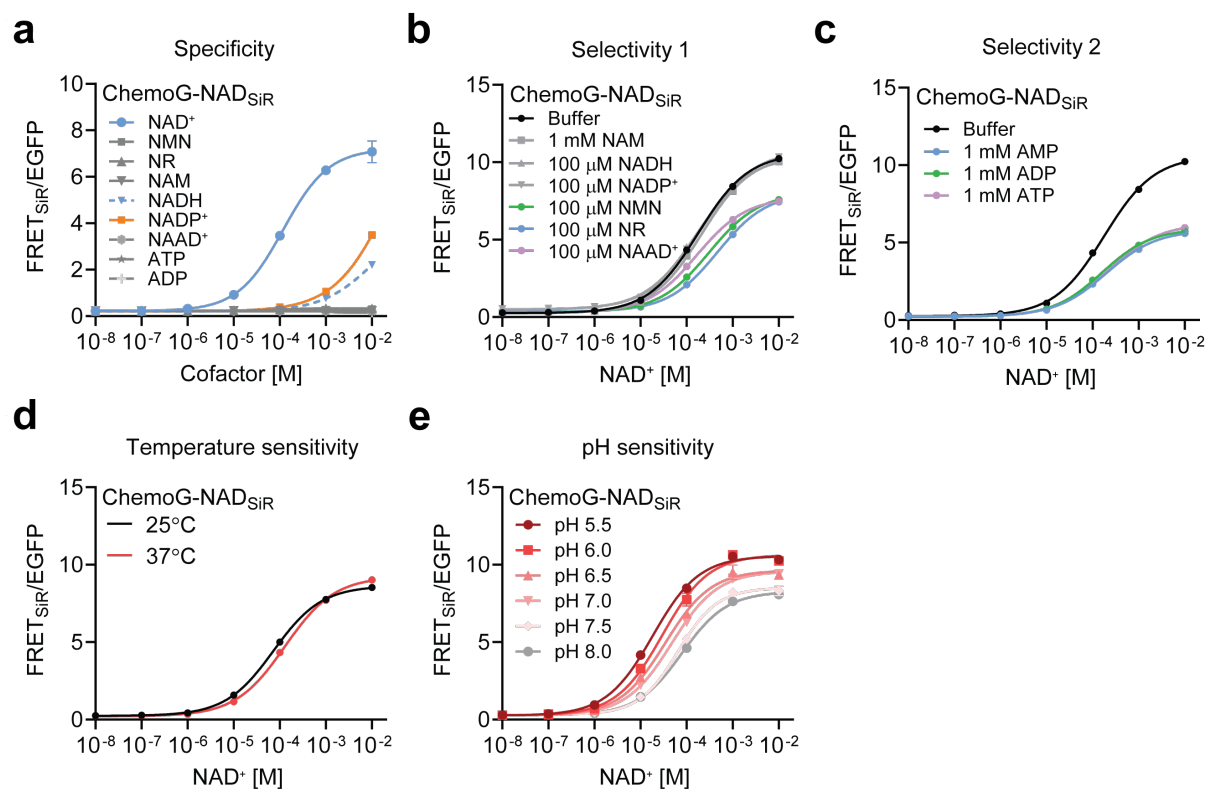


Figure 28 | Characterization of ChemoG-NAD.

a-e. Dose-response curves of ChemoG-NAD_{SiR} upon titration with NAD⁺ and structurally related metabolites (**a**), titration of NAD⁺ in presence of structurally related metabolites (**b-c**), titration of NAD⁺ at different temperatures (**d**) and at different pH (**e**). Shown are the FRET_{SiR}/EGFP ratios. Adapted from Hellweg *et al.*⁷⁸

Next, I created a color palette of ChemoX NAD⁺ biosensors by labeling ChemoG-NAD with different rhodamine-based fluorophores (**Figure 29a-c**), or by replacing EGFP with EBFP2 and mRuby2 (**Figure 29d-f**, **Table 8**), analogous to the development of the ChemoX-CaM and ChemoX-ATP sensors.

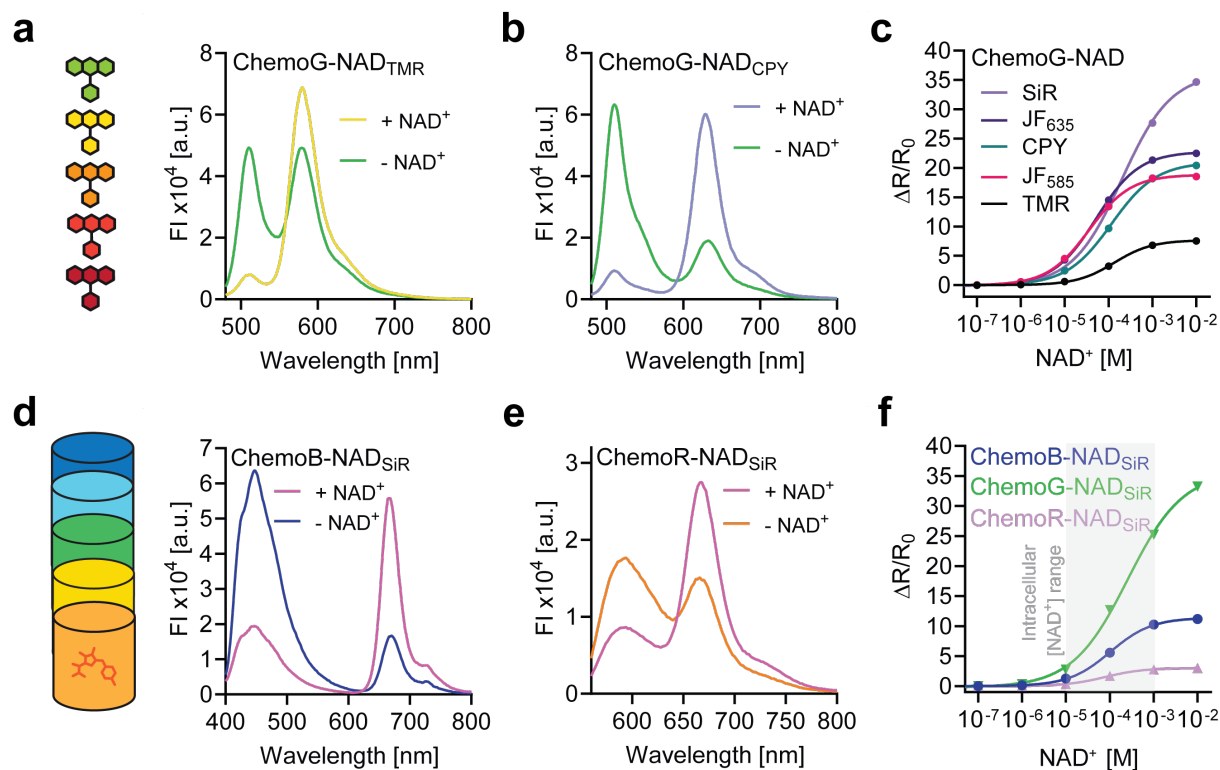


Figure 29 | Color palette of chemogenetic NAD^+ biosensors.

a, b, d, e. Fluorescence intensity (FI) emission spectra of ChemoG-NAD labeled with different FRET acceptors (**a, b**) or ChemoX-NAD sensors based on different fluorescent protein FRET donors (**d, e**). **c, f.** Dose-response curves of ChemoG-NAD labeled with different FRET acceptors (**c**) or ChemoX-NAD sensors (**f**). Plotted are the FRET/FP ratio changes ($\Delta R/R_0$). Adapted from Hellweg *et al.*⁷⁸

Among the tested FRET acceptors, labeling with SiR resulted in the largest dynamic range ($^{\text{Max}}\Delta R/R_0 = 34.7 \pm 0.4$), whereas the TMR-labeled sensor demonstrated the lowest dynamic range for ChemoG-NAD ($^{\text{Max}}\Delta R/R_0 = 7.5 \pm 0.1$), both of which are in agreement with data previously obtained for ChemoG-CaM (**Table 6**). Comparing the different FRET donors, ChemoR-NAD-SiR performed substantially worse than both ChemoB-NAD_{SiR} and ChemoG-NAD_{SiR}, also consistent with observations for ChemoX-CaM (**Table 5**) and ChemoX-ATP (**Table 7**).

Table 8 | Overview of chemogenetic NAD⁺ biosensors.

C₅₀ = NAD⁺ concentration at half-maximal response, Max $\Delta R/R_0$ = maximal change of FRET/FP ratio in absence and presence of NAD⁺. Adapted from Hellweg *et al.*⁷⁸

Construct	FRET pair	Affinity mutation ttLigA	Interface mutations		C ₅₀	Max $\Delta R/R_0$	Hill slope
			FP	HT7			
1	EGFP/TMR	-	A206K	-	38 μ M	10.1 \pm 0.1	1.6
2	EGFP/TMR	V291A	A206K	-	75 μ M	6.2 \pm 0.1	1.2
3	EGFP/TMR	Y225W	A206K	-	129 μ M	6.3 \pm 0.1	1.2
4	EGFP/SiR	Y225W-V291A	A206K	-	205 μ M	2.0 \pm 0.1	0.9
5	EGFP/SiR	Y225W-V291A	A206K-T225R	-	167 μ M	18.1 \pm 0.3	1.0
6 (ChemoG-NAD)	EGFP/SiR	Y225W-V291A	A206K-T225R	L271E	200 μ M	34.7 \pm 0.4	0.8
ChemoG-NAD	EGFP/TMR	Y225W-V291A	A206K-T225R	L271E	136 μ M	7.5 \pm 0.1	1.0
ChemoG-NAD	EGFP/JF ₅₈₅	Y225W-V291A	A206K-T225R	L271E	36 μ M	18.5 \pm 0.1	0.9
ChemoG-NAD	EGFP/CPY	Y225W-V291A	A206K-T225R	L271E	117 μ M	20.4 \pm 0.1	0.8
ChemoG-NAD	EGFP/JF ₆₃₅	Y225W-V291A	A206K-T225R	L271E	52 μ M	22.5 \pm 0.1	0.9
7	EGFP/SiR	Y225W-V291A	A206K	L271E- E143R-E147R	25 μ M	32.5 \pm 0.3	0.8
ChemoB-NAD	EBFP2/SiR	Y225W-V291A	A206K	L271E	103 μ M	11.2 \pm 0.1	0.9
ChemoR-NAD	mRuby2/SiR	Y225W	A206K	-	78 μ M	3.0 \pm 0.1	1.0

To assess the functionality of the ChemoX-NAD sensors in detecting fluctuations of intracellular NAD⁺, I generated U-2 OS cell lines stably expressing the sensors at different subcellular localizations. To alter intracellular NAD⁺ levels, I perturbed the so-called salvage pathway by either supplying it with high concentrations of NR¹¹¹, or inhibiting the rate-limiting conversion of NAM to NMN using the nicotinamide phosphoribosyltransferase (NAMPT) inhibitor FK866¹¹² (**Figure 30a**).

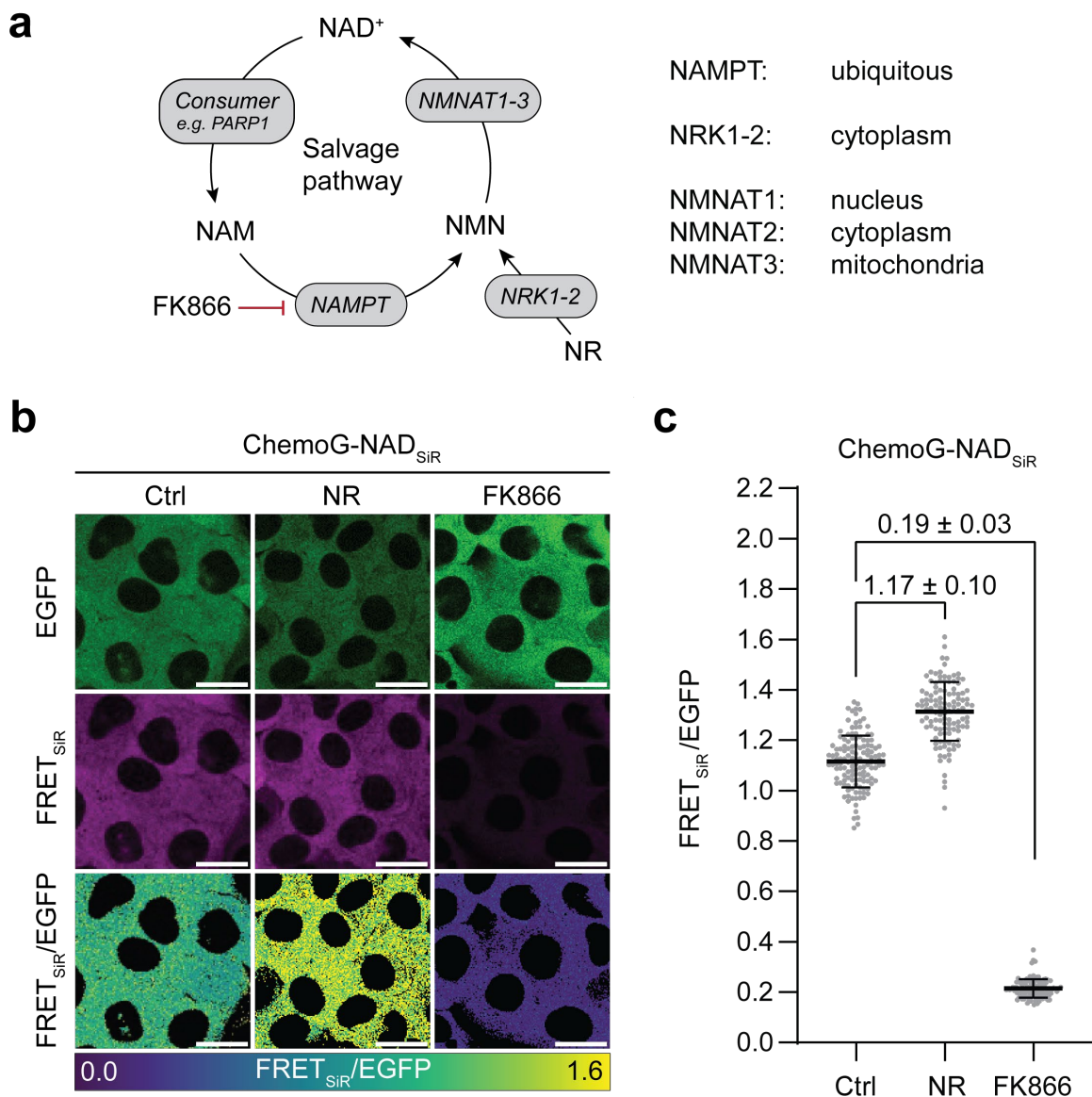


Figure 30 | Characterization of ChemoG-NAD in U-2 OS cells.

a. Schematic representation of intracellular NAD⁺ biosynthesis *via* the salvage pathway. Enzymes are highlighted in grey boxes. FK866 inhibits the catalytic activity of NAMPT, the rate-limiting enzyme of the salvage pathway. External administration of NR feeds into the salvage pathway, increasing NAD⁺ production. Subcellular localizations of enzymes are shown on the right. **b.** Fluorescent images of U-2 OS cells expressing ChemoG-NAD in the cytosol labeled with SiR. Images were acquired with a confocal microscope. Shown are the EGFP and FRET_{SiR} emission channels, and the ratiometric projection of the FRET_{SiR} and EGFP emission channels upon treatment with DMSO (Ctrl), 1 mM NR or 100 nM FK866 for 24 h. Scale bars = 25 μm. **c.** Plotted are the FRET_{SiR}/EGFP ratios of individual U-2 OS cells (grey spheres) expressing ChemoG-NAD_{SiR} in the cytosol and the mean of all cells (black bar) plus standard deviation. Cells were treated as described in **b**. The fold-differences between treatments and control are shown as mean plus standard deviation. Adapted from Hellweg *et al.*⁷⁸

First, I tested ChemoG-NAD, which was localized in the cytosol and labeled with SiR. Upon treatment with 1 mM NR, the $\text{FRET}_{\text{SiR}}/\text{EGFP}$ ratio increased 1.17-fold, in agreement with the enhanced production of NAD^+ (**Figure 30b-c**). Conversely, inhibition of NAMPT with FK866 resulted in a strong FRET decrease (0.19-fold), demonstrating the capability of ChemoG-NAD_{SiR} to report on both up- and downregulation of intracellular NAD^+ levels. I observed the same trends when I localized the sensor to the nucleus using a nuclear localization sequence (NLS, ChemoG-NAD-NLS) or to the mitochondrial matrix using the mitochondrial targeting sequence of Cox8 (ChemoG-NAD-mito, **Figure 31**), confirming its functionality in these compartments as well. Noteworthy, the $\text{FRET}_{\text{SiR}}/\text{EGFP}$ ratio exhibited considerable variability within the mitochondria across different cells, suggesting potential differences in cellular metabolic states or a broader heterogeneity in mitochondrial NAD^+ levels compared to other compartments¹¹³. Among the other ChemoX-NAD biosensors, ChemoB-NAD_{SiR} showed response amplitudes comparable to those of ChemoG-NAD_{SiR} in the cytosol ($\Delta R/R_0$ NR = 1.17 ± 0.21 , $\Delta R/R_0$ FK866 = 0.34 ± 0.09 , **Figure 32a-b**). ChemoR-NAD_{SiR}, on the other hand, displayed much smaller responses (NR = 1.02 ± 0.04 , FK866 = 0.70 ± 0.03), in agreement with the performances during the *in vitro* titrations.

Next, I tested the multiplexing capacity of the ChemoX-NAD biosensors. For this purpose, I co-expressed ChemoB-NAD in the cytosol and ChemoG-NAD in the mitochondria of U-2 OS cells. After labeling both sensors with SiR, I detected the donor FP signals (EBFP2 and EGFP) and the FRET_{SiR} signals of both sensors through separate excitation of EBFP2 and EGFP (**Figure 33a**). I detected fluorescence signals in the expected subcellular localizations, and the sensors showed virtually no bleed-through between the different channels. To demonstrate the potential of the ChemoX-NAD biosensors in dissecting compartmentalized NAD^+ dynamics, I sought to monitor the differential regulation of subcellular NAD^+ pools during acute genotoxic stress. For this purpose, I used the DNA alkylating agent *N*-methyl-*N'*-nitro-*N*-nitrosoguanidine (MNNG), which is known to selectively reduce cytosolic and nuclear NAD^+ over mitochondrial NAD^+ through hyperactivation of PARP1¹¹⁴ (**Figure 33b**), a phenomenon referred to as ‘mitochondrial oasis effect’¹¹⁵. I co-expressed ChemoB-NAD in the cytosol and ChemoG-NAD in the mitochondria of U-2 OS cells and treated the cells with MNNG. As expected, the cytosolic NAD^+ levels rapidly decreased reaching a plateau 20 min post-MNNG addition, while the mitochondrial

NAD⁺ pool showed only a minor reduction (**Figure 33c-d**). Notably, the decrease of cytosolic NAD⁺ upon treatment with MNNG was comparable to the decrease upon treatment with FK866 ($\Delta R/R_0$ MNNG = -70.0 ± 6.3 %, $\Delta R/R_0$ FK866 = -81.2 ± 3.0 %), highlighting the dramatic up-regulation of PARP1 activity during genotoxic stress. I observed the same trends when co-expressing the two sensors in the nucleus and mitochondria of U-2 OS cells (**Figure 34**).

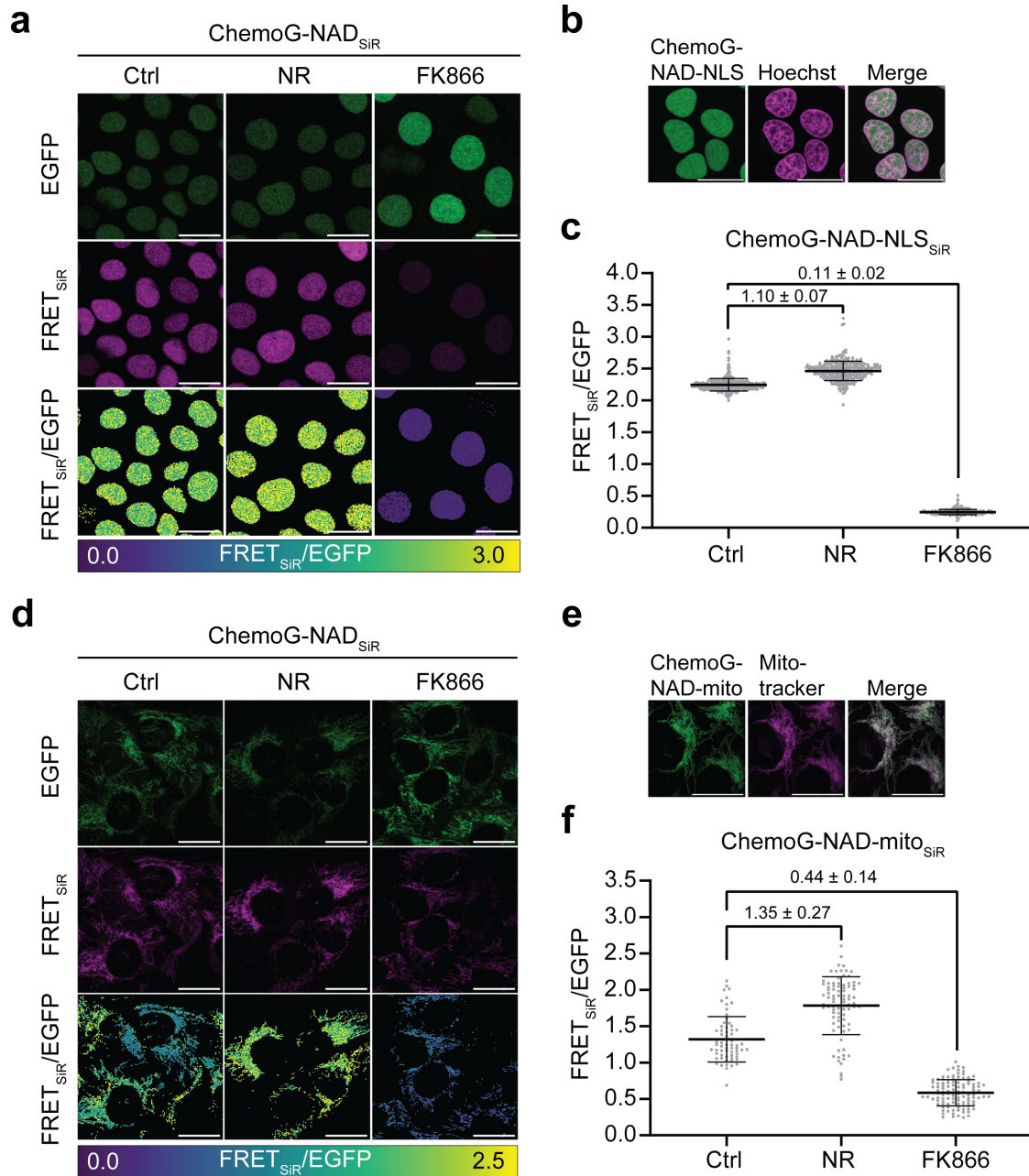


Figure 31 | Performance of ChemoG-NAD at different subcellular localizations.

a, d. Fluorescent images of U-2 OS cells expressing ChemoG-NAD in the nucleus (ChemoG-NAD-NLS, **a**) or mitochondria (ChemoG-NAD-mito, **d**) labeled with SiR. Images were acquired with a confocal microscope. Shown are the EGFP and FRET_{SiR} emission channels, and the ratiometric projection of the FRET_{SiR} and EGFP emission channels upon treatment with DMSO (Ctrl), 1 mM NR or 100 nM FK866 for 24 h. Scale bars = 25 μm. **b, e.** Fluorescent images of U-2 OS cells expressing ChemoG-NAD in the nucleus (ChemoG-NAD-NLS, **b**) or mitochondria (ChemoG-NAD-mito, **e**) stained with Hoechst 33342 (**b**) or MitoTracker RedFM (**e**). **c, f.** Plotted are the FRET_{SiR}/EGFP ratios of individual U-2 OS cells (grey spheres) expressing ChemoG-NAD_{SiR} in the nucleus (**c**) or mitochondria (**f**) and the mean of all cells (black bar) plus standard deviation. Cells were treated as described in **a** and **d**. The fold-differences between treatments and control are shown as mean plus standard deviation. Adapted from Hellweg *et al.*⁷⁸

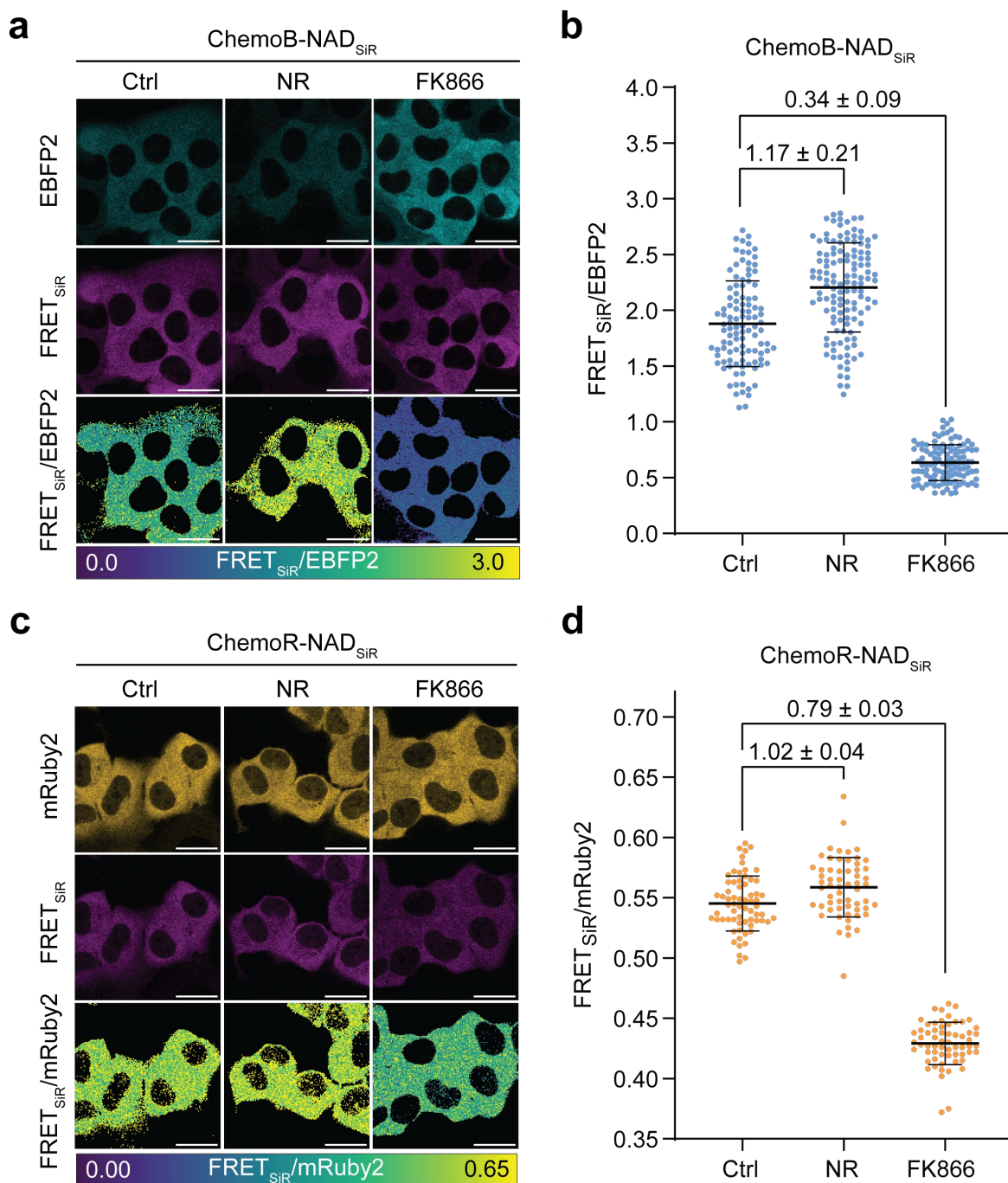


Figure 32 | Characterization of ChemoX-NAD sensors in U-2 OS cells.

a, c. Fluorescent images of U-2 OS cells expressing ChemoB-NAD (**a**) or ChemoR-NAD (**c**) in the cytosol labeled with SiR. Images were acquired with a confocal microscope. Shown are the FP and FRET_{SiR} emission channels, and the ratiometric projection of the FRET_{SiR} and FP emission channels upon treatment with DMSO (Ctrl), 1 mM NR or 100 nM FK866 for 24 h. Scale bars = 25 μ m. **b, d.** Plotted are the FRET_{SiR}/FP ratios of individual U-2 OS cells (spheres) expressing ChemoB-NAD_{SiR} (**b**) or ChemoR-NAD_{SiR} (**d**) in the cytosol and the mean of all cells (black bar) plus standard deviation. Cells were treated as described in **a** and **c**. The fold-differences between treatments and control are shown as mean plus standard deviation. Adapted from Hellweg *et al.*⁷⁸

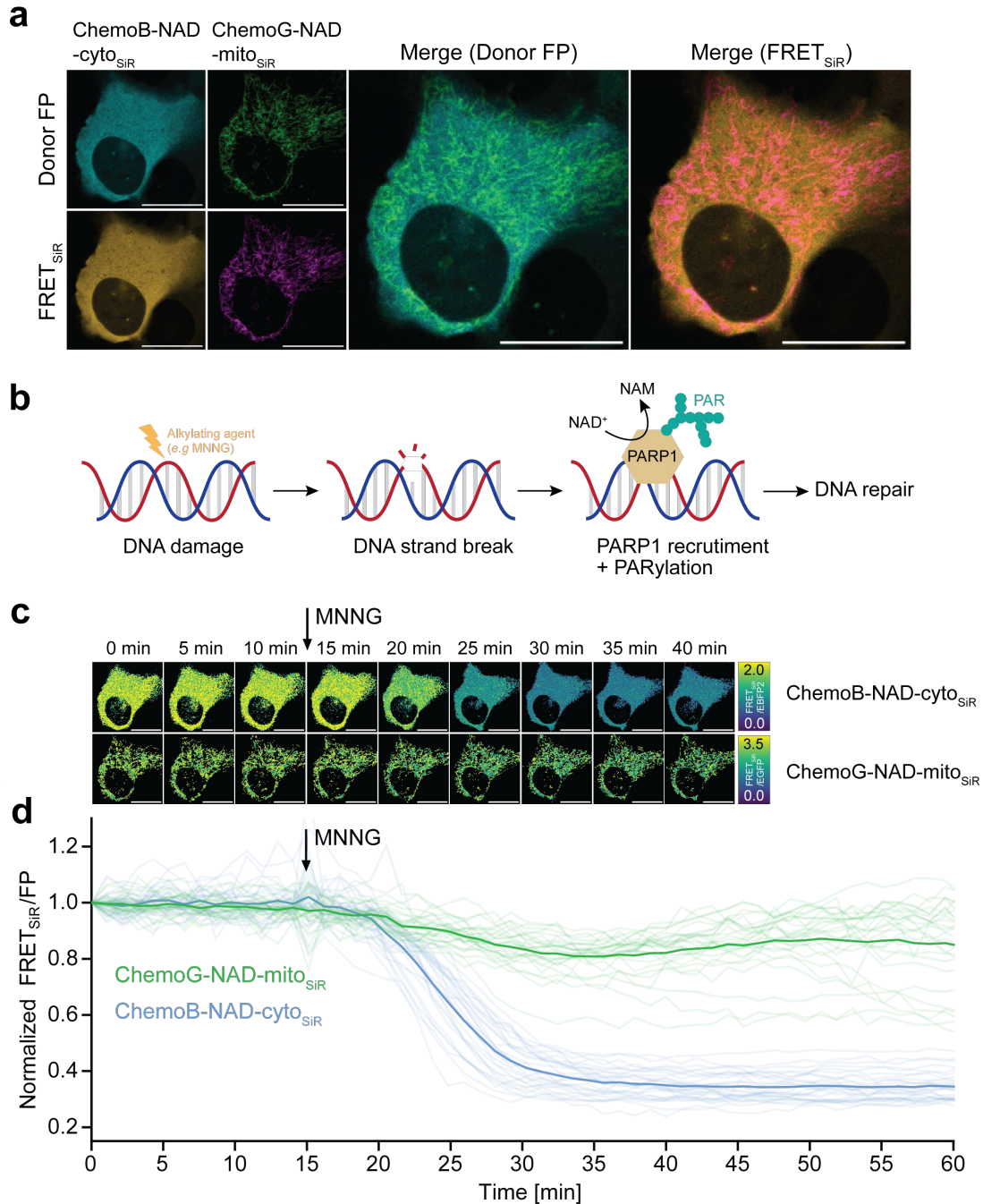


Figure 33 | Multiplexing of subcellular NAD⁺ pools during acute genotoxic stress.

a. Fluorescent images of U-2 OS cells co-expressing ChemoB-NAD and ChemoG-NAD in the cytosol and mitochondria, respectively. Sensors were labeled with SiR. Images were acquired with a confocal microscope. Shown are the FP and FRET_{SiR} emission channels, and the merge of the FP and FRET_{SiR} emission channels. Scale bars = 25 μm. **b.** Schematic representation of the early DNA damage response. A genotoxic stressor (e.g., an alkylating agent like MNNG) induces a DNA strand break, resulting in the recruitment and hyperactivation of PARP1. PARP1 consumes NAD⁺ to poly-ADP-ribosylate itself and adjacent biomolecules (PARylation), leading to downstream DNA repair responses. **c.** Ratiometric projections of FRET_{SiR}/FP ratios derived from fluorescent images of U-2 OS cells co-expressing ChemoB-NAD and ChemoG-NAD in the cytosol and mitochondria,

respectively. Projections are shown for different time points. The addition of 100 μM MNNG is indicated with an arrow. **d.** Plotted are the mean (thick line) and individual traces (thin lines) of $\text{FRET}_{\text{SiR}}/\text{FP}$ ratios of U-2 OS cells co-expressing ChemoB-NAD and ChemoG-NAD in the cytosol and mitochondria, respectively. The addition of 100 μM MNNG is indicated with an arrow. $\text{FRET}_{\text{SiR}}/\text{FP}$ ratios were normalized to $t = 0$ min. Adapted from Hellweg *et al.*⁷⁸

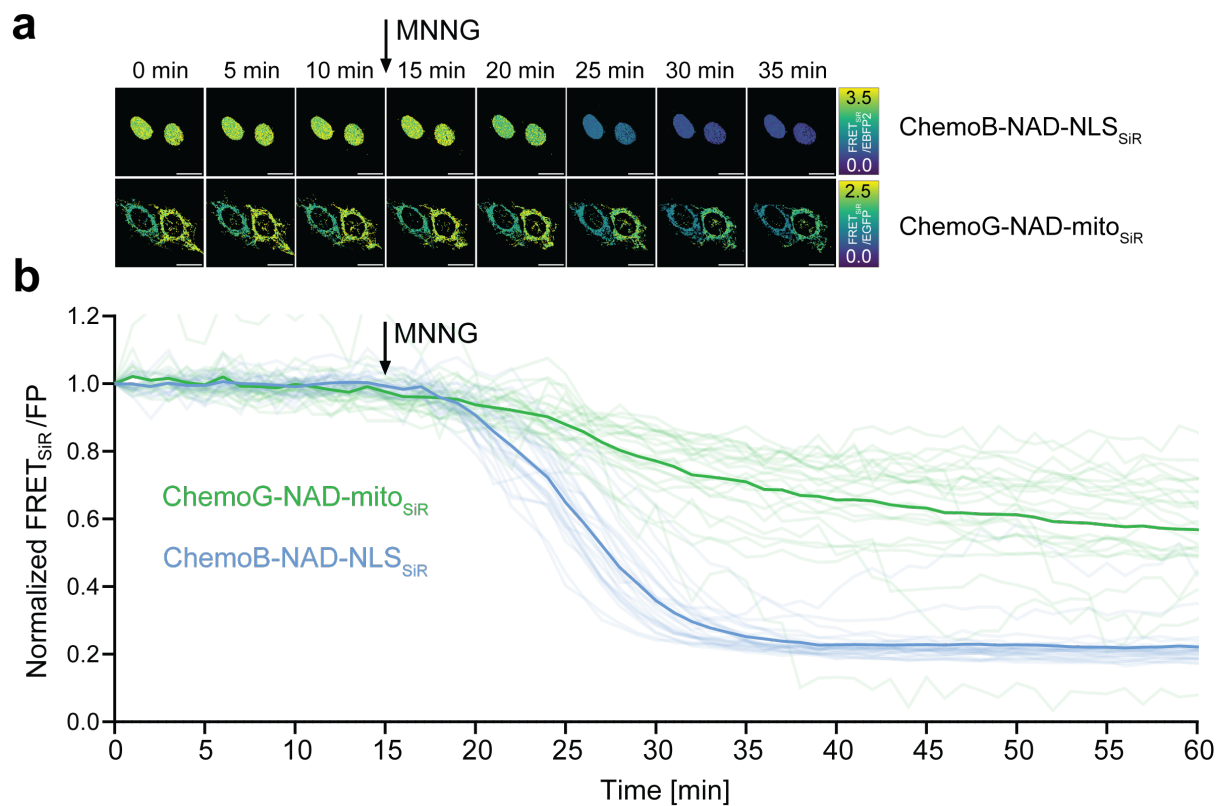


Figure 34 | Multiplexing of subcellular NAD^+ pools in the nucleus and mitochondria.

a. Ratiometric projections of $\text{FRET}_{\text{SiR}}/\text{FP}$ ratios derived from fluorescent images of U-2 OS cells co-expressing ChemoB-NAD and ChemoG-NAD in the nucleus (ChemoB-NAD-NLS) and mitochondria (ChemoG-NAD-mito), respectively. Projections are shown for different time points. The addition of 100 μM MNNG is indicated with an arrow. **b.** Plotted are the mean (thick line) and individual traces (thin lines) of $\text{FRET}_{\text{SiR}}/\text{FP}$ ratios of U-2 OS cells co-expressing ChemoB-NAD and ChemoG-NAD in the nucleus and mitochondria, respectively. The addition of 100 μM MNNG is indicated with an arrow. $\text{FRET}_{\text{SiR}}/\text{FP}$ ratios were normalized to $t = 0$ min. Adapted from Hellweg *et al.*⁷⁸

2.7. Converting ChemoG-NAD into a red-shifted single-channel fluorescence lifetime sensor

Despite the enhanced multiplexing capacity of ChemoX biosensors, their dependence on two emission channels can still pose practical limitations. Moreover, the performance of ChemoR biosensors remains suboptimal, limiting the applicability of ChemoX biosensors with red-shifted wavelengths. Given that the ChemoX design incorporates rhodamine-based fluorophores whose photophysical properties can be modulated by changes in their direct environment^{38, 47}, I explored whether the transient formation of the ChemoX interface upon conformational changes of the sensor could modulate the brightness of rhodamine-based fluorophores. This would enable the creation of ChemoX biosensors with a single emission channel while fully exploiting the brightness and photostability of rhodamine-based fluorophores with far-red emission wavelengths.

For this purpose, I titrated ChemoG-NAD_{SiR} against NAD⁺ and recorded the emission spectra of SiR upon direct excitation of the fluorophore (**Figure 35a**). Indeed, the fluorescence intensity (FI) of SiR increased with rising NAD⁺ concentrations in the ChemoG-NAD context but not when SiR was labeled to HT7 only (**Figure 35b**). I observed the same trend for ChemoG-CaM_{SiR} and ChemoG-ATP_{SiR} in a dose-dependent manner for their cognate analyte (**Figure 35c**), suggesting that the FI of rhodamine-based fluorophores is modulated by direct interactions within the ChemoG interface.

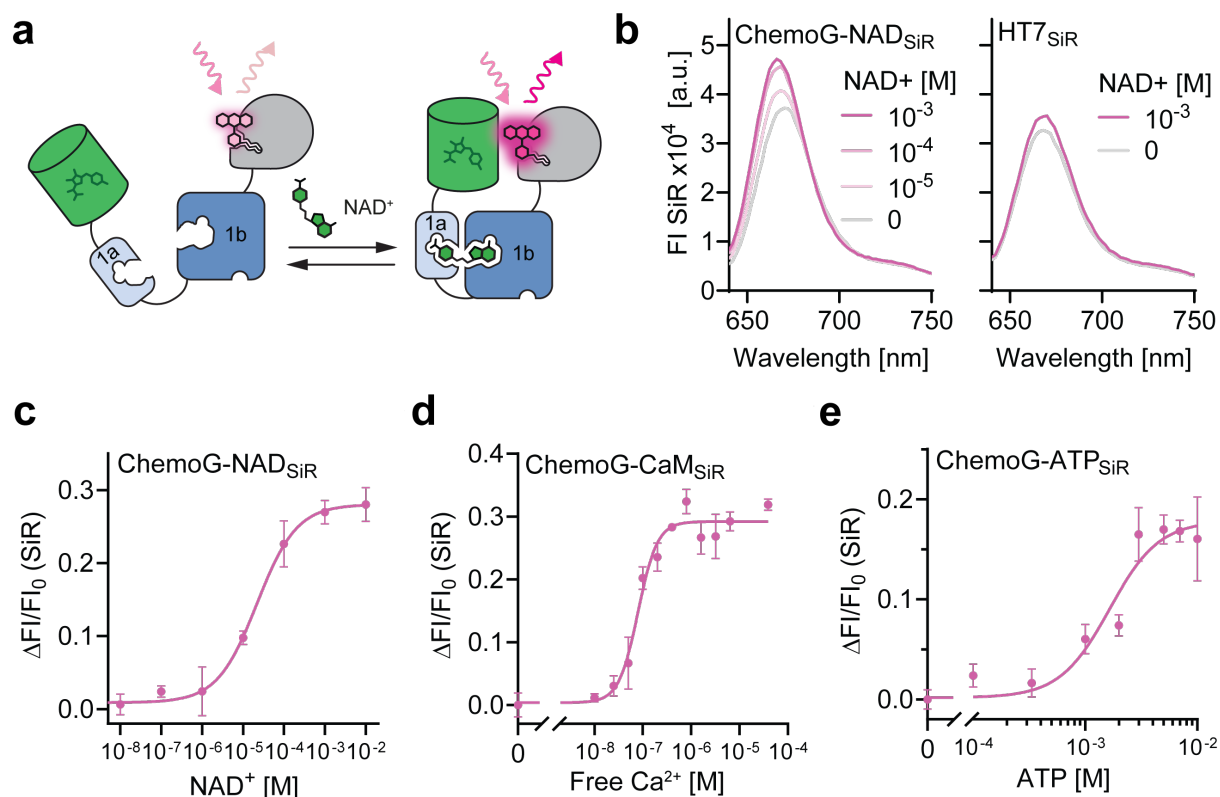


Figure 35 | Fluorescence intensity of SiR is modulated in the ChemoG sensor context.

a. Cartoon representing the fluorogenic response of SiR in the context of ChemoG-NAD upon direct excitation. Formation of the ChemoG interface in the closed state of the sensor affects the photophysical properties of SiR and thereby increases its fluorescence intensity. **b.** Fluorescence intensity (FI) emission spectra of SiR labeled to ChemoG-NAD (left graph) or HT7 (right graph) at different NAD⁺ concentrations. **c-e.** Dose-response curves of ChemoG biosensors upon direct excitation of SiR. Plotted are the FI changes of SiR ($\Delta FI/FI_0$) upon titration with the cognate analyte of the respective sensor. Adapted from Hellweg *et al.*⁷⁸

Building on these results, I aimed to enhance the dynamic range, which can be achieved by either improving the maximal brightness in the closed state of the sensor and/or by reducing the basal brightness in the open state of the sensor. Considering that many rhodamine-based fluorophores already exhibit excellent brightness upon labeling to HT7 (**Table 3**), my strategy focused on the latter approach. Inspired by previous work of Dr. Michelle Frei in our lab, I substituted P174 on HT7 of ChemoG-NAD with a tryptophan (P174W), which is known to reduce the FI of fluorophores labeled to HT7⁴⁷. This modification reduced the basal FI of SiR by $57.2 \pm 0.7\%$ (**Figure 36a**). Upon titration with NAD⁺, the FI increased by $121.8 \pm 5.0\%$ ($^{Max}\Delta FI/FI_0$) reaching a maximum FI equivalent to that of HT7_{SiR}. Since the residues on the surface of EGFP are likely the

main contributors of the increased FI, the EGFP chromophore became dispensable. Therefore, I replaced EGFP with ShadowG, a practically non-fluorescent EYFP derivative engineered for a very low quantum yield¹¹⁶ (0.005 vs 0.6 for EGFP), and incorporated the same ChemoG interface mutations. This sensor was named ChemoD-NAD, where ‘D’ stands for ‘dark’ based on the non-fluorescent character of ShadowG, transforming the two-channel sensor design into a single-channel sensor design (**Figure 36c**). The overall FI of ChemoD-NAD_{SiR} further decreased compared to ChemoG-NAD(P174W)_{SiR}, yielding a $\text{Max}\Delta\text{FI}/\text{FI}_0$ of $161.1 \pm 5.0\%$ (**Figure 36b-d**). Yet, ChemoD-NAD_{SiR} remained relatively bright with a maximal FI 85.9 % of HT7_{SiR} at saturating NAD⁺ concentrations.

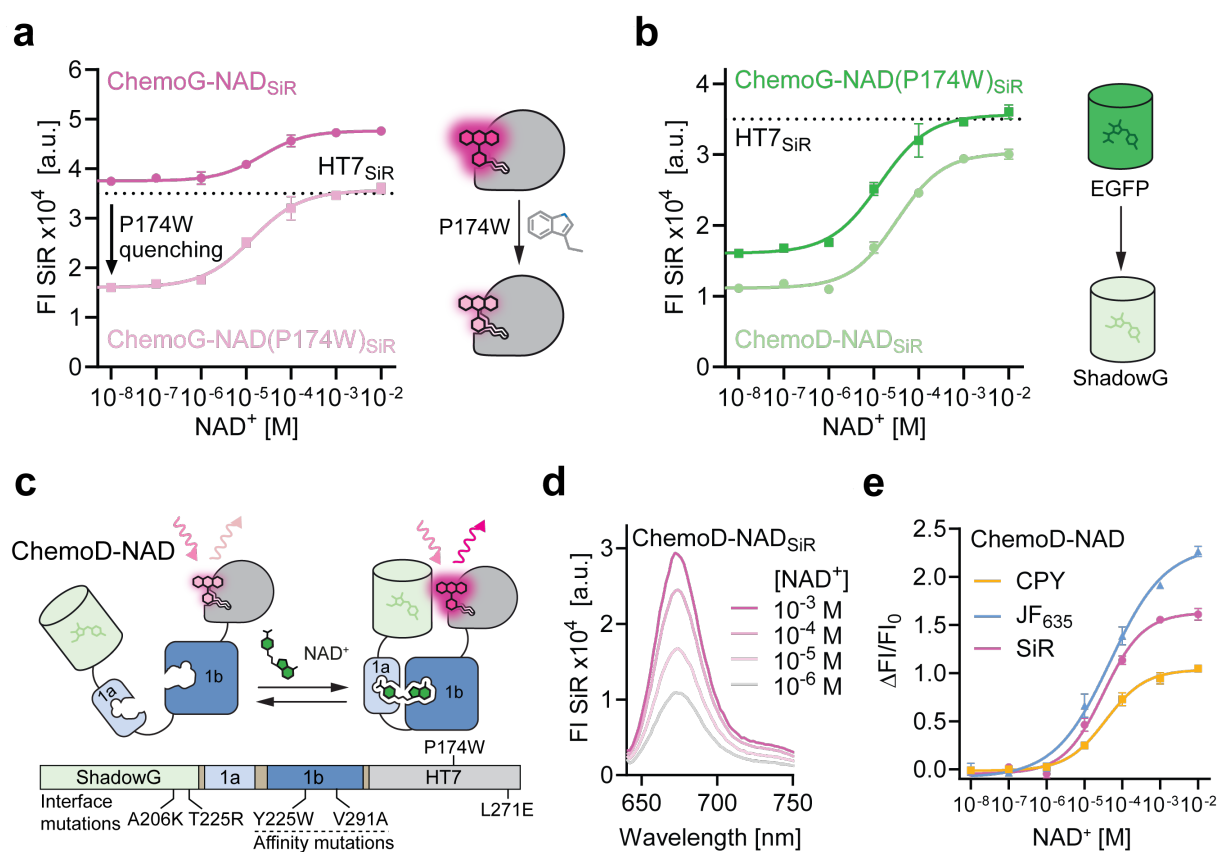


Figure 36 | Development of single-channel NAD⁺ biosensors with far-red emission wavelengths.

a, b. Dose-response curves of the fluorescence intensities (FI) of SiR labeled to ChemoG-NAD, ChemoG-NAD containing the mutation P174W on HT7, or ChemoD-NAD. The FI of SiR labeled to HT7 is shown as dotted line. **c.** Schematic representation of ChemoD-NAD. In comparison to ChemoG-NAD, the mutation P174W was incorporated into HT7 and EGFP was exchanged with the non-fluorescent ShadowG. **d.** Fluorescence intensity (FI) emission spectra of SiR labeled to ChemoD-NAD at different NAD⁺ concentrations. **e.** Dose-response curves of ChemoG-NAD labeled with different rhodamine-based fluorophores. Plotted are the FI changes ($\Delta\text{FI}/\text{FI}_0$). Adapted from Hellweg *et al.*⁷⁸

ChemoD-NAD was also compatible with other rhodamine-based fluorophores, such as CPY or JF₆₃₅ (**Figure 36e, Table 9**), providing spectral flexibility in the far-red emission range. Labeling the sensor with JF₆₃₅ resulted in the largest dynamic range ($^{\text{Max}}\Delta\text{FI}/\text{FI}_0 = 226.6 \pm 4.3 \%$). This fluorophore exhibited superior performances in other sensor designs as well⁵⁹, possibly due to its enhanced fluorogenicity that makes it particularly sensitive to environmental changes.

Table 9 | Overview of ChemoD-NAD biosensors.

Max λ_{Em} = maximal emission wavelength of labeled fluorophore, C_{50} = NAD⁺ concentration at half-maximal response, Max $\Delta\text{FI}/\text{FI}_0$ = maximal change of fluorescence intensity (FI) in absence and presence of NAD⁺. Adapted from Hellweg *et al.*⁷⁸

Construct	Fluorophore	Max λ_{Em}	C_{50}	Max $\Delta\text{FI}/\text{FI}_0$	Hill slope
ChemoG-NAD	SiR	666 nm	21.0 μM	28.0 \pm 1.9 %	0.89
ChemoG-NAD(P174W)	SiR	666 nm	13.5 μM	121.8 \pm 5.0 %	0.79
ChemoD-NAD	SiR	666 nm	32.7 μM	161.1 \pm 5.0 %	0.84
ChemoD-NAD	CPY	628 nm	36.8 μM	104.7 \pm 1.2 %	0.83
ChemoD-NAD	JF ₆₃₅	662 nm	47.5 μM	226.6 \pm 4.3 %	0.59

The mutation P174W was previously shown to quench the FI primarily by reducing the quantum yield of the fluorophore labeled to HT7⁴⁷. Since a change in quantum yield correlates with a concomitant change in fluorescence lifetime of the excited fluorophore, I tested whether the FI changes of ChemoD-NAD_{SiR} also translate to changes in fluorescence lifetime. This would be particularly interesting because fluorescence lifetime measurements offer a robust quantification method that is less susceptible to fluctuations in sensor concentration, a common drawback associated with non-ratiometric biosensors. The average fluorescence lifetime (τ) of SiR labeled to ChemoD-NAD increased from 2.21 ns in absence of NAD⁺ to 3.37 ns in presence of 1 mM NAD⁺, yielding a maximal τ change ($^{\text{Max}}\Delta\tau$) of 1.16 ± 0.01 ns (**Figure 37a**).

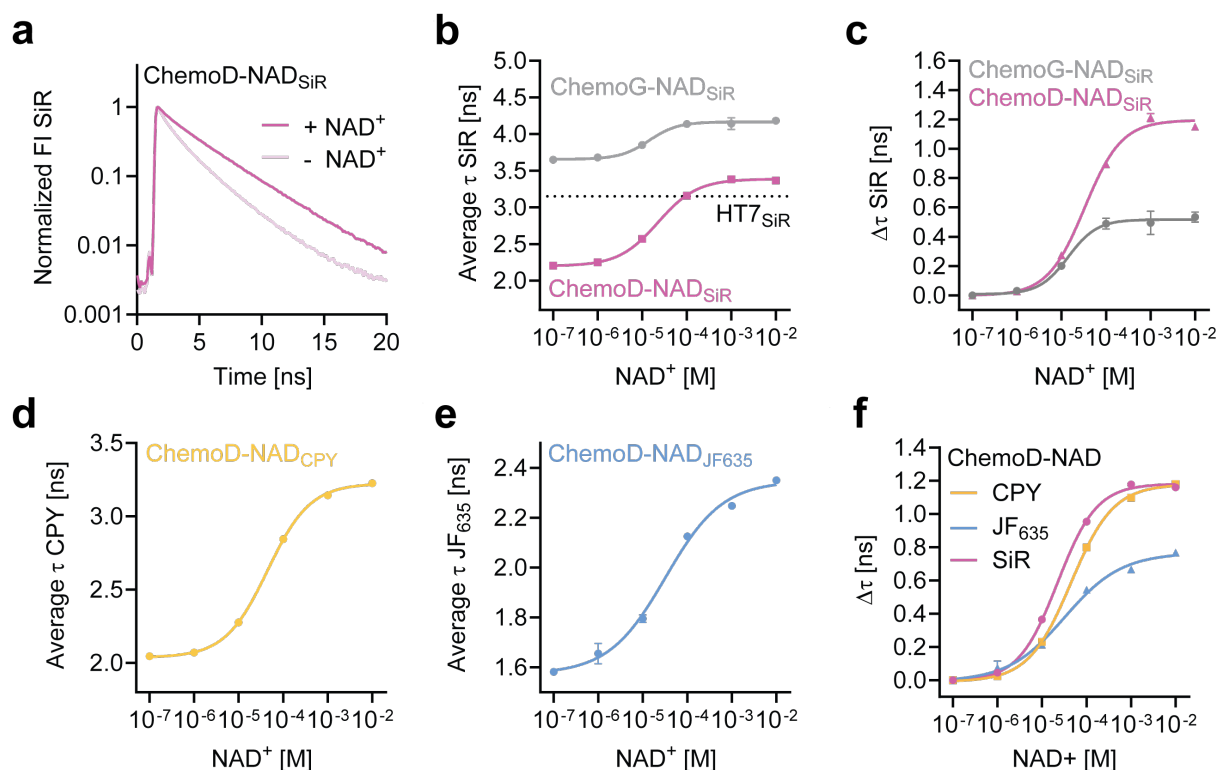


Figure 37 | ChemoD-NAD as fluorescence lifetime sensor for NAD⁺.

a. Fluorescence lifetime decay curves of ChemoD-NAD_{SiR} in absence (-NAD⁺) or presence of 1 mM NAD⁺ (+NAD⁺). **b, d, e.** Dose-response curves of the fluorescence lifetime (τ) of rhodamine-based fluorophores labeled to ChemoG-NAD or ChemoD-NAD. The τ of SiR labeled to HT7 is shown as dotted line. **c, f.** τ changes ($\Delta\tau$) of rhodamine-based fluorophores labeled to ChemoD-NAD plotted against the NAD⁺ concentration. Adapted from Hellweg *et al.*⁷⁸

Analogous to changes with respect to FI, ChemoD-NAD_{SiR} exhibited a larger dynamic range compared to ChemoG-NAD_{SiR} ($^{\text{Max}}\Delta\tau = 0.53 \pm 0.03$ ns) and an overall decreased τ , presumably due to the quenching effect of P174W (**Figure 37b-c**). Moreover, CPY and JF₆₃₅ showed comparable modulations in their τ in the ChemoD-NAD sensor context (**Figure 37d-e, Table 10**). Surprisingly, JF₆₃₅, the fluorophore with the largest FI change, exhibited the smallest change in τ ($^{\text{Max}}\Delta\tau = 0.77 \pm 0.01$ ns). It is possible that a major part of the FI change of JF₆₃₅ stems from alterations in the absorption rather than quantum yield, whereas CPY and SiR might be modulated predominantly by changes in their quantum yield. Determination of the extinction coefficient and quantum yield of the ChemoD-NAD sensors in the open and closed state could provide insights into the observed discrepancies.

Table 10 | Overview of ChemoD-NAD sensors based on fluorescence lifetime.

Max λ_{Em} = maximal emission wavelength of labeled fluorophore, C_{50} = NAD^+ concentration at half-maximal response, Max $\Delta\tau/\tau_0$ = maximal change of fluorescence lifetime (τ) in absence and presence of NAD^+ . Adapted from Hellweg *et al.*⁷⁸

Construct	Fluorophore	Max λ_{Em}	C_{50}	Max $\Delta\tau/\tau_0$	Hill slope
ChemoG-NAD	SiR	666 nm	14.2 μ M	0.53 \pm 0.03 ns	1.34
ChemoD-NAD	SiR	666 nm	22.4 μ M	1.16 \pm 0.01 ns	0.99
ChemoD-NAD	CPY	628 nm	36.8 μ M	1.18 \pm 0.01 ns	0.91
ChemoD-NAD	JF ₆₃₅	662 nm	47.5 μ M	0.77 \pm 0.01 ns	0.68

Next, I characterized the performance of ChemoD-NAD in U-2 OS cells *via* confocal fluorescence microscopy and fluorescence lifetime imaging microscopy (FLIM). I expressed the sensor in the cytosol and labeled it with CPY, JF₆₃₅ or SiR. Upon addition of MNNG, I detected a rapid decrease in FI (CPY = -44.8 ± 5.8 %, JF₆₃₅ = -54.5 ± 5.1 %, SiR = -43.8 ± 7.5 %) and τ (CPY = -0.93 ± 0.08 ns, JF₆₃₅ = -0.22 ± 0.07 ns, SiR = -0.68 ± 0.09 ns) for all three fluorophores (**Figure 38**), indicating strong depletion of intracellular NAD^+ during genotoxic stress. In line with the performance during NAD^+ titrations, JF₆₃₅ exhibited the largest change in FI, but the smallest τ change. CPY, on the other hand, showed the largest response in terms of τ . Noteworthy, the FI of ChemoD-NAD_{JF635} and ChemoD-NAD_{SiR} fluctuated substantially right after the addition of MNNG to the cells, caused by temporary drifts in the focal plane. This effect was merely detectable for the τ measurements, although the FI and τ values were determined from the same fluorescence images, highlighting that τ measurements represent the more robust quantification method.

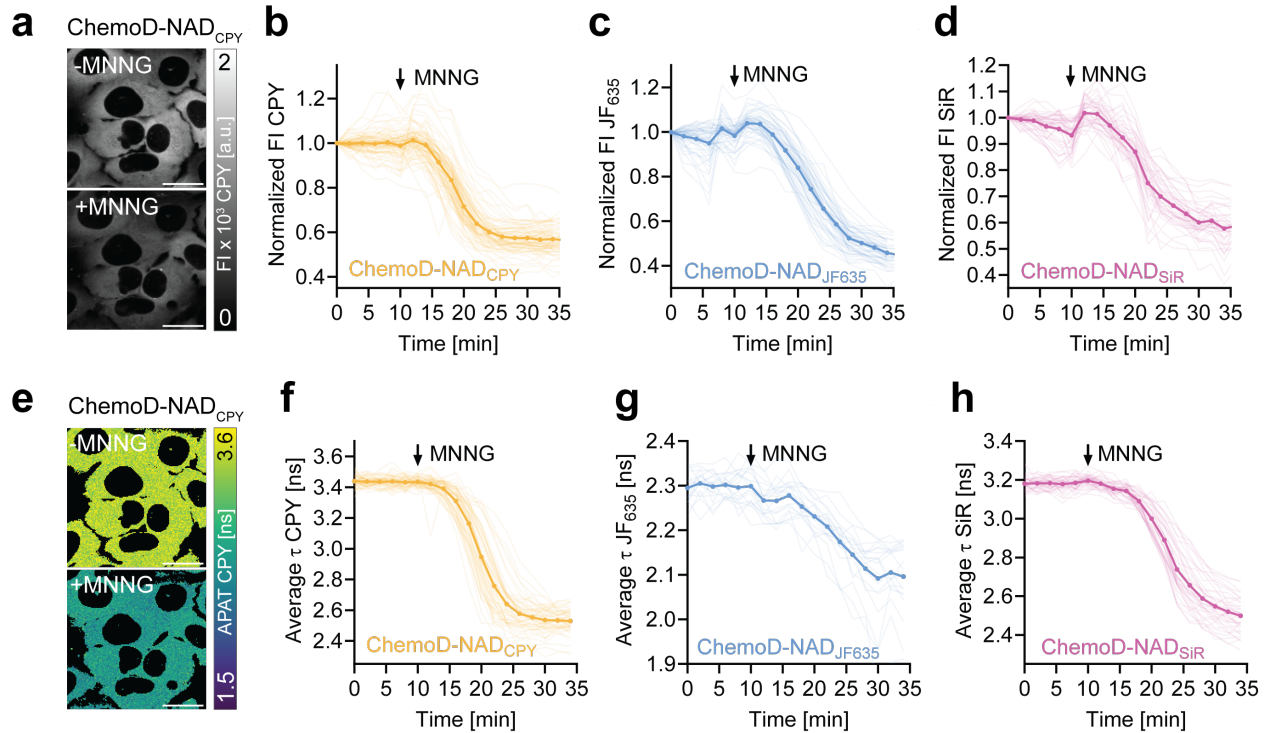


Figure 38 | Characterization of ChemoD-NAD in U-2 OS cells.

a, d. Fluorescent images of U-2 OS cells expressing ChemoD-NAD in the cytosol labeled with CPY. Images were acquired with a confocal microscope. Shown are the fluorescence intensity (FI, **a**) or average photon arrival time (APAT, **e**) before (-MNNG) or after treatment with 100 μM MNNG (+MNNG). Scale bars = 25 μm. Plotted are the mean (thick line) and individual traces (thin lines) of FI (**b-d**) or average fluorescence lifetime (τ , **f-h**) of U-2 OS cells expressing ChemoD-NAD_{CPY} in the cytosol. The addition of 100 μM MNNG is indicated with an arrow. FI was normalized to $t = 0$ min. Adapted from Hellweg *et al.*⁷⁸

2.8. Converting fluorescence-based ChemoG biosensors into bioluminescence-based ChemoL biosensors

In contrast to fluorophores, luciferases produce light through enzymatic turnover of specific substrates (*e.g.*, luciferins or coelenterazines) omitting the need of external light sources. Hence, the conversion of fluorescent ChemoX biosensors into bioluminescent counterparts would offer advantages for certain experimental settings, including stable signals for long-term imaging without concerns of photobleaching, and high signal-to-noise ratios for *in vivo* imaging. Furthermore, the possibility to omit external laser excitation sources minimizes phototoxicity and potential damage to the biological sample. Finally, bioluminescent sensors can be easily adapted for high-throughput screening applications due to their simplicity and compatibility with microplate readers.

Initially, I replaced EGFP in the ChemoG-NAD sensor design with the small luciferase NanoLuc¹¹⁷ serving as a bioluminescence resonance energy transfer (BRET) donor for the fluorophore labeled to HT7. However, the BRET between NanoLuc and CPY, labeled to HT7, proved to be very weak, limiting the dynamic range of the sensor (data not shown). Inspired by the Nano-lantern design^{118, 119}, I instead fused a circularly permuted version of NanoLuc (cpNanoLuc) to the N-terminus of ChemoG-NAD, establishing a constant BRET pair between cpNanoLuc and EGFP. I employed a circularly permuted version of NanoLuc because it improved the BRET efficiency with EGFP (data not shown). In presence of its substrate (*e.g.*, furimazine), cpNanoLuc would excite EGFP *via* BRET, which would subsequently undergo FRET in the ChemoG context creating a BRET-FRET system (**Figure 39a**). This system preserves the overall architecture and advantages of the ChemoG FRET sensor design, including a large dynamic range.

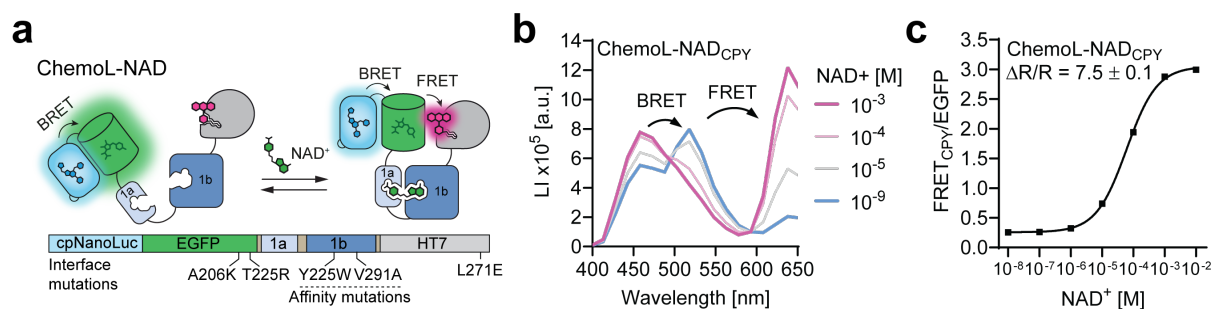


Figure 39 | Converting ChemoG-NAD into the bioluminescent sensor ChemoL-NAD.

a. Schematic representation of the bioluminescent NAD^+ sensor ChemoL-NAD. N-terminal fusion of a circularly permuted NanoLuc (cpNanoLuc) to ChemoG-NAD established a constant BRET pair between cpNanoLuc and EGFP in presence of the NanoLuc substrate furimazine. **b.** Luminescence intensity (LI) emission spectra of ChemoL-NAD labeled with CPY, at different NAD^+ concentrations. BRET between cpNanoLuc and EGFP, and FRET between EGFP and CPY are highlighted with arrows. **c.** Dose-response curve of ChemoL-NAD labeled with CPY. $\Delta R/R_0 = \text{maximal FRET}_{\text{CPY/EGFP}}$ ratio change. Adapted from Hellweg *et al.*⁷⁸

The bioluminescent sensor was named ChemoL-NAD, where ‘L’ stands for ‘luminescence’. Acquisition of the luminescence intensity (LI) emission spectra of ChemoL-NAD_{CPY} revealed 3 emission peaks. The first one at around 458 nm, corresponding to cpNanoLuc; a second peak at 518 nm, corresponding to EGFP (BRET); and a final peak at 638 nm, corresponding to CPY (FRET, **Figure 39b**). Upon titration with NAD^+ , the EGFP peak decreased while the CPY (FRET) peak increased substantially with a maximal $\text{FRET}_{\text{CPY/EGFP}}$ ratio change ($^{\text{Max}}\Delta R/R_0$) of 7.5 ± 0.1 and a C_{50} around $60.5 \mu\text{M}$ NAD^+ (**Figure 39c**). The dynamic range of ChemoL-NAD_{CPY} was notably smaller compared to that of ChemoG-NAD_{SiR} ($^{\text{Max}}\Delta R/R_0 = 34.7 \pm 0.4$). While the increase in FRET_{CPY} is very large for ChemoL-NAD_{CPY} (6.0 ± 0.1), the decrease in the EGFP signal for ChemoL-NAD is limited by the cpNanoLuc emission, which largely overlaps with the EGFP emission. Nevertheless, the dynamic range of ChemoL-NAD_{CPY} was sufficient to report on changes of intracellular NAD^+ levels in U-2 OS cells upon perturbation of the salvage pathway. The $\text{FRET}_{\text{CPY/EGFP}}$ ratio of ChemoL-NAD_{CPY} expressed in the cytosol, nucleus or mitochondria decreased substantially upon pharmacological inhibition of the salvage pathway with FK866, which could be compensated by supplementation with NR (**Figure 40a-c**). These trends were consistent with the results obtained from cell experiments using ChemoG-NAD_{SiR} (**Figure 30** and **Figure 31**). In addition to end-point cell measurements, ChemoL-NAD_{CPY} could be

also used to monitor in real-time the depletion of cytosolic NAD^+ during genotoxic stress. The $\text{FRET}_{\text{CPY}}/\text{EGFP}$ decreased substantially ($\Delta R/R_0 = -84.8 \pm 0.2 \%$) upon treatment of the cells with MNNG, while addition of medium only had no effect on the $\text{FRET}_{\text{CPY}}/\text{EGFP}$ ratio (Figure 40d-e).

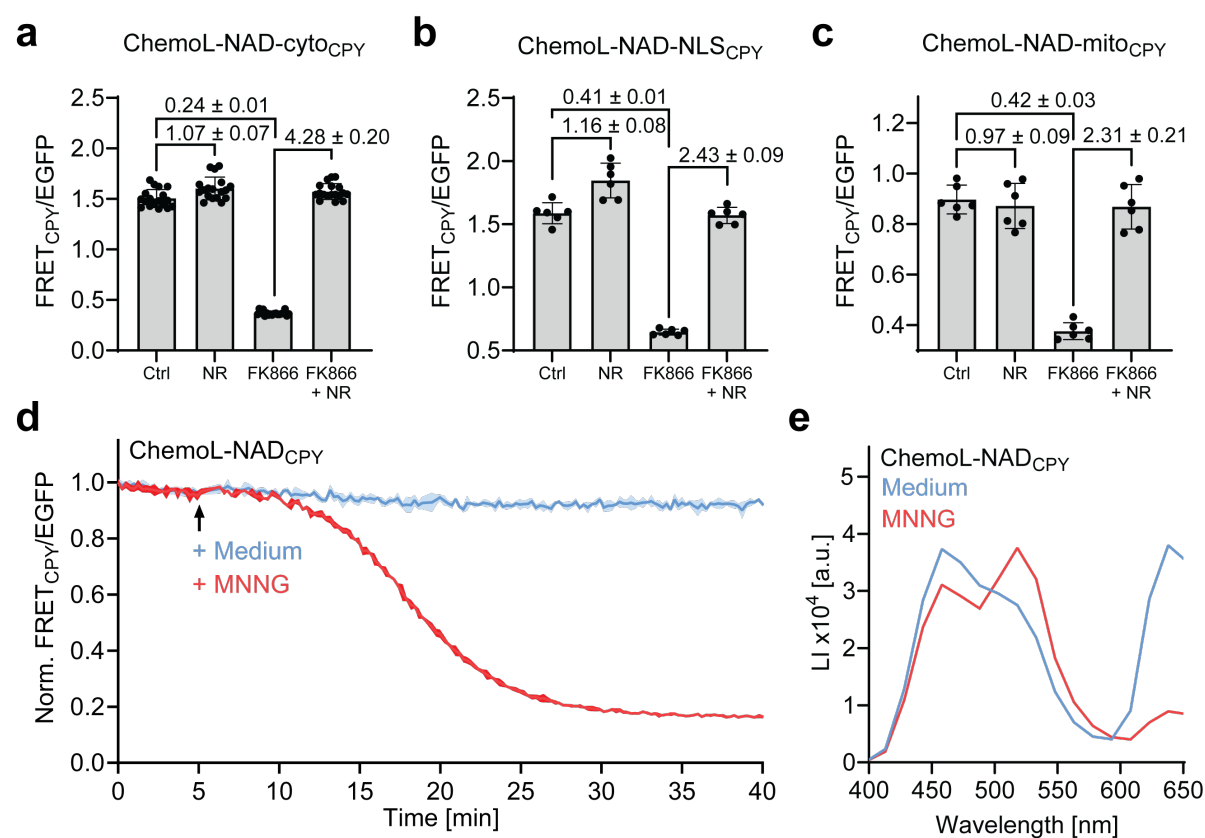


Figure 40 | Characterization of ChemoL-NAD in U-2 OS cells.

a-c. $\text{FRET}_{\text{CPY}}/\text{EGFP}$ ratios of ChemoL-NAD expressed in the cytosol (**a**), nucleus (**b**) or mitochondria (**c**) of U-2 OS cells and labeled with CPY. Cells were treated with DMSO (Ctrl), 1 mM NR, 100 nM FK866 or both for 24 h. $\text{FRET}_{\text{CPY}}/\text{EGFP}$ ratios were measured with a multiwell plate reader. Shown are the mean ratios (bar plus standard deviation) of single well measurements (black circle) from 3 biological replicates. Fold-change differences between treatments are shown as mean plus standard deviation. **d.** Plotted are the mean of $\text{FRET}_{\text{CPY}}/\text{EGFP}$ ratios (thick line) plus standard deviation (shadow) of U-2 OS cells expressing ChemoL-NAD in the cytosol. The addition of 100 μM MNNG or medium is indicated with an arrow. $\text{FRET}_{\text{CPY}}/\text{EGFP}$ ratios were normalized to $t = 0$ min. **e.** Luminescence intensity (LI) emission spectra of ChemoL-NAD at the end of the time course measurement from **d**. Adapted from Hellweg *et al.*⁷⁸

Given that a simple fusion of cpNanoLuc to the N-terminus of EGFP was sufficient to transform the fluorescence-based ChemoG-NAD sensor into a bioluminescence-based sensor, I applied the same approach to convert ChemoG-CaM and ChemoG-ATP into corresponding ChemoL sensors. ChemoL-CaM labeled with CPY (**Figure 41a**) exhibited a dynamic range of $^{\text{Max}}\Delta R/R_0 = 9.1 \pm 0.1$ and a C_{50} of approximately 96.6 nM Ca^{2+} (**Figure 41b-c**). When expressed in the cytosol of HeLa Kyoto cells, ChemoL-CaM_{CPY} was able to detect elevations of intracellular Ca^{2+} levels. Upon treatment with the Ca^{2+} ionophore ionomycin, the $\text{FRET}_{\text{CPY/EGFP}}$ ratio increased 8.2-fold (± 0.5). Treatment of the cells with histamine resulted in a transient, but relatively minor change in the $\text{FRET}_{\text{CPY/EGFP}}$ ratio (2.6-fold ± 0.1) that is notably smaller compared to what I have observed using ChemoG-CaM_{SiR} during fluorescence microscopy experiments. The reduced response of ChemoL-CaM_{CPY} might be due to several reasons. Firstly, the temporal resolution of the bioluminescent measurements in the plate reader was substantially lower (10.5 s) compared to the fluorescence measurements using the widefield microscope (0.8 s), plus the plate reader measurements had to be paused to add the stimulators to the cells (ca. 30 s pause). During the cell experiments with ChemoG-CaM_{SiR}, I observed the maximum FRET ratio change after approximately 15 s. It is therefore possible that the temporal resolution was not sufficient to capture the maximal FRET ratio change during the plate reader measurements. Second, the dynamic range of ChemoL-CaM_{CPY} is 4.0-fold lower compared to ChemoG-CaM_{SiR}.

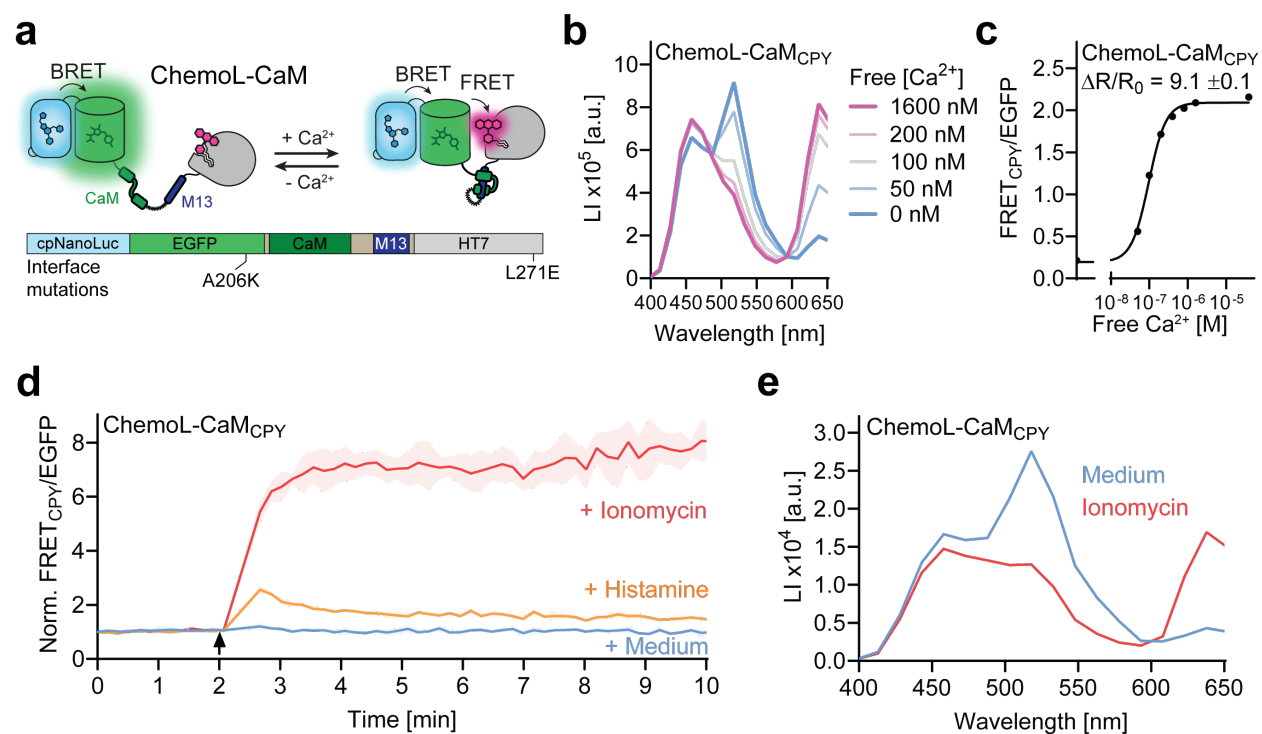


Figure 41 | Bioluminescent calcium sensor ChemoL-CaM.

a. Schematic representation of the bioluminescent calcium sensor ChemoL-CaM. **b.** Luminescence intensity (LI) emission spectra of ChemoL-CaM labeled with CPY, at different free calcium concentrations. **c.** Dose-response curve of ChemoL-CaM labeled with CPY. $\Delta R/R_0$ = maximal FRET_{CPY}/EGFP ratio change. **d.** Plotted are the mean of FRET_{CPY}/EGFP ratios (thick line) plus standard deviation (shadow) of HeLa Kyoto cells expressing ChemoL-CaM in the cytosol. The addition of 1 μ M ionomycin, 10 μ M histamine or medium is indicated with an arrow. FRET_{CPY}/EGFP ratios were normalized to t = 0 min. **e.** Luminescence intensity (LI) emission spectra of ChemoL-CaM at the end of the time course measurement from **d**. Anna Edenhofer helped with the characterization of the ChemoL-CaM sensor. Adapted from Hellweg *et al.*⁷⁸

The conversion of ChemoG-ATP into ChemoL-ATP (**Figure 42a**) was also successful. When labeled with CPY, ChemoL-ATP displayed a dynamic range of $^{Max}\Delta R/R_0 = 6.1 \pm 0.1$ and a C_{50} at 1.0 mM ATP (**Figure 42b-c**). The performance of all three ChemoL sensors is summarized in **Table 11**. Similar to the imaging data for ChemoG-ATP_{SiR} (**Figure 26c**), ChemoL-ATP_{CPY} was able to detect the depletion of intracellular ATP levels in HeLa Kyoto cells upon inhibition of glycolysis with 2DG ($\Delta R/R_0 = -71.6 \pm 1.6$ %), which could partially be recovered by addition of high concentrations of D-glucose (**Figure 42d-e**).

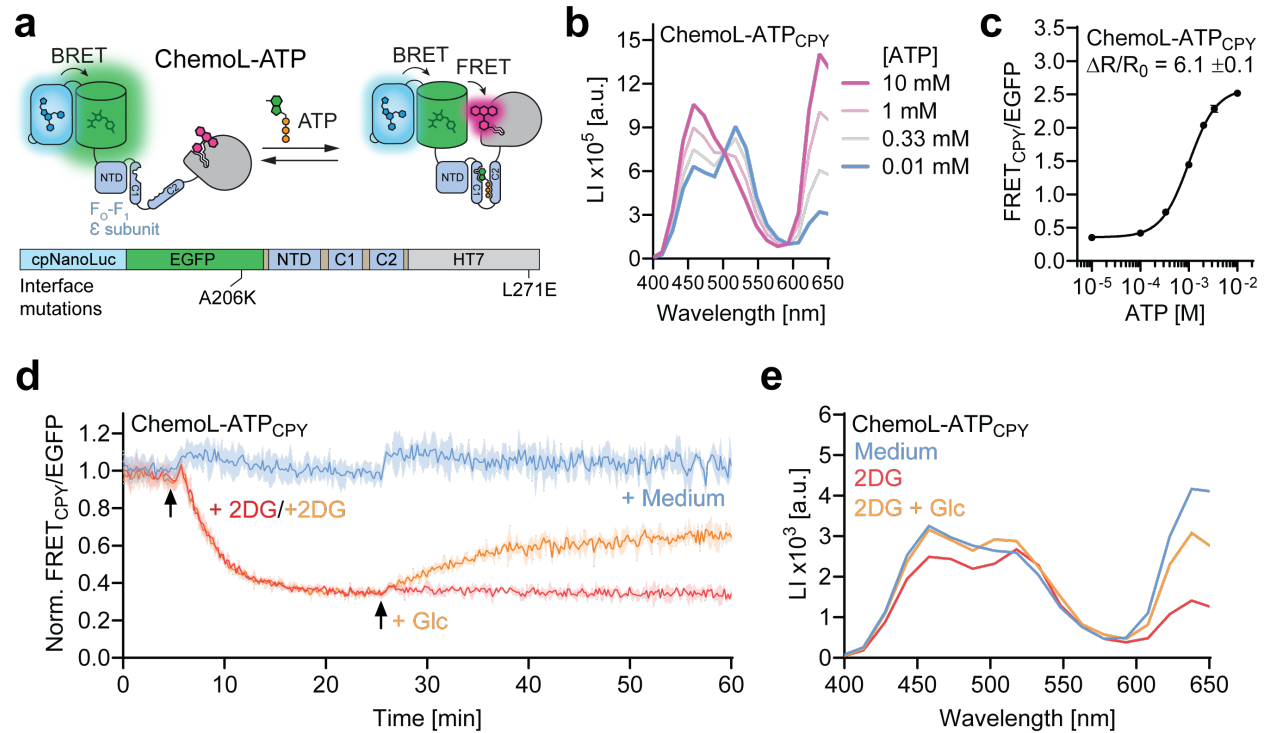


Figure 42| Bioluminescent ATP sensor ChemoL-ATP.

a. Schematic representation of the bioluminescent ATP sensor ChemoL-ATP. **b.** Luminescence intensity (LI) emission spectra of ChemoL-ATP labeled with CPY, at different ATP concentrations. **c.** Dose-response curve of ChemoL-ATP labeled with CPY. $\Delta R/R_0 =$ maximal FRET_{CPY/EGFP} ratio change. **d.** Plotted are the mean of FRET_{CPY/EGFP} ratios (thick line) plus standard deviation (shadow) of HeLa Kyoto cells expressing ChemoL-ATP in the cytosol. The addition of 10 mM 2-deoxy-D-glucose (2DG), 20 mM D-glucose (Glc) or medium is indicated with an arrow. FRET_{CPY/EGFP} ratios were normalized to $t = 0$ min. **e.** Luminescence intensity (LI) emission spectra of ChemoL-ATP at the end of the time course measurement from **d**. Adapted from Hellweg *et al.*⁷⁸

Table 11| Overview of the bioluminescent ChemoL sensors.

C_{50} = Analyte concentration at half-maximal response, $\text{Max } \Delta R/R_0$ = maximal change of FRET_{CPY/EGFP} ratio in absence and presence of analyte. Adapted from Hellweg *et al.*⁷⁸

Construct	FRET pair	Interface mutations		C_{50}	Max $\Delta R/R_0$	Hill slope
		FP	HT7			
ChemoL-CaM	EGFP/CPY	A206K	L271E	96.6 nM	9.1 ± 0.1	1.95
ChemoL-ATP	EGFP/CPY	A206K	L271E	1.0 mM	6.1 ± 0.1	1.52
ChemoL-NAD	EGFP/CPY	A206K-T225R	L271E	60.5 μ M	7.5 ± 0.1	0.89

The FRET ratio of the ChemoL sensors could be detected using a microplate reader equipped with a luminescence module, rendering the data acquisition and data analysis simpler compared to fluorescence microscopy. However, the plate reader records the ensemble of all cells in a respective well, whereas fluorescence microscopy provides single-cell resolution. Thus, the bioluminescent ChemoL biosensors are particularly useful for applications, where throughput and high signal-to-background is more important than spatial or temporal precision.

2.9. Development of a fluorescent biosensor for NMN

Nicotinamide mononucleotide (NMN) serves as the direct precursor of NAD⁺ for its biosynthesis *via* the salvage pathway. Together with other NAD⁺ precursors, NMN has been shown to effectively increase NAD⁺ levels in different mouse models¹²⁰, thereby improving physiological functions and holding promise for therapeutic interventions in conditions like cardiovascular diseases, diabetes, and neurological disorders^{121, 122}. Beyond its function as an NAD⁺ booster, NMN was recently recognized to regulate the activity of the NAD⁺ hydrolase sterile alpha and TIR motif-containing 1 (SARM1)¹²³, a sensor for metabolic stress implicated in axonal degeneration¹²⁴. Despite the emerging role of NMN as a regulator of biological functions, little is known about its cellular uptake, intracellular distribution and metabolism, and whether potential compartmentalization of NMN may have implications on cellular processes similar to NAD⁺. To address this gap in knowledge, I aimed to utilize the ChemoX platform for the development of a fluorescent NMN biosensor, which would allow to study the dynamics of NMN with high spatiotemporal precision. I searched the literature for proteins that undergo a large conformational change upon binding to NMN. The DNA ligase A from the bacterium *Enterococcus faecalis* (efLigA) was previously used to develop a biosensor for NAD⁺¹⁰⁴. However, subsequent characterizations of this biosensor revealed that it also responds to NMN with a C₅₀ of approximately 100 μM¹⁰⁴. This finding is not unexpected considering the large conformational change of efLigA when bound to NMN *versus* NAD⁺^{108, 125} (**Figure 43a-c**). Based on this information, I hypothesized that the efLigA could serve as a suitable sensing unit for an NMN biosensor. Similar to the ChemoG-NAD design, I flanked EGFP and HT7 around a catalytically inactive mutant of efLigA (K120L-D286N,

efLigAⁱ) and labeled the construct with TMR. Upon titration with NMN and structurally-related metabolites (nicotinamide [NAM], NR and NAD⁺), I observed a heterogeneous response behavior. The FRET_{TMR}/EGFP ratio increased in presence to NAD⁺ (**Figure 44a**), suggesting that the conformational change of the efLigAⁱ brings the FRET pair in closer proximity, resembling the response of ChemoG-NAD based on ttLigA (**Figure 27c**).

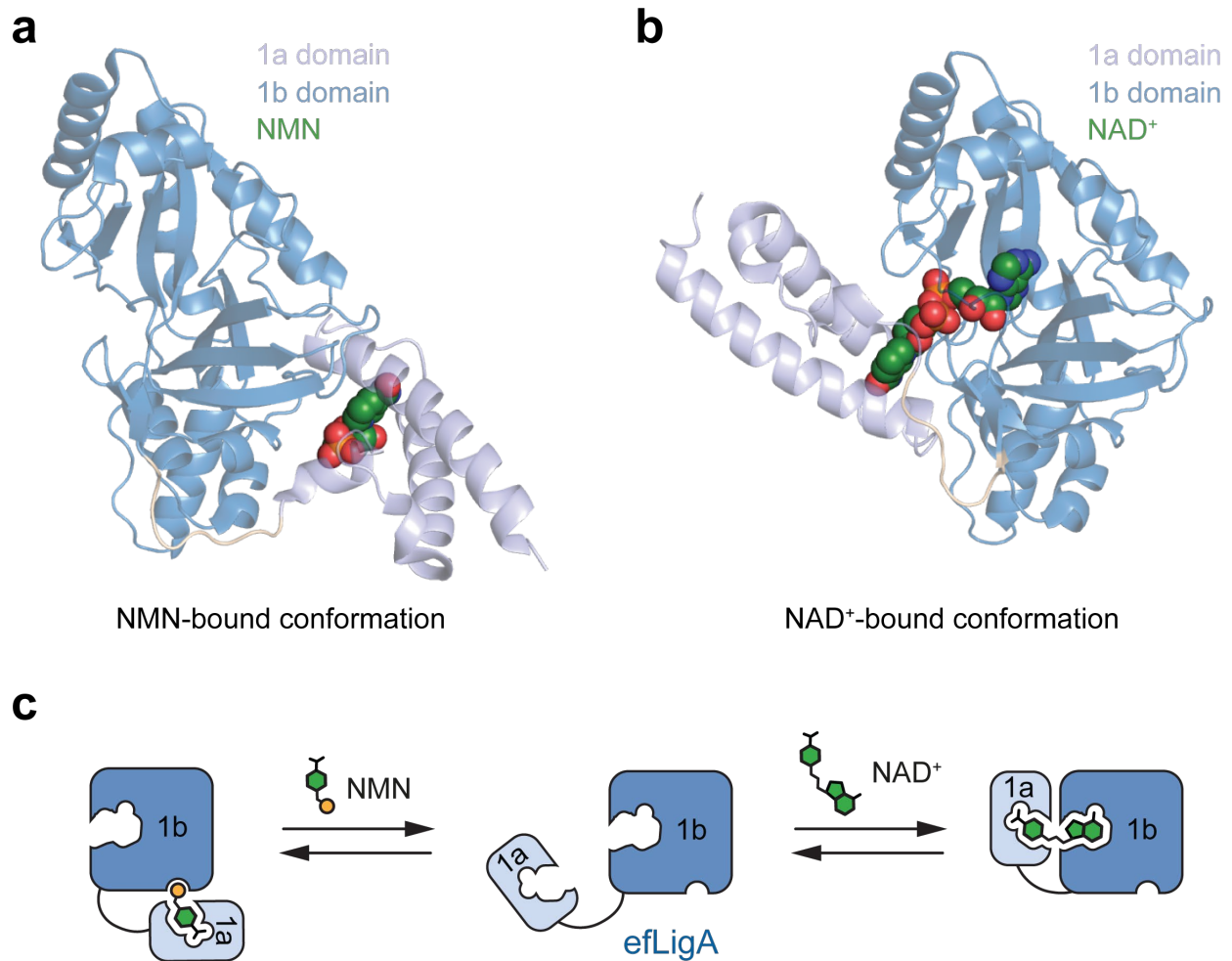


Figure 43 | Conformational changes of the bacterial DNA ligase A from *Enterococcus faecalis*.

a-b. X-ray crystal structures of bacterial DNA ligase A from *Enterococcus faecalis* (efLigA) bound to NMN (PDB: 1TA8, **a**) or NAD⁺ (PDB: 1TAE, **b**). Protein is shown as cartoon. NMN and NAD⁺ are depicted as spheres. **c.** Cartoon representing the conformational change of efLigA upon binding to NMN or NAD⁺.

Titration with NMN or NR, on the other hand, resulted in a decreased FRET_{TMR}/EGFP ratio, which aligns with structural data from the literature indicating that the efLigAⁱ adopts distinct

conformations when bound to NMN or NAD⁺ (**Figure 44b**). To render the sensor specific for NMN, I mutated Y227 on the 1b domain of efLigAⁱ, a key residue involved in the binding of NAD⁺ *via* π -stacking interactions with its adenosine moiety. This would prevent the formation of the NAD⁺-specific conformation. Indeed, the mutation Y227R abolished the response for NAD⁺, while the sensor remained responsive to NMN with a C₅₀ of approximately 8 μ M (**Figure 44c-d**).

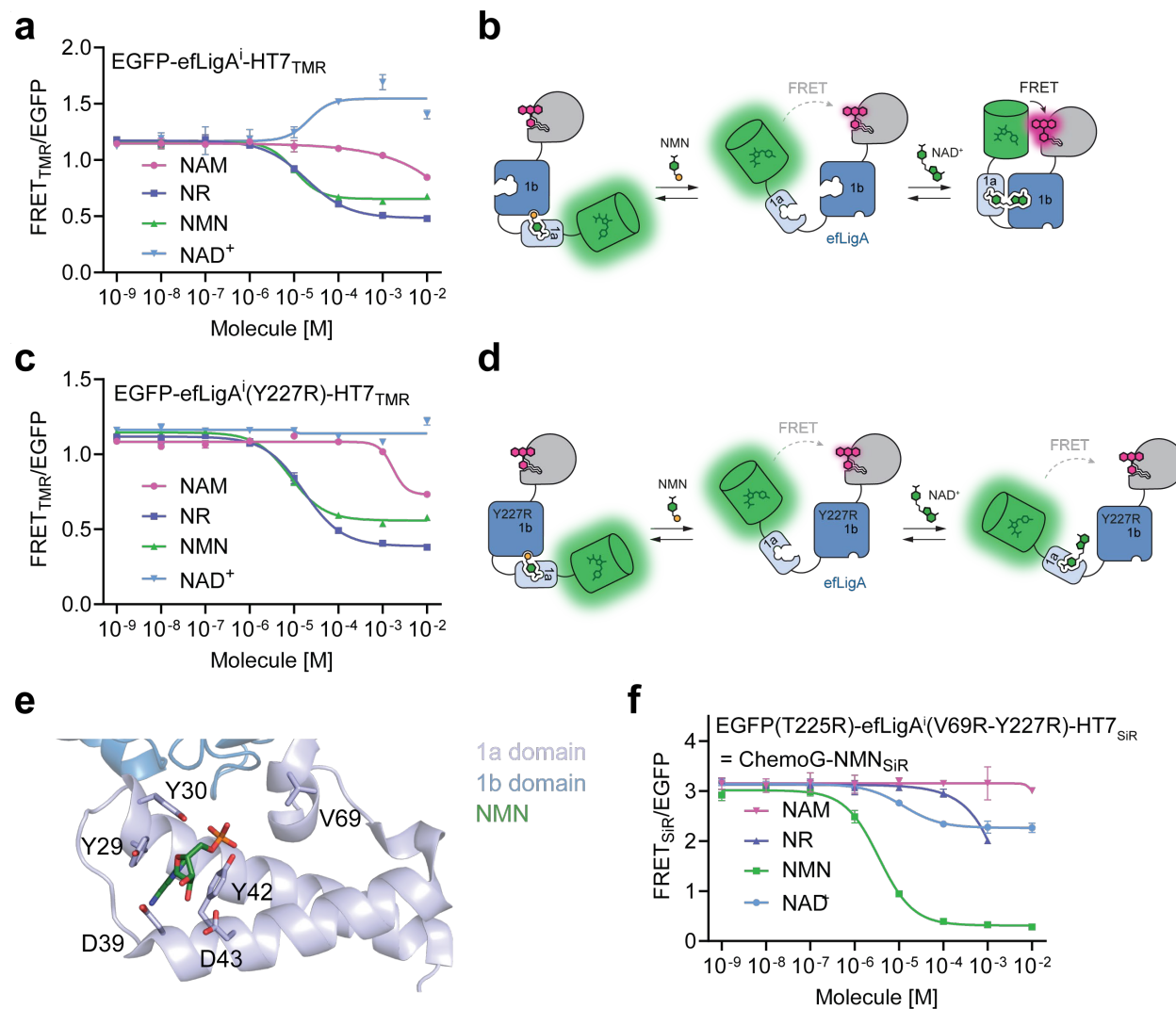


Figure 44 | Development of the chemogenetic NMN biosensor ChemoG-NMN.

a, c, f. Dose-response curves of sensor constructs upon titration with nicotinamide (NAM), nicotinamide riboside (NR), NMN or NAD⁺. Sensors were labeled with TMR (**a, c**) or SiR (**f**). The efLigA was rendered catalytically inactive (efLigAⁱ) by introducing the mutations K120L and D286N. **b, d.** Cartoons representing the conformational changes and functioning of the sensor variants corresponding to **a** and **c**, respectively. **e.** X-ray crystal structure of the efLigA bound to NMN (PDB: 1TA8). Zoom-in of the NMN-binding site (1a domain). Protein is shown as cartoon. Side chain residues and NMN are shown as sticks.

Since intracellular NMN concentrations are estimated to be at approximately $1\ \mu\text{M}$ ¹²⁶, I aimed to further optimize the response range of the sensor. Guided by the structural information available for efLigA, I substituted valine 69 with an arginine (V69R), potentially stabilizing the phosphate group of NMN (**Figure 44e**). Additionally, I introduced the ChemoG interface mutation T225R on EGFP to increase the dynamic range of the sensor. When labeled with SiR, this sensor variant, named ChemoG-NMN, exhibited a C_{50} of $3.5\ \mu\text{M}$ for NMN and a dynamic range of $^{\text{Max}}\Delta R/R_0 = 9.3 \pm 0.3$ (**Figure 44f**).

Surprisingly, the sensor regained its responsiveness for NAD^+ . In contrast to the initial sensor construct, the FRET ratio decreased with increasing NAD^+ concentrations, suggesting that the mutated efLigAⁱ in ChemoG-NMN adopts a different conformation when bound to NAD^+ compared to the initial efLigAⁱ. Yet, this conformation seems to be different from the NMN-bound conformation as well, since the FRET ratios at saturating NMN and NAD^+ concentrations are notably different ($\text{FRET}_{\text{SiR/EGFP NMN}} = 0.28 \pm 0.01$, $\text{FRET}_{\text{SiR/EGFP NAD}^+} = 2.27 \pm 0.08$). Structural characterization of efLigA by Gejawali *et al.*¹⁰⁸ and Lahiri *et al.*¹²⁵ revealed that most of the binding affinity of NAD^+ to the 1a domain is attributed to its NMN moiety binding. Therefore, I hypothesized that NAD^+ can still bind to ChemoG-NMN *via* the 1a domain.

To test this hypothesis, I titrated ChemoG-NMN with NMN in absence or in presence of increasing NAD^+ concentrations. Consistent with the NAD^+ titrations, the basal $\text{FRET}_{\text{SiR/EGFP}}$ ratio decreased with increasing NAD^+ concentrations (**Figure 45a**). Furthermore, the C_{50} for NMN shifted from $3.2\ \mu\text{M}$ in the absence of NAD^+ to $28.9\ \mu\text{M}$ in the presence of $1\ \text{mM}\ \text{NAD}^+$, suggesting that NMN and NAD^+ are competing for the same binding site. Indeed, structural analysis of adenylylated LigA from *Haemophilus influenzae* (hiLigA, PDB: 3UQ8) revealed the same binding mode of NAD^+ to the 1a domain when compared to the crystal structure of efLigA bound to NMN (PDB: 1TA8, **Figure 45b-c**). In addition to the interactions with the highly conserved hiLigA side chain residues Y22, H23, D32, Y35, D36 and R154, which bind the NMN part of NAD^+ , the adenosine moiety of NAD^+ forms interactions with the side chain residues F39, H40, K43 and Q61, potentially stabilizing its binding to the 1a domain. At the corresponding positions, efLigA possesses side chain residues that could establish similar contacts with NAD^+ (*i.e.*, Y46,

K47, V50 and Q67). To disrupt the binding of NAD⁺ to ChemoG-NMN, I mutated the efLigA residues Y46, K47 and Q67 into alanine and V50 into a tryptophan. V50 seemed unlikely to form similar contacts as K43 in hiLigA, but might sterically clash with NAD⁺ when replaced with a bulkier side chain residue like tryptophan. However, all mutants remained sensitive to NAD⁺ (Figure 45d-g).

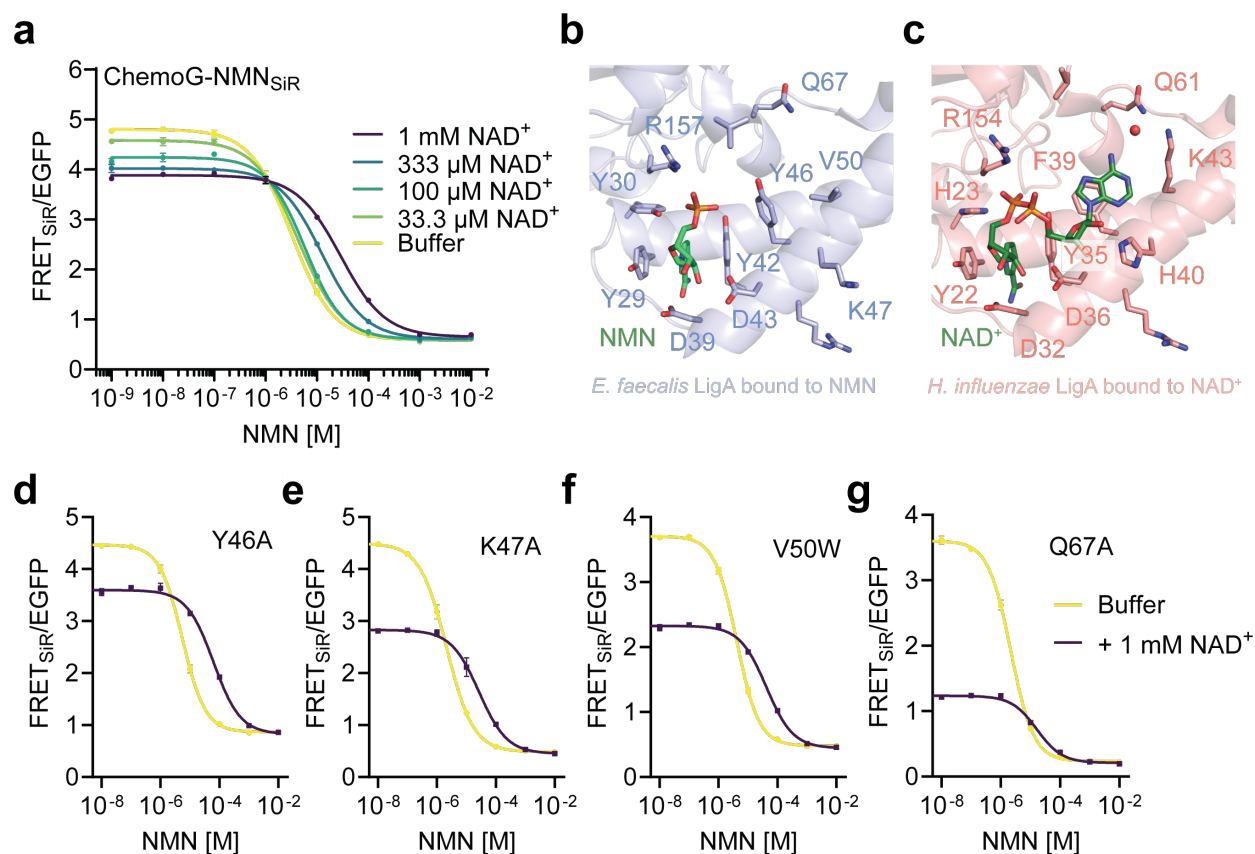


Figure 45 | ChemoG-NMN is sensitive to changes in NAD⁺ concentrations.

a, d-g. Dose-response curves of ChemoG-NMN (**a**) and sensor variants with point mutations in efLigA (**d-g**) in absence (buffer) or presence of different NAD⁺ concentrations. **b-c.** X-ray crystal structures of efLigA bound to NMN (PDB: 1TA8, **b**) and pre-adenylated LigA from *Haemophilus influenzae* bound to NAD⁺ (PDB: 3UQ8, **c**). Shown are the zoom-ins on the NMN-binding site (1a domain). Protein is shown as cartoon. Side chain residues, NMN and NAD⁺ are shown as sticks. Dr. Miroslaw Tarnawski acquired the X-ray crystal structures.

To get further insights into the binding of NAD^+ to the sensor, I acquired in collaboration with Dr. Mirosław Tarnawski (Max-Planck-Institute for Medical Research, Heidelberg) a crystal structure of the $\text{efLigA}^i(\text{V69R-Y227R})$ mutant used for ChemoG-NMN. $\text{efLigA}^i(\text{V69R-Y227R})$ adopts the same conformation when bound to NMN and NAD^+ . Both nucleotides form interactions with the highly conserved ‘NMN-binding’ side chain residues (Y29, Y30, D39, Y42, D43 and R157, **Figure 46a-b**). Furthermore, R69 establishes direct contact with the phosphate of NMN, explaining the shift in the C_{50} for ChemoG-NMN towards lower NMN concentrations. One of the phosphates of NAD^+ is also stabilized through interactions with R69. However, the adenosine part of NAD^+ does not engage in direct interactions with the 1a domain, but points away from the protein towards the solvent (**Figure 46b**), as opposed to the observations from the hiLigA crystal structure. This would also explain why the efLigA mutations Y46A, K47A, V50W and Q67A did not abolish the NAD^+ sensitivity of ChemoG-NMN.

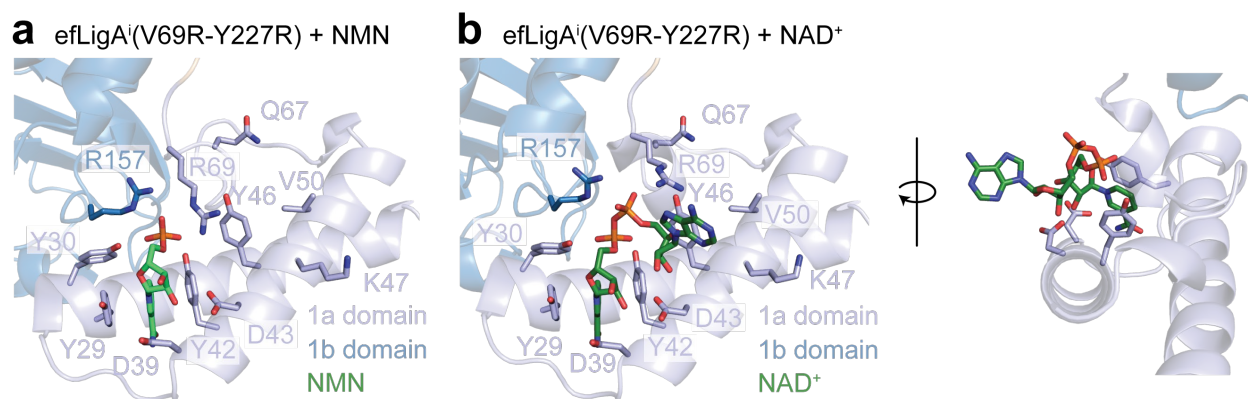


Figure 46 | Structural analysis of $\text{efLigA}^i(\text{V69R-Y227R})$.

a-b. X-ray crystal structures of catalytically inactive $\text{efLigA}^i(\text{V69R-Y227R})$ bound to NMN (**a**) or NAD^+ (**b**). Protein is shown as cartoon. Side chain residues, NMN and NAD^+ are shown as sticks. Both NMN and NAD^+ are bound at the same binding site, while the adenosine part of NAD^+ points out towards the solvent.

Despite this NAD^+ sensitivity, I assessed whether ChemoG-NMN was able to detect fluctuations of intracellular NMN. I expressed ChemoG-NMN in the cytosol (ChemoG-NMN-cyto) or in the nucleus (ChemoG-NMN-NLS) of U-2 OS cells and labeled the sensor with SiR. To correct

for potential artifacts caused by changes in NAD⁺, I also monitored the intracellular NAD⁺ levels with ChemoG-NAD in the respective subcellular compartment. For the perturbation of intracellular NMN, I knocked down or pharmacologically inhibited enzymes involved in the salvage pathway (**Figure 47a**). To increase NMN levels, I knocked down one or both of the two isoforms of nicotinamide mononucleotide adenylyltransferase (NMNAT1 and 2), which catalyze the conversion of NMN into NAD⁺ in the nucleus and cytosol, respectively. To decrease NMN levels, I either knocked down NAMPT or pharmacologically inhibited its activity using FK866. The NAMPT knockdown substantially reduced the mRNA expression levels down to 5.2 ± 0.3 % (**Figure 47b**). The NMNAT1 mRNA expression levels were reduced to 57.8 ± 0.5 % upon single knockdown of NMNAT1 or to 69.7 ± 0.9 % for the double knockdown of NMNAT1 and 2. The knockdowns of NMNAT2 were not successful and therefore excluded from subsequent data analysis.

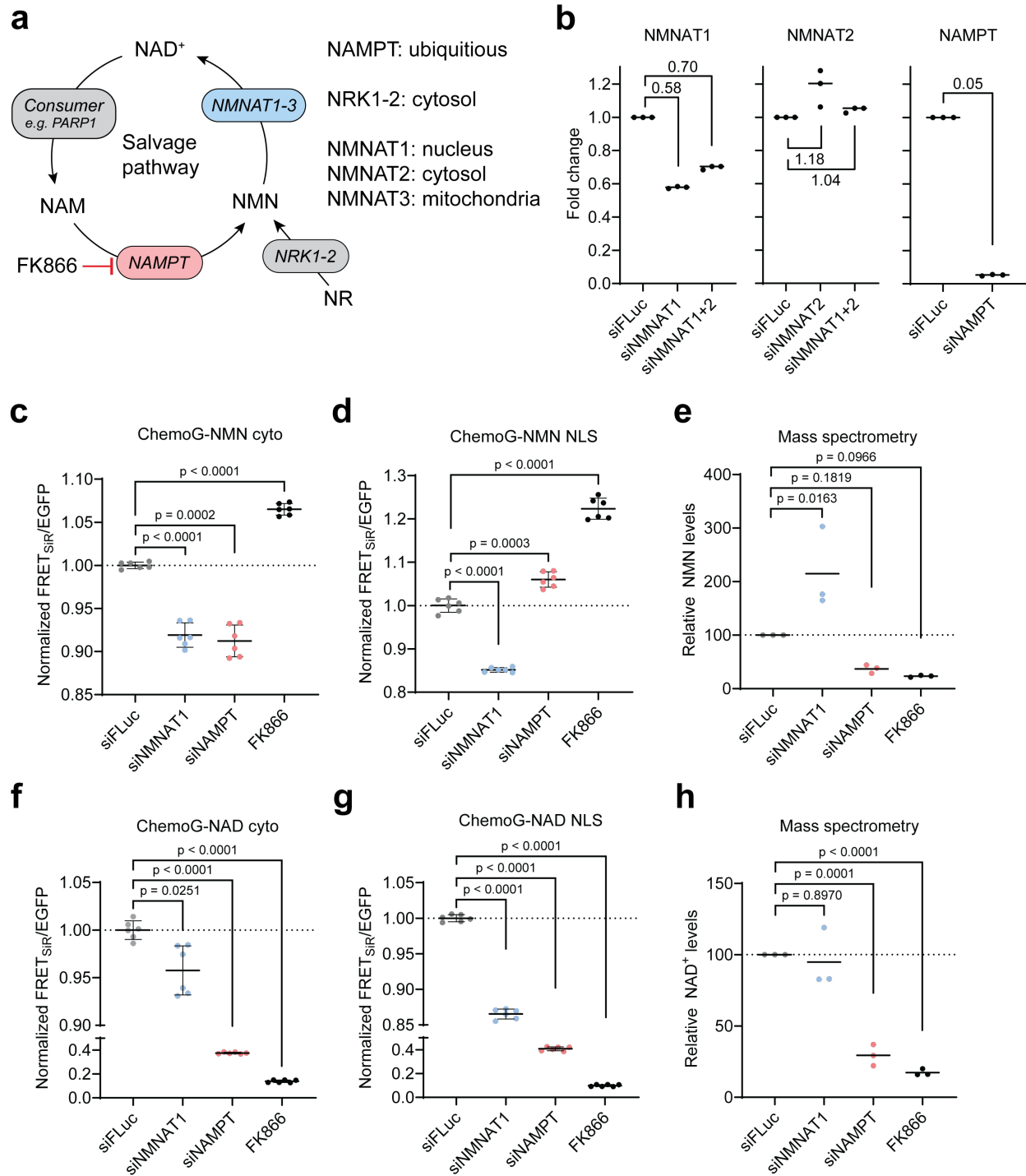


Figure 47 | Assessing intracellular NMN and NAD⁺ levels upon perturbation of the salvage pathway.

a. Schematic representation of the intracellular salvage pathway. Intracellular localizations of enzymes are highlighted on the right side. **b.** mRNA expression levels of NMNAT1, NMNAT2 and NAMPT after knockdown with siRNAs. The difference in expression levels are shown as fold-change compared to a control knockdown (siFLuc). **c-d, f-g.** FRET_{SIR}/EGFP ratios of ChemoG-NMN (**c-d**) and ChemoG-NAD (**f-g**) expressed in the cytosol (cyto) or nucleus (NLS) of U-2 OS cells after siRNA knockdown or pharmacological treatment with FK866. Shown are the means (black bar) plus standard deviations of 6 technical replicates

(spheres) derived from 2 biological replicates. The FRET_{SiR}/EGFP ratios were normalized to the ratio after control knockdown with siFLuc (dotted line). **e, h.** Relative NMN (**e**) and NAD⁺ (**h**) levels of U-2 OS cells after siRNA knockdown or pharmacological treatment with FK866. Values were determined *via* mass spectrometry using whole-cell lysates. Shown are the means (black bar) of 3 biological replicates (spheres).

Knockdown of NMNAT1 resulted in a significant FRET_{SiR}/EGFP ratio decrease of ChemoG-NMN in the cytosol (-8.1 ± 1.3 %) and nucleus (-13.5 ± 0.6 %, **Figure 47c-d**) indicating an elevation of NMN in both compartments. This suggested that reduced NMN production in the nucleus *via* NMNAT1 also affects cytosolic NMN levels, for example through diffusion of NMN from the nucleus into the cytosol. This is in line with the subcellular distribution of NAD⁺, which is known to be freely exchangeable between the nucleus and the cytosol¹⁰⁷. However, the FRET ratio decrease of ChemoG-NMN could be potentially also due to the slightly reduced NAD⁺ levels detected with ChemoG-NAD (**Figure 47f-g**). Analysis of cell lysates *via* mass spectrometry (MS) revealed a 114.8 % ($\pm 62.5\%$) increase of whole-cell NMN levels upon NMNAT1 knockdown, whereas whole-cell NAD⁺ levels seemed to be hardly affected (-5.1 ± 17.0 %, **Figure 47e, h**), suggesting that the FRET ratio change of ChemoG-NMN is likely due to changes in NMN levels rather than NAD⁺.

Pharmacological inhibition of NAMPT with FK866 led to significantly increased FRET_{SiR}/EGFP ratios of ChemoG-NMN in both compartments (cytosol = $+6.5 \pm 0.6$ %, nucleus = $+22.4 \pm 2.2$ %, **Figure 47c-d**), indicating an expected decrease of intracellular NMN levels. The FRET ratio of ChemoG-NAD decreased to a notably larger extent in both compartments (cytosol = -86.1 ± 1.0 %, nucleus = -90.1 ± 0.8 %, **Figure 47f-g**), indicative for a strong depletion of NAD⁺. However, the MS data of whole-cell lysates showed similar trends for both NMN (-76.6 ± 1.4 %) and NAD⁺ (-82.6 ± 1.9 %, **Figure 47e, h**). According to the competition titrations of ChemoG-NMN with NAD⁺, a strong decrease in NAD⁺ could decrease the FRET ratio of ChemoG-NMN, if the basal NMN concentrations are in the low micromolar range (**Figure 45a**). This might explain why the relative FRET ratio change of ChemoG-NMN is notably smaller compared to ChemoG-NAD upon FK866 treatment. Another reason might be the smaller dynamic range of ChemoG-NMN_{SiR} (9.3 ± 0.3) compared to ChemoG-NAD_{SiR} (34.7 ± 0.4).

Knockdown of NAMPT decreased whole-cell levels of NMN (-63.0 ± 6.4 %) and NAD^+ (-70.5 ± 6.1 %, **Figure 47e, h**) as well, although to a lesser extent compared to pharmacological inhibition with FK866. In line with the MS data, the $\text{FRET}_{\text{SiR}}/\text{EGFP}$ ratio of ChemoG-NMN increased in the nucleus ($+6.0 \pm 1.6$ %) indicative for decreased NMN levels. However, I observed the opposite trend in the cytosol (-8.8 ± 1.7 %). Since the relative changes of cytosolic and nuclear NAD^+ are comparable upon knockdown of NAMPT (-62.4 ± 0.6 % and -59.2 ± 1.5 %, respectively), the effect of the NAD^+ sensitivity on ChemoG-NMN should be more or less similar in both cases.

A potential explanation for this contradictory observation could be that other pathways or mechanisms might compensate for the reduced NMN production by NAMPT to different extents in the two compartments. For example, the NR kinases NRK1 and NRK2, which are both localized in the cytosol, might bypass the production of NMN from NAM and instead utilize NR. Alternatively, mitochondrial NMN might be specifically exported into the cytosol. However, such mechanisms would conflict with the previous hypothesis that NMN can be freely exchanged between the nucleus and the cytosol. Considering these contradictory results and the fact that significant changes in intracellular NAD^+ likely affect the FRET ratio of ChemoG-NMN, I was not able to draw reliable conclusions on subcellular NMN dynamics using this sensor.

Chapter 3 – Discussion

3.1. Design of FRET pairs with high FRET efficiencies

During the course of this study, I developed a suite of chemogenetic FRET pairs, named ChemoX. This system is based on a fluorescent protein (FP) FRET donor and a rhodamine-based FRET acceptor labeled to the self-labeling protein (SLP) HaloTag7 (HT7). Building upon the serendipitous finding that the rhodamine-based fluorophore tetramethylrhodamine (TMR) establishes specific interactions with the surface of enhanced green fluorescent protein (EGFP) when labeled to HT7, I engineered the interface between EGFP and HT7 in order to further stabilize these interactions. This allowed me to develop FRET pairs with near-quantitative FRET efficiencies (up to 96.6 %). Through structural analysis and determination of an apparent equilibration dissociation constant of the optimized FRET pair design ChemoG5, I revealed that the improvement in FRET was achieved by stabilization of an existing conformation favorable for high FRET efficiency, rather than changes in the distance or relative orientation between the EGFP chromophore and the fluorophore labeled to HT7. Similar observations were made in previous studies, where the introduction of specific interactions between two FPs^{70, 71, 127, 128}, or an FP and heme-bound cytochrome b_{562} ¹²⁹ substantially improved the FRET efficiency.

Compared to FRET pairs based on two FPs, the ChemoX design allows tuning of the spectral properties of the FRET acceptor on demand by labeling HT7 with the desired fluorophore. That said, it seems intriguing to substitute also the FP FRET donor with an SLP that can be labeled orthogonally to the other SLP, *i.e.*, labeling of the two SLPs with two different fluorophores. This would enhance the spectral versatility of the FRET pair even further. Additionally, a FRET pair exclusively based on synthetic fluorophores might possess overall superior photostability compared to FP-based systems. However, engineering an interface similar to ChemoG5 between the two fluorophores labeled to the SLPs would be necessary to achieve efficient FRET. Otherwise, the SLPs might exhibit high degrees of freedom with no defined conformation that would favor efficient FRET. Vecchia and colleagues recently developed sensors based on two SLPs by exchanging the FP FRET pair of established biosensors with SNAP-tag and HT7. While this approach

allowed them to use different rhodamine-based fluorophores as FRET donor and acceptor, the FRET efficiencies as well as the dynamic range of these sensors are relatively low (~60% FRET ratio change)¹³⁰, underscoring the importance of stabilizing interface mutations in order to establish high efficiency FRET pairs. This hypothesis is supported by my findings that cyanine fluorophores are not well compatible with the ChemoG5 design, and that stabilizing interactions between the FRET pair are essential for efficient FRET.

Substitution of EGFP with FPs of different color allowed me to expand the spectral properties of the chemogenetic FRET pair design. Grafting the ChemoG5 interface onto different FPs was straightforward for those with high sequence homology to EGFP. However, implementation of FPs with poor sequence homology to EGFP, such as mScarlet or mNeonGreen (data not shown), proved challenging. Structure-guided incorporation of ChemoG5 mutations onto these FPs barely improved the FRET efficiency, suggesting that bulky side chain residues or electrostatic charges on FPs like mScarlet might clash with side chain residues on HT7 or lead to increased repulsion from HT7, respectively. Considering the recent advancements of FPs with respect to their brightness and photostability¹³¹⁻¹³⁴, it would be of great interest to implement FPs with low sequence homology to EGFP by pursuing a more comprehensive mutagenesis screen on the surfaces of FPs and HT7 with the aim of identifying mutants with improved FRET efficiencies. To this end, future efforts may focus on generating mutant libraries of FP-HT7 fusion constructs *via* error-prone PCR, which are then screened for improved FRET upon labeling with SiR using high-throughput methods like yeast surface display.

Despite the preference for EGFP-derived FPs and rhodamine-based fluorophores, the ChemoX design offers high spectral flexibility with maximal FRET donor emission wavelengths ranging from 448 nm (EBFP2) to 569 nm (mScarlet) and maximal FRET acceptor emission wavelengths from 556 nm (JF₅₂₅) to 686 nm (JF₆₆₉). Although the spectral overlap of ChemoX FRET pairs can vary substantially (126-fold difference between EBFP2/JF₆₆₉ and mScarlet/SiR), all FRET pair combinations tested in this study exhibited FRET efficiencies above 91 %. Based on the optimized ChemoX FRET pair design, I was able to develop FRET-based biosensors with increased multiplexing capacity and the ability to optimize their dynamic range.

3.2. Improving the dynamic range of FRET-based biosensors

The dynamic range of a fluorescent biosensor determines its sensitivity for detecting changes in the biological activity or concentration of the analyte of interest.

In this study, I exploited the engineered ChemoX interface to tune the FRET efficiency of FRET-based biosensors in both their open and closed state. By choosing the number and type of interface mutations, I was able to reinforce interactions between the FRET pair and thereby enhance the FRET efficiency in the closed state of the sensor. The spectral flexibility of the ChemoX design, on the other hand, allowed me to use FRET pairs with large spectral separation reducing the FRET efficiency in the open state of the sensor. The combination of both, interface mutations and a large spectral separation of the FRET pair, demonstrated to be paramount for the development of FRET biosensors with large dynamic ranges. This approach has proven to be quite universal, as it was applicable to three different sensor designs (Ca^{2+} , ATP and NAD^+) and required testing of only a handful of variants. Similar strategies in previous studies, involving dimerization mutations on two FPs⁶⁹⁻⁷² or the fusion of small dimerization domains to the FRET pairs⁷³, have also resulted in improved dynamic ranges of FRET biosensors. However, these adaptations were primarily limited to CFP-YFP-based sensors, or resulted in only marginally improved dynamic ranges. Notably, the dynamic ranges of ChemoB- and ChemoG-ATP (~5.0-fold and ~11.1-fold, respectively), both developed in this study, are far superior compared to other ratiometric ATP biosensors, such as ATeam 1.03⁹⁴ and GO-ATeam⁷⁴ (~1.4-fold and ~1.0-fold, respectively), which will enable the detection of more subtle changes in intracellular ATP levels.

CFP-YFP FRET pairs exhibit a large spectral overlap, which leads to increased spectral crosstalk and overall limits the dynamic range of FRET-based biosensors. I observed similar limitations for ChemoX biosensors based on FRET pairs with large spectral overlap such as EGFP/TMR or mScarlet/SiR. I demonstrated that sensors based on FRET pairs with large spectral separation (*e.g.*, ChemoG- CaM_{SiR} and ChemoB- CaM_{SiR}) exhibited larger dynamic ranges compared to those based on FRET pairs with poor spectral separation (*e.g.*, ChemoG- CaM_{TMR} and YC 3.6).

In line with this observation, optimizing the dynamic range of ChemoX sensors based on RFPs proved to be challenging. The spectral overlap of mScarlet and SiR is 3-fold larger than that of commonly used CFP-YFP FRET pairs, likely contributing to the reduced dynamic range of these sensors. Additionally, the poor applicability of ChemoG interface mutations on RFPs limits optimization of the FRET efficiency, further hampering the ability to enhance the dynamic range of ChemoR sensors. As discussed in the previous subchapter, efforts to identify interface mutations between HT7 and RFPs, as well as other FPs with low sequence homology to EGFP, represents an exciting opportunity to extend the toolbox of ChemoX biosensors with large dynamic ranges.

An additional factor that might contribute to the large dynamic ranges of ChemoX biosensors is the enhanced fluorescence intensity of rhodamine-based fluorophores (not due to FRET, but upon direct excitation) that I observed in the closed state of ChemoG biosensors. Direct interactions between the FP surface and the rhodamine-based fluorophore upon formation of the ChemoG interface in the closed sensor state might lead to rigidification of the fluorophore or affect its open-closed equilibrium. Based on this hypothesis, the fluorescence intensity increase may stem from an increase in absorption (*i.e.*, higher extinction coefficient), increase in quantum yield, or both. An elevated absorption of the FRET acceptor would contribute to a larger spectral overlap and thereby improve the FRET efficiency, whereas an increased quantum yield of the FRET acceptor would amplify the FRET signal. Both phenomena would result in an increased FRET/FP ratio in the closed state and thereby improve the dynamic range of the sensors. The determination of the extinction coefficient and quantum yield of the FRET acceptor in the open and closed state of the sensors might help to understand the mechanism behind the fluorescence intensity increase.

Overall, the modular architecture of FRET biosensors allows for the straightforward integration of new sensing units and FRET pairs to improve the performance of existing sensors or to develop new ones. Consequently, the ChemoX FRET system should be applicable to other established FRET-based biosensors, and help to improve their dynamic range and spectral flexibility, as demonstrated for Ca^{2+} and ATP sensors in this study.

3.3. Multiplexing capacity of current ChemoX biosensors

Simultaneous monitoring of multiple cellular processes, signaling pathways, and metabolite concentrations is crucial to gain comprehensive insights into cellular dynamics and interactions. Understanding how different processes coexist and influence each other in real-time in the same cell allows for a more accurate depiction of cellular behavior and regulatory mechanisms. Overall, the ability to monitor multiple aspects of cellular function concurrently enhances our understanding of cellular physiology and pathology, thereby offering valuable insights to advance biomedical research and clinical applications. Fluorescent biosensors have proven instrumental in this regard, as they can be targeted to subcellular localizations and enable real-time monitoring of dynamic processes in physiologically-relevant conditions using live-cell imaging techniques.

Multiplexing fluorescent biosensors is limited by the spectral range accessible with current sensor designs and imaging techniques. While sensors based on a single fluorescent moiety occupy less spectral space and thereby allow larger numbers of biosensors to be multiplexed, their intensimetric readout is sensitive to changes in sensor concentration. In contrast, ratiometric readout modalities such as FRET-based systems offer more robust detection, but often require a larger spectral space. To reduce the spectral demand of ratiometric biosensors, researchers have devised different strategies, for example, using the same FRET acceptor for multiple FRET sensors¹³⁵, developing large Stokes shift FPs for single excitation of multiple FRET sensors¹³⁶, developing photochromic FRET donors¹³⁷, or employing FRET between identical fluorophores (*i.e.*, homo-FRET)¹³⁸.

Here, the ChemoX sensor design employs different FP FRET donors that can be excited with negligible crosstalk, while utilizing the same FRET acceptor labeled to HT7 (*e.g.*, SiR) for all sensors. This setup enables multiplexing of BFP-, GFP- and RFP-based ChemoX FRET sensors. I demonstrated the multiplexing capacity of ChemoX sensors by co-expressing two NAD⁺ biosensors based on ChemoB_{SiR} and ChemoG_{SiR} FRET pairs at two different subcellular localizations. This allowed me to monitor the differential regulation of cytonuclear and mitochondrial NAD⁺ pools during acute genotoxic stress. Given the significance of intracellular NAD⁺ compartmentalization in regulating diverse biological processes^{105, 107, 139}, the ChemoX-NAD biosensors represent

a major advance for the investigation of these processes, as they overcome the spectral incompatibility of previously developed NAD⁺ biosensors. This will allow monitoring of subcellular NAD⁺ dynamics across multiple compartments simultaneously providing more comprehensive insights into the regulation of compartmentalized NAD⁺ and its impact on biological processes.

Although technically possible, co-expression of additional biosensors, like ChemoR-NAD, proved challenging at the time due to low transfection efficiencies or highly heterogeneous expression levels (data not shown). Recent experiments in the lab have shown that viral expression vectors (*e.g.*, adeno-associated viruses) improve homogeneous co-expression in the same cell, which might help to address this technical limitation in the future.

Since many fluorescent biosensors are based on GFP or CFP-YFP FRET pairs, efforts have been made to implement red or even near-infrared FPs into biosensors designs, which allowed multiplexing of up to six different parameters in the same cell¹⁴⁰⁻¹⁴². Furthermore, protein engineering of SLPs combined with the development of synthetic fluorophores with improved performance (*i.e.*, increased brightness, photostability and cell permeability) gave rise to chemogenetic biosensors with excellent photophysical properties in the far-red spectral range⁴⁹. While some of these chemogenetic designs are based on FRET, like the NAD(P)-Snifits⁷⁶, others are based on a single environmentally-sensitive fluorophore whose fluorescence intensity is modulated by interactions with the sensing units upon binding of the cognate analyte^{58,59}. In a similar approach, I exploited the environmental sensitivity of rhodamine-based fluorophores for the development of fluorescent ChemoD biosensors with far-red emission wavelengths. The fluorescence intensity of ChemoD biosensors is modulated by the reversible interaction between the fluorophore labeled to HT7 and the surface of a FP. Since only the surface of the FP is involved in this modulation, I exchanged EGFP with the virtually non-fluorescent protein ShadowG and thereby converted the sensor from a two-color into a single-color system. Similar to ChemoX FRET sensors, the FP/fluorophore interaction is altered upon conformational changes of the sensing unit, rendering the ChemoD sensor design highly modular. This should allow for the straightforward integration of other sensing units and thereby enable the development of single-color fluorescent biosensors with red-shifted excitation and emission wavelengths compatible for multiplexing purposes.

Nevertheless, the change in fluorescence intensity of ChemoD biosensors is relatively modest (up to 227 % for ChemoD-NAD_{JF635}) compared to other intensimetric sensors. To improve their dynamic range, one could further reduce the fluorescence intensity of the sensor in its open state by introducing additional fluorescence-quenching mutations. While lowered basal fluorescence intensities could potentially enhance the dynamic range of ChemoD sensors, it is important to note that the overall fluorescence intensity (*i.e.*, brightness) should not be compromised excessively, as this might increase photodamage of the biological sample due to higher laser excitation power needed, and potentially decrease the signal-to-background ratios during image acquisition.

In comparison to the fluorescence intensity changes of ChemoD sensors, their fluorescence lifetime is altered to a relatively large extent (up to 1.16 ns for ChemoD-NAD_{CPY}), being comparable to state-of-the-art fluorescence lifetime sensors like Tq-Ca-FLITS¹⁴³ (1.30 ns). Moreover, fluorescence lifetime provides an inherently quantifiable parameter, which is not affected by changes in sensor concentration, as opposed to purely intensity-based readouts. FRET biosensors can be read out *via* changes in fluorescence lifetime of the FRET donor as well, and their spectral demand can be reduced by using “dark” FRET acceptors with extremely low quantum yields, such as ShadowG. However, they still depend on FRET pairs with a suitable spectral overlap, whereas ChemoD biosensors function independently of a secondary fluorophore.

Nevertheless, current limitations prevent multiplexing of two or more ChemoD biosensors simultaneously as they all utilize HT7 and therefore cannot be labeled with different fluorophores at the same time. Future efforts may focus on the implementation of orthogonal SLPs to expand their multiplexing capacity. Since the fluorescence intensity and lifetime is modulated by the interaction between the fluorophore labeled to the SLP and the surface of ShadowG, it would be necessary to establish a comparable interface between the newly integrated SLPs and ShadowG. Alternatively, the recently developed exchangeable HT7 ligands (xHTLs)¹⁴⁴ enabled multiplexing of two orthogonal HT7 variants. Thus, using xHTLs in combination with ChemoD sensors based on such HT7 variants could enable multiplexing of two ChemoD sensors. Preliminary results indicated that xHTLs can be used in the ChemoG FRET sensor context, however, the signal-to-background

ratio of ChemoD sensors labeled with xHTLs in cells was very low and consequently hampered fluorescence lifetime measurements (data not shown).

3.4. Specificity and selectivity of current ChemoX biosensors

Cells are equipped with a diverse array of proteins and other biomacromolecules that enable them to sense changes in their external and internal environment, integrate these cues and ultimately adapt to them in an adequate manner. Inspired by these systems, researchers have utilized the sensing units of proteins for the development of fluorescent biosensors. While the use of naturally-occurring sensing units often provides sensors with affinity and specificity for the target analyte that is physiologically relevant, they tend to be promiscuous to structurally-related analytes.

I encountered similar problems during the development of the biosensors ChemoG-NAD and ChemoG-NMN. Both are based on a bacterial DNA ligase A (LigA) composed of two subdomains, 1a and 1b, that bind either NMN or the adenosine part of NAD⁺, respectively. The response of ChemoG-NAD was affected by millimolar concentrations of ATP, ADP and AMP, which is likely due to binding to the 1b domain *via* their adenosine moiety. Consequently, attempts to decrease the binding of these nucleotides to the 1b domain would inherently also decrease the binding of NAD⁺, making it difficult to optimize the selectivity of the sensor. Since ATP and ADP are present at much higher concentrations in cells than AMP, potential fluctuations in the free concentration of adenosine nucleotides could be corrected for by using fluorescent biosensors for ATP and ADP ratio. Furthermore, ChemoG-NAD was also sensitive to NAD⁺ precursors like NR or NMN or its reduced form NADH, albeit at substantially higher concentrations than their estimated intracellular concentrations¹¹⁰, and should therefore not interfere with the sensor response during live cell experiments. Other NAD⁺ biosensors, including the cpVenus-NAD¹⁰⁴ and FiNad¹⁴⁵ sensors, exhibit similar sensitivities towards structurally-related molecules and pH. Thus, for measurements of free NAD⁺ at a single subcellular localization, the previously developed

NAD-Snifit⁷⁶ might be better suited due to its insensitivity towards pH and structurally-related molecules.

During this study, the development of an NMN biosensor based on the same type of sensing unit (LigA) proved challenging because the intracellular concentration of NMN is estimated to be several orders of magnitude lower than NAD⁺. Rendering the LigA selective for NMN requires a binding affinity that is significantly higher for NMN than NAD⁺. However, through structural analysis of the engineered LigA, I could show that both nucleotides bind to the 1a domain exclusively *via* the NMN moiety. Thus, decreasing the binding of NAD⁺ would inherently compromise binding of NMN as well. In a parallel study, Chen and colleagues developed a bioluminescent biosensor for NMN based on the same LigA that I used for ChemoG-NMN¹⁴⁶. They engineered the LigA such that the 1a and 1b domains dimerize upon binding to NMN, analogously to the binding mechanism of ChemoG-NAD for NAD⁺. Surprisingly, their sensor response is reported to be not affected by NAD⁺, although they introduced only a single point mutation in the 1a domain at a position that, according to the crystal structure of this LigA mutant, is not involved in the binding of NMN. Consequently, the 1a domain should maintain its binding affinity for NAD⁺ also. A side-by-side comparison of this sensor together with ChemoG-NMN will be therefore helpful to verify their findings.

In retrospect, utilizing LigA as a sensing unit proved to be a challenging starting point for the development of an NMN biosensor. However, other naturally-occurring proteins that are known to bind NMN, such as CD38 or SARM1, exhibit similar binding affinities for NAD⁺ as well^{147, 148}, posing the same selectivity challenges as for LigA. Thus, strategies to identify, evolve or even generate proteins with high selectivity for the analyte of interest in a straightforward manner would greatly facilitate the development of novel biosensors. Directed evolution approaches like the yeast two-hybrid system allow for the rapid engineering of sensing units with high selectivity¹⁴⁹; however, they are limited to target analytes that are orthogonal to the cellular system in which they are being evolved.

Kang and colleagues recently developed a method that enabled the generation of single domain antibody (sdAb)-based heterodimerization systems for the small molecule cannabidiol¹⁵⁰. They

immobilized a biotinylated version of cannabidiol to identify a primary binder against the small molecule *via* phage surface display. The primary binder was subsequently produced and immobilized to identify a complementing binder that selectively binds in presence of the small molecule. By physically connecting the two binders, their small molecule-dependent dimerization could serve as sensing mechanism for an intramolecular FRET sensor, analogous to the 1a and 1b domains of LigA (**Figure 48a**). While this system could be applicable to other small molecules, including intracellular metabolites, the conjugation of a biotin or other affinity handles might not be straightforward or even accessible for every small molecule. Alternatively, the rapid progress in the design of *de novo* proteins using *in silico* modeling algorithms holds great promise for the development of biosensors (**Figure 48b**). Using such models, the lab of David Baker has recently generated biosensors for proteins and small molecules, demonstrating the potential of these approaches in creating new sensing units or even entirely new sensor architectures in a generalizable manner¹⁵¹⁻

155.

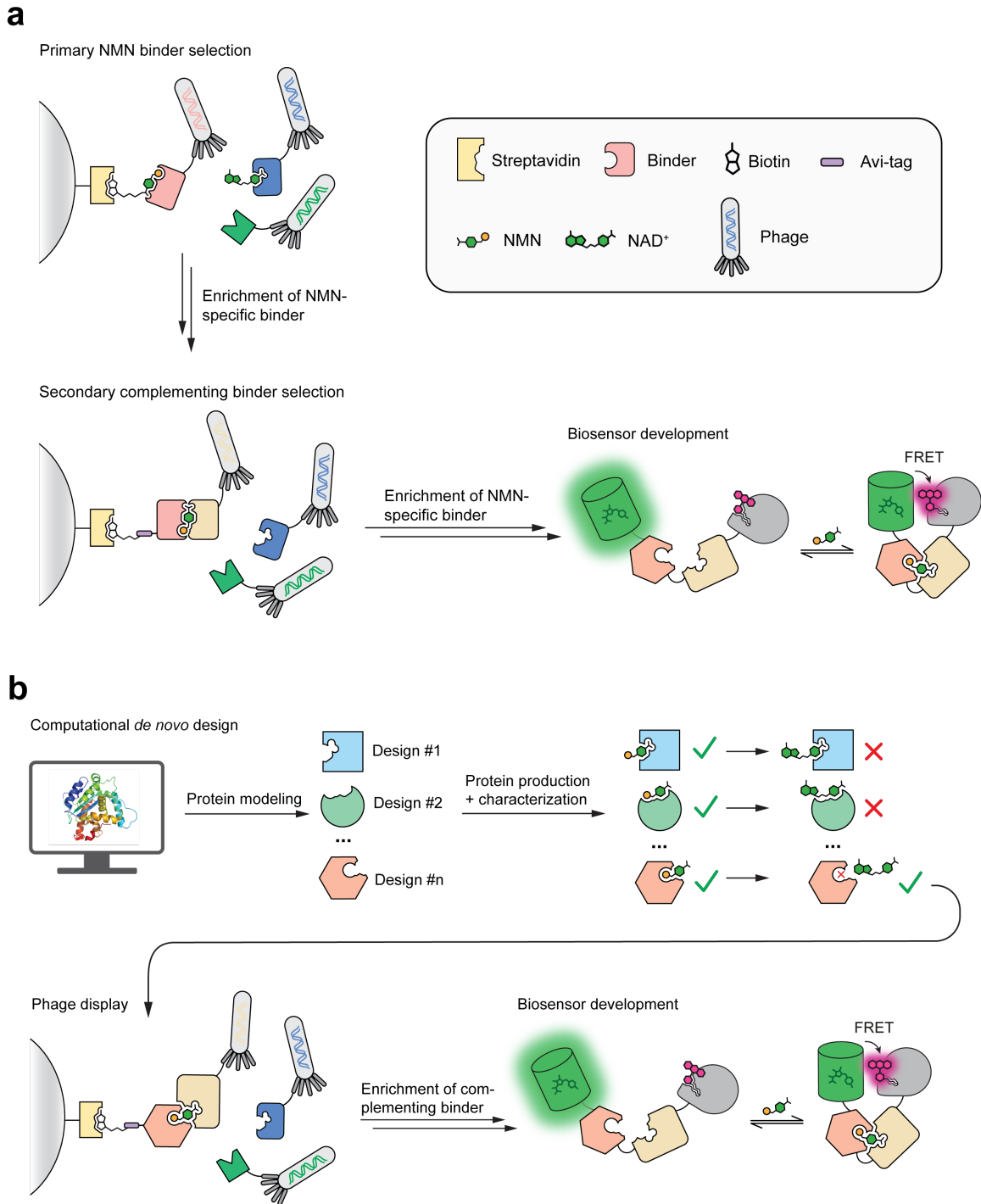


Figure 48 | Possible strategies to develop selective sensing units for biosensors.

a-b. Schematic representation of the development of selective NMN binders *via* phage surface display (**a**) or *via in silico* modeling of *de novo* NMN binding proteins (**b**).

In addition to promiscuous binding to structurally-related analytes, sensing units can be also influenced by other parameters, like pH or temperature^{156, 157}. These responses may have relevance in physiological contexts; however, they can introduce imaging artifacts, known as 'aliasing,' which may lead to false conclusions. Thus, it is crucial to minimize or correct for aliasing effects whenever possible. During the characterization of the ChemoX biosensors, I observed a noticeable pH- and temperature-dependent change in the response of several sensors. pH titrations of ChemoG1-5_{SIR} and data on the characterizations of the template biosensors from the literature suggested that these sensitivities are likely due to the sensing units rather than the FRET pair. During live cell experiments, artifacts caused by changes in intracellular pH or the ambient temperature can be corrected for by co-expressing a pH sensor and monitoring the ambient temperature, respectively. Ideally, one would engineer the biosensor to be more robust against these types of sensitivities. However, rational optimization of such properties is far from trivial. To address this issue, Koveal and colleagues devised a method that allows screening of thousands of sensor mutants evaluating multiple parameters, such as pH dependency and target binding affinity, simultaneously¹⁵⁸. Utilizing this method, they were able to develop a fluorescent biosensor for lactate with negligible pH sensitivity. Implementing similar approaches in the future could help to reduce the pH and temperature sensitivities of current ChemoX biosensors.

Finally, the expression of biosensors can interfere with cellular functions, for example, by sequestering the target analyte and thereby reducing its availability for cellular processes. This can lead to skewed experimental results that do not represent the physiological state of the cell. While this phenomenon, often referred to as 'buffering effect'¹⁵⁹, is negligible for analytes like NAD⁺ or ATP that are present at high concentrations inside cells, it becomes relevant for those present at concentrations comparable to or even below the concentration of the biosensor, such as Ca²⁺ or NMN. Reducing the effective sensor concentration using weak expression promoters or generating stable knock-ins of the sensor under control of low expression promoters can reduce such buffering effects. Additionally, performing functional assays that are related to the biological processes of the target analyte, cell viability and proliferation assays, or gene and protein expression analyses, can help to assess potential buffering effects.

3.5. Future *in vivo* applications of ChemoX biosensors

Fluorescent biosensors can be expressed in specific tissues or cell types in living organisms. Such an *in vivo* setting allows researchers to study the complexity of cellular processes in the physiologically most relevant context. For instance, one of the most frequently used sensor systems to interrogate neurological behavior *in vivo* is the GCaMP series⁵¹. These sensors are based on a circularly permuted GFP and were extensively optimized in the last decades for their application *in vivo*⁹¹. While GCaMP and other GFP-based sensors^{160, 161} paved the way for a better understanding of biological processes, especially in neurobiology, their spectral properties are suboptimal for deep tissue imaging. The use of two- or even three-photon fluorescence microscopy can enhance tissue penetration of the excitation laser, but often requires high laser powers and still faces limitations with regard to the emission wavelength of GFP.

To render the emission wavelengths of fluorescent biosensors more amenable to *in vivo* imaging purposes, red¹⁶² and even near-infrared¹⁴² FP-based sensors have been explored, albeit with greater challenges in their development⁵⁵. Furthermore, the recent emergence of chemogenetic designs based on SLPs and synthetic fluorophores offers biosensors with improved brightness in the far-red spectral range⁵⁹. The ChemoD biosensors that I developed in the course of this study, represent a promising alternative in this regard. However, compared to FP-based sensors that can be fully genetically encoded, SLP-based sensors need to be labeled with an externally administered fluorophore substrate. Moreover, comprehensive characterizations of rhodamine-based fluorophores revealed poor bioavailability of fluorophores with pronounced environmental sensitivity¹⁶³, such as JF₆₃₅, which are frequently used for the development of chemogenetic biosensors. Nevertheless, the less environmentally-sensitive fluorophore CPY showed great performance in the context of ChemoD-NAD and has recently been demonstrated as a promising fluorophore for *in vivo* applications¹⁶⁴. Thus, ChemoD biosensors hold promise for *in vivo* applications, although their performance in such settings has yet to be determined.

Bioluminescent biosensors present another avenue for *in vivo* imaging. They bypass the need for external laser excitation sources and exhibit higher signal-to-background ratios compared to fluorescence-based systems, thereby enabling non-invasive imaging in living animals. For instance, the

recent development of bioluminescent Ca^{2+} sensors based on a BRET pair between the luciferase NanoLuc and an RFP allowed tracking of Ca^{2+} waves in mouse brains^{165, 166}. Similarly, ChemoL biosensors have the potential to be used for non-invasive *in vivo* imaging purposes in the future. The far-red emission wavelengths of FRET acceptors that can be used with ChemoL sensors exhibit advantageous properties, as they allow deeper penetration through tissue. In this study, I tested only CPY as FRET acceptor; however, fluorophores with further red-shifted emission wavelengths and good bioavailability, such as JF₆₆₉, are conceptually compatible with this sensor design. Additionally, ChemoL sensors provide a ratiometric readout, which can correct for fluctuations in overall bioluminescence intensity. However, exogenous labeling of the FRET acceptor remains a potential limitation. Moreover, the overall signal intensity of bioluminescent biosensors is relatively weak compared to fluorescent biosensors due to restricted bioavailability of luciferase substrates, in particular in the brain. Ongoing efforts by different groups in developing new luciferase substrates as well as HT7 fluorophore substrates with improved bioavailability will enable the development of brighter and more robust sensors for non-invasive imaging *in vivo*, facilitating real-time tracking of cellular processes in freely moving animals.

Chapter 4 – Conclusion and Outlook

I successfully demonstrated the potential of the ChemoX design for both improving the dynamic range and diversifying the spectral properties of established FRET biosensors (*i.e.*, Ca^{2+} and ATP), and for developing new biosensors (*i.e.*, NAD^+ and NMN). The integration of HaloTag7 into the design provides spectral flexibility based on the inherent ability of self-labeling proteins to be conjugated with any fluorophore of choice. Future efforts may focus on implementing fluorescent proteins with improved spectral and photophysical properties, or orthogonal self-labeling proteins as FRET donor, to further expand the spectral versatility of the ChemoX FRET system. However, their successful implementation will depend on establishing a compatible interface with the FRET acceptor, given that the specific interface between ChemoX FRET pairs proved to be key for the generation of high efficiency FRET pairs and the development of biosensors with large dynamic ranges.

Notably, the ChemoX-ATP biosensors provide a ratiometric readout for monitoring intracellular ATP dynamics with unprecedented sensitivity and high spatiotemporal resolution.

The enhanced multiplexing capacity of ChemoX biosensors will facilitate their use in combination with other fluorescent or optogenetic tools, enabling simultaneous monitoring of cellular processes across diverse subcellular locations. This will advance our understanding of compartmentalization and its role in regulating cellular functions. In particular, the ChemoX-NAD biosensors hold great promise in this regard, as they enable multiplexing of free NAD^+ levels in different subcellular compartments, which was not possible with previously developed NAD^+ biosensors.

Moreover, the ability to adapt the readout of ChemoX FRET biosensors into fluorescence lifetime-based biosensors with far-red emission wavelengths, or into bioluminescent biosensors, holds promise for *in vivo* applications. Although the restricted bioavailability of current fluorophore and luciferase substrates might limit their use in such settings, ongoing efforts in developing substrates with improved pharmacokinetics may overcome these caveats in the future.

While ChemoX represents a powerful reporting unit for biosensors owing to its versatility and modularity, the performance of biosensors also relies on the robustness and specificity of the

coupled sensing unit. However, engineering sensing units with optimized properties can pose challenges, as I have demonstrated in this study as well as others in previous studies. Therefore, future efforts should focus on establishing strategies that enable the generation of robust and highly specific sensing units for a given target in a straightforward manner. Coupled with the ChemoX system, this would enable the development of high-performance biosensors for any analyte or biological activity of interest.

Materials and Methods

This section was adapted from Hellweg *et al.*⁷⁸

Reagents, chemicals and fluorophores

All reagents and chemicals used in the experiments are detailed in **Table M1**. Chloroalkane (CA) fluorophore substrates were obtained either *via* synthesis by Bettina Réssy and Dominik Schmidt (Max-Planck-Institute for Medical Research, Heidelberg, Germany) following protocols based on literature, generously provided by Dr. Alexey N. Butkevich (Max-Planck-Institute for Medical Research, Heidelberg, Germany) or Dr. Luke Lavis (Howard Hughes Medical Institute, Ashburn, VA, USA), or purchased from Promega. Detailed information regarding the fluorophore substrates is listed in **Table M2**. All fluorophore substrates were dissolved as 1 mM stock in water-free DMSO and prepared as small aliquots to reduce repetitive freeze-thaw cycles. Aliquots were stored at -20 °C and freshly thawed for all experiments.

Table M1 | Reagents and chemicals used for all experiments.

Adapted from Hellweg *et al.*⁷⁸

Reagent/chemical	Vendor	Catalogue number
KOD Hot Start Master Mix	Sigma-Aldrich	71842
Q5® Site-Directed Mutagenesis Kit	NEB	E0554S
QIAprep Spin Miniprep Kit	Qiagen	27106
GeneJET Endo-Free Plasmid-Maxiprep-Kit	ThermoFisher	K0861
Isopropyl-β-D-thiogalactopyranoside (IPTG)	Roth	CN084
Phenylmethylsulfonyl fluoride (PMSF)	ThermoScientific	36978
Lysozyme	ThermoScientific	89833
HisPur™ Ni-NTA Superflow Agarose	ThermoScientific	25217
4-20 % Mini Protean TGX stain-free gel	Bio-Rad	568094
Amicon® Ultra 4 mL Centrifugal Filters	Merck	UFC803024 (30 kDa) UFC805024 (50 kDa)
Glycerol	Merck	356350
Bovine serum albumin (BSA)	Roth	01634
4-(2-hydroxyethyl)-1-piperazineethanesulfonic acid (HEPES)	Sigma-Aldrich	H4034
Sodium chloride (NaCl)	Merck	106404
Dimethyl sulfoxide (DMSO)	Applichem	A36720100
Calcium chloride	Roth	A1191

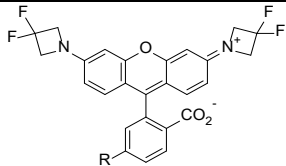
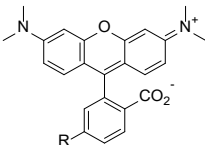
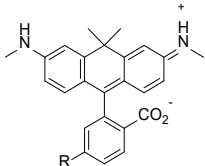
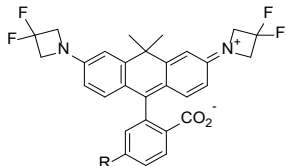
Materials and Methods

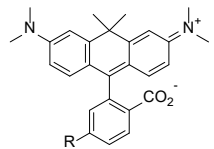
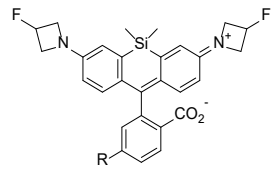
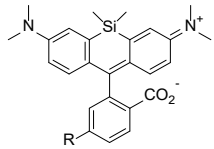
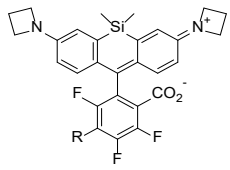
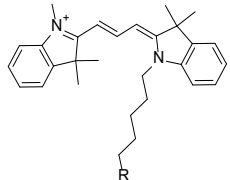
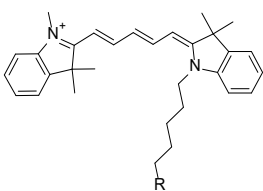
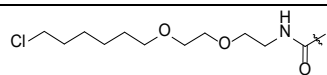
ethylene glycol-bis(β -aminoethyl ether)-N,N,N',N'-tetraacetic acid (EGTA)	Sigma-Aldrich	E4378
Calcium Calibration buffer Kit #1	Life technologies	C3008MP
SPG pH 4.0 - 1 M buffer	Jena Bioscience	CSS-389
SPG pH 10.0 - 1 M buffer	Jena Bioscience	CSS-390
Histamine	Sigma-Aldrich	H7250
Ionomycin	Sigma-Aldrich	I9657
cOmplete™ Protease inhibitor cocktail	Roche	11836153001
CelLytic™ M	Sigma-Aldrich	C2978
1x PBS pH 7.4	Gibco	10010015
1x HBSS with calcium and magnesium	Corning	21-023-CMR
TrypLE™ Express	Gibco	12604013
DMEM high glucose +GlutaMAX™	Gibco	31966021
DMEM high glucose, phenol red-free	Gibco	31053028
DMEM no glucose, phenol red-free	Gibco	A1443001
Sodium pyruvate (100x)	Gibco	11360070
GlutaMAX™ Supplement (100x)	Gibco	35050038
Fetal bovine serum (FBS, heat-inactivated)	Gibco	10500064
Opti-MEM™, reduced serum	Gibco	31985047
Lipofectamine 3000 Transfection Reagent	Invitrogen	L3000001
Lipofectamine RNAiMAX Transfection Reagent	Invitrogen	13778150
Adenosine-5'-triphosphate (ATP) magnesium salt	Sigma-Aldrich	A9187
Adenosine-5'-diphosphate (ADP) disodium salt	Sigma-Aldrich	1897
Adenosine-5'-monophosphate (AMP) sodium salt	Sigma-Aldrich	A1752
Guanosine-5'-triphosphate (GTP) sodium salt	Sigma-Aldrich	10106399001
2-Deoxy-D-glucose (2DG)	TCI Chemicals	D0051
D-glucose monohydrate	Roth	6780
Nicotinamide (NAM)	Sigma-Aldrich	72340
Nicotinamide riboside (NR)	Combi-Blocks	HB-5832
Nicotinamide mononucleotide (NMN)	Sigma-Aldrich	N3501
Nicotinamide adenine dinucleotide (NAD ⁺)	Roche	10127965001
Nicotinamide adenine dinucleotide phosphate (NADP ⁺)	Roth	AE13.3
Nicotinamide adenine nucleotide, reduced (NADH)	Roth	AE12.2
Nicotinic acid adenine dinucleotide (NAAD ⁺)	Sigma-Aldrich	N4256
FK866	Selleckchem	S2799
N-methyl-N'-nitro-N-nitrosoguanidine (MNNG)	Biozol	N529925
MitoTracker™ Red FM	Invitrogen	M22425
Hoechst 33342	Invitrogen	H3570

Penicillin-Streptomycin (Pen/Strep)	Gibco	15140122
NanoBRET™ Nano-Glo Substrate	Promega	N157C
Extracellular NanoLuc® Inhibitor	Promega	N235A
Nano-Glo™ Substrate	Promega	N113B
DL-2-Amino-5-phosphonovaleric acid (APV)	SantaCruz	sc-201503
NBQX disodium salt	Sigma-Aldrich	N183
SYBR® Green Quantitative RT-PCR Kit	Sigma-Aldrich	QR0100
Black non-binding flat bottom 96 well plates	Perkin Elmer	6005720
Black low volume flat bottom 384 well plates	Corning	3820
White non-binding flat bottom 96 well plates	Perkin Elmer	6005290
White 96 well plate, cell culture treated	BrandTech	782090
White low volume flat bottom 384 well plates	Corning	3824
Black 96 well glass bottom imaging plate	IBL, Cellvis	P96-1.5H-N
Black 24 well glass bottom imaging plate	IBL, Cellvis	P24-1.5H-N

Table M2| Chloroalkane fluorophore substrates used in all experiments.

Adapted from Hellweg *et al.*⁷⁸ Ex_{max} = maximum excitation wavelength. Em_{max} = maximum emission wavelength.

Number	Structure	Name	Ex _{max} /Em _{max} [nm]	Source, reference
1		JF ₅₂₅ -CA	525/549	Gift from Dr. Luke Lavis, HHMI, Ashburn, VA, USA ¹⁶³
2		TMR-CA	548/572	Purchased from Promega, Madison, WI, USA ⁸¹
3		580CP-CA	582/607	Gift from Dr. Alexey N. Butkevich, Max-Planck-Institute for Medical Research, Heidelberg, Germany ¹⁶⁷
4		JF ₅₈₅ -CA	585/609	Gift from Dr. Luke Lavis, HHMI, Ashburn, VA, USA ¹⁶³

5		CPY-CA	606/626	Butkevich <i>et al.</i> ¹⁶⁸
6		JF ₆₃₅ -CA	635/652	Gift from Dr. Luke Lavis, HHMI, Ashburn, VA, USA ¹⁶³
7		SiR-halo (=SiR-CA)	643/662	Lukinavicius <i>et al.</i> ³⁸
8		JF ₆₆₉ -CA	669/682	Gift from Dr. Luke Lavis, HHMI, Ashburn, VA, USA ¹⁶³
9		Cy3-CA	554/568	Wilhelm and Kuehn <i>et al.</i> ⁴⁵
10		Cy5-CA	649/666	Wilhelm and Kuehn <i>et al.</i> ⁴⁵
<hr/> <p>R =  Chloroalkane (CA), JF = Janelia Fluor.</p>				

Plasmids and cloning

All oligonucleotides that were used for molecular cloning were purchased from Sigma-Aldrich. Synthetic genes were obtained from Eurofins or Integrated DNA Technologies. The KOD Hot Start Master Mix (Sigma-Aldrich, Merck) was used for PCRs according to the manufacturer's protocol. PCR-amplified products were analyzed via standard agarose gel electrophoresis to verify correct size of the DNA. Gibson assembly¹⁶⁹ served as the standard method for molecular cloning procedures. Oligonucleotides for Gibson assembly-based molecular cloning were designed with 24 bp overhangs. Transformation of assembled plasmid DNA into electrocompetent *Escherichia coli* (*E. coli*) strain E. cloni 10G (Novagen) was achieved via standard electroporation.

Oligonucleotides for site-directed mutagenesis were designed based on the online tool NE-BaseChanger (<https://nebasechanger.neb.com/>) and used together with the Q5[®] Site-Directed Mutagenesis Kit (NEB) according to the manufacturer's protocol, including transformation of DNA into chemically competent *E. coli* strain NEB 5-alpha (NEB) via heat-shock. Cloned Plasmids were amplified by inoculation of 5 mL lysogeny broth (LB) medium, supplemented with 100 µg/mL Ampicillin (LB-Amp), with single colonies of transformed *E. coli* and grown at 37 °C shaking at 220 rpm. Plasmid DNA was extracted using the QIAprep Spin Miniprep Kit (Qiagen) according to the manufacturer's protocol. pAAV plasmids used for the production of adeno-associated viruses (AAVs) were amplified following a modified protocol (see below). Correct DNA sequences were validated by Sanger sequencing (Eurofins). Plasmid DNA was stored in Milli-Q[®] water at -20 °C until further use.

Constructs intended for subsequent protein expression in *E. coli* were cloned into a pET-51b(+) vector (Novagen) backbone, flanked either by 1) an N-terminal Strep-tag[®]II and enterokinase cleavage sequence plus a C-terminal poly-histidine (10x His) tag or 2) an N-terminal 10x His tag followed by a tobacco etch virus (TEV) cleavage sequence (ENLYFQG). Protein sequences are detailed in Supplementary Table XX.

Constructs intended for subsequent expression in HeLa Kyoto or U-2OS cells were cloned into a pCDNA5/FRT or pCDNA5/FRT/TO vector (ThermoScientific). If applicable, the constructs were flanked by N- and/or C-terminal localization sequences for targeted expression at specific subcellular localizations (localization sequences are listed in *Protein sequences*). Codons of constructs containing redundant sequences or sequences with high sequence similarity (*e.g.*, EBFP2 and EGFP) were adapted to reduce undesired recombination events between the sequences. A T2A self-cleaving peptide sequence¹⁷⁰ was used for co-translational expression of multiple constructs. YC 3.6⁶⁵ was reconstructed by molecular cloning from Yellow Cameleon-Nano140 (Addgene plasmid #519668, kind gift of Takeharu Nagai) and subcloned into the pET-51b(+) vector. ATeam 1.03 was subcloned from Addgene plasmid #51958 (kind gift Takeharu Nagai) into the pET-51b(+) vector.

Constructs intended for expression in hippocampal rat neurons were cloned into a pAAV2-hSyn vector (Addgene plasmid #1010612, kind gift from E. Schreiter). The constructs were flanked by an N-terminal nuclear export signal (NES) sequence (for sequence information see *Protein*

sequences). pAAV2-hSyn plasmids were cloned and amplified in *E. coli* strain NEB stable (NEB) grown at 30 °C in Erlenmeyer flasks. Plasmid DNA was extracted using the GeneJET Endo-Free Plasmid-Maxiprep-Kit (ThermoFisher) following the manufacturer's manual. Intact open reading frame and inverted terminal repeat sequences were verified by Sanger sequencing (Eurofins). Plasmid DNA was then used for downstream production of recombinant AAV (rAAV) particles.

Protein production

E. coli strain BL21 (DE3)-pLysS (Sigma-Aldrich) was transformed with plasmid DNA via electroporation. 5 mL LB-Amp medium was inoculated with transformed bacteria and grown o.n. at 37 °C and 220 rpm shaking. O.n. cultures were diluted 1:200 in 0.1-1 L LB-Amp (in 0.5-5 L flasks). The main cultures were grown at 37 °C and 220 rpm until reaching an optical density at 600 nm (OD₆₀₀) of 0.6-0.8. The temperature was downregulated to 16 °C and 0.5 mM isopropyl- β -D-thiogalactopyranoside (IPTG) was added to induce protein expression. The cultures were grown for 20-24 h before harvesting the cells by centrifugation at 4,500 g and 4 °C for 10 min. All subsequent steps were performed on ice unless stated otherwise. Cell pellets were resuspended in 30 mL ice-cold lysis buffer supplemented with 1 mM phenylmethylsulfonyl fluoride (PMSF) and 250 μ g/mL lysozyme. See **Table M3** for detailed information on buffers used for protein purification. Cell suspensions were sonicated for 7 min (50 % on/off cycles, 70 % amplitude, SONOPULS Bandelin) to extract proteins from bacteria via cell lysis. Cell debris were cleared by centrifugation at 10,000 g and 4 °C for 15 min. Purification of 10x His-tagged proteins was achieved by incubation of cleared cell lysates with 0.5-1 mL Ni-NTA resin (HisPur™ Ni-NTA Superflow Agarose, ThermoScientific) for 1 h at 4 °C on a roller shaker. The Ni-NTA beads were then washed with 10 column volumes ice-cold wash buffer in 5 mL polypropylene columns. 10x His-tagged proteins were eluted with 1.5 mL ice-cold elution buffer. Finally, the elution buffer was exchanged with ice-cold Activity buffer using Amicon Ultra Centrifugal Filters (Millipore) with an appropriate molecular weight cutoff.

Concentration of purified proteins was determined based on the Lambert-Beer law. The absorbance at 280 nm (A₂₈₀) was measured using a Nanodrop 2000c spectrophotometer (pathlength = 0.1 cm). The extinction coefficient at 280 nm for the different proteins was extrapolated from the amino acid sequence using the Geneious software. Protein purity was confirmed by standard SDS-

PAGE using 4–20 % Mini-PROTEAN TGX Stain-free Precast Protein Gels (BioRad). Purified proteins were prepared as 45 % (w/v) glycerol stocks and stored at -20 °C until further use.

Table M3 | Buffers used for protein purification.

Buffer	Composition
Extraction buffer	50 mM KH ₂ PO ₄ , 300 mM NaCl, 5 mM imidazole, pH 8.0
Wash buffer	50 mM KH ₂ PO ₄ , 300 mM NaCl, 10 mM imidazole, pH 7.5
Elution buffer	50 mM KH ₂ PO ₄ , 300 mM NaCl, 500 mM imidazole, pH 7.5
Activity buffer	50 mM HEPES, 50 mM NaCl, pH 7.3
2x Laemmli buffer	31.5 mM Tris-HCl, 1% SDS, 0.005 % Bromophenol blue, 10 % glycerol, pH 6.8
TEV buffer	25 mM Na ₂ HPO ₄ , 200 mM NaCl, pH 8.0

Protein crystallization

HaloTag7, ChemoG1, ChemoG5 and the Ligase A mutant from *Enterococcus faecalis* were produced and purified as described in *Protein production*. Afterwards, 6x His tag-purified proteins were diluted in 40 mL (final volume) TEV cleavage buffer (see **Table M3**) and 10x His-tagged TEV protease was added at a 30:1 ratio (mg protein of interest (POI): mg TEV). The mix was incubated o.n. at 4 °C to cleave the N-terminal 10x His-TEV sequence. On the next day, the mix was filtered (0.22 µm filter) and run on a HisTrap FF crude column (Cytiva) using an ÄktaPure FPLC (Cytiva). Non-cleaved POI and the TEV protease were retained by the resin while the cleaved POI was collected from the flow-through. Size exclusion chromatography of the cleaved POI was performed on a HiLoad 26/600 Superdex 75 pg column (Cytiva) together with a buffer exchange into Activity buffer. Purified HaloTag7, ChemoG1 and ChemoG5 were labeled at 5 µM protein concentration with 10 µM CA fluorophore substrate (ChemoG1+5 with TMR-CA, HaloTag7 with Cy3-CA) for 4 h at room temperature (RT). The labeled proteins (*i.e.*, HaloTag7_{Cy3}, ChemoG1_{TMR} and ChemoG5_{TMR}) and the eLigAⁱ(V69R-Y151R) were concentrated to 10 – 20 mg/mL.

The eLigAⁱ(V69R-Y151R) was supplemented with 1 mM NAD⁺ or 1 mM NMN prior to crystallization. Crystallization was carried out using the vapor-diffusion method at 20 °C. Initial

crystallization screening was performed with a Mosquito LCP crystallization robot (TTP Lab-Tech, Melbourn, UK) using commercial sparse-matrix crystallization screens. The screens were set up by mixing 100 nl of protein solution and 100 nl reservoir solution in 96-well sitting-drop plates. Identified crystallization conditions were optimized in 24-well crystallization plates using hanging-drop technique. Crystals of efLigAⁱ(V69R-Y151R) with NMN were grown by mixing protein solution supplemented with 1 mM NMN and a reservoir solution containing 0.1 M MES pH 6.0, 1.0 M lithium chloride, 18 % (m/v) PEG 6000 at a 1:1 ratio. Crystals of efLigAⁱ(V69R-Y151R) in complex with NAD⁺ were obtained by mixing equal volumes of protein solution containing 1 mM NAD⁺ and precipitant solution composed of 0.2 M disodium tartrate, 20 % (m/v) PEG 3350. Crystals of efLigAⁱ(V69R-Y151R) with NMN were briefly washed in cryoprotectant solution consisting of the reservoir solution supplemented with 20 % (v/v) glycerol before flash-cooling in liquid nitrogen. Crystals of efLigAⁱ(V69R-Y151R) with NAD⁺ were rinsed in the reservoir solution supplemented with 20 % (v/v) ethylene glycol, prior to flash-cooling in liquid nitrogen.

Crystals of HaloTag7_{Cy3} were grown by mixing equal volumes of protein solution and a reservoir solution containing 0.2 M magnesium acetate, 19 % (m/v) PEG 3350. Crystals of ChemoG1_{TMR} and ChemoG5_{TMR} were obtained by mixing equal volumes of protein solution and precipitant solution composed of 0.085 M Tris-HCl pH 8.5, 0.17 M sodium acetate, 15 % (v/v) glycerol, 27 % (m/v) PEG 4000 or 0.1 M Tris-HCl pH 8.5, 0.2 M magnesium chloride, 30 % (m/v) PEG 4000, respectively. Crystals of HaloTag7_{Cy3} and ChemoG5_{TMR} were briefly washed in cryoprotectant solution consisting of the reservoir solution supplemented with 20 % (v/v) glycerol before flash-cooling in liquid nitrogen, whereas crystals of ChemoG1_{TMR} were flash-cooled directly in the mother liquor.

X-ray diffraction data collection and structure determination

Single crystal X-ray diffraction data were collected at 100 K on the X10SA beamline at the SLS (PSI, Villigen, Switzerland). All data were processed with XDS. The structure of HaloTag7_{Cy3} was determined by molecular replacement (MR) using Phaser and HaloTag7_{TMR} coordinates (PDB ID: 6Y7A) as a search model. The structure of ChemoG1_{TMR} was determined using HaloTag7_{TMR} (PDB ID: 6Y7A) and GFP (PDB ID: 1GFL) coordinates, the ChemoG1_{TMR} model was used to determine the ChemoG5_{TMR} structure. Geometrical restraints for Cy3 and TMR ligands were

generated using the Grade server. The structure of eFLigAⁱ(V69R-Y151R) with bound NMN was determined by molecular replacement (MR) with Phaser using the adenylation domain of *Enterococcus faecalis* ligase (PDB: 1TA8) coordinates as a search model. The structures of eFLigAⁱ(V69R-Y151R) with bound NAD⁺ was determined using the eFLigAⁱ(V69R-Y151R):NMN model. The final models were optimized in iterative cycles of manual rebuilding using Coot and refinement using Refmac5 and phenix.refine. Data collection and refinement statistics are summarized in Methods **Table M4**, model quality was validated with MolProbity16 as implemented in PHENIX.

Atomic coordinates and structure factors have been deposited in the Protein Data Bank (PDB) under accession codes: 8B6R (HaloTag7_{Cy3}), 8B6S (ChemoG1_{TMR}), 8B6T (ChemoG5_{TMR}). Refined crystal structures were analyzed and represented using the software PyMol.

Ilme Schlichting is acknowledged for X-ray data collection. Diffraction data were collected at the Swiss Light Source, beamline X10SA, of the Paul Scherrer Institute, Villigen, Switzerland.

Table M4 | Data collection and refinement statistics.

	HaloTag7 _{Cy3} 8B6R	ChemoG1 _{TMR} 8B6S	ChemoG5 _{TMR} 8B6T	<i>EFLigA</i> -V69R NMN bound	<i>EFLigA</i> -V69R NAD ⁺ bound
Data collection					
Space group	<i>P4</i> ₂ <i>2</i> ₁ <i>2</i>	<i>P1</i>	<i>P1</i> ₂ <i>1</i>	<i>C222</i> ₁	<i>C121</i>
Unit-cell parameters					
<i>a</i> , <i>b</i> , <i>c</i> (Å)	112.56, 112.56, 44.33	46.19, 63.71, 89.42	46.60, 64.04, 172.95	49.24, 104.75, 135.63	90.67, 86.88, 57.17
<i>α</i> , <i>β</i> , <i>γ</i> (°)	90.00, 90.00, 90.00	93.56, 91.02, 90.85	90.00, 97.67, 90.00	90.00, 90.00, 90.00	90.00, 100.69, 90.00
Radiation source	PXII-X10SA, SLS	PXII-X10SA, SLS	PXII-X10SA, SLS	PXII-X10SA, SLS	PXII-X10SA, SLS
Wavelength (Å)	0.99988	0.99996	0.99992	0.99988	0.99988
Temperature (K)	100	100	100	100	100
Resolution range (Å)	50-1.50 (1.60-1.50)	50-1.80 (1.90-1.80)	50-2.00 (2.10-2.00)	50-1.70 (1.80-1.70)	50-2.00 (2.10-2.00)
No. of observed reflections	341056 (60343)	182229 (26711)	216345 (30251)	255656 (38826)	200411 (26793)
No. of unique reflections	46121 (7965)	89852 (13310)	66470 (9089)	38964 (6039)	29017 (3905)
Multiplicity	7.4 (7.6)	2.0 (2.0)	3.3 (3.3)	6.6 (6.4)	6.9 (6.9)
Completeness (%)	99.9 (99.9)	95.3 (94.3)	97.0 (97.8)	99.9 (99.9)	98.4 (97.5)
<i>R</i> _{merge} (%)	6.8 (65.7)	4.1 (40.0)	8.6 (41.0)	5.7 (47.5)	10.9 (63.5)
<i><I/σ(I)></i>	18.2 (3.4)	12.0 (2.1)	8.5 (3.4)	17.5 (3.7)	13.4 (3.6)

Materials and Methods

CC _{1/2} (%) [#]	99.9 (90.2)	99.8 (75.2)	99.5 (87.4)	99.9 (90.4)	99.8 (89.3)
Refinement					
Molecules per a.u.	1	2	2	1	1
No. of reflections	46120	89842	66470	38961	29014
No. of reflections in test set	2306	4492	3399	1949	1451
Resolution range (Å)	41.25-1.50	46.18-1.80	46.18-2.00	37.24-1.70	34.36-2.00
No. of non-hydrogen atoms					
Protein	2365	8273	8276	2568	2535
Ligand/ion	72	146	134	27	44
Water	297	460	308	280	269
Total	2734	8879	8718	2875	2848
<i>R</i> (%)	16.20	17.28	22.06	18.66	18.19
<i>R</i> _{free} (%)	19.19	20.08	24.51	21.71	20.36
RMS deviations from ideal					
bonds (Å)	0.013	0.007	0.002	0.008	0.002
angles (°)	1.229	1.094	0.779	0.944	0.491
<i>B</i> -factors (Å ²)					
Protein	14.80	26.03	20.62	26.92	26.44
Ligand/ion	23.87	22.14	17.73	28.58	41.74
Water	24.40	29.14	19.67	34.76	31.86
Average	16.08	26.13	20.54	27.70	27.19
Wilson B (Å ²)	14.42	24.95	22.88	25.81	24.84
Ramachandran statistics (%)					
favored regions	95.9	97.5	96.8	99.0	98.4
allowed regions	4.1	2.5	3.2	1.0	1.6
disallowed regions	0	0	0	0	0
Clashscore	1.04	1.33	3.03	1.74	0.59

[#]as implemented in XDS¹⁷¹. Values in parentheses are for the highest resolution shell.

Fluorescence spectroscopy measurements

All fluorescence-based measurements using recombinant proteins were carried out in black non-binding flat bottom 96 well plates (Perkin Elmer) at 100 µL final volume or in black low-volume flat bottom 384 well plates (Corning) at 20 uL final volume. Proteins were prepared in Activity buffer supplemented with 0.2 mg/mL BSA unless stated differently. FRET-based measurements were performed at protein concentrations between 50–200 nM. If applicable, the proteins were incubated with 2 molar equivalents of CA fluorophore substrates for 1 h at RT to label HaloTag7. Measurements based on the fluorescence intensity change of directly excited CA fluorophores

(*e.g.*, ChemoD-NAD_{SiR}) were performed at 200 nM CA fluorophore substrate concentration in the presence of 1 μ M HaloTag7-based proteins (to ensure that all of the CA fluorophore substrate is labeled).

Measurements were performed at 37 °C using a Multimode Spark 20M microplate reader (Tecan) with built-in monochromators, unless stated differently. Flash numbers, gain, excitation and emission wavelengths were adjusted depending on the fluorescent protein and CA fluorophore substrate. Bandwidths of excitation and emission were set to 20 nm and 10 nm, respectively. For the acquisition of fluorescence emission spectra, the step size was set to 2 nm. Detailed settings regarding excitation and emission wavelengths can be found in **Table M5**. Pipetted multi well plates were temperature-equilibrated for 15 min inside the temperature-adjusted Tecan before the measurement.

Table M5 | Tecan settings used for fluorescence-based measurements.

Adapted from Hellweg *et al.*⁷⁸ FI = fluorescence intensity.

Fluorescent protein/fluorophore	Max. emission wavelength	Excitation wavelength	Emission wavelength range	Type of measurement
EBFP2	446 nm	360 nm	400-800 nm	FRET
mCerulean3	474 nm	400 nm	440-800 nm	FRET
EGFP	510 nm	440 nm	480-800 nm	FRET
Venus	528 nm	460 nm	494-800 nm	FRET
mKO2	566 nm	510 nm	550-800 nm	FRET
TagRFP	584 nm	510 nm	550-800 nm	FRET
mRuby2	594 nm	510 nm	550-800 nm	FRET
mRuby3	594 nm	510 nm	550-800 nm	FRET
mScarlet	594 nm	520 nm	560-800 nm	FRET
mCherry	610 nm	530 nm	570-800 nm	FRET
YC 3.6	474/528 nm	400 nm	440-650 nm	FRET
ATeam 1.03	474/528 nm	400 nm	440-650 nm	FRET
CPY	628 nm	580 nm	610-750 nm	FI
JF ₆₃₅	662 nm	610 nm	640-750 nm	FI
SiR	666 nm	610 nm	640-750 nm	FI

Luminescence spectroscopy measurements

All luminescence-based measurements using recombinant sensor proteins were carried out in white non-binding flat bottom 96 well plates (Perkin Elmer) at 100 μ L final volume or in white low-volume flat bottom 384 well plates (Corning) at 20 μ L final volume. Proteins were prepared in Activity buffer supplemented with 0.2 mg/mL BSA unless stated differently. 200 nM sensor protein was labeled with 2 molar equivalents of CPY-CA (400 nM) for 1 h at RT. Luminescence measurements were performed at final protein concentrations of 500 pM in the presence of Nano-Glo Luciferase Assay Substrate (Promega) diluted 1:1000. For live cell experiments, 1:1000 diluted cell-impermeable NanoLuc inhibitor (Promega) was added to the medium to prevent undesired luminescence signal from sensors derived from dead or lysed cells.

All luminescence-based measurements were performed at 37 °C using a Multimode Spark 20M microplate reader (Tecan) with built-in luminescence module. Pipetted multi well plates were temperature-equilibrated for 15 min inside the temperature-adjusted Tecan before the measurement. Luminescence emission spectra were recorded from 398-653 nm with a step size of 15 nm and an integration time of 200 ms. For live cell experiments, luminescence was acquired for the FRET donor (EGFP) between 505-530 nm and the FRET acceptor between 625-650 nm.

Analysis of biosensor response to varying concentrations of analytes

Analytes were dissolved in Activity buffer supplemented with 0.2 mg/mL BSA as 10x stock solutions of the final concentration used in the titration experiment. 10x stock solutions were serially diluted to obtain 10x solutions at different analyte concentrations. 10x solutions were added to prepared protein solutions inside the multi well plate to reach 1x analyte concentrations. For titrations in presence of competing analytes, the competing analyte (*e.g.*, NAM) was added to the Activity buffer in which the analyte of interest (*e.g.*, NAD⁺) was serially diluted.

Calcium titrations

Precise calcium concentrations were adjusted with the Calcium Calibration Buffer Kit (Life technologies) following the manufacturer's manual. The dissociation constant K_D EGTA used for the calculation of free calcium was set to 107.9 nM, based on the experimental conditions (pH 7.2 and 37 °C). Calcium biosensors were prepared at 10x concentrations (2 μ M) and diluted to 1x concentrations (200 nM) in the respective calcium calibration buffer.

pH sensitivity assay

Two sodium phosphate buffers (SPG pH 4.0 & 10.0, both 1 M, Jena Bioscience) were mixed to adjust different pH (5.5-8.0) by mixing the buffers in specific ratios following the manufacturer's manual. The prepared pH buffer solutions were diluted 10-fold (0.1 M final concentration), and supplemented with 0.2 mg/mL BSA and 50 mM NaCl. Proteins were prepared at 10x concentrations (2 μ M) and diluted to 1x final concentrations (200 nM) in the respective pH buffer.

Determination of the FRET efficiency

The fraction of FRET donor fluorescence intensity (FI) quenched in the presence of FRET acceptor was used to calculate the FRET efficiency (E) based on the following equation:

$$E = 1 - \frac{FI_{DA}}{FI_D} \quad (1)$$

where FI_{DA} and FI_D represent the maximum FI values of the FRET donor in presence or absence of the FRET acceptor, respectively.

Determination of the spectral overlap

R_0 is the Förster radius which was calculated using the following equation:

$$R_0 = 0.211 \sqrt[6]{\kappa^2 \times n^{-4} \times \Phi_D \times J(\lambda)} \quad (2)$$

where κ is the orientation factor (set to 0.667), n is the refractive index (set to 1.33), Φ_D is the quantum yield of the donor and $J(\lambda)$ is the spectral overlap of the FRET donor emission and FRET acceptor excitation spectra, which was calculated using the following equation:

$$J(\lambda) = \frac{\int_0^\infty F_D(\lambda) \times \epsilon_A(\lambda) \times \lambda^4 d\lambda}{\int_0^\infty F_D(\lambda) d\lambda} \quad (3)$$

where F_D is the normalized FRET donor fluorescence emission at the wavelength λ , $\epsilon_A(\lambda)$ is the extinction coefficient of the FRET acceptor at the wavelength λ . Spectral overlaps were determined using the software [a|e Fluortools](#). The excitation and emission spectra were loaded into the software for calculation of the spectral overlap. Excitation spectra were normalized to the maximum extinction coefficient of the respective fluorophore.

Determination of the FRET ratio and FRET ratio changes

FRET ratios (R), defined as the ratio of FRET acceptor signal divided by FRET donor signal (*e.g.*, FRET_{SIR}/EGFP), were determined based on the FI or luminescent intensity (LI) values at the maximum emission wavelengths of the FRET donor and acceptor. FRET ratio changes (R/R₀) were determined by dividing the FRET ratio R at a given concentration of analyte or time by the FRET ratio R₀ at the lowest analyte concentration or time = 0 min. To plot the FRET ratio changes against analyte concentration or time, the FRET ratio changes were calculated on the following equation:

$$\Delta R/R_0 = \frac{R}{R_0} - 1 \quad (4)$$

The dynamic range of a given biosensor was defined as the maximum FRET ratio change (^{max}ΔR/R₀) using the FRET ratio R at saturating concentration of the analyte.

Determination of fluorescence intensity changes

FI changes (FI/FI₀) were determined by dividing the FI at a given concentration of analyte or time by the fluorescence intensity FI₀ at the lowest analyte concentration or time = 0 min. To plot the FI changes against analyte concentration or time, the FI changes were calculated on the following equation:

$$\Delta FI/FI_0 = \frac{FI}{FI_0} - 1 \quad (5)$$

The dynamic range of a given biosensor was defined as the maximum FI change (^{max}ΔFI/FI₀) using the fluorescence intensity FI at saturating concentration of the analyte.

Data processing and fitting

Acquired data were mathematically processed using the Excel software (Microsoft) and subsequently inserted in GraphPad Prism (version 10.1.1). For titration experiments, the processed data was used to fit a sigmoidal dose response based on the following equation:

$$Y = \text{Bottom} + \frac{x^H * (\text{Top} - \text{Bottom})}{x^H + C50^H} \quad (6)$$

where Y is the response (R, ΔR/R₀, FI, ΔFI/FI₀, τ or Δτ), Bottom and Top are the lower and upper plateau of the response, respectively, x is the analyte concentration, H is the Hill coefficient

and C_{50} is the analyte concentration at which the response is half-maximal. Graphs representing the calculated and fitted data were created using the GraphPad Prism software (version 10.1.1).

Cell culture

All cell experiments, except the electric field stimulation of neurons, were performed using HeLa Kyoto (RRID:CVCL_192219) or U-2 OS Flp-In T-REx cells. These cells were cultured in high glucose (4.5 g/L) DMEM + GlutaMAX™ medium (Gibco) supplemented with 10 % heat-inactivated FBS (Gibco). Cells were maintained at 37 °C and 5 % CO₂ in a humidified cell culture incubator. Stringent sterile procedures were followed during cell handling, conducted within a laminar flow hood. Cultures were passaged every 2-4 days or upon reaching confluency, with a maximum culture period of 4 weeks. Regular PCR assays were performed to monitor for Mycoplasma contamination, with no evidence of contamination detected throughout the study.

Generation of stable cell lines

The Flp-In T-REx system¹⁷² was used for the generation of cell lines stably expressing proteins of interest (POI). U-2 OS Flp-In T-REx cells were seeded in a T-25 cell culture dish. At 80 % confluency, the cells were co-transfected with a pCDNA5/FRT or pCDNA5/FRT/TO plasmid encoding the POI and the plasmid pOG44 (Invitrogen), encoding the Flp recombinase, in a 1:10 ratio (POI:pOG44, total 4 µg DNA). Transfections were performed using the Lipofectamine 3000 Transfection Reagent (Invitrogen) following the manufacturer's manual. Transfected cells were replenished with fresh cell culture medium supplemented with 100 µg/mL Hygromycin B (ThermoScientific) 14-16 h post transfection. This allowed selection of cells that integrated the transfected plasmid stably into the genome. 48 h after addition of the selection medium, cells were replenished with fresh cell culture medium and grown to confluency. To obtain a pool of cells with homogenous expression levels, selected cells were sorted by fluorescence-activated cell sorting (FACS) using a FACSMelody Cell sorter (BD Biosciences). Cells were sorted either for EGFP fluorescence (blue laser, excitation: 488 nm, emission: 530/30 BP filter) or for SiR fluorescence (red laser, excitation: 640 nm, emission: 660/10 BP filter) after o.n. labeling with SiR-CA. Selected cells that were transfected with a pCDNA5/FRT/TO plasmid, were additionally incubated with 200 ng/mL doxycycline 24 h before sorting to induce expression of the POI.

Transfection and labeling of HeLa Kyoto and U-2 OS Flp-In T-REx cells

Cells were grown to 80 % confluency for the day of transfection. pCDNA5/FRT or pCDNA5/FRT/TO plasmid DNA was freshly prepared for transfection using the Lipofectamine 3000 Transfection Reagent (Invitrogen) following the manufacturer's manual. The transfection mix was incubated for 15 min at RT and then pre-pipetted into wells of a black (fluorescence microscopy) or white (luminescence) 96 or 24 well imaging plate (Cellvis). Cells were subsequently added to the wells at 60 % confluency and incubated with the transfection mix for 8-14 h. Cells were afterwards replenished with fresh cell culture medium. If applicable, cells were incubated o.n. with cell culture medium supplemented with 500 nM CA fluorophore substrate 24 h post-transfection to label HaloTag7-containing proteins. Excess CA fluorophore substrate was removed by washing the cells 3x with fresh cell culture medium without phenol red (= imaging medium). Cells were then used for further downstream preparations.

Stable cell lines were labeled with CA fluorophore substrates in the same way as transiently transfected cells. 200 ng/mL doxycycline was added to stable cell lines generated with a pCDNA5/FRT/TO plasmid 24 h before labeling with CA fluorophore.

Co-localization staining with Hoechst and MitoTracker

Nuclear staining with Hoechst 33342 (Invitrogen) and mitochondrial staining with Mitotracker Red FM (Invitrogen) were achieved by following the manufacturer's manual. Briefly, cells were incubated in fresh imaging medium containing either 8 μ M Hoechst 33342 or 100 nM Mitotracker Red FM. After 30 min, cells were replenished in fresh imaging medium. Cells were not labeled with CA fluorophore substrates to avoid spectral crosstalk with the subcellular staining. Fluorescence microscopic images were acquired using a confocal microscope. Hoechst 33342 staining was visualized with a UV laser (355 nm excitation wavelength) and fluorescence emission was acquired at 400-450 nm emission wavelengths. Mitotracker Red FM staining was visualized with a white light laser (600 nm excitation wavelength) and fluorescence emission was acquired at 620-670 nm emission wavelengths.

Preparation of neuron cultures

The day before preparation of the neurons, black 24 well imaging plates with glass bottom were coated with poly-L-ornithine (100 μ g/mL, diluted in water) for 20 min at RT. Excess of poly-L-

ornithine was removed by washing the wells 2x with PBS pH 7.4 (Gibco). A second coating step was performed by treating the wells with laminin (1 $\mu\text{g}/\text{mL}$, diluted in 1x HBSS supplemented with 1x Penicillin/Streptomycin (Pen/Strep, Gibco) and 200 μM kynurenic acid) for 1 h at RT. Coated plates were stored in the fridge until further use. Neurons were isolated from hippocampi of sacrificed new born rat pups (0-1 day, WISTAR rats) as described previously¹⁷³. Briefly, the brain was extracted by dissecting the skull-cap in a posterior-anterior direction. The hippocampi were removed and placed into ice-cold 1x HBSS supplemented with 0.25 % trypsin and incubated for 20 min at 37 °C to enable a simpler separation of the neurons. Trypsin activity was quenched by addition of DMEM (Gibco) containing 10 % heat-inactivated FBS (Gibco). The neurons were collected by centrifugation at 200 g for 5 min at RT. The cell pellet was washed 3x with 1x HBSS and subsequently resuspended in 5 mL Neurobasal medium without phenol red (NB, Gibco) supplemented with 1x Pen/Strep, GlutaMAX™ and B27. Neurons were mechanically separated using a pipette until obtaining a homogeneous solution. The mix was filtered through a cell strainer (40 μm pore diameter) and the number of live cells was determined using the Countess® II FL Automated Cell Counter (ThermoScientific). 55,000 cells were seeded in well of the pre-coated 24 well imaging plate in 1 mL NB medium. NB medium was replenished 2 h after seeding. Seeded neurons were maintained in a humidified cell culture incubator at 37 °C and 5 % CO₂. Stringent sterile procedures were followed during cell handling, conducted within a laminar flow hood. All reagents were sterile-filtered with a 0.2 μm filter.

Production of recombinant AAVs

rAAVs were produced as described previously¹⁷⁴. Briefly, HEK293 cells (ACC305, DSMZ23) were co-transfected with pRV1 (encoding AAV2 Rep and Cap sequences), pH21 (encoding AAV1 Rep and Cap sequences), pFD6 (Adenovirus helper plasmid) and the pAAV2-hSyn plasmid encoding the POI using Polyethylenimine 25,000 (PEI25,000, Sigma-Aldrich). 5 days post transfection, cells were harvested by centrifugation at 1,000 g for 5 min and 4 °C. The pelleted cells were lysed using TNT extraction buffer (20 mM Tris pH 7.5, 150 mM NaCl, 1 % Triton-X-100, 10 mM MgCl₂). The cell lysate was centrifuged at 3,000 g for 5 min and 4 °C to clear it from any cell debris. To decrease viscosity of the cell lysate, 50 U/mL Benzonase (final concentration, Sigma-Aldrich) was added and incubated for 30-60 min at 37 °C. The cell lysate was subsequently run on an AVB Sepharose HiTrap column, pre-equilibrated in PBS pH 7.4, using an Äkta-Quick FPLC (Cytiva) to purify the rAAVs. The rAAVs were eluted with 50 mM glycine-

HCl pH 2.7. Finally, the elution buffer was exchanged with ice-cold PBS pH 7.4 using Amicon Ultra Centrifugal Filters (Millipore) with a molecular weight cutoff of 100 kDa. Purified rAAVs were aliquoted in 10 μ L, flash frozen and stored at -80 °C until further use. The titer of purified rAAV particles was determined via quantitative PCR (qPCR), as described previously¹⁷⁵. rAAV particles for AAV2/1-hSyn1-NES-ChemoG-CaM had a titer of 1×10^{13} particles/mL.

AAV transduction and labeling of rat hippocampal neurons

Rat hippocampal neurons were prepared as described in *Preparation of neuron cultures*. After 8 days in vitro (DIV), the neurons were transduced with 5×10^9 rAAV particles by adding 50 μ L NB medium containing 0.5 μ L of the rAAV stock. After 12 DIV, sensor expression was validated by fluorescence (EGFP) and the sensor was labeled by adding 100 μ L NB medium containing 2 μ M SiR-CA (final concentration 200 nM) to the neurons. After labeling, excess SiR-CA was not removed from the medium due to negligible background fluorescence of SiR upon EGFP excitation. Neurons were subsequently used for further downstream experiments as described in *Live cell experiments with ChemoG-CaM in rat hippocampal neurons* and *Widefield microscopy*.

Confocal microscopy

All confocal microscopy experiments were conducted utilizing a laser-scanning confocal microscope (Leica SP8, Leica Microsystems). The microscope setup included a Leica TCS SP8 X scan-head, a HC PL APO 40x/1.10 water motCORR CS2 objective, a SuperK white light laser, a 405 nm diode laser, an OPAL 355 nm laser and hybrid photodetectors for single molecule detection (HyD SMD). To maintain stable experimental conditions, the microscope was housed within an environmental chamber with built-in temperature control set to 37 °C, CO₂ control set to 5 %, and humidity control set to 68 %. Prior to imaging, the imaging plate underwent a 30-minute temperature equilibration period on the confocal microscope stage. Microscopic images were captured at a resolution of 512x512 pixels (12- or 16-bit), a scan speed of 400 Hz and a pixel dwell time of 3.16 μ s. The pinhole size was set to 1 Airy unit, and the laser pulse rate was maintained at 80 MHz, unless stated otherwise. Imaging with multiple excitation wavelengths was performed using a sequential scan mode between frames. If applicable, Z-stacks were acquired with a step size of 1 μ m. Additional details can be found in **Table M6**.

Widefield microscopy

All confocal microscopy experiments were conducted utilizing a DMI8 widefield microscope (Leica, Leica Microsystems). The microscopy setup included an HC PL APO 20x/0.80 dry objective, a 470 nm LED, and an external filter wheel with a 474/24 nm bandpass filter (excitation EGFP), a 525/50 nm bandpass filter (emission EGFP) and a 700/75 nm bandpass filter (emission FRET) (Leica Microsystems). To maintain stable experimental conditions, the microscope was housed within an environmental chamber with built-in temperature control set to 37 °C and CO₂ control set to 5 %. Prior to imaging, the imaging plate underwent a 30-minute temperature equilibration period on the confocal microscope stage. Microscopic images of HeLa Kyoto cells expressing ChemoG-CaM were captured at a resolution of 512x512 pixels (16-bit), an exposure time of 500 ms, 4x4 binning and a cycle time of 766 ms. Microscopic images of rat hippocampal neurons were captured at a resolution of 256x256 pixel (16-bit), an exposure time of 50 ms, 8x8 binning and a cycle time of 81 ms. If applicable, Z-stacks were acquired with a step size of 1 µm. EGFP fluorescence was acquired using for excitation and a for emission. Additional details can be found in **Table M6**.

Fluorescence lifetime imaging microscopy

All fluorescence lifetime imaging microscopy (FLIM) experiments were conducted at 37 °C utilizing a laser-scanning confocal microscope (Leica SP8, Leica Microsystems; see *Confocal microscopy*) equipped with a Fast Lifetime Contrast system (FALCON, Leica Microsystems).

FLIM measurements of biosensors were performed with 500 nM CA fluorophore substrate and 2 µM protein in Activity buffer supplemented with 0.2 mg/mL BSA. The mix was labeled for 1 h at RT. Analytes were titrated with the labeled biosensor in a black 96 well imaging plate (Cellvis) as described in *Analysis of biosensor response to varying concentrations of analytes*.

Stable cell lines were used for live cell experiments. Seeding and labeling of the cells were performed as described in *Transfection and labeling of HeLa Kyoto and U-2 OS Flp-In T-REx cells*.

Prior to imaging, the imaging plate underwent a 30-minute temperature equilibration period on the confocal microscope stage. The motorized correction ring of the objective (HC PL APO 40x/1.10 water motCORR CS2) was adjusted for each imaging plate. For each well, the confocal volume was focused to the maximum fluorescence intensity of the labeled CA fluorophore

substrate. The setup of excitation and emission wavelengths was adjusted for the specific CA fluorophore substrate (refer to **Table M6** for details). FLIM images were captured at a resolution of 512x512 pixel (8-bit), a scan speed of 400 Hz, 12 line repetitions and 1 frame repetition at a laser pulse rate of 40 MHz. with a pinhole size of 1 Airy unit, a scan speed of 400 Hz, 12 line repetitions, and 1 frame repetition, using a laser pulse rate of 40 MHz. The pinhole size was set to 1 Airy unit. Laser power adjustments were made to keep photon arrivals below 1 per laser pulse. Image processing and calculation of average fluorescence lifetimes was performed using the LAS X Software (Leica Microsystems). Post-acquisition, intensity-thresholding was applied to eliminate nonspecific background signals. Average fluorescence lifetimes were determined using the through non-exponential reconvolution, with mono- (ChemoG-NAD and HaloTag7) or triexponential (ChemoD-NAD) decay models globally fitted to the fluorescence decay data. Regions of interest (ROI) were manually delineated for live cell experiments. Exclusion criteria for ROIs were based on saturated fluorescence intensity (FI) values or $X^2 > 1.2$. The derived average intensity-weighted fluorescence lifetimes are depicted. Figure panels were generated using FastFLIM images.

Table M6 | Spectral settings for fluorescence microscopy.

Microscope	FP/fluorophore	Laser	Excitation [nm]	Emission [nm]
Confocal	EGFP	WLL	480	490-540
Confocal	EBFP2	405 nm Diode	405	420-470
Confocal	mCerulean3/mseCFP	405 nm Diode	405	460-500
Confocal	Venus	WLL	505	515-565
Confocal	mRuby3/mScarlet	WLL	550	570-620
Confocal	TMR (FRET)	-	-	550-600
Confocal	CPY (FRET)	-	-	620-670
Confocal	SiR (FRET)	-	-	650-700
Confocal	cpVenus (FRET)	-	-	515-565
Confocal	CPY	WLL	610	620-670
Confocal	JF ₆₃₅	WLL	620	635-685
Confocal	SiR	WLL	640	650-700

Widefield	EGFP	470 nm LED (474/24 BP filter)	470	525/50 BP filter
Widefield	SiR (FRET)	-	-	700/75 BP filter

Live cell experiments with ChemoG-CaM in HeLa Kyoto cells

HeLa Kyoto cells were transiently transfected and labeled with SiR-CA (fluorescence microscopy) or CPY-CA (luminescence). A 2x solution of histamine (20 μ M) or ionomycin (2 μ M) was prepared in imaging medium and temperature-equilibrated at 37 °C. The 2x solution was added in a 1:1 volume ratio directly to the well at the indicated time point using an Eppendorf pipette (final concentration histamine = 10 μ M, ionomycin = 1 μ M). The time course was stopped when a stable plateau was reached.

Live cell experiments with ChemoG-CaM in rat hippocampal neurons

Seeded rat hippocampal neurons were transduced with AAVs and labeled with SiR-CA in phenol red-free NB medium supplemented with Pen/Strep, GLutaMAX™ and B27. Measurements were performed on a widefield microscope. A 10x solution containing the synaptic blockers APV (SantaCruz) and NBQX (Sigma) was prepared and added to the neurons 30 min prior imaging to reach 1x final concentrations (25 μ M APV, 10 μ M NBQX). A custom-built cap stimulator equipped with platinum electrodes was used for electric field stimulation of the neurons. The device was connected to a stimulation control unit and placed on top of the imaging plate with the electrodes inserted into the medium, as described previously¹⁷⁶. Electrical stimulation parameters were set to 80 Hz, 100 mA and 1 ms pulse width in 10 s intervals to trigger action potentials ranging from 1-200.

Live cell experiments with ATP biosensors in HeLa Kyoto cells

ATP biosensor experiments were conducted in transiently transfected HeLa Kyoto cells. ChemoX sensors were labeled with SiR-CA (fluorescence microscopy) or CPY-CA (luminescence). After labeling, the imaging medium was exchanged with glucose-free imaging medium 1 h prior to the live cell experiment. A 2x solution of 2-deoxy-D-glucose (2DG, 20 mM) and a 5x solution of D-glucose (Glc, 100 mM) were prepared in glucose-free imaging medium and temperature-equilibrated at 37 °C. The 2x solution of 2DG was added in a 1:1 volume ratio directly to the well at

the indicated time point using an Eppendorf pipette (final concentration 2DG = 10 mM). The 5x Glc solution was added in a 1:4 volume ratio (5x Glc:volume in well) in the same way. The time course was stopped when a stable plateau was reached.

Live cell experiments with NAD⁺ biosensors in U-2 OS cells

NAD⁺ biosensor experiments were conducted either using stable cell lines (ChemoB-NAD, ChemoG-NAD, ChemoG-NAD-NLS, ChemoG-NAD-mito, ChemoD-NAD, ChemoL-NAD) or in transiently transfected U-2 OS cells (ChemoR-NAD, ChemoL-NAD-NLS, ChemoL-NAD-mito). Multiplexing experiments were conducted by transiently transfecting one of the NAD⁺ biosensors (*e.g.*, ChemoG-NAD-mito) into a stable cell line expressing the other NAD⁺ biosensor (*e.g.*, ChemoB-NAD). ChemoX sensors were labeled with SiR-CA (fluorescence microscopy) or CPY-CA (luminescence).

For end-point measurements, the cells were treated with 100 nM FK866 and/or 1 mM NR for 24 h in imaging medium and subsequently imaged without washing out the small molecules. FK866 was prepared from 1 mM DMSO stock solution. NR was prepared from a 1 M water stock solution. For time course experiments, the imaging medium was exchanged with 1x HBSS 1h prior to acquisition. A 2x solution of *N*-methyl-*N'*-nitro-*N*-nitrosoguanidine (MNNG) was prepared in 1x HBSS and temperature-equilibrated 30 min before the start of the experiment (extended incubations of MNNG in 1x HBSS resulted in strongly reduced responses). The 2x solution of MNNG was added in a 1:1 volume ratio directly to the well at the indicated time point using an Eppendorf pipette (final concentration MNNG = 100 μ M). The time course was stopped when a stable plateau was reached.

Image analysis

The software Fiji¹⁷⁷ was used for processing and analysis of images acquired by fluorescence microscopy. If applicable, z-stacks were projected into a composite image based on maximum intensity. Subsequently, background subtraction was performed with a rolling ball radius of 50 pixels. Contrast and brightness adjustments were made if necessary, but adjusted in the same way for each channel of a given image, unless stated otherwise. Processed images were used for downstream quantification.

FRET/FP ratio images were generated by dividing the intensity values of the processed FRET channel image (*e.g.*, FRET_{SIR}) by the intensity values of the processed FRET donor channel image (*e.g.*, EGFP) using the image calculator function in Fiji. More specifically, the image of the processed FRET channel was first duplicated and thresholded using Otsu's method¹⁷⁸. The thresholded image was used to create a binary mask, which was then applied to images of both the FRET donor and FRET channel. The resulting FRET channel image was divided by the FRET donor channel and converted into a 32-bit format.

Quantification of FI values were performed on manually delineated ROIs representing a single cell. Exclusion criteria for ROIs were based on saturated FI values and cells with a poor apparent viability. The mean FI intensity of each ROI was then used for further downstream calculations (*e.g.*, FRET/FRET donor ratio).

FastFLIM images were processed in a similar fashion for representation purposes. More specifically, the FastFLIM images were exported together with the corresponding FI images. The FI image was processed as described above and used to create a binary mask applied to the FastFLIM images. The masked FastFLIM images were solely used for representation, but not for quantification purposes.

siRNA Knockdown experiments

All knockdown experiments were performed with siRNA. siRNAs were ordered from Sigma (si-FLuc, Cat.# EHUFLUC) or Microsynth (siNMNAT1, siNMNAT2, siNAMPT) and stored at -20 °C. siRNAs ordered from Microsynth were synthesized with 5'- and 3'-overhangs (dTdT) to increase stability. See **Table M7** for further details.

Stable cell lines expressing ChemoG-NAD or ChemoG-NMN were grown to 80 % confluency for the day of transfection. siRNA was freshly prepared in Opti-MEM for transfection using the Lipofectamine RNAiMAX Transfection Reagent (Invitrogen) following the manufacturer's manual. The transfection mix was incubated for 15 min at RT and then pre-pipetted into wells of a black 96 well imaging plate (Cellvis). Cells were subsequently added to the wells at 60 % confluency and incubated with the transfection mix for 48 h (final siRNA concentration of 25 nM was used). Cells were afterwards replenished with fresh cell culture medium supplemented with 200 nM SiR-CA and labeled o.n. Excess CA fluorophore substrate was removed by washing the

cells 3x with fresh cell culture medium. Cells were then used for further downstream preparations. 72 h post-transfection, the cells were washed with PBS pH 7.4 before adding 50 μ L TrypLE™ Express to detach the cells. Trypsin activity was quenched by adding 100 μ L PBS pH 7.4 supplemented with 2 % heat-inactivated FBS. The cell suspensions were transferred into a U-shaped 96 well plate and used for downstream analysis using the flow cytometer.

Table M7 | siRNA properties.

Target	Sequence	Vendor
Firefly Luciferase (FLuc)	Mix of siRNA sequences; see Ref ¹⁷⁹ for details	Sigma
Human NMNAT1	5'-CAG CCU GAU CCU AUU GUU GCA TT-3'	Microsynth
Human NMNAT2	5'-CAC GGU GAU GCG GUA UGA AGA TT-3'	Microsynth
Human NAMPT	5'-AUG GGU UGC AGU ACA UUC UUA TT-3'	Microsynth

Flow cytometry analysis

Flow cytometry experiments were performed using an LSRFortessa X-20 flow cytometer equipped with high-throughput module and a blue laser (488 nm excitation wavelength) which was used for measuring FSC and SSC (488/10 BP filter, no mirror), EGFP emission (530/30 BP filter, 505 LP mirror) and FRET_{SiR} emission (710 BP filter, 685 LP mirror). Labeled ChemoG-NAD cells were used to adjust the voltage for each detector to be in the linear range. The same voltage settings were used for all cell lines and all treatments. 10,000 events per condition were measured. Per condition, 3 technical replicates (*i.e.*, 3 wells) were measured and 2 biological replicates were performed in total.

The acquired data was analyzed using the software FlowJo™. Gating strategy involved the removal of dead cells and cell debris (SSC-A over FSC-A), removal of cell doublets (SSC-H over SSC-A) and the selection of EGFP- and FRET_{SiR}-positive cells. The median of the FRET_{SiR}/EGFP ratio was determined for gated cells and used for data representation.

Quantitative PCR analysis

Quantitative PCR (qPCR) analysis was performed to determine the degree of mRNA reduction after siRNA knockdown in the stable cell line expressing ChemoG-NMN. Cells were grown to

80 % confluency and transfection was carried out as described in *siRNA Knockdown experiments* but in a 6 well plate format. 72 h post-transfection, the cells were detached by trypsin digest and harvested by centrifugation at 300 g for 5 min at RT. The supernatant was carefully removed and the cells washed once with PBS pH 7.4. Cell pellets were snap frozen in liquid nitrogen and stored at -80 °C until further use. For RNA extraction, the cell pellets were thawed on ice and RNA extracted using the RNeasy kit (Qiagen) following the manufacturer's manual. RNA concentration and purity were determined using a Nanodrop 2000c spectrophotometer.

The SYBR® Green Quantitative RT-PCR Kit (Sigma) was used for qPCR following the manufacturer's manual. All steps were carried out on ice. Briefly, 200 ng total extracted RNA was diluted in 8 µL RNase-free water and mixed with 12 µL mastermix containing 10 µL 2x SYBR Green Ready Mix, 0.1 µL M-MLV RT, 1 µL forward primer (4 µM) and 1 µL reverse primer (4 µM) in a white PCR 96 well plate. Technical triplicates were performed for each siRNA knockdown sample and a negative control with no RNA template was included. See for sequences of primers used. The pipetted plate was sealed with a transparent plastic foil to prevent evaporation and centrifuged at 500 g for 1 min at RT to collect the entire reaction volume at the bottom of each well. The plate was then placed into a CFX96 Touch Deep Well Real-Time PCR Detection System (BioRad) and qPCR was carried out using the following settings: 44 °C for 30 min (reverse transcription), 94 °C for 2 min (initial denaturation) and 40 cycles at i) 94 °C for 15 s (denaturation) and ii) 60 °C for 1 min (hybridization and elongation). SYBR Green fluorescence was monitored in real-time. Acquired data was analyzed using the CFX Maestro software. The threshold for quantification was set to 3000 RFU and the cycle at which the SYBR Green fluorescence surpassed this threshold (C_t) was determined for each qPCR reaction. For normalization, the C_t value of the target (*e.g.*, NMNAT1) was subtracted by the C_t value of GAPDH both derived from the same knockdown condition (*e.g.*, NMNAT1 knockdown) (= ΔC_t). The ΔC_t value of each target knockdown condition (*e.g.*, NMNAT1) was then subtracted by the ΔC_t value of the control condition (FLuc knockdown) (= $\Delta\Delta C_t$). The $\Delta\Delta C_t$ value was used to calculate the fold change in expression level of the target mRNA by calculating the antilog value to the base of 2 ($2^{-\Delta\Delta C_t}$).

Table M8 | qPCR primers.

Target	Sequence
Human GAPDH forward	5'-GTC TCC TCT GAC TTC AAC AGC G-3'
Human GAPDH reverse	5'-ACC ACC CTG TTG CTG TAG CCA A-3'
Human NMNAT1 forward	5'-GTG GAA AGA GAC TCT GAA GGT GC-3'
Human NMNAT1 reverse	5'-CTT GTG TTT CAG TCC ACT TCC TC-3'
Human NMNAT2 forward	5'-GTA GTG ACC TGC TGG AGT CCT T-3'
Human NMNAT2 reverse	5'-ATG ATT CGG TCT GTG TCG GCT G-3'
Human NAMPT forward	5'-AGG GTT ACA AGT TGC TGC CAC C-3'
Human NAMPT reverse	5'-CTC CAC CAG AAC CGA AGG CAA T-3'

Quantification of intracellular NMN and NAD⁺ levels via mass spectrometry

Quantification of whole-cell contents of NMN and NAD⁺ was performed to determine changes in intracellular NMN and NAD⁺ levels after siRNA knockdown in the stable cell line expressing ChemoG-NMN. Cells were grown to 80 % confluency and transfection was carried out as described in *siRNA Knockdown experiments* but in a 6 well plate format. 72 h post-transfection, the cells were detached by trypsin digest and harvested by centrifugation at 5000 g for 5 min at 4 °C. An aliquot was taken before centrifugation to determine the cell count. The supernatant was carefully removed and the cells washed once with PBS pH 7.4. The cell pellet was resuspended in 10 µL PBS pH 7.4 and mixed with 10 µL internal standard containing U-¹³C isotopically labeled metabolite yeast extract (Cambridge Isotope Laboratories, Cat.#: ISO1). Control samples contained 10 µL distilled water instead of the cell pellet. 80 µL 70 % ethanol (buffered with 50 mM HEPES pH 7.3) was added to the mix before shaking it for 3 min at 80 °C and 1,000 rpm using an Eppendorf ThermoMixer to lyse the cells. The lysates were vortexed for 2 min and then centrifuged for 10 min at 10,000 g and 4 °C to remove cell debris. 50 µL of the supernatant was diluted in 450 µL 50 mM sodium acetate pH 8.0 and submitted for metabolite quantification via mass spectrometry.

10 μ L of the diluted samples were injected on a Thermo Scientific Hypercarb column (1 x 100 mm) operated at 80 °C. On-column separation of the sample contents was achieved using a Shimadzu Nexera UPLC system operated in gradient mode and hyphenated to a Sciex QT6500+ triple quadrupole mass spectrometer. At a total flow rate of 0.2 mL/min the following gradient was applied: 0 -1.8 min 5 % solvent B isocratic, 1.8 -10 min solvent B increased to 95 %, 10 -13 min 95 % solvent B isocratic, 13 – 13.1 min reset to 5 % solvent B and 13.1 -19 min isocratic re-equilibration of the chromatographic starting conditions, whereas solvent A consisted of 7.5 mM NH_4Ac + 0.05 % (v/v) NH_4OH in ULC/MS water (Biosolve) and solvent B a solution of 0.05 % (v/v) NH_4OH in ULC/MS acetonitrile (Biosolve).

The eluates were subjected to an electrospray ionization process with the following applied settings: Curtain gas (CUR) 40, collision gas (CAD) Medium, ionspray voltage (IS) 5500 (+)/-4500 (-), ion source gas 1 (GS1) 60 and GS2 55. The resulting ion stream was processed in the multiple reaction monitoring (MRM) mode. The corresponding compound specific parameters are provided in table XX. The mass spectrometer was operated using the Analyst 1.7 software from Sciex.

Table M9| MRM method information for the LC-MS/MS analysis of NMN and NAD^+ .

Q1 [Da]	Q3 [Da]	Dwell time [ms]	ID	DP [V]	EP [V]	CE [V]	CXP [V]	ESI Polarity
335.2	123.1	200	NMN.1	30	10	19	14.5	+
335.2	80	100	NMN.2	30	10	72	9	+
346.15	129.1	100	H-NMN	30	10	19	14.5	+
683	555	100	H-NAD.1	-35	-10	-20	-35	-
661.9	540	200	NAD.1	-35	-10	-20	-35	-
661.9	79	100	NAD.2	-35	-10	-130	-9	-

Data analysis was performed using the PeakView 2.2 and the MultiQuant 3.0.3 software from Sciex. NAD^+ or NMN signals were only considered as valid with a signal to noise ratio above 10.

Statistics and reproducibility

All in vitro measurements were performed at least in 3 technical replicates. Shown are the mean plus standard deviation. All cell experiments were performed at least in 3 biological replicates (*i.e.*, on 3 different days), unless stated differently. Shown are the mean plus standard deviation. For flow cytometry experiments, the median plus standard deviation is shown. Statistical significance of a sample group over a reference group was determined by performing a one-way ANOVA based on the Dunnett's test using the Software GraphPad Prism (version 8.1.0). Calculated p values are stated in the graphs. Microscopy images are representative snapshots of experiments.

Graphical design

All cartoons were created using Adobe Illustrator.

Bibliography

1. Bar-Peled, L. & Kory, N. Principles and functions of metabolic compartmentalization. *Nat Metab* **4**, 1232-1244 (2022).
2. Wojtovich, A.P., Berry, B.J. & Galkin, A. Redox Signaling Through Compartmentalization of Reactive Oxygen Species: Implications for Health and Disease. *Antioxid Redox Signal* **31**, 591-593 (2019).
3. Sampson, E.M. & Bobik, T.A. Microcompartments for B12-dependent 1,2-propanediol degradation provide protection from DNA and cellular damage by a reactive metabolic intermediate. *J Bacteriol* **190**, 2966-2971 (2008).
4. Clapham, D.E. Calcium signaling. *Cell* **131**, 1047-1058 (2007).
5. Campbell, S.L. & Wellen, K.E. Metabolic Signaling to the Nucleus in Cancer. *Mol Cell* **71**, 398-408 (2018).
6. Quiros, P.M., Mottis, A. & Auwerx, J. Mitonuclear communication in homeostasis and stress. *Nat Rev Mol Cell Biol* **17**, 213-226 (2016).
7. Wang, Y. et al. SLC25A39 is necessary for mitochondrial glutathione import in mammalian cells. *Nature* **599**, 136-140 (2021).
8. Bensard, C.L. et al. Regulation of Tumor Initiation by the Mitochondrial Pyruvate Carrier. *Cell Metab* **31**, 284-300 e287 (2020).
9. Kishi, J.Y. et al. Light-Seq: light-directed in situ barcoding of biomolecules in fixed cells and tissues for spatially indexed sequencing. *Nat Methods* **19**, 1393-1402 (2022).
10. Zhang, H., Delafield, D.G. & Li, L. Mass spectrometry imaging: the rise of spatially resolved single-cell omics. *Nat Methods* **20**, 327-330 (2023).
11. Chen, W.W., Freinkman, E., Wang, T., Birsoy, K. & Sabatini, D.M. Absolute Quantification of Matrix Metabolites Reveals the Dynamics of Mitochondrial Metabolism. *Cell* **166**, 1324-1337 e1311 (2016).
12. Karp, M.T. & Vuorinen, P.I. Simultaneous extraction and combined bioluminescent assay of oxidized and reduced nicotinamide adenine dinucleotide. *Methods Enzymol* **122**, 147-152 (1986).
13. Lagorio, M.G., Cordon, G.B. & Iriel, A. Reviewing the relevance of fluorescence in biological systems. *Photochem Photobiol Sci* **14**, 1538-1559 (2015).
14. Stokes, G.G. On the Change of Refrangibility of Light. *Philosophical Transactions of the Royal Society of London* **142**, 463-562 (1852).

15. Forster, T. *Zwischenmolekulare Energiewanderung Und Fluoreszenz. *Ann Phys-Berlin* **2**, 55-75 (1948).
16. Shimomura, O., Johnson, F.H. & Saiga, Y. Extraction, purification and properties of aequorin, a bioluminescent protein from the luminous hydromedusan, Aequorea. *J Cell Comp Physiol* **59**, 223-239 (1962).
17. Ormo, M. et al. Crystal structure of the Aequorea victoria green fluorescent protein. *Science* **273**, 1392-1395 (1996).
18. Yang, F., Moss, L.G. & Phillips, G.N., Jr. The molecular structure of green fluorescent protein. *Nat Biotechnol* **14**, 1246-1251 (1996).
19. Cubitt, A.B. et al. Understanding, improving and using green fluorescent proteins. *Trends Biochem Sci* **20**, 448-455 (1995).
20. Reid, B.G. & Flynn, G.C. Chromophore formation in green fluorescent protein. *Biochemistry* **36**, 6786-6791 (1997).
21. Brejc, K. et al. Structural basis for dual excitation and photoisomerization of the Aequorea victoria green fluorescent protein. *Proc Natl Acad Sci U S A* **94**, 2306-2311 (1997).
22. Heim, R., Prasher, D.C. & Tsien, R.Y. Wavelength mutations and posttranslational autoxidation of green fluorescent protein. *Proc Natl Acad Sci U S A* **91**, 12501-12504 (1994).
23. Heim, R. & Tsien, R.Y. Engineering green fluorescent protein for improved brightness, longer wavelengths and fluorescence resonance energy transfer. *Curr Biol* **6**, 178-182 (1996).
24. Matz, M.V. et al. Fluorescent proteins from nonbioluminescent Anthozoa species. *Nat Biotechnol* **17**, 969-973 (1999).
25. Shcherbakova, D.M., Baloban, M. & Verkhusha, V.V. Near-infrared fluorescent proteins engineered from bacterial phytochromes. *Curr Opin Chem Biol* **27**, 52-63 (2015).
26. Cormack, B.P., Valdivia, R.H. & Falkow, S. FACS-optimized mutants of the green fluorescent protein (GFP). *Gene* **173**, 33-38 (1996).
27. Campbell, R.E. et al. A monomeric red fluorescent protein. *Proc Natl Acad Sci U S A* **99**, 7877-7882 (2002).
28. Shaner, N.C. et al. Improved monomeric red, orange and yellow fluorescent proteins derived from *Discosoma* sp. red fluorescent protein. *Nat Biotechnol* **22**, 1567-1572 (2004).
29. Pedelacq, J.D., Cabantous, S., Tran, T., Terwilliger, T.C. & Waldo, G.S. Engineering and characterization of a superfolder green fluorescent protein. *Nat Biotechnol* **24**, 79-88 (2006).
30. Zacharias, D.A., Violin, J.D., Newton, A.C. & Tsien, R.Y. Partitioning of lipid-modified monomeric GFPs into membrane microdomains of live cells. *Science* **296**, 913-916 (2002).

31. Gadella, T.W.J., Jr. et al. mScarlet3: a brilliant and fast-maturing red fluorescent protein. *Nat Methods* **20**, 541-545 (2023).
32. Ando, R. et al. StayGold variants for molecular fusion and membrane-targeting applications. *Nat Methods* (2023).
33. Nagendrappa, G. Sir William Henry Perkin: The Man and his 'Mauve'. *Resonance* **15**, 779-793 (2010).
34. Lavis, L.D. & Raines, R.T. Bright building blocks for chemical biology. *ACS Chem Biol* **9**, 855-866 (2014).
35. Wang, L. et al. A general strategy to develop cell permeable and fluorogenic probes for multicolour nanoscopy. *Nat Chem* **12**, 165-172 (2020).
36. Grimm, J.B. et al. A general method to fine-tune fluorophores for live-cell and in vivo imaging. *Nat Methods* **14**, 987-994 (2017).
37. Grimm, J.B. et al. Carbofluoresceins and carborhodamines as scaffolds for high-contrast fluorogenic probes. *ACS Chem Biol* **8**, 1303-1310 (2013).
38. Lukinavicius, G. et al. A near-infrared fluorophore for live-cell super-resolution microscopy of cellular proteins. *Nat Chem* **5**, 132-139 (2013).
39. Johnson, L.V., Walsh, M.L. & Chen, L.B. Localization of Mitochondria in Living Cells with Rhodamine-123. *Proc Natl Acad Sci-Biol* **77**, 990-994 (1980).
40. Lukinavicius, G. et al. Fluorogenic probes for live-cell imaging of the cytoskeleton. *Nat Methods* **11**, 731-733 (2014).
41. Baskin, J.M. et al. Copper-free click chemistry for dynamic in vivo imaging. *Proc Natl Acad Sci USA* **104**, 16793-16797 (2007).
42. Keppler, A. et al. A general method for the covalent labeling of fusion proteins with small molecules in vivo. *Nat Biotechnol* **21**, 86-89 (2003).
43. Gautier, A. et al. An engineered protein tag for multiprotein labeling in living cells. *Chem Biol* **15**, 128-136 (2008).
44. Los, G.V. et al. HaloTag: a novel protein labeling technology for cell imaging and protein analysis. *ACS Chem Biol* **3**, 373-382 (2008).
45. Wilhelm, J. et al. Kinetic and Structural Characterization of the Self-Labeling Protein Tags HaloTag7, SNAP-tag, and CLIP-tag. *Biochemistry* **60**, 2560-2575 (2021).
46. Hoelzel, C.A. & Zhang, X. Visualizing and Manipulating Biological Processes by Using HaloTag and SNAP-Tag Technologies. *Chembiochem* **21**, 1935-1946 (2020).
47. Frei, M.S. et al. Engineered HaloTag variants for fluorescence lifetime multiplexing. *Nat Methods* **19**, 65-70 (2022).

48. Deguchi, T. et al. Direct observation of motor protein stepping in living cells using MINFLUX. *Science* **379**, 1010-1015 (2023).
49. Cook, A., Walterspiel, F. & Deo, C. HaloTag-Based Reporters for Fluorescence Imaging and Biosensing. *Chembiochem* **24**, e202300022 (2023).
50. Greenwald, E.C., Mehta, S. & Zhang, J. Genetically Encoded Fluorescent Biosensors Illuminate the Spatiotemporal Regulation of Signaling Networks. *Chem Rev* **118**, 11707-11794 (2018).
51. Zhang, Y. & Looger, L.L. Fast and sensitive GCaMP calcium indicators for neuronal imaging. *J Physiol* (2023).
52. Mishina, N.M. et al. Live-Cell STED Microscopy with Genetically Encoded Biosensor. *Nano Lett* **15**, 2928-2932 (2015).
53. Siloto, R.M.P. & Weselake, R.J. Site saturation mutagenesis: Methods and applications in protein engineering. *Biocatal Agric Biote* **1**, 181-189 (2012).
54. Rappleye, M. et al. Optogenetic Microwell Array Screening System: A High-Throughput Engineering Platform for Genetically Encoded Fluorescent Indicators. *ACS Sens* **8**, 4233-4244 (2023).
55. Nasu, Y., Shen, Y., Kramer, L. & Campbell, R.E. Structure- and mechanism-guided design of single fluorescent protein-based biosensors. *Nat Chem Biol* **17**, 509-518 (2021).
56. Nakai, J., Ohkura, M. & Imoto, K. A high signal-to-noise Ca(2+) probe composed of a single green fluorescent protein. *Nat Biotechnol* **19**, 137-141 (2001).
57. Barnett, L.M., Hughes, T.E. & Drobizhev, M. Deciphering the molecular mechanism responsible for GCaMP6m's Ca²⁺-dependent change in fluorescence. *PLoS One* **12**, e0170934 (2017).
58. Wang, L., Hiblot, J., Popp, C., Xue, L. & Johnsson, K. Environmentally Sensitive Color-Shifting Fluorophores for Bioimaging. *Angew Chem Int Ed Engl* **59**, 21880-21884 (2020).
59. Deo, C. et al. The HaloTag as a general scaffold for far-red tunable chemigenetic indicators. *Nat Chem Biol* **17**, 718-723 (2021).
60. Li, J. et al. Engineering of NEMO as calcium indicators with large dynamics and high sensitivity. *Nat Methods* **20**, 918-924 (2023).
61. Miyawaki, A. et al. Fluorescent indicators for Ca²⁺ based on green fluorescent proteins and calmodulin. *Nature* **388**, 882-887 (1997).
62. Vecchia, M.D. et al. Spectrally Tunable Forster Resonance Energy Transfer-Based Biosensors Using Organic Dye Grafting. *ACS Sens* **7**, 2920-2927 (2022).
63. Zhang, D., Redington, E. & Gong, Y. Rational engineering of ratiometric calcium sensors with bright green and red fluorescent proteins. *Commun Biol* **4**, 924 (2021).

64. Fritz, R.D. et al. A versatile toolkit to produce sensitive FRET biosensors to visualize signaling in time and space. *Sci Signal* **6**, rs12 (2013).
65. Nagai, T., Yamada, S., Tominaga, T., Ichikawa, M. & Miyawaki, A. Expanded dynamic range of fluorescent indicators for Ca(2+) by circularly permuted yellow fluorescent proteins. *Proc Natl Acad Sci U S A* **101**, 10554-10559 (2004).
66. Xue, L. et al. Probing coenzyme A homeostasis with semisynthetic biosensors. *Nat Chem Biol* **19**, 346-355 (2023).
67. Komatsu, N. et al. Development of an optimized backbone of FRET biosensors for kinases and GTPases. *Mol Biol Cell* **22**, 4647-4656 (2011).
68. Thestrup, T. et al. Optimized ratiometric calcium sensors for functional in vivo imaging of neurons and T lymphocytes. *Nat Methods* **11**, 175-182 (2014).
69. Vinkenborg, J.L. et al. Genetically encoded FRET sensors to monitor intracellular Zn2+ homeostasis. *Nat Methods* **6**, 737-740 (2009).
70. Kotera, I., Iwasaki, T., Imamura, H., Noji, H. & Nagai, T. Reversible dimerization of Aequorea victoria fluorescent proteins increases the dynamic range of FRET-based indicators. *ACS Chem Biol* **5**, 215-222 (2010).
71. Trigo-Mourino, P., Thestrup, T., Griesbeck, O., Griesinger, C. & Becker, S. Dynamic tuning of FRET in a green fluorescent protein biosensor. *Sci Adv* **5**, eaaw4988 (2019).
72. Gohil, K., Wu, S.Y., Takahashi-Yamashiro, K., Shen, Y. & Campbell, R.E. Biosensor Optimization Using a Forster Resonance Energy Transfer Pair Based on mScarlet Red Fluorescent Protein and an mScarlet-Derived Green Fluorescent Protein. *ACS Sens* **8**, 587-597 (2023).
73. Grunberg, R. et al. Engineering of weak helper interactions for high-efficiency FRET probes. *Nat Methods* **10**, 1021-1027 (2013).
74. Nakano, M., Imamura, H., Nagai, T. & Noji, H. Ca(2)(+) regulation of mitochondrial ATP synthesis visualized at the single cell level. *ACS Chem Biol* **6**, 709-715 (2011).
75. Farrants, H., Hiblot, J., Griss, R. & Johnsson, K. Rational Design and Applications of Semisynthetic Modular Biosensors: SNIFITs and LUCIDs. *Methods Mol Biol* **1596**, 101-117 (2017).
76. Sallin, O. et al. Semisynthetic biosensors for mapping cellular concentrations of nicotinamide adenine dinucleotides. *Elife* **7** (2018).
77. Hellweg, L. Development of a new strategy for the semi-synthetic design of calcium sensors. *Unpublished Master's thesis (Heidelberg University)* (2020).

78. Hellweg, L. et al. A general method for the development of multicolor biosensors with large dynamic ranges. *Nat Chem Biol* **19**, 1147-1157 (2023).
79. Frei, M.S. et al. Engineered HaloTag variants for fluorescence lifetime multiplexing. *Nature Methods* **19**, 65-+ (2022).
80. Bucevicius, J., Keller-Findeisen, J., Gilat, T., Hell, S.W. & Lukinavicius, G. Rhodamine-Hoechst positional isomers for highly efficient staining of heterochromatin. *Chemical Science* **10**, 1962-1970 (2019).
81. Grimm, J.B. et al. A general method to improve fluorophores for live-cell and single-molecule microscopy. *Nat Methods* **12**, 244-250, 243 p following 250 (2015).
82. Ai, H.W., Shaner, N.C., Cheng, Z., Tsien, R.Y. & Campbell, R.E. Exploration of new chromophore structures leads to the identification of improved blue fluorescent proteins. *Biochemistry* **46**, 5904-5910 (2007).
83. Markwardt, M.L. et al. An improved cerulean fluorescent protein with enhanced brightness and reduced reversible photoswitching. *PLoS One* **6**, e17896 (2011).
84. Nagai, T. et al. A variant of yellow fluorescent protein with fast and efficient maturation for cell-biological applications. *Nat Biotechnol* **20**, 87-90 (2002).
85. Prasher, D.C., Eckenrode, V.K., Ward, W.W., Prendergast, F.G. & Cormier, M.J. Primary structure of the *Aequorea victoria* green-fluorescent protein. *Gene* **111**, 229-233 (1992).
86. Bindels, D.S. et al. mScarlet: a bright monomeric red fluorescent protein for cellular imaging. *Nat Methods* **14**, 53-56 (2017).
87. Horikawa, K. et al. Spontaneous network activity visualized by ultrasensitive Ca(2+) indicators, yellow Cameleon-Nano. *Nat Methods* **7**, 729-732 (2010).
88. Sauve, R. et al. Ca²⁺ oscillations induced by histamine H1 receptor stimulation in HeLa cells: Fura-2 and patch clamp analysis. *Cell Calcium* **12**, 165-176 (1991).
89. Sauve, R., Simoneau, C., Parent, L., Monette, R. & Roy, G. Oscillatory activation of calcium-dependent potassium channels in HeLa cells induced by histamine H1 receptor stimulation: a single-channel study. *J Membr Biol* **96**, 199-208 (1987).
90. Zucker, R.S. Calcium- and activity-dependent synaptic plasticity. *Curr Opin Neurobiol* **9**, 305-313 (1999).
91. Zhang, Y. et al. Fast and sensitive GCaMP calcium indicators for imaging neural populations. *Nature* **615**, 884-891 (2023).
92. Khakh, B.S. & Burnstock, G. The double life of ATP. *Sci Am* **301**, 84-90, 92 (2009).
93. White, D. & Yang, Q.L. Genetically Encoded ATP Biosensors for Direct Monitoring of Cellular ATP Dynamics. *Cells* **11** (2022).

94. Imamura, H. et al. Visualization of ATP levels inside single living cells with fluorescence resonance energy transfer-based genetically encoded indicators. *Proc Natl Acad Sci U S A* **106**, 15651-15656 (2009).
95. Lobas, M.A. et al. A genetically encoded single-wavelength sensor for imaging cytosolic and cell surface ATP. *Nat Commun* **10**, 711 (2019).
96. Kitajima, N. et al. Real-time in vivo imaging of extracellular ATP in the brain with a hybrid-type fluorescent sensor. *Elife* **9** (2020).
97. Greiner, J.V. & Glonek, T. Intracellular ATP Concentration and Implication for Cellular Evolution. *Biology (Basel)* **10** (2021).
98. Traut, T.W. Physiological concentrations of purines and pyrimidines. *Mol Cell Biochem* **140**, 1-22 (1994).
99. Wick, A.N., Drury, D.R., Nakada, H.I. & Wolfe, J.B. Localization of the Primary Metabolic Block Produced by 2-Deoxyglucose. *Journal of Biological Chemistry* **224**, 963-969 (1957).
100. Aft, R.L., Zhang, F.W. & Gius, D. Evaluation of 2-deoxy-D-glucose as a chemotherapeutic agent: mechanism of cell death. *Brit J Cancer* **87**, 805-812 (2002).
101. Canto, C., Menzies, K.J. & Auwerx, J. NAD(+) Metabolism and the Control of Energy Homeostasis: A Balancing Act between Mitochondria and the Nucleus. *Cell Metab* **22**, 31-53 (2015).
102. Houtkooper, R.H., Canto, C., Wanders, R.J. & Auwerx, J. The secret life of NAD+: an old metabolite controlling new metabolic signaling pathways. *Endocr Rev* **31**, 194-223 (2010).
103. Canto, C. et al. AMPK regulates energy expenditure by modulating NAD+ metabolism and SIRT1 activity. *Nature* **458**, 1056-1060 (2009).
104. Cambronne, X.A. et al. Biosensor reveals multiple sources for mitochondrial NAD(+). *Science* **352**, 1474-1477 (2016).
105. Ryu, K.W. et al. Metabolic regulation of transcription through compartmentalized NAD(+) biosynthesis. *Science* **360** (2018).
106. Challa, S. et al. Ribosome ADP-ribosylation inhibits translation and maintains proteostasis in cancers. *Cell* **184**, 4531-+ (2021).
107. Guldenpfennig, A. et al. Absence of mitochondrial SLC25A51 enhances PARP1-dependent DNA repair by increasing nuclear NAD+ levels. *Nucleic Acids Res* **51**, 9248-9265 (2023).
108. Gajiwala, K.S. & Pinko, C. Structural rearrangement accompanying NAD+ synthesis within a bacterial DNA ligase crystal. *Structure* **12**, 1449-1459 (2004).
109. Veech, R.L., Eggleston, L.V. & Krebs, H.A. The redox state of free nicotinamide-adenine dinucleotide phosphate in the cytoplasm of rat liver. *Biochem J* **115**, 609-619 (1969).

110. Trammell, S.A. & Brenner, C. Targeted, LCMS-based Metabolomics for Quantitative Measurement of NAD(+) Metabolites. *Comput Struct Biotechnol J* **4**, e201301012 (2013).
111. Tempel, W. et al. Nicotinamide riboside kinase structures reveal new pathways to NAD+. *PLoS Biol* **5**, e263 (2007).
112. Hasmann, M. & Schemainda, I. FK866, a highly specific noncompetitive inhibitor of nicotinamide phosphoribosyltransferase, represents a novel mechanism for induction of tumor cell apoptosis. *Cancer Research* **63**, 7436-7442 (2003).
113. Chen, L. et al. Mitochondrial heterogeneity in diseases. *Signal Transduct Target Ther* **8**, 311 (2023).
114. Zong, W.X., Ditsworth, D., Bauer, D.E., Wang, Z.Q. & Thompson, C.B. Alkylating DNA damage stimulates a regulated form of necrotic cell death. *Gene Dev* **18**, 1272-1282 (2004).
115. Yang, H. et al. Nutrient-sensitive mitochondrial NAD+ levels dictate cell survival. *Cell* **130**, 1095-1107 (2007).
116. Murakoshi, H., Shibata, A.C.E., Nakahata, Y. & Nabekura, J. A dark green fluorescent protein as an acceptor for measurement of Forster resonance energy transfer. *Sci Rep* **5**, 15334 (2015).
117. Kopish, K. et al. NanoLuc: a Smaller, Brighter, and More Versatile Luciferase Reporter. *Eur J Cancer* **48**, 57-57 (2012).
118. Saito, K. et al. Luminescent proteins for high-speed single-cell and whole-body imaging. *Nat Commun* **3**, 1262 (2012).
119. Suzuki, K. et al. Five colour variants of bright luminescent protein for real-time multicolour bioimaging. *Nature Communications* **7** (2016).
120. Song, Q. et al. The Safety and Antiaging Effects of Nicotinamide Mononucleotide in Human Clinical Trials: an Update. *Adv Nutr* **14**, 1416-1435 (2023).
121. Xie, N. et al. NAD(+) metabolism: pathophysiologic mechanisms and therapeutic potential. *Signal Transduct Target Ther* **5**, 227 (2020).
122. Rajman, L., Chwalek, K. & Sinclair, D.A. Therapeutic Potential of NAD-Boosting Molecules: The In Vivo Evidence. *Cell Metab* **27**, 529-547 (2018).
123. Figley, M.D. et al. SARM1 is a metabolic sensor activated by an increased NMN/NAD(+) ratio to trigger axon degeneration. *Neuron* **109**, 1118-1136 e1111 (2021).
124. Gerdts, J., Brace, E.J., Sasaki, Y., DiAntonio, A. & Milbrandt, J. SARM1 activation triggers axon degeneration locally via NAD(+) destruction. *Science* **348**, 453-457 (2015).
125. Lahiri, S.D. et al. Structure guided understanding of NAD+ recognition in bacterial DNA ligases. *ACS Chem Biol* **7**, 571-580 (2012).

126. Trammell, S.A.J. & Brenner, C. Targeted, Lcms-Based Metabolomics for Quantitative Measurement of Nad+Metabolites. *Comput Struct Biotec* **4** (2013).
127. Vinkenburg, J.L., Evers, T.H., Reulen, S.W.A., Meijer, E.W. & Merkx, M. Enhanced sensitivity of FRET-based protease sensors by redesign of the GFP dimerization interface. *Chembiochem* **8**, 1119-1121 (2007).
128. Grünberg, R. et al. Engineering of weak helper interactions for high-efficiency FRET probes. *Nature Methods* **10**, 1021-+ (2013).
129. Arpino, J.A.J. et al. Structural Basis for Efficient Chromophore Communication and Energy Transfer in a Constructed Didomain Protein Scaffold. *Journal of the American Chemical Society* **134**, 13632-13640 (2012).
130. Vecchia, M.D. et al. Spectrally Tunable Forster Resonance Energy Transfer-Based Biosensors Using Organic Dye Grafting. *ACS Sens* (2022).
131. Gadella, T.W.J. et al. mScarlet3: a brilliant and fast-maturing red fluorescent protein. *Nature Methods* **20**, 541-+ (2023).
132. Ivorra-Molla, E. et al. A monomeric StayGold fluorescent protein. *Nature Biotechnology* (2023).
133. Ando, R. et al. StayGold variants for molecular fusion and membrane-targeting applications. *Nature Methods* **21** (2024).
134. Zhang, H. et al. Bright and stable monomeric green fluorescent protein derived from StayGold. *Nat Methods* (2024).
135. Aye-Han, N.N., Allen, M.D., Ni, Q. & Zhang, J. Parallel tracking of cAMP and PKA signaling dynamics in living cells with FRET-based fluorescent biosensors. *Mol Biosyst* **8**, 1435-1440 (2012).
136. Shcherbakova, D.M., Hink, M.A., Joosen, L., Gadella, T.W. & Verkhusha, V.V. An orange fluorescent protein with a large Stokes shift for single-excitation multicolor FCCS and FRET imaging. *J Am Chem Soc* **134**, 7913-7923 (2012).
137. Roebroek, T. et al. Simultaneous readout of multiple FRET pairs using photochromism. *Nat Commun* **12**, 2005 (2021).
138. Habif, M., Corbat, A.A., Silberberg, M. & Grecco, H.E. CASPAM: A Triple-Modality Biosensor for Multiplexed Imaging of Caspase Network Activity. *ACS Sens* **6**, 2642-2653 (2021).
139. Challa, S. et al. Ribosome ADP-ribosylation inhibits translation and maintains proteostasis in cancers. *Cell* **184**, 4531-4546 e4526 (2021).

140. Shcherbakova, D.M., Cox Cammer, N., Huisman, T.M., Verkhusha, V.V. & Hodgson, L. Direct multiplex imaging and optogenetics of Rho GTPases enabled by near-infrared FRET. *Nat Chem Biol* **14**, 591-600 (2018).
141. Mehta, S. et al. Single-fluorophore biosensors for sensitive and multiplexed detection of signalling activities. *Nat Cell Biol* **20**, 1215-1225 (2018).
142. Qian, Y. et al. A genetically encoded near-infrared fluorescent calcium ion indicator. *Nat Methods* **16**, 171-174 (2019).
143. van der Linden, F.H. et al. A turquoise fluorescence lifetime-based biosensor for quantitative imaging of intracellular calcium. *Nat Commun* **12**, 7159 (2021).
144. Kompa, J. et al. Exchangeable HaloTag Ligands for Super-Resolution Fluorescence Microscopy. *J Am Chem Soc* **145**, 3075-3083 (2023).
145. Zou, Y. et al. Illuminating NAD(+) Metabolism in Live Cells and In Vivo Using a Genetically Encoded Fluorescent Sensor. *Dev Cell* **53**, 240-252 e247 (2020).
146. Liuqing Chen, P.W., Guan Huang, Wenxiang Cheng, Kaijing Liu, Qiuliyang Yu Quantitative dynamics of intracellular NMN by genetically encoded biosensor. *bioRxiv* (2023).
147. Jiang, Y. et al. The NAD(+)-mediated self-inhibition mechanism of pro-neurodegenerative SARM1. *Nature* **588**, 658-663 (2020).
148. Liu, Q. et al. Covalent and noncovalent intermediates of an NAD utilizing enzyme, human CD38. *Chem Biol* **15**, 1068-1078 (2008).
149. Beltran, J. et al. Rapid biosensor development using plant hormone receptors as reprogrammable scaffolds. *Nat Biotechnol* **40**, 1855-1861 (2022).
150. Kang, S. et al. COMBINES-CID: An Efficient Method for De Novo Engineering of Highly Specific Chemically Induced Protein Dimerization Systems. *J Am Chem Soc* **141**, 10948-10952 (2019).
151. Linna An, M.S., Long Tran, Sagardip Majumder, Inna Goreshnik, Gyu Rie Lee, David Juergens, Justas Dauparas, Ivan Anishchenko, Brian Coventry, Asim K. Bera, Alex Kang, Paul M. Levine, Valentina Alvarez, Arvind Pillai, Christoffer Norn, David Feldman, Dmitri Zorine, Derrick R. Hicks, Xinting Li, Mariana Garcia Sanchez, Dionne K. Vafeados, Patrick J. Salveson, Anastassia A. Vorobieva, David Baker De novo design of diverse small molecule binders and sensors using Shape Complementary Pseudocycles. *bioRxiv* (2023).
152. Gyu Rie Lee, S.J.P., Christoffer Norn, Doug Tischer, Justas Dauparas, Ivan Anischenko, Jaron A. M. Mercer, Alex Kang, Asim Bera, Hannah Nguyen, Inna Goreshnik, Dionne Vafeados, Nicole Roullier, Hannah L. Han, Brian Coventry, Hugh K. Haddox, David R. Liu, Andy Hsien-

- Wei Yeh, David Baker Small-molecule binding and sensing with a designed protein family. *bioRxiv* (2023).
153. Justas Dauparas, G.R.L., Robert Pecoraro, Linna An, Ivan Anishchenko, Cameron Glasscock, D. Baker Atomic context-conditioned protein sequence design using LigandMPNN. *bioRxiv* (2023).
 154. Zhang, J.Z. et al. Computationally designed sensors detect endogenous Ras activity and signaling effectors at subcellular resolution. *Nat Biotechnol* (2024).
 155. Quijano-Rubio, A. et al. De novo design of modular and tunable protein biosensors. *Nature* **591**, 482-487 (2021).
 156. Xi, C., Diao, J. & Moon, T.S. Advances in ligand-specific biosensing for structurally similar molecules. *Cell Syst* **14**, 1024-1043 (2023).
 157. Koveal, D. Functional principles of genetically encoded fluorescent biosensors for metabolism and their quantitative use. *J Neurochem* (2023).
 158. Koveal, D. et al. A high-throughput multiparameter screen for accelerated development and optimization of soluble genetically encoded fluorescent biosensors. *Nat Commun* **13**, 2919 (2022).
 159. McMahan, S.M. & Jackson, M.B. An Inconvenient Truth: Calcium Sensors Are Calcium Buffers. *Trends Neurosci* **41**, 880-884 (2018).
 160. Sun, F. et al. Next-generation GRAB sensors for monitoring dopaminergic activity in vivo. *Nat Methods* **17**, 1156-1166 (2020).
 161. Hefendehl, J.K. et al. Mapping synaptic glutamate transporter dysfunction in vivo to regions surrounding Abeta plaques by iGluSnFR two-photon imaging. *Nat Commun* **7**, 13441 (2016).
 162. Dana, H. et al. Sensitive red protein calcium indicators for imaging neural activity. *Elife* **5** (2016).
 163. Grimm, J.B. et al. A general method to optimize and functionalize red-shifted rhodamine dyes. *Nat Methods* **17**, 815-821 (2020).
 164. Huppertz, M.C. et al. Recording physiological history of cells with chemical labeling. *Science* **383**, 890-897 (2024).
 165. Oh, Y. et al. An orange calcium-modulated bioluminescent indicator for non-invasive activity imaging. *Nat Chem Biol* **15**, 433-436 (2019).
 166. Tian, X. et al. A luciferase prosubstrate and a red bioluminescent calcium indicator for imaging neuronal activity in mice. *Nat Commun* **13**, 3967 (2022).
 167. Lukinavicius, G. et al. Fluorescent dyes and probes for super-resolution microscopy of microtubules and tracheoles in living cells and tissues. *Chem Sci* **9**, 3324-3334 (2018).

168. Butkevich, A.N. et al. Fluorescent Rhodamines and Fluorogenic Carbopyronines for Super-Resolution STED Microscopy in Living Cells. *Angew Chem Int Ed Engl* **55**, 3290-3294 (2016).
169. Gibson, D.G. et al. Enzymatic assembly of DNA molecules up to several hundred kilobases. *Nat Methods* **6**, 343-345 (2009).
170. Kim, J.H. et al. High cleavage efficiency of a 2A peptide derived from porcine teschovirus-1 in human cell lines, zebrafish and mice. *PLoS One* **6**, e18556 (2011).
171. Karplus, P.A. & Diederichs, K. Linking crystallographic model and data quality. *Science* **336**, 1030-1033 (2012).
172. Malecki, M.J. et al. Leukemia-associated mutations within the NOTCH1 heterodimerization domain fall into at least two distinct mechanistic classes. *Mol Cell Biol* **26**, 4642-4651 (2006).
173. Mertes, N. et al. Fluorescent and Bioluminescent Calcium Indicators with Tuneable Colors and Affinities. *J Am Chem Soc* **144**, 6928-6935 (2022).
174. Zolotukhin, S. et al. Production and purification of serotype 1, 2, and 5 recombinant adeno-associated viral vectors. *Methods* **28**, 158-167 (2002).
175. Aurnhammer, C. et al. Universal real-time PCR for the detection and quantification of adeno-associated virus serotype 2-derived inverted terminal repeat sequences. *Hum Gene Ther Methods* **23**, 18-28 (2012).
176. Wardill, T.J. et al. A Neuron-Based Screening Platform for Optimizing Genetically-Encoded Calcium Indicators. *Plos One* **8** (2013).
177. Schindelin, J. et al. Fiji: an open-source platform for biological-image analysis. *Nat Methods* **9**, 676-682 (2012).
178. Otsu, N. A Threshold Selection Method from Gray-Level Histograms. *IEEE Transactions on Systems, Man, and Cybernetics* **9**, 62-66 (1979).
179. Theis, M. & Buchholz, F. MISSION esiRNA for RNAi screening in mammalian cells. *J Vis Exp* (2010).

Appendix

Protein sequences

Static FRET constructs

>ChemoG5

MVSKGEELFTGVVPIIVELDGDVNGHKFSVSSEGEEDATYGKLTTLKFICTTGKLPVPWPT-
 LVTTTLTYGVQCFSRYPDHMKQHDFFKSAMPEGYVQERTIFFKDDGNYKTRAEVKFEGDTLVNRIELKGIDFKEDGNI
 LGHKLEYNNSHNVIYIMADKQKNGIKVNFKIRHNIEDGVSQVLADHYQONTPIGDGPVLL-
 PDNHYLSTQS¹LSKDPNEKRDHMLLEFV²AAGITLGMDELYKIGTGFPFDPHYVEVLGERMHYVDVGPRDGTPLVF
 LHGNPTSSYVWRNIIPHVAPTHRCIAPDLIGMGKSDKPDLYFFDDHVRFMDFIEAL-
 GLEEVVLVIHDWGSALGFHWAKRNPERVKGIAFMFIRPIPTWDEWP³FAR⁴TFQAFRTTDVGRKLIIDQNVFIEGT
 LPMGVVRLTEVEMDHYREPFLNPVDREPLWRFPNELPIAGEPA-
 NIVALVEEYMDWLHQSPVPKLLFWGTPGVLIIPAEARLAKSLPNCKAVDIGPG⁵NLLQEDNPDIGSEIARWLSTL
 EISG

>ChemoB

MVSKGEELFTGVVPIIVELDGDVNGHKFSVRSEGEEDATY¹GKLTTLKFICTTGKLPVPWPT-
 LVTTLSHGVCFFARYPDHMKQHDFFKSAMPEGYVQERTIFFKDDGTYKTRAEVKFEGDTLVNRIELKGVDFKEDGNI
 LGHKLEYNFNSHNIYIMAVKQKNGIKVNFKIRHNVEDGVSQVLADHYQONTPIGDGPVLL-
 PDSHYLSTQS²LSKDPNEKRDHMLLEFR³AAGITLGMDELYKIGTGFPFDPHYVEVLGERMHYVDVGPRDGTPLVF
 LHGNPTSSYVWRNIIPHVAPTHRCIAPDLIGMGKSDKPDLYFFDDHVRFMDFIEAL-
 GLEEVVLVIHDWGSALGFHWAKRNPERVKGIAFMFIRPIPTWDEWP⁴FAR⁵TFQAFRTTDVGRKLIIDQNVFIEGT
 LPMGVVRLTEVEMDHYREPFLNPVDREPLWRFPNELPIAGEPA-
 NIVALVEEYMDWLHQSPVPKLLFWGTPGVLIIPAEARLAKSLPNCKAVDIGPG⁶NLLQEDNPDIGSEIARWLSTL
 EISG

>ChemoC

MVSKGEELFTGVVPIIVELDGDVNGHKFSVSSEGEEDATYGKLTTLKFICTTGKLPVPWPT-
 LVTTLSWGVQCFARYPDHMKQHDFFKSAMPEGYVQERTIFFKDDGNYKTRAEVKFEGDTLVNRIELKGIDFKEDGNI
 LGHKLEYNAIHGNVIYITADKQKNGIKANFGLNCNIEDGVSQVLADHYQONTPIGDGPVLL-
 PDNHYLSTQS¹LSKDPNEKRDHMLLEFV²AAGITLGMDELYKIGTGFPFDPHYVEVLGERMHYVDVGPRDGTPLVF
 LHGNPTSSYVWRNIIPHVAPTHRCIAPDLIGMGKSDKPDLYFFDDHVRFMDFIEAL-
 GLEEVVLVIHDWGSALGFHWAKRNPERVKGIAFMFIRPIPTWDEWP³FAR⁴TFQAFRTTDVGRKLIIDQNVFIEGT
 LPMGVVRLTEVEMDHYREPFLNPVDREPLWRFPNELPIAGEPA-
 NIVALVEEYMDWLHQSPVPKLLFWGTPGVLIIPAEARLAKSLPNCKAVDIGPG⁵NLLQEDNPDIGSEIARWLSTL
 EISG

>ChemoY

MVSKGEELFTGVVPIIVELDGDVNGHKFSVSSEGEEDATYGKLTTLKLICTTGKLPVPWPT-
 LVTTTLGYGLQCFARYPDHMKQHDFFKSAMPEGYVQERTIFFKDDGNYKTRAEVKFEGDTLVNRIELKGIDFKEDGNI
 LGHKLEYNNSHNVIYITADKQKNGIKANFKIRHNIEDGGVQLADHYQONTPIGDGPVLL-
 PDNHYLSYQS¹LSKDPNEKRDHMLLEFV²AAGITLGMDELYKIGTGFPFDPHYVEVLGERMHYVDVGPRDGTPLVF
 LHGNPTSSYVWRNIIPHVAPTHRCIAPDLIGMGKSDKPDLYFFDDHVRFMDFIEAL-
 GLEEVVLVIHDWGSALGFHWAKRNPERVKGIAFMFIRPIPTWDEWP³FAR⁴TFQAFRTTDVGRKLIIDQNVFIEGT

LPMGVVRPLTEVEMDHYREPFLNPDREPLWRFPNELPIAGEPA-
NIVALVEEYMDWLHQSPVPKLLFWGTPGVLIPPAEAAARLAKSLPNCKAVDIGPGNLLQEDNPDIGSEIARWLSTL
EISG

>ChemoR

MVSKGEAVIKEFMRFKVHMEGSMNGHEFEIEGEGEGRPYEGTQTAKLKVTKGGPLPFSWDIL-
SPQFMYGSRAFTKHPADIPDYKQSFPEGFKWERVMNFEDGGAVTVTQDTSLEDGTLIYKVKLRGTNFPDGPVMQK
KTMGWEASTERLYPEDGVLKGDIKMALRLKDGGRYLADFKTTYKAKKPVQMP-
GAYNVDRKLIITSHNEDYTVVEQYERSEGRHSTGGMDELYKIGTGFPFDPHYVEVLGERMHYVDVGPDRGTPVLFLH
GNPTSSYVWRNIIIPHVAPTHRCIAPDLIGMGKSDKPDLYFFDDHVRFMDFIEAL-
GLEEVVLVIHDWGSALGFHWAKRNPERVKGIAFMEFIRPIPTWDEWPEFARETFOAFRTTQVGRKLIIDQNVFIEGT
LPMGVVRPLTEVEMDHYREPFLNPDREPLWRFPNELPIAGEPA-
NIVALVEEYMDWLHQSPVPKLLFWGTPGVLIPPAEAAARLAKSLPNCKAVDIGPGLNLLQEDNPDIGSEIARWLSTL
EISG

EGFP, EBFP2, mCerulean3, Venus, mScarlet, HaloTag7

Interface mutations

Calcium sensors

>ChemoG-CaM

MVSKGEELFTGVVPIIIVELDGDVNGHKFSVSGEGEGDATYGKLTTLKFICTTGKLPVPWPPT-
 LVTTTLTYGVQCFRSRYPDHMKQHDFFKSAMPEGYVQERTIFFKDDGNYKTRAEVKFEEDTLVNRIELKGIDFKEDGNI
 LGHKLEYNNSHNHYIMADKQKNGIKVNFKIRHNIEDGVSQVLADHYQONTPIGDGPVLL-
 PDNHYLSTQSKLSKDPNEKRDMVLLLEFVTAAGITGGTLPDQLTEEQIAEFKEAFSLFDKDGDTITTKELGTMRS
 LGQNPTAEALQDMINEVDADGDGTIDFPEFLTMMARKMKD TDSEEEIREAFRVFDKDGNGYI-
 SAAELRHVMTNLGEKLTDEEVDEMIREADIDGDGQVNYEEFVVMMTAK**EFPPPPPPPPPPPPPPPPPPPPPPPPPPPP**
PPPGGSMVDSSRRKFNKTGKALRAIGRLSSLESSGGIGTGFPFDPHYVEVLGERMHYVDVGPRDGT PVLFLHGNPTSS
 YVWRNIIPHVAPTHRCIAPDLIGMGKSDKPDLYFFDDHVRFMDFIEALGLEEVVLI-
 HDWGSALGFHWAKRNPVVKIAFMFIRPIPTWDEWPEFARETFOAFRTTDVGRKLIIDQNVFIEGTLPMGVVRPL
 TEVEMDHYREPFLNPVDREPLWRFPNELPIAGEPA-
 NIVALVEEYMDWLHQSPVKLLFWGTPGVLIIPPAEAARLAKSLPNCKAVDIGPGENLLQEDNPDLIGSEIARWLSTL
 EISG

>ChemoB-CaM

MVSKGEELFTGVVPIIIVELDGDVNGHKFSVRGEGEGDATY**G**KLTTLKFICTTGKLPVPWPPT-
 LVTTLSHGVCFARYPDHMKQHDFFKSAMPEGYVQERTIFFKDDGTYKTRAEVKFEEDTLVNRIELKGVDFKEDGNI
 LGHKLEYNFNSHNHYIMAVKQKNGIKVNFKIRHNVEDGVSQVLADHYQONTPIGDGPVLL-
 PDSHYLSTQSKLSKDPNEKRDMVLLLEFRTAAGITGGTLPDQLTEEQIAEFKEAFSLFDKDGDTITTKELGTMRS
 LGQNPTAEALQDMINEVDADGDGTIDFPEFLTMMARKMKD TDSEEEIREAFRVFDKDGNGYI-
 SAAELRHVMTNLGEKLTDEEVDEMIREADIDGDGQVNYEEFVVMMTAK**EFPPPPPPPPPPPPPPPPPPPPPPPPPPPP**
PPPGGSMVDSSRRKFNKTGKALRAIGRLSSLESSGGIGTGFPFDPHYVEVLGERMHYVDVGPRDGT PVLFLHGNPTSS
 YVWRNIIPHVAPTHRCIAPDLIGMGKSDKPDLYFFDDHVRFMDFIEALGLEEVVLI-
 HDWGSALGFHWAKRNPVVKIAFMFIRPIPTWDEWPEFARETFOAFRTTDVGRKLIIDQNVFIEGTLPMGVVRPL
 TEVEMDHYREPFLNPVDREPLWRFPNELPIAGEPA-
 NIVALVEEYMDWLHQSPVKLLFWGTPGVLIIPPAEAARLAKSLPNCKAVDIGPGENLLQEDNPDLIGSEIARWLSTL
 EISG

>ChemoC-CaM

MVSKGEELFTGVVPIIIVELDGDVNGHKFSVSGEGEGDATYGKLTTLKFICTTGKLPVPWPPT-
 LVTTLSWGVCFARYPDHMKQHDFFKSAMPEGYVQERTIFFKDDGNYKTRAEVKFEEDTLVNRIELKGIDFKEDGNI
 LGHKLEYNAIHGNYITADKQKNGIKANFGLNCNIEDGVSQVLADHYQONTPIGDGPVLL-
 PDNHYLSTQSKLSKDPNEKRDMVLLLEFVTAAGITGGTLPDQLTEEQIAEFKEAFSLFDKDGDTITTKELGTMRS
 LGQNPTAEALQDMINEVDADGDGTIDFPEFLTMMARKMKD TDSEEEIREAFRVFDKDGNGYI-
 SAAELRHVMTNLGEKLTDEEVDEMIREADIDGDGQVNYEEFVVMMTAK**EFPPPPPPPPPPPPPPPPPPPPPPPPPPPP**
PPPGGSMVDSSRRKFNKTGKALRAIGRLSSLESSGGIGTGFPFDPHYVEVLGERMHYVDVGPRDGT PVLFLHGNPTSS
 YVWRNIIPHVAPTHRCIAPDLIGMGKSDKPDLYFFDDHVRFMDFIEALGLEEVVLI-
 HDWGSALGFHWAKRNPVVKIAFMFIRPIPTWDEWPEFARETFOAFRTTDVGRKLIIDQNVFIEGTLPMGVVRPL
 TEVEMDHYREPFLNPVDREPLWRFPNELPIAGEPA-
 NIVALVEEYMDWLHQSPVKLLFWGTPGVLIIPPAEAARLAKSLPNCKAVDIGPGENLLQEDNPDLIGSEIARWLSTL
 EISG

>ChemoY-CaM

MVSKGEELFTGVVPIIIVELDGDVNGHKFSVSGEGEGDATYGKLTTLKLICTTGKLPVPWPPT-
 LVTTTLGYGLQCFARYPDHMKQHDFFKSAMPEGYVQERTIFFKDDGNYKTRAEVKFEEDTLVNRIELKGIDFKEDGNI
 LGHKLEYNNSHNHYITADKQKNGIKANFKIRHNIEDGGVQLADHYQONTPIGDGPVLL-
 PDNHYLSYQSKLSKDPNEKRDMVLLLEFVTAAGITGGTLPDQLTEEQIAEFKEAFSLFDKDGDTITTKELGTMRS
 LGQNPTAEALQDMINEVDADGDGTIDFPEFLTMMARKMKD TDSEEEIREAFRVFDKDGNGYI-
 SAAELRHVMTNLGEKLTDEEVDEMIREADIDGDGQVNYEEFVVMMTAK**EFPPPPPPPPPPPPPPPPPPPPPPPPPPPP**

PPPGSMVDSSRRKFNKTGKALRAIGRLSSLES^{GG}IGTGFPFDPHYVEVLGERMHYVDVGPRDGT^{PVLF}FLHGNPTSS
YVWRNII^{PHV}APTHRCIAPDLIGMGKSDK^{PDLG}YFFDDHVR^{FMDAF}IEALGLEEV^{LV}I-
HDWGSALGFHWAKR^{NPERV}KGIAFM^EFIRPIPTWDEW^{PEFA}RET^{FQAF}RTTDVGR^{KLI}IDQNV^{FIEG}TLPMGV^{RPL}
TEVEMDHY^{REP}FLNPVDRE^{PLWR}FPNELPIAGEPA-
NIVALVEEYMDWLHQSPV^{PKLL}FWGT^{PGVLI}PPAEAAR^{LAKSL}PNCKAVD^{IGP}GENLLQEDNPDLIGSEIARWLSTL
EISG

>ChemoR-CaM

MVSKGEELIKENMRMKVMEGSVNGHQFKCTGEGEGNPYMG^{TQ}TMRIK^{VI}E^{GG}PLPFAFD-
ILATSFMYGSRT^{FI}KYPK^{GIP}DF^{FF}KQ^{SF}PEGFT^{WERV}TRYEDGGV^{VTVM}QD^{TS}LEDG^{CLV}YHV^{QV}RGV^{NF}PSNG^{PVM}
QKKT^{KG}WEPNTE^{MMY}PADGGL^{RGY}THMALKVDGGG^{HLS}CSFV^{TTY}RSK^{KT}VG^{NI}KMPG^IHAV-
DHRLE^{LEE}SDNEM^{FV}VQ^{RE}HAVAK^{FAG}LGGG^{MDEL}YK^{GGT}LPD^{QL}TEE^QIAEF^KEAF^{SL}FDK^{DG}DTIT^{TK}ELG^{TV}
M^{RS}LQ^{NP}TEAELQ^{DM}INEVDADGD^{GT}ID^FPE^{FL}T^{MM}ARK^{MK}DT^DSEEE^IREAF-
RV^{FD}K^{DG}NG^{YI}SAAEL^{RHV}MTNLGE^{KL}TDEE^VDEMI^{READ}ID^GD^GQ^VNYEE^{FV}VM^{TAKE}EFPPPPPPPPPPPPPPPP
PPPPPPPPPPPPPPGGSMVDSSRRKFNKTGKALRAIGRLSSLES^{GG}IGTGFPFDPHYVEVLGERMHYVDVGPRDGT^P
V^LFLHGNPTSSYVWRNII^{PHV}APTHRCIAPDLIGMGKSDK^{PDLG}YFFDDHVR^{FMDAF}IEAL-
GLEEV^{LV}IHDWGSALGFHWAKR^{NPERV}KGIAFM^EFIRPIPTWDEW^{PEFA}RET^{FQAF}RTTDVGR^{KLI}IDQNV^{FIEG}T
LPMGV^{RPL}TEVEMDHY^{REP}FLNPVDRE^{PLWR}FPNELPIAGEPA-
NIVALVEEYMDWLHQSPV^{PKLL}FWGT^{PGVLI}PPAEAAR^{LAKSL}PNCKAVD^{IGP}GENLLQEDNPDLIGSEIARWLSTL
EISG

>ChemoL-CaM

MGLSGDQMGQIEKIFKV^{VY}PVDDH^{HF}KVILHYG^{TL}VIDG^{VT}PNMID^{YF}GR^{PY}E^GIAV^{FD}GK-
KITVT^{GT}LWNG^{NKI}IDER^LINPD^GSL^LFRV^TING^{VT}GW^RL^CERILAG^{GT}GG^{SG}GTGGSMV^{FT}LE^DFV^DWR^QTAG^{YN}
LDQV^{LE}QGG^{VSS}LFQ^NLGV^{SV}TP^IQR^IVL^SGEN^LKID^IH^{VI}I^PYEV^SKGEEL^{FT}GV^PIL-
VELD^{GD}VNG^HK^FSVS^GEGEG^DATY^GKL^TLK^FICT^TGK^LPV^PW^PTL^VT^TLT^YGV^QCF^SRY^PDM^KQ^HD^FF^KSAM^{PE}GY
VQ^{ERT}I^FFK^{DD}GN^{YK}TRAE^VK^FEG^DTL^VN^RIEL^KGID^FKED^GN^IL^GH^KLE^YN^YNS^HN^VY^I-
MAD^KQ^KNG^IK^VN^FKIR^HN^IED^GSV^QLAD^HY^QNT^PIG^DGP^VLL^{PD}N^HY^LST^QSLS^KDP^NE^KR^DH^MV^LLE^FV^TAAG^I
TGG^TLPD^{QL}TEE^QIAEF^KEAF^{SL}FDK^{DG}DTIT^{TK}ELG^{TV}M^{RS}LQ^{NP}TEAEL-
Q^{DM}INEVDADGD^{GT}ID^FPE^{FL}T^{MM}ARK^{MK}DT^DSEEE^IREAF^RV^{FD}K^{DG}NG^{YI}SAAEL^{RHV}MTNLGE^{KL}TDEE^VDEMI
READ^{ID}G^DG^QV^{NY}EE^{FV}VM^{TAKE}-
FPPPPPPPPPPPPPPPPPPPPPPPPPPPPPPPPPPGGSMVDSSRRKFNKTGKALRAIGRLSSLES^{GG}IGTGFPFDPHYVEV
LGERMHYVDVGPRDGT^{PVLF}FLHGNPTSSYVWRNII^{PHV}APTHRCIAPDLIGMGK^S-
DKPDLG^{YFF}DDHVR^{FMDAF}IEALGLEEV^{LV}IHDWGSALGFHWAKR^{NPERV}KGIAFM^EFIRPIPTWDEW^{PEFA}RET^F
QAF^{RT}TDVGR^{KLI}IDQNV^{FIEG}TLPMGV^{RPL}TEVEMDHY^{REP}FLNPVDRE^{PLWR}FPNEL-
PIAGEPANIVALVEEYMDWLHQSPV^{PKLL}FWGT^{PGVLI}PPAEAAR^{LAKSL}PNCKAVD^{IGP}GENLLQEDNPDLIGSEI
ARWLSTLEISG

EGFP, EBFP2, mCerulean3, Venus, mRuby2, cpNanoLuc, HaloTag7

Calmodulin, M13 peptide, Linker

Interface mutations

ATP sensors

>ChemoG-ATP

MVSKGEELFTGVVPIVELDGDVNGHKFSVSGEGEGDATYGKLTTLKFICTTGKLPVPWPPT-
 LVTTLLTYGVQCFRSRYPDHMKQHDFFKSAMPEGYVQERTIFFKDDGNYKTRAEVKFECDTLVNRIELKGIDFKEDGNI
 LGHKLEYNYNSHNVYIMADKQKNGIKVNFKIRHNIEDGSQLADHYQONTPIGDGPVLL-
 PDNHYLSTQSLSKDPNEKRDMVLLLEFVTAAGITGGGMKTVKVNITTPDGPVYDADIEMVSVRAESGDLGILPGHI
 PTKAPLKI GAVRLKKDGQTEMVAVSGGTVEVRPDHVTINAQAAETAEGIDKE-
 RAEAAARQRAQERLNSQSDDTDIRRAELALQRALNRLDVAGKANEFGGGIGTGFPFDPHYVEVLGERMHYVDVGPDRG
 TPVFLFHGNPTSSYVWRNII PHVAPTHRCIAPDLIGMGKSDKPDLYFFDDHVRFMDFIE-
 ALGLEEVVLVIHDWGSALGFHWAKRNPERVKGIAFMFIRPIPTWDEWPEFARETFQAFRTTVDVGRKLIIDQNVFIE
 GTLPMGVVRPLTEVEMDHYREPFLNPVDREPLWRFPNELPIAGEPA-
 NIVALVEEYMDWLHQSPVPKLLFWGTPGVLI PPAEAARLAKSLPNCKAVDIGPGENLLQEDNPDIGSEIARWLSTL
 EISG

>ChemoB-ATP

MVSKGEELFTGVVPIVELDGDVNGHKFSVRGEGEGDATY G KLTTLKFICTTGKLPVPWPPT-
 LVTTLSHGVCFAFYDPHMKQHDFFKSAMPEGYVQERTIFFKDDGTYKTRAEVKFECDTLVNRIELKGVDFKEDGNI
 LGHKLEYNFNSHNIYIMAVKQKNGIKVNFKIRHNVEDGSQLADHYQONTPIGDGPVLL-
 PDSHYLSTQSLSKDPNEKRDMVLLLEFRTAAGITGGGMKTVKVNITTPDGPVYDADIEMVSVRAESGDLGILPGHI
 PTKAPLKI GAVRLKKDGQTEMVAVSGGTVEVRPDHVTINAQAAETAEGIDKE-
 RAEAAARQRAQERLNSQSDDTDIRRAELALQRALNRLDVAGKANEFGGGIGTGFPFDPHYVEVLGERMHYVDVGPDRG
 TPVFLFHGNPTSSYVWRNII PHVAPTHRCIAPDLIGMGKSDKPDLYFFDDHVRFMDFIE-
 ALGLEEVVLVIHDWGSALGFHWAKRNPERVKGIAFMFIRPIPTWDEWPEFARETFQAFRTTVDVGRKLIIDQNVFIE
 GTLPMGVVRPLTEVEMDHYREPFLNPVDREPLWRFPNELPIAGEPA-
 NIVALVEEYMDWLHQSPVPKLLFWGTPGVLI PPAEAARLAKSLPNCKAVDIGPGENLLQEDNPDIGSEIARWLSTL
 EISG

>ChemoR-ATP

MVSKGEELIKENMRMKVMEGSVNGHQFKCTGEGEGNPYMGQTQTMRIKVIIEGGPLPFAFD-
 ILATSFMYGSRTFIKYPKGI P DFFKQSFPEGFTWERVTRYEDGGVVTVMQDTSLEDGCLVYHVQVRGVNFPSNGPVM
 QKKTGWEPNTEMMYPADGGLRGYTHMALKVDGGHLSCSFVTTYRSKKTVGNIKMPGIHAV-
 DHRLEERLEESDNEMFVVQREHAVAKFAGLGGGMDELYKGGGMKTVKVNITTPDGPVYDADIEMVSVRAESGDLGILP
 GHIPTKAPLKI GAVRLKKDGQTEMVAVSGGTVEVRPDHVTINAQAAETAEGIDKE-
 RAEAAARQRAQERLNSQSDDTDIRRAELALQRALNRLDVAGKANEFGGGIGTGFPFDPHYVEVLGERMHYVDVGPDRG
 TPVFLFHGNPTSSYVWRNII PHVAPTHRCIAPDLIGMGKSDKPDLYFFDDHVRFMDFIE-
 ALGLEEVVLVIHDWGSALGFHWAKRNPERVKGIAFMFIRPIPTWDEWPEFARETFQAFRTTVDVGRKLIIDQNVFIE
 GTLPMGVVRPLTEVEMDHYREPFLNPVDREPLWRFPNELPIAGEPA-
 NIVALVEEYMDWLHQSPVPKLLFWGTPGVLI PPAEAARLAKSLPNCKAVDIGPGENLLQEDNPDIGSEIARWLSTL
 EISG

>ChemoL-ATP

MGLSGDQMGQIEKIFKVVPVDDHHFKVILHYGTLVIDGVTNPMIDYFGRPYEGIAVFDGK-
 KITVTGTLWNGNKIIDERLINPDGSLFRVVTINGVTGWRLCERILAGGTGGSGGTGGSMVFTLEDFVGDWRQTAGYN
 LDQVLEQGGVSSLFQNLGVSVTPIQRIVLSENGLKIDIHVII PYEVSKEELFTGVVPI-
 VELDGDVNGHKFSVSGEGEGDATYGKLTTLKFICTTGKLPVPWPPTLVTTLLTYGVQCFRSRYPDHMKQHDFFKSAMPEGY
 VQERTIFFKDDGNYKTRAEVKFECDTLVNRIELKGIDFKEDGNILGHKLEYNYNSHNVYI-
 MADKQKNGIKVNFKIRHNIEDGSQLADHYQONTPIGDGPVLLPDNHYLSTQSLSKDPNEKRDMVLLLEFVTAAGI
 TGGGMKTVKVNITTPDGPVYDADIEMVSVRAESGDLGILPGHIPTKAPLKI GAVRL-
 KKDQTEMVAVSGGTVEVRPDHVTINAQAAETAEGIDKERAEAAARQRAQERLNSQSDDTDIRRAELALQRALNRLDV

AGKANEFGGGIGTGFPFDPHYVEVLGERMHYVDVGPRDGT PVLFLHGNPTSSYVWRNIIPH-
VAPTHRCIAPDLIGMGKSDKPD LGYFFDDHVRFM DAFIEALGLEEVVLVIHDWGSALGFHWAKRNP ERVKGI AFMEF
IRPIPTWDEWPEFARETFQAFRTTDVGRKLIIDQNVFIEGTLPMGVVRPLTEVEMDHYREP-
FLNPVDREPLWRFPNELPIAGEPANIVALVEEYMDWLHQSPVPKLLFWGTPGVLI PPAAEARLAKSLPNCKAVDIGP
G²NLLQEDNPDLIGSEIARWLSTLEISG

EGFP, EBFP2, mRuby2, cpNanoLuc, HaloTag7

F_O-F₁ ϵ subunit, Linker

Interface mutation

NAD⁺ sensors

>ChemoG-NAD

MVSKGEELFTGVVPIVELDGDVNGHKFSVSGEGEGDATYGKLTTLKFICTTGKLPVPWPT-
 LVTTLLTYGVQCFSRYPDHMKQHDFFKSAMPEGYVQERTIFFKDDGNYKTRAEVKFEGDTLVNRIELKGIDFKEDGNI
 LGHKLEYNNSHNVIYIMADKQKNGIKVNFKIRHNIEDGSQLADHYQONTPIGDGPVLL-
 PDNHYLSTQSLSKDPNEKRDHMLLEFVLAAGITGGTMTLEEARKRVNELRDLIRYHNYRYVVLADPEISDAEYDR
 LLRELKELEERFPELKS PDSPTLQVGARPLEATFRPVRHPTRMYSLDNFNLDELKA FEERI -
 ERALGRKGPFAYTVEHLDVGLSVNLYYEEGVLVYGATRGDGEVGEVETQNLTTIPTIPRRLKGVPERLEVRGEVYMP
 IEAFLRLNEELEERGERIFKNPRNAAAGSLRQKDPRI TAKRGLRAT -
 FWALGLGLEEVEREGVATQFALLHWLKEKGFVVEHGYARAVGAEGVEAVYQDWLKKRRALPFEANGVAVKLDDELALW
 RELGYTARAPRFAIAYKFPSSG-
 GIGTGFPFDPHYVEVLGERMHYVDVGPRDGT PVLFLHGNPTSSYVWRNII PHVAPTHRCIAPDLIGMGKSDKPD LGY
 FFDDHVRFMDAFIEALGLEEVVLIHDWGSALGFHWAKRNPERVKGI AFMEFIRPIPTWDEW-
 PEFARETFQAFRTT DVGRKLIIDQNVFIEGTLPMGVVRPLTEVEMDHYREPFLNPVDREPLWRFPNELPIAGEPANI
 VALVEEYMDWLHQSPVPKLLFWGTPGVLI PPAEAARLAKSLPNCKAVDIG-
 PGNLLQEDNPDLIGSEIARWLSTLEISG

>ChemoB-NAD

MVSKGEELFTGVVPIVELDGDVNGHKFSVRGEGEGDATY G KLTTLKFICTTGKLPVPWPT-
 LVTTLSHGVCFARYPDHMKQHDFFKSAMPEGYVQERTIFFKDDGYKTRAEVKFEGDTLVNRIELKGVDFKEDGNI
 LGHKLEYNFNSHNIYIMAVKQKNGIKVNFKIRHNVEDGSQLADHYQONTPIGDGPVLL-
 PDSHYLSTQSLSKDPNEKRDHMLLEFVLAAGITGGTMTLEEARKRVNELRDLIRYHNYRYVVLADPEISDAEYDR
 LLRELKELEERFPELKS PDSPTLQVGARPLEATFRPVRHPTRMYSLDNFNLDELKA FEERI -
 ERALGRKGPFAYTVEHLDVGLSVNLYYEEGVLVYGATRGDGEVGEVETQNLTTIPTIPRRLKGVPERLEVRGEVYMP
 IEAFLRLNEELEERGERIFKNPRNAAAGSLRQKDPRI TAKRGLRAT -
 FWALGLGLEEVEREGVATQFALLHWLKEKGFVVEHGYARAVGAEGVEAVYQDWLKKRRALPFEANGVAVKLDDELALW
 RELGYTARAPRFAIAYKFPSSG-
 GIGTGFPFDPHYVEVLGERMHYVDVGPRDGT PVLFLHGNPTSSYVWRNII PHVAPTHRCIAPDLIGMGKSDKPD LGY
 FFDDHVRFMDAFIEALGLEEVVLIHDWGSALGFHWAKRNPERVKGI AFMEFIRPIPTWDEW-
 PEFARETFQAFRTT DVGRKLIIDQNVFIEGTLPMGVVRPLTEVEMDHYREPFLNPVDREPLWRFPNELPIAGEPANI
 VALVEEYMDWLHQSPVPKLLFWGTPGVLI PPAEAARLAKSLPNCKAVDIG-
 PGNLLQEDNPDLIGSEIARWLSTLEISG

>ChemoR-NAD

MVSKGEELIKENMRMKVVMESVNGHQFKCTGEGEGNPYMGQTMTRIKVIIEGGPLPFAFD-
 ILATSFMYGSRTFIKYPKGI P DFFKQSFPEGFTWERVTRYEDGGVVTVMQDTSLEDGCLVYHVQVRGVNFPSNGPVM
 QKKTGWEPNTEMMPADGGLRGYTHMALKVDGGGHLSCSFVTTYRSKKT VGNIKMPGIHAV-
 DHRLERLEESDNEMFVQREHAVAKFAGLGGGMDELYKGGTMTLEEARKRVNELRDLIRYHNYRYVVLADPEISDAE
 YDRLLRELKELEERFPELKS PDSPTLQVGARPLEATFRPVRHPTRMYSLDNFNLDELKA -
 FEERIERALGRKGPFAYTVEHLDVGLSVNLYYEEGVLVYGATRGDGEVGEVETQNLTTIPTIPRRLKGVPERLEVRG
 EYMPIEAFRLRLNEELEERGERIFKNPRNAAAGSLRQKDPRI TAKRGLRATFWALGLGLEE-
 VEREGVATQFALLHWLKEKGFVVEHGYARAVGAEGVEAVYQDWLKKRRALPFEANGVAVKLDDELALWRELGYTARAP
 RFAIAYKFPSSGGIGTGFPFDPHYVEVLGERMHYVDVGPRDGT PVLFLHGNPTSSYV-
 WRNII PHVAPTHRCIAPDLIGMGKSDKPD LGYFFDDHVRFMDAFIEALGLEEVVLIHDWGSALGFHWAKRNPERVK
 GI AFMEFIRPIPTWDEWPEFARETFQAFRTT DVGRKLI -
 IDQNVFIEGTLPMGVVRPLTEVEMDHYREPFLNPVDREPLWRFPNELPIAGEPANI VALVEEYMDWLHQSPVPKLLF
 WGT PGVLI PPAEAARLAKSLPNCKAVDIG PGNLLQEDNPDLIGSEIARWLSTLEISG

>ChemoD-NAD

MVSKGEELFTGVVPIILVELDGDVNGHKFSVSSEGEDATYGKLTLLKLICTTGKLPVPWPPT-
LVTTFFGYGLMCFARYPDHMKQHDFFKSAMPEGYVQERTIFFKDDGNYKTRAEVKFEEDTLVNRIELKGIDFKEDGNI
LGHKLEYNWNNSHNVIIMADKQKNGIKVNFKIRHNIEDGSVQLADHYQONTPIGDGPVLL-
PDNHYLSTQSKLSKDPNEKRDHMLLEFVRAAGITGGTMTLEEARKRVNELRDLIRYHNYRYVVLADPEISDAEYDR
LLRELKELEERFPELKSPDSPTLQVGARPLEATFRPVRHPTRMYSLDNAFNLDELKAFEERI-
ERALGRKGPFAYTVEHVDGLSVNLYEEGVLVYGATRGEVGEVETQNLITPTIPRRLKGVPERLEVRGEVYMP
IEAFRLNNEELEERGERIFKNPRNAAAGSLRQKDPRI TAKRGLRAT-
FWALGLGLEEVEREGVATQFALLHWLKEKGFVVEHGYARAVGAEGVEAVYQDWLKKRRALPFEANGVAVKLEDELALW
RELGYTARAPRFAIAYKFPSSG-
GIGTGFPFDPHYVEVLGERMHYVDVGRDGT PVLFLHGNPTSSYVWRNII PHVAPTHRCIAPDLIGMGKSDKPDLY
FFDDHVRFMDAFIEALGLEEVVLVIHDWGSALGFHWAKRNPVERVKGI AFMEFIRPIPTWDEW-
PEFARETFQAFRTT DVGRKLIIDQNVFIEGTLPMGVVRPLTEVEMDHYREPFLNPVDREPLWRFPNELPIAGEPANI
VALVEEYMDWLHQSPVPKLLFWGTPGVLI PPAAEARLAKSLPNCKAVDIG-
PGENLLQEDNPDLIGSEIARWLSTLEISG

>ChemoL-NAD

MGLSGDQMGQIEKIFKVVPVDDHHFKVILHYGTLVIDGVTNPMIDYFGRPYEGIAVFDGK-
KITVTGTLWNGNKIIDERLINPDGSLFRVTVINGVTGWRLCERILAGGTGGSGGTGGSMVFTLEDFVGDWRQTAGYN
LDQVLEQGGVSSLFQNLGVSVTPIQRIVLSGENGLKIDIHVIIPYEVSKEELFTGVVPIIL-
VELDGDVNGHKFSVSSEGEDATYGKLTLLKFICTTGKLPVPWPPTLVTTLTYGVCFSRYPDHMKQHDFFKSAMPEGY
VQERTIFFKDDGNYKTRAEVKFEEDTLVNRIELKGIDFKEDGNILGHKLEYNNSHNVIIMADKQKNGIKVNFKIRHNI
EDGSVQLADHYQONTPIGDGPVLLPDNHYLSTQSKLSKDPNEKRDHMLLEFVRAAGITGGTMTLEEARKRVNELRDLIRY
HNYRYVVLADPEISDAEYDRLLRELKELEERFPELKSPD-
SPTLQVGARPLEATFRPVRHPTRMYSLDNAFNLDELKAFEERIERALGRKGPFAYTVEHVDGLSVNLYEEGVLVY
GATRGEVGEVETQNLITPTIPRRLKGVPERLEVRGEVYMPIEAFRLNNEELEERGER-
IFKNPRNAAAGSLRQKDPRI TAKRGLRATFWALGLGLEEVEREGVATQFALLHWLKEKGFVVEHGYARAVGAEGVEA
VYQDWLKKRRALPFEANGVAVKLEDELALWRELGYTARAPRFAIAYKFPSSG-
GIGTGFPFDPHYVEVLGERMHYVDVGRDGT PVLFLHGNPTSSYVWRNII PHVAPTHRCIAPDLIGMGKSDKPDLY
FFDDHVRFMDAFIEALGLEEVVLVIHDWGSALGFHWAKRNPVERVKGI AFMEFIRPIPTWDEW-
PEFARETFQAFRTT DVGRKLIIDQNVFIEGTLPMGVVRPLTEVEMDHYREPFLNPVDREPLWRFPNELPIAGEPANI
VALVEEYMDWLHQSPVPKLLFWGTPGVLI PPAAEARLAKSLPNCKAVDIG-
PGENLLQEDNPDLIGSEIARWLSTLEISG

EGFP, EBFP2, mRuby2, ShadowG, cpNanoLuc, HaloTag7

ttLigA, Linker

Interface mutations

Mutations rendering *ttLigA* catalytically inactive (K116L, D288N)

Affinity mutations *ttLigA* (Y225W, V291A)

HT7^{P174W}

NMN sensor

>ChemoG-NMN

MVSKEELFTGVVPIVELDGDVNGHKFSVSSEGEEDATYGKLTTLKFICTTGKLPVPWPT-
 LVTTLLTYGVQCFSTRYPDHMKQHDFFKSAMPEGYVQERTIFFKDDGNYKTRAEVKFEQDTLVNRIELKGIDFKEDGNI
 LGHKLEYNYNSHNVIYIMADKQKNGIKVNFKIRHNIEDGQSVQLADHYQQNTPIGDGPVLL-
 PDNHYLSTQSKLSKDPNEKRDMVLLLEFVRAAGITGGTPLTLTAATTRAQELRKQLNQYSHEYVVKDQPSVEDYVYD
 RLYKELVDIETEFDDLITPDSPTQRGGKVLSGFEKAPHDIPMYSLNDGFSKEDI-
 FAFDERVRKAIGKPVAYCCELLDIDGLAISLRYENGVFVRGATRGDGTGENITENLRTVRSVPMRLTEPISVEVRGE
 CYMPKQSFVALNEEREENGQDI FANPRNAAAGSLRQLDTKIVAKRNLNTFLRTVAD-
 FGPMKAKTQFEALEELSAIGFRTNPERQLCQS IDEVWAYIEEYHEKRSTLPYEINIGIVIKVNEFALQDELGFTVKAP
 RWAIAAYKFPSSGGIGTGFPFDPHYVEVLGERMHYVDVGPRDGT PVLFLHGNPTSSYV-
 WRNII PHVAPTHRCIAPDLIGMKSDDKPDLYFFDDHVRFMDFIEALGLEEVVLIHDWGSALGFHWAKRNPVERK
 GIAFMFIRPIPTWDEWPEFARETTFQAFRTTVDVGRKLI-
 IDQNVFIEGTLPMGVVRPLTEVEMDHYREPFLNPVDREPLWRFPNELPIAGEPANIVALVEEYMDWLHQSPVPKLLF
 WGTGVLIPPAEAARLAKSLPNCKAVDIGPGLNLLQEDNPDLIGSEIARWLSTLEISG

EGFP, HaloTag7

eLigA, Linker

Interface mutations

Mutations rendering *eLigA* catalytically inactive (K116L, D288N)Affinity mutations *eLigA* (V69R)

Purification sequences

WSHPQFEKGA^{DDDDK}VPH [...] APGFSSISA^{HHHHHHHHHHH}

Strep-tag[®]II sequence, enterokinase cleavage sequence, 10x his-tag sequence, linker

^{HHHHHHHHHHH}ENLYFQGGG [...]

10x his-tag sequence, TEV cleavage sequence, linker

Localization sequences

[...] LPPLERLTL (pCDNA5 plasmids)

LQNELALKLAGLDINKTGGG [...] (pAAV2 plasmids)

Nuclear exit signal (NES)

[...] KSGLRSRADPKKKRKVDPKKKRKVDPKKKRKVGSTGSR

Nuclear localization sequence (NLS)

METDTLLLWVLLLWVPGSTGDYPYDVPDYA [...] EQKLISEED-

LNAVGDQTQEVIVVPHSLPFKVVVISAILALVVLTIISLIILIMLWQKKPR

Exterior plasma membrane localization sequence (IgKchL[...]PDGFR_{tm})

[...] MATATPVPPRMGSRAGGPTTPLSPTRL SRLQEKEELRELNDR LAVYIDKVR SLETEN-
SALQLQVTEREEVREGRELTGLKALYETELADARRALDDTARERAKLQIELGKCKAEHDQLLLNY
AKKESDLNGAQIKLREYEAALNSKDAALATALGDKKSLEGDLEDLKDQIAQLEA-
SLAAAKKQLADETLLKVDLENRCQSLTEDLEFRKSMYEEEINETRKHETRLVEVDSGRQIEYE
YKLAQALHEMREQHDAQVRLYKEELEQTYHAKLENARLSSEMNTSTVNSAREELMESRM-
RIESLSSQLSNLQKESRACLERIQELEDLLAKEKDNSRMLTDKEREMAEIRDQMQQQLNDYEQ
LLDVKLALDMEISAYRKLEGEERLKLSPSPSSRVTVSRASSRSVRT-
TRGKRKRVDVEESEASSSVSISHSASATGNVCIEEIDVDGKFIRLKN TSEQDQPMGGWEMIRKI
GDTSVSYKYTSRYVLKAGQTVTIWAANAGVTASPTDLIWKNQNSWGTGEDVKVILKNS-
QGEEVAQRSTVFKTTIPEEEEEEEEAAGVVVEEELFHQQGTPRASNRSCAIM

Nuclear envelope (LaminB1) localization sequence

4x [MSVLTPLLLRGLTGSARRLPVPRAKIHSLSVLTPLLL RGLTGSARRLPVPRAKIHSL] [...]

Mitochondrial localization sequence (Cox8) (N-terminal, 4 copies)

List of peer-reviewed publications

Lars Hellweg, Anna Edenhofer, Lucas Barck, Magnus-Carsten Huppertz, Michelle S. Frei, Mirosław Tarnawski, Andrea Bergner, Birgit Koch, Kai Johnsson & Julien Hiblot. **A general method for the development of multicolor biosensors with large dynamic ranges.** *Nature Chemical Biology* (2023).

Anka Guldenpfennig, Ann-Katrin Hopp, Lukas Muskalla, Patrick Manetsch, Fabio Raith, Lars Hellweg, Cyril Dördelmann, Deena M. Leslie Pedrioli, Kai Johnsson, Giulio Superti-Furga, Michael O. Hottiger. **Absence of mitochondrial SLC25A51 enhances PARP1-dependent DNA repair by increasing nuclear NAD⁺ levels.** *Nucleic Acids Research* (2023).

Lars Hellweg, Martin Pfeifer, Lena Chang, Mirosław Tarnawski, Andrea Bergner, Jana Kress, Julien Hiblot, Jürgen Reinhardt, Kai Johnsson, Philipp Leippe. **AspSnFR: A Genetically-Encoded Biosensor for Real-Time Monitoring of Aspartate in Live Cells.** Accepted in *Cell Chemical Biology* (2024).